Materials Science Department

Skin Interfaced, Graphene-based Bioelectronics for Biomedical Applications

Tomás Pinto e Cruz de Oliveira Pinheiro

Master in Biomedical Engineering

Doctorate in Nanotechnologies and Nanosciences

NOVA University Lisbon

November 2024

Materials Science Department

Skin Interfaced, Graphene-based Bioelectronics for Biomedical Applications

Tomás Pinto e Cruz de Oliveira Pinheiro

Master in Biomedical Engineering

Adviser: Elvira Maria Correia Fortunato
Full Professor, NOVA University Lisbon

Co-advisers: Maria Goreti Ferreira Sales
Full Professor, Universidade de Coimbra
Henrique Vazão de Almeida
Assistant Researcher, NOVA University Lisbon

Examination Committee:

Chair: Prof. Dr. Ana Aguiar-Ricardo,
Full Professor, NOVA School of Science and Technology

Rapporteurs: Dr. Daniela Iacopino,
Principal Researcher, Tyndall National Institute
Prof. Cecília de Carvalho Castro e Silva,
Assistant Professor, Mackenzie Institute for Research in Graphene and Nanotechnologies

Adviser: Prof. Dr. Elvira Maria Correia Fortunato,
Full Professor, NOVA School of Science and Technology

Members: Prof. Dr. Maria Paula Borges de Lemos Macedo,
Full Professor, NOVA Medical School
Prof. Dr. Hugo Manuel Brito Águas,
Associate Professor, NOVA School of Science and Technology
Dr. Sara Abalde-Cela,
Principal Researcher, International Iberian Nanotechnology Laboratory

Doctorate in Nanotechnologies and Nanosciences

NOVA University Lisbon
November 2024

Skin Interfaced, Graphene-based Bioelectronics for Biomedical Applications

This document was created with Microsoft Word text processor and the NOVAthesis Word template.

AGRADECIMENTOS

Os últimos 4 anos no CENIMAT foram um período extremamente gratificante de crescimento pessoal e profissional, o qual devo a um conjunto grande de pessoas, ao qual quero expressar a minha gratidão e agradecimento, pelos desafios físicos, mentais e intelectuais que culminam com o fim do doutoramento.

Esta jornada não seria possível sem agradecer aos meus orientadores, que deram um apoio crucial durante todo este percurso. Começo por agradecer à professora Elvira Fortunato, pela oportunidade de fazer parte e partilhar este espaço de trabalho fantástico e frutuoso que é o CENIMAT, pela orientação e ajuda, pelo incentivo e pelo examplo que dá aos seus alunos, de como ter uma atitude positiva e ambiciosa deve ser um requisito de qualquer investigador. Agradeço à professora Goreti Sales, pelo apoio e incentivo ao longo do trabalho, que mesmo à distância, foi sempre fundamental para afinar e melhorar o trabalho ao longo do percurso. Agradeço ao Dr. Henrique Almeida, por todas as trocas de ideias, discussões e disponibilidade ímpar, fundamentais para levar este trabalho a bom porto. E agradeço à Dr. Carolina Marques, que no período em que fez parte da equipa, deixou uma marca indelével de apoio e dedicação essenciais.

Queira também agradecer ao prof. Rodrigo Martins, que juntamente com a professora Elvira Fortunato, criaram e impulsionaram as excelentes condições a que temos acesso hoje em dia no CENIMAT&CEMOP, para fazermos a investigação de excelência que sempre nos mostram como objectivo. Obrigado pela confiaça que demonstrou em mim ao longo do percurso.

Agradeço também à Fundação para a Ciência e Tecnologia, pelo financiamento necessário para desenvolver o meu trabalho e participar no desenvolvimento da ciência em Portugal

Durante estes quatro anos de doutoramento, tive o privilégio de partilhar esta jornada com muitas pessoas, de um talento imenso e que ajudaram de forma fundamental. Começo pela Carolina Marques, que paticipou na minha jornada no CENIMAT desde o seu início, e foi sempre uma fonte de inspiração e ajuda, com a qual foi optimo ter partilhado grande parte da minha caminhada. Às minhas colegas de gabinete, Maria Pereira e Sara Silvestre. Partilhamos esta jornada, desde bolseiros a futuros doutores, e portanto muitos momentos além do trabalho. Obrigado pelos infindáveis cafés, momentos de conversa e incentivo mútuo e pelo companheirismo. Neste grupo incluo também o Henrique Almeida, obrigado pelas conversas, sobre todos os temas, do Benfica a política, e pelos desabafos que ajudaram sempre. Queria agradecer à Alexandra Gonçalves, por toda a ajuda, disponibilidade, que nos providencia as melhores condições de trabalho e um laboratório sempre a brilhar. Queria agradecer ao Emanuel Carlos, pela amizade, boa disposição e dedicação que deixa como exemplo. À Maria Morais pela partilha de laboratório, de visitas infindáveis e também o exemplo de altruísmo, por estar sempre disponível a ajudar e apagar fogos. Queria agradecer ao João Coelho, por todos os momentos de boa disposição e conselhos de como fazer o caminho de aluno de doutoramento. E a muitas outras pessoas, incluíndo o prof. Pedro Barquinha, Rita Branquinho, Joana Pinto, Hugo Águas, Rui Igreja, à Joana Neto, Catia Figueiredo, Diana Gaspar, Daniela Gomes, Marta Corvo, Jonas Deurmeier, Asal Kiazadeh, Tomás Calmeiro, Bruno Veigas, Inês Cunha, Mariana Cortinhal, Guilherme Ribeiro, Rui André, Daniel Cardoso, André Rosa, Joana Caetano entre muitos outros que com os quais tive o prazer que conviver e trabalhar.

Tenho também de agradecer ao secretariado e à gestão, pela disponibilidade e prontidão: Pedro Correia, Luís Milhano, Osvaldo Delgado, Valéria Gomes, Bárbara Nóbrega.

Agradeço muito aos meus grandes happy mestres, por serem sempre uma fonte de apoio, pela caminhada da amizade que partilhamos e continuaremos a partilhar por longos anos. Ao Bernardo Gonçalves, à Inês Marques, à Maria Afonso, à Mariana Carvalho, ao Rodrigo Lima e ao Rui Varandas.

Por fim, quero agradecer à minha grande família, pelo apoio incondicional e pelos valores que me transmitiram e permitem chegar aqui. Ao Henrique e à Catarina, pelas conversas e cervajas a más horas. Aos meus irmãos, Manuel, Martim, Carolina, Francisco e Vicente, espero ser um bom exemplo, como vocês também são, mesmo sendo o mais velho. Aos meus avós, que sempre me deram um carinho e incentivo infindáveis. Aos meus restantes primos e tios, que são muitos para enumerar, mas têm todos espaço no coração e o meu agradecimento. Á Ana, pelo interesse que sempre demonstrou pelo meu trabalho, pelo incentivo e pela ajuda. Obrigado ao meu pai, pelo exemplo do dia-a-dia, pelos sacrificios, e por todo o apoio. E à minha mãe, espero que estejas orgulhosa e continues a olhar por mim.

"Wonder is the desire of knowledge."
St. Thomas Aquinas

ABSTRACT

Carbon nanomaterials, more specifically graphene, have become highly valuable resources in the development of soft conductors, for highly conformable, epidermic biomedical devices. From the different graphene synthesis and processing techniques available nowadays, Direct Laser Writing (DLW) has become increasingly investigated, for the simultaneous synthesis and patterning of three-dimensional, porous graphene geometries, through the synthesis of Laser-Induced Graphene (LIG). Significant advancements have been made in the synthesis and translation of LIG derived from petroleum-based aromatic polymers, towards wearable device fabrication. However, the exploration of more accessible, less environmentally impactful materials derived from vegetable biomass, such as paper substrates, is lacking in comparison.

In this thesis, a longitudinal study is presented, aiming at developing LIG synthesis strategies on paper substrates, to determine their potential as suitable substrates for high efficiency graphitization and patterning, towards on-skin biomedical applications. At a first stage, focus is given on the study and optimizations of LIG synthesis and laser processing strategies to develop paper-based electrochemical sensors. At a second stage, novel strategies to develop conformable, paper-based LIG soft conducting architectures, through the development of material transfer methods, is explored. Finally, these flexible, conformable LIG architectures are translated into functional devices, where LIG bioelectrodes are explored for the acquisition of electrophysiological signals, iontophoresis-based stimulation for sweat secretion and electrochemical sweat sensing applications, for non-invasive glucose sensing.

Overall, novel laser processing strategies developed in this work include paper in the toolbox of highly efficient LIG precursors, with the developed manufacturing approaches demonstrating compatibility for on-skin, bioelectronics applications for different biomedical applications.

Keywords: Laser-induced graphene, bioelectronics, electrochemical sensors, glucose biosensors, wearable devices

RESUMO

Nanomateriais de carbono, mais especificamente o grafeno, tornaram-se recursos altamente valiosos no desenvolvimento de condutores macios, para dispositivos biomédicos epidérmicos altamente conformáveis. Das diferentes técnicas de síntese e processamento de grafeno atualmente disponíveis, Direct Laser Writing (DLW) tem sido cada vez mais investigado, para a síntese e padronização simultanea de geometrias tridimensionais e porosas de grafeno, através da síntese de Grafeno Induzido por Laser (LIG). Avanços significativos foram feitos na síntese e translação de LIG derivado de polímeros aromáticos à base de petróleo, para o fabrico de dispositivos epidermicos. No entanto, a utilização de materiais mais acessíveis e com menor impacto ambiental, derivados de biomassa vegetal, como os substratos de papel, não têm o mêsmo nível de desenvolvimento.

Nesta tese, é apresentado um estudo longitudinal, com o objetivo de desenvolver estratégias de síntese de LIG em substratos de papel, para determinar o seu potencial como substratos adequados para grafitização e padronização, para aplicações biomédicas na pele. Numa primeira fase, foi realizado um estudo focado na otimização da síntese de LIG e estratégias de processamento laser para o desenvolvimento de sensores electroquímicos baseados em papel. Numa segunda fase, novas estratégias para desenvolver arquitecturas condutoras flexíveis e conformáveis de LIG à base de papel são exploradas, através do desenvolvimento de métodos de transferência. Finalmente, a integração destas arquitecturas LIG flexíveis e conformáveis é traduzida em dispositivos funcionais, onde bioelectrodos à base de LIG são explorados para a aquisição de sinais electrofisiológicos, estimulação baseada em iontoforese para a secreção de suor e aplicações electroquímicas de deteção de suor, para deteção não invasiva de glucose.

De um modo geral, as novas estratégias de processamento laser desenvolvidas neste trabalho incluem o papel como um precursor compativel para a síntese de LIG, com as abordagens de fabrico desenvolvidas a demonstrarem compatibilidade com aplicações bioelectrónicas na pele para diferentes aplicações biomédicas.

Palavras chave: grafeno induzido por laser, bioelectronica, sensores electroquímicos, sensores de glucose, dispositivos epidermicos.

CONTENTS

LIST OF FIGURES

LIST OF TABLES

ABBREVIATIONS

AC – alternate current

ADLW -additive direct laser writing

AFM - atomic force microscopy

BGM – blood glucose meter

BR - Britton-Robisson buffer

BSA – bovine serum albumin

CAGR – compound annual growth

CE – counter electrode

CGM – continuous glucose monitor

CNT – carbon nanotube

CPE – constant phase element

CuNP – copper nanoparticles

CuOx - copper oxide

CV – cyclic voltammetry

CVD – chemical vapor deposition

CW – continuous wave

DLW – direct laser writing

ECG – electrocardiogram

EDS – energy dispersive x-ray spectroscopy

EEG – electroencephalography

EIS – electrochemical impedance spectroscopy

EMG – electromyogram

FTIR – Fourier transform infrared spectroscopy
GO – graphene oxide
GOx – glucose oxidase
HET – heterogenous electron transfer
HRP – horseradish peroxidase
IC – integrated circuit
IF – interstitial fluid
IR – infrared
IoT – internet-of-things
LEG – laser-engraved graphene
LIG – laser-induced graphene
LOD – limit of detection
LSG – laser-scribed graphene
MEM – minimum essential medium
MPA – multiphoton absorption
MSC – microsupercapacitor
NP – nanoparticles
PAH – polycyclic aromatic hydrocarbon
PBI – polybenzimidazole
PBS – phosphate buffer saline
PDMS – polydimethylsiloxane
PEI – polyetherimide
PEO – polyethylene oxide
PES – polyethersulfone
PHH – polycyclic heavy hydrocarbon
PI – polyimide
PLA – pulsed laser annealing
PLD – pulsed laser deposition
PLLA – poly-l-lactic acid
PMMA - polymethyl methacrylate
PPI – points per inch
PRF – pulse repetition frequency
PtNP – platinum nanoparticle
PU – polyurethane

PVD – physical vapor deposition
PW – pulse width
PWM – pulse width modulation
QD – quantum dots
R2R – roll-to-roll
RE – reference electrode
RMS – root mean square
RS – resistive switching
S2S – sheet-to-sheet
SCE – standard calomel electrode
SDLW – subtractive direct laser writing
SEBS - styrene-ethylene-buthylene-styrene
sEMG – surface electromyography
SHE – standard hydrogen electrode
SNR – signal-to-noise ratio
SPA – single-photon absorption
SPE – screen-printed electrode
SWV – square wave voltammetry
TDLW – transformative direct laser writing
TENG – triboelectric nanogenerator
TFT – thin-film transistor
TPA – two-photon absorption
TP-DLW – two-photon direct laser writing
TRL – technology readiness level
UV – ultraviolet
WE – working electrode
XPS – x-ray photoelectron spectroscopy
XRD – x-ray diffraction
ZnO - zinc oxide

SYMBOLS

δ	Laser beam penetration depth
λ	Wavelength
v	Frequency/scan rate
ΔE_p	Anodic-cathodic peak potential separation
Δw	Weight difference
ω_0	Laser beam radius at focus
$\omega(z)$	Laser beam radius
A	Area
A_e	Electrochemically active surface area
A_g	Electrode geometric area
aVF	Augmented vector foot
aVL	Augmented vector left
aVR	Augmented vector right
BPM	Beats per minute
C	Concentration
C/O	Carbon-oxygen element ratio
dB	Relative logarithmic unit of signal ratio
D	Diffusion coefficient

D_O	Diffusion coefficient for oxidized species
D_R	Diffusion coefficient for reduced species
E_P	Laser pulse energy
F	Faraday constant
I^2	Laser light intensity
I_D	Raman D peak intensity
I_{2D}	Raman 2D peak intensity
I_G	Raman G peak intensity
k_0	Heterogeneous electron transfer rate constant
k_e	Extinction coefficient
L_a	Crystallite size in the a plane
n	Number of electrons participating in an electrochemical reaction
R	Universal gas constant
R_{sh}	Sheet resistance
R_s	Solution resistance
R_{CT}	Charge transfer resistance
RMS	Root-mean square
rpm	Rotation per minute
RSD	Relative standard deviation
S	Sensor sensitivity
SD	Standard deviation
T	Absolute temperature
t	Time
VA	Volume-to-area ratio
V_{PP}	Peak-to-peak potential
z	laser beam defocus

1

MOTIVATION AND AIM

1.1 Societal context

One of the fastest growing trends in our society and in academic research is development of non-invasive and minimally intrusive platforms for monitorization of biophysical and biochemical parameters directly from the body [1]. These wearable sensors present themselves as alternatives to established, commercial technologies, in settings where rigid, inflexible and large designs are not suitable. As such, these devices have found applications in many sectors, including in sports [2], military [3], entertainment [4], agriculture [5] and in the healthcare sector, as tools for diagnostics and prognosis [6,7]. The constant demand for accessible, fast, reliable, and accurate diagnostic and prognostic tools has led to the need for delocalized monitorization of health status, outside clinical facilities, as evidenced, for example, by the COVID-19 pandemic [8]. Driven by this great interest in such portable, worn tools and systems, various market analysis indicate a steep increase in market values, for example with the wearable sensor market expecting a compound annual growth rate (CAGR) of around 17% until 2028 [9] and the medical wearable market expecting a CAGR of 18% until 2030 [10] (**Figure 1.1a**). More specifically in Europe, market size and growth reports for wearable medical devices predict a rise to USD 100 billion in 2033, from a value a size of USD 10.65 billion in 2023, mainly boosted by remote patient monitoring in several scenarios, including devices for vital sign monitoring, sleep monitoring and therapeutic devices, from insulin/glucose monitoring systems to rehabilitation devices [11].

Other growth factors are also associated to other aspects, including the increasing acceptance of the public towards these technologies, but also aspects related to a rise in prevalence of chronic complications, such as diabetes mellitus, and the increase in geriatric population, leading to less capacity of global healthcare systems to locally treat patients [12]. As such, different device formats have been presented for distinct sensing tasks, from wrist-worn devices, smartclothes and more recently, skin-worn electronic patches (**Figure 1.1b**) [7], that can be complementary used in clinical protocols within telemedicine schemes for personalized healthcare [13].

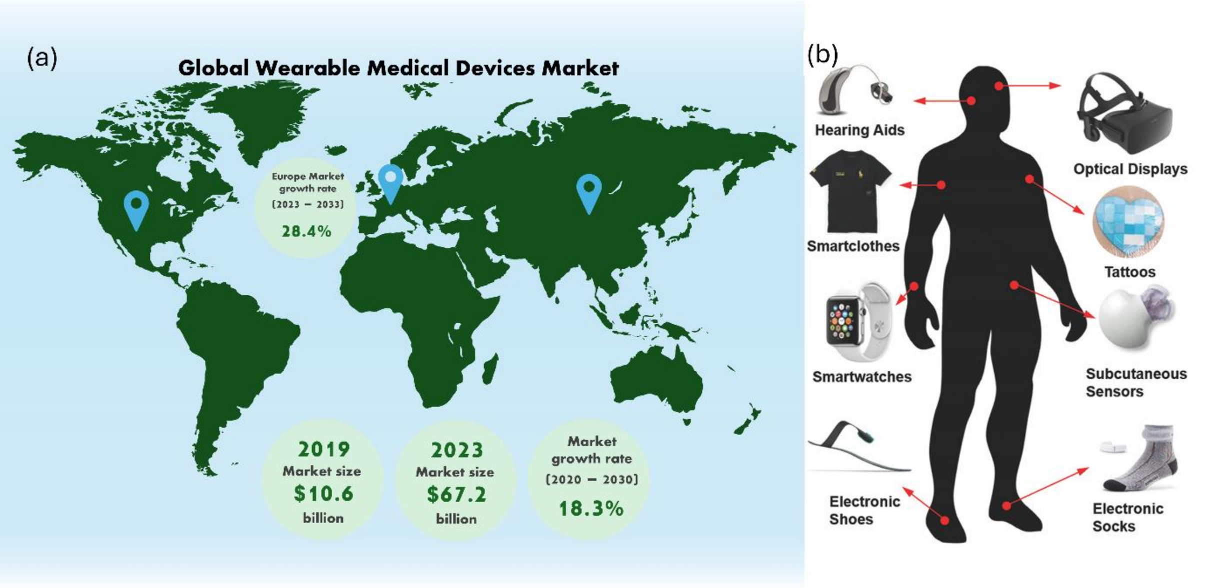

Figure 1.1 - World medical wearables market. (a) Market size and growth analysis globally and in Europe. Adapted from [10, 11]. Different wearable device formats present in the market and in research. Reproduced with permission [7]. Copyright 2018, Wiley-VCH.

In this context, many commercial devices able to monitor several relevant biophysical parameters already exist in the wearables market. These are mostly recognizable by, for example, smartwatches capable of measuring step count, heart rate and temperature, amongst other physiological information that can be relevant for diagnosis [8]. However, these commercial options lack integration of more comprehensive physiological information retrieval, for example by sourcing relevant biochemical information from the body. The first such example was the Glucowatch, the first FDA approved, commercial wrist-worn non-invasive glucose monitor, that did not receive positive acceptance by users due to various drawbacks in its use and performance. As such, biochemical-based diagnostic tools have mostly remained in the category of portable biosensors, being the main example the several commercial alternative glucometers, that are one of the main drives in the biosensors market. However, it is accepted that non-invasive, wearable biosensing systems can bring several benefits [14]. Conventionally, blood has been the biological matrix of choice to identify and quantify relevant analytes for diagnostic of several complications. In opposition, wearable devices are designed and developed with the intention of accessing information in more easily sampled biological fluids, such as saliva, tears, sweat or interstitial fluid, that allow for minimally or non-invasive extraction [15]. In this setting, sweat has been one of the matrices of choice, since it is highly accessible both by passive and active sampling methods for continuous physiological information retrieval, while containing a myriad of chemical information that has been less explored for the purpose of diagnosis and health monitoring [16].

1.2 Scientific context

With the purpose of bridging the gap between current accepted technologies and future wearable tools, capable of providing more comprehensive physiological information, development and application of multifunctional materials must be a key aspect, within the framework of bioelectronics. This field was sparked by the discovery of bioelectricity within biological systems by Luigi Galvani [17], leading to present devices capable of measuring a myriad of physiological phenomenon. In the context of biochemical diagnosis, electrochemical biosensors have been a great research focus, including in the setting of wearable devices. For these devices, several materials have been explored, both in the electrode transducing materials, support substrates and the recognition elements employed for the biosensing task. Such materials include hydrogels, conductive polymers and carbon-based materials, amongst others, employed using versatile fabrication techniques, such as inkjet, screen and 3D printing. In terms of capturing and measuring biological phenomenon, the development of immunoassays, enzyme electrodes and more recently, the use of synthetic recognition elements, are landmarks that helped boost the performance of bioelectronic sensing systems (**Figure 1.2**).

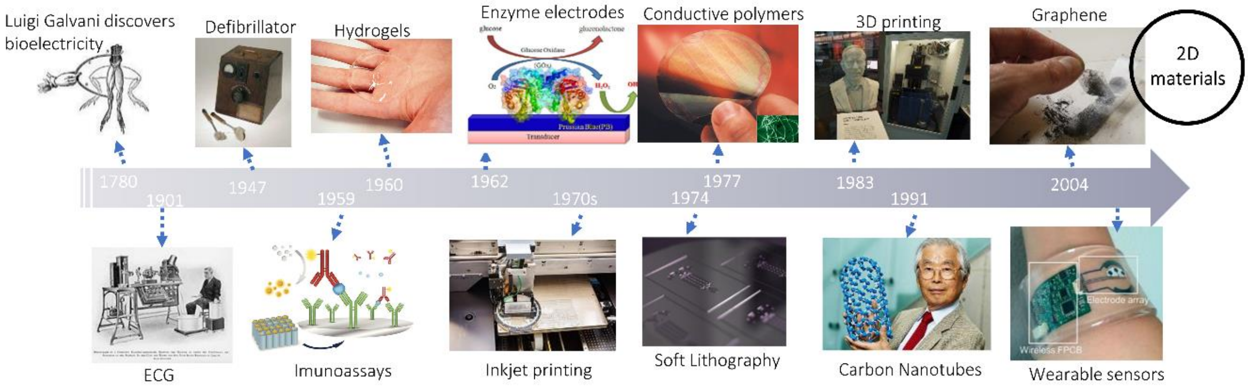

Figure 1.2 - Landmarks in bioelectronics, from materials to fabrication techniques.

More recently, the discovery of graphene and other two-dimensional (2D) materials have further boosted several properties and capabilities of such devices for bioelectronic applications, due to many outstanding mechanical and electrical properties, allowing for higher flexibility and conformability [18].

Graphene is a 2D carbon material, characterized by a honeycomb arrangement of carbon atoms within a single-atom thick lattice. Each carbon atom is linked to other three additional carbon atoms, except at sheet edges, resulting in a sp^2 hybridization of C-C linkages, that contain both sigma (σ) and pi (π) bonds [19]. Due to this hybridization, in-plane σ bonds containing one electron give graphene outstanding mechanical strength, while π bonds in the z-axis overlap and create a continuous π orbital across the entire graphene sheet. This orbital is responsible for turning graphene into a highly conductive material since electrons at this orbital are delocalized and can flow through the 2D sheet extension (**Figure 1.3**).

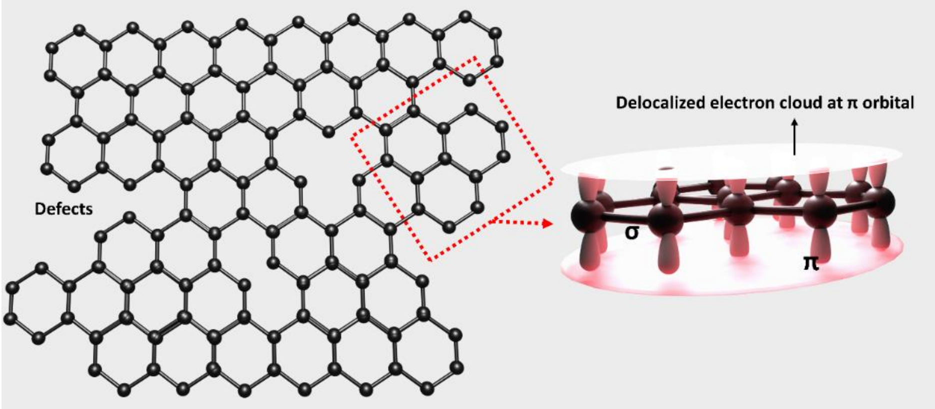

Figure 1.3 - Composition and bonds of graphene lattices.

This conductivity has been meticulously studied for different purposes, with the material being characterized as a zero bandgap semiconductor, with many interesting properties that make it a useful material for several applications, while presenting drawbacks to others [20]. Outstanding electrical conductivity and mobility, high thermal conductivity, great strength, light transparency and the possibility to chemically tune physical properties, rendered graphene as a wonder material that has been studied in high-performance electronic components such as transistors and memories, heat and energy storage elements, composite materials, transparent electrodes and biosensors [21].

This material had been hypothesized in the past, by studying graphite and its structure, made of layered graphene lattices. However, it was firstly isolated by Andre Geim and Konstantin Novoselov in 2004, by employing a physical exfoliation method of graphite using scotch tape, followed by transferring to an oxidized silicon substrate [22]. Since then, many different graphene synthesis methods have been developed, presenting several advantages and disadvantages. They are divided into top-down approaches, where graphite is used as the source material, and bottom-up approaches, where hydrocarbon molecules are used as templates for build-up reactions that lead to the synthesis of graphene lattices [21]. Examples of top-down approaches are mechanical, liquid phase and electrochemical exfoliation, reduction of graphite oxide and arc discharge, capable of effectively separating graphene lattices within graphite. Most common bottom-up approaches include chemical vapor deposition (CVD), epitaxial growth in different substrates, pyrolysis production and more recently, laser assisted synthesis methods. A comparison between several synthesis methods is drawn in **Table 1.1**, regarding their advantages and drawbacks.

Table 1.1 - Comparison of top-down and bottom-up graphene synthesis methods. Adapted from [23].

Method	Description	Advantages	Disadvantages
Top-down methods			
Mechanical exfoliation	First method of graphene isolation, using adhesive tape for separation. Other methods employ AFM tips	High quality graphene sheets with low defects; easily performed	Slow method, with low yield; mainly employed to study graphene properties and not production
Electrochemical exfoliation	Use of graphite sacrificial electrode and separation and collection of graphene within employed electrolyte	Graphite flakes of different layer content are produced, able to be separated by centrifugation	Electrolyte and surfactant molecules difficult to remove and influence properties of resulting graphene
Liquid exfoliation	Solvent-assisted exfoliation by chemical or thermal mechanisms; Sonication of graphite in solvents; exfoliation of graphite oxide to obtain graphene oxide	Hazardous and expensive solvents, solvent contamination and effect over properties, low flake sizes	Synthesis of graphene derivative with different properties, including graphene oxide and defect dense graphene, due to harsh synthesis conditions
Bottom-up methods			
CVD	Pyrolytic synthesis of graphene lattices by imposing high temperatures and pressures over gaseous atmospheres onto a metal substrate	High-quality graphene, with large sheet areas, capable of producing monolayer graphene	Several process factors influence the number of layers; need for transfer deteriorates quality and causes deformation; Expensive technique
Epitaxial growth	Graphene synthesis from silicon carbide (SiC) at high temperature and vaccum, leading to sublimation of Si and graphitization of remaining carbon	High quality graphene	Difficulty to produce few layers graphene; SiC substrates are expensive, rendering the technique less scalable for commercial applications

Analysis of the state-of-the-art synthesis methods of graphene encapsulated in **Table 1.1** show that some technological drawbacks still exist for large scale, scalable production and use of graphene. These are mostly related to standardization of resulting graphene from different techniques and finding suitable techniques that allow for high synthesis throughput at lower costs [24]. Several researchers are attempting to bridge these gaps between research and industrialization, with more accessible, higher yield fabrication techniques. Some examples are laser-assisted techniques, that will be discussed in the following chapters, and similar pyrolysis inspired methods, such as flash joule heating [24,25]. At the same time, drawbacks related to transfer, stacking and patterning of synthesized graphene are also a consideration, since current state-of-the-art synthesis methods are not capable of localized synthesis within customizable geometries. As such, the use of graphene in functional architectures towards the production of consumer electronics needs additional processes, for assembly of multilayered graphene patterns.

In this framework, graphene has been mainly employed in the printed electronics field, where the synthesis is followed by the formulation of graphene inks and their printing into the required geometry, targeting a specific application (**Figure 1.4**). Graphene inks with very distinct properties can be produced, depending on the concentration of graphene, selected solvent and presence of surfactants or polymers that aid in stabilization of graphene phases [26]. Several challenges remain in ink formulations within flexible substrates, including the stability of graphene sheets, suitable viscosities and surface tensions compatible with the selected printing methods and adequate adhesion to the substrate, while recurringly using toxic solvents and reagents. Thus, the burden of optimization of such resources is laborious and time consuming, although it is of high importance to potentiate the use of graphene in areas such as

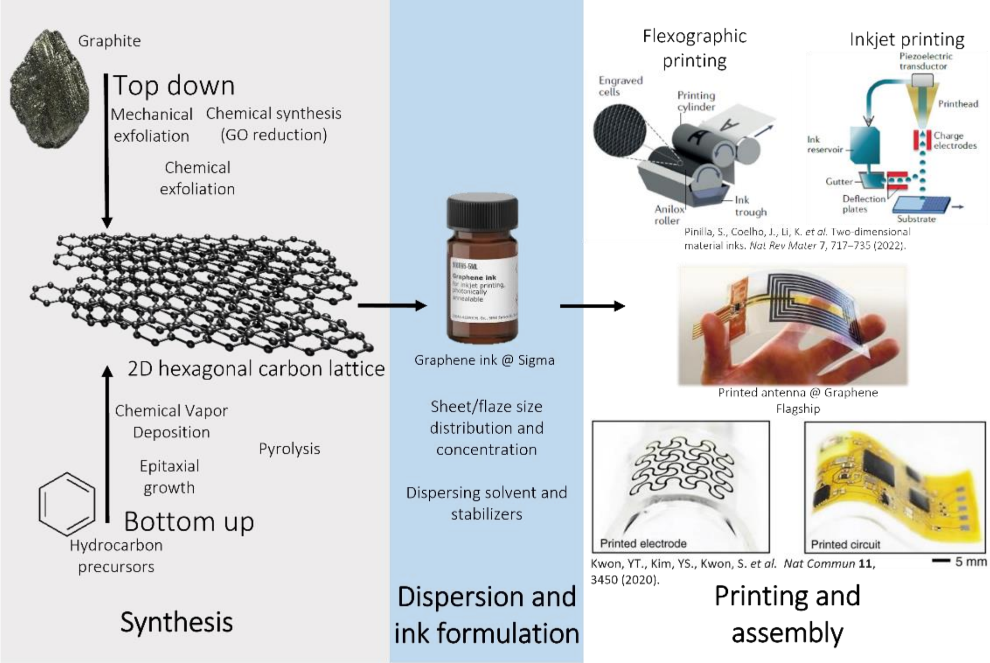

Pinilla, S., Coelho, J., Li, K. *et al.* Two-dimensional material inks. *Nat Rev Mater* 7, 717–735 (2022).

Kwon, YT., Kim, YS., Kwon, S. *et al.* *Nat Commun* **11**, 3450 (2020).

Figure 1.4 - Framework of application of graphene for printed electronics fabrication.

bioelectronics. Finally, the need for a printing technique further increases the final cost of this multi-step process, making it less accessible.

In this context, researchers have worked on reaching alternative fabrication technologies that can improve on these aspects of accessibility and ease of synthesis and patterning of graphene-based electronics. One of the most recently explored methods has been Direct Laser Writing (DLW) of carbon-based polymers, to synthesize and pattern a graphitic material named in the literature as laser-induced graphene (LIG). For LIG, the straightforward fabrication stands on the need for minimal infrastructure and precursor materials, in a maskless, catalyst-free, non-toxic synthesis route, allowing for low-cost, high-throughput patterning of graphitic structures with very high selectivity and localized conversion, within fully customizable geometries [27]. LIG has found space in the production of planar microelectronic devices, due to the resulting porous nature of the three-dimensionally stacked 2D lattices of the converted graphene structures, that circumvent some cumbersome processes of single layer graphene transfer, patterning and stacking for the production of functional architectures [28,29]. Most of these applications have been developed on plastic polymers, mainly polyimide (PI), resulting in LIG with very attractive intrinsic properties [27]. More recently, other precursor substrates have been put forward to improve on the accessibility and environmental impact of such plastic substrates [30]. Although LIG has recently established itself as a very attractive material for the simultaneous synthesis and patterning of multi-layered graphene for development of consumer electronic elements, some challenges on the synthesis and application of this material within bioelectronics can still be addressed.

1.3 Objectives

Due to the relevant and attractive characteristic of LIG for the fabrication of microelectronic components and devices, as well as its suitability for the development of new approaches for wearable device fabrication, this graphitic material was selected as the topic of study, with the purpose of tackling some of the challenges described before, that inspire the main goals of this work, which are:

- Use of more accessible and sustainable materials for LIG synthesis, capable of providing alternatives to conventional aromatic polymer precursors. The use of paper substrates is envisioned as viable alternatives to develop LIG-based bioelectronic applications.

- Study and optimization of LIG produced from paper precursors, with the purpose of reaching and even surpassing the state of the art of conductive properties reported in the literature for conventional aromatic polymer precursors.

- Apply patterned and optimized LIG from such substrates towards the fabrication of bioelectronic applications, with focus on electrochemical sensor development. Different strategies are explored to develop electrodes using the envisioned precursors, but also their translation towards wearable scenarios, using transfer methodologies and elastomeric support materials.

- As a final goal, the integration of paper-based LIG bioelectrodes for skin interfaced bioelectronic applications is targeted, where the material can be used both for the detection of physiological signals directly in the body and for electrical stimulation. Electrophysiological signal acquisition electrodes and electrode arrays and iontophoresis-based sweat stimulation system for electrochemical sweat glucose quantification are targeted, based on laser processing paradigms developed throughout the work.

1.4 Thesis outline

- **Chapter 1** provides a societal and scientific context of the presented work, along with motivations and aim of the study.
- **Chapter 2** provides an extensive overview on DLW as the main material synthesis and fabrication approach used in this work. A review detailing the main operating variables associated with this technique, material synthesis outcomes and state of the art of DLW-based device processing, with a focus on electrochemical sensing and wearable devices, is given.
- **Chapter 3** describes the main results obtained for the synthesis of laser-induced graphene (LIG) derived from two distinct paper substrates, along with material characterization, to determine the most suitable substrate of study. Furthermore, the implementation of paper-derived LIG for electrochemical sensor development and glucose biosensing implementation is also described.
- **Chapter 4** is dedicated to deepening the study of DLW fabrication variables and their influence, through process-property optimization experiments. Alternative study metrics are proposed, to establish the underlaying pulse width modulation parameters that influence the properties of LIG and electrochemical cells toward electrochemical sensing applications.
- **Chapter 5** describes a one-step synthesis method through DLW for the fabrication of LIG/CuNPs hybrid materials. The resulting composite surfaces are characterized and their use for nonenzymatic sensing of glucose in the physiological concentration range found in sweat is described.
- **Chapter 6** focuses on boosting the conductive properties of paper-based LIG, through substrate chemical composition modeling, towards the fabrication of LIG soft conductors. To achieve this, a novel transfer methodology based on a water-induced peel-off strategy is presented, used for the construction of conformable LIG architercture for wearable sensing.
- **Chapter 7** expands on the application of transferred, paper-based LIG for the development of skin-interfaced devices for bioelectronics applications, focusing on LIG-skin interface properties. Devices for electrophysiological signal acquisition (ECG and EMG) and iontophoresis-based sweat stimulation, extraction and analysis are described and characterized.
- **Chapter 8** presents conclusions drawn from this work, along with future considerations for further maturing of the technologies developed in this work and their implementation.

1.5 Research output

The main results presented in this thesis, described in the 8 chapters of the document, have been published in several high-impact peer-reviewed publications and presented in national and international symposiums and conferences, listed below.

Publications

- **Pinheiro, T.**, Morais, M., Silvestre, S., Carlos, E., Coelho, J., Almeida, H. V., ... & Martins, R. Direct Laser Writing: From Materials Synthesis and Conversion to Electronic Device Processing. *Advanced Materials*, **2024**, 2402014.
- Claro, P. I., **Pinheiro, T.**, Silvestre, S. L., Marques, A. C., Coelho, J., Marconcini, J. M., ... & Martins, R. Sustainable carbon sources for green laser-induced graphene: A perspective on fundamental principles, applications, and challenges. *Appl. Phys. Rev*, **2022**, *9*(4), 041305.
- **Pinheiro, T.**, Silvestre, S., Coelho, J., Marques, A. C., Martins, R., Sales, M. G. F., & Fortunato, E. Laser-induced graphene on paper toward efficient fabrication of flexible, planar electrodes for electrochemical sensing. *Advanced Materials Interfaces*, **2021** 8(22), 2101502.
- **Pinheiro, T.**, Rosa, A., Ornelas, C., Coelho, J., Fortunato, E., Marques, A. C., & Martins, R. (2023). Influence of CO2 laser beam modelling on electronic and electrochemical properties of paper-based laser-induced graphene for disposable pH electrochemical sensors. *Carbon Trends*, **2023**, 11, 100271.
- **Pinheiro, T.**, Caetano, J., Fortunato, E., Sales, M. G. F., Almeida, H., & Martins, R. One-Step Laser Synthesis of Copper Nanoparticles and Laser-Induced Graphene in a Paper Substrate for Non-Enzymatic Glucose Sensing. *Advanced Sensor Research*, **2024**, 2400052.
- **Pinheiro, T.**, Correia, R., Morais, M., Coelho, J., Fortunato, E., Sales, M. G. F., ... & Martins, R. Water peel-off transfer of electronically enhanced, paper-based laser-induced graphene for wearable electronics. *ACS nano*, *16*(12), **2022**, 20633-20646.
- **Pinheiro, T.** Stretchable interfaces come in from the cold. *Nature Electronics*, **2024**, *7*(1), 4-5.
- Silvestre, S. L., **Pinheiro, T.,** Marques, A. C., Deuermeier, J., Coelho, J., Martins, R., ... & Fortunato, E. Cork derived laser-induced graphene for sustainable green electronics. *Flexible and Printed Electronics*, **2022**, 7(3), 035021.
- Coelho, J., Correia, R. F., Silvestre, S., **Pinheiro, T.**, Marques, A. C., Correia, M. R. P., ... & Martins, R. Paper-based laser-induced graphene for sustainable and flexible microsupercapacitor applications. *Microchimica Acta*, **2023**, 190(1), 40.

- Klem, M. D. S., Abreu, R., **Pinheiro, T.**, Coelho, J., Alves, N., & Martins, R. Electrochemical Deposition of Manganese Oxide on Paper-Based Laser-Induced Graphene for the Fabrication of Sustainable High-Energy-Density Supercapacitors. *Advanced Sustainable Systems*, **2024**, 2400254.
- Abreu, R., dos Santos Klem, M., **Pinheiro, T.**, Pinto, J. V., Alves, N., Martins, R., ... & Coelho, J. Direct laser writing of MnOx decorated laser-induced graphene on paper for sustainable microsupercapacitor fabrication. *FlatChem*, **2024**, 46, 100672.
- **Pinheiro, T.**, Cardoso, A. R., Sousa, C. E., Marques, A. C., Tavares, A. P., Matos, A. M., ... & Sales, M. G. F. Paper-based biosensors for COVID-19: a review of innovative tools for controlling the pandemic. *ACS Omega*, **2021**, 6(44), 29268-29290.
- Morais, M., Marques, A. C., Ferreira, S. H., **Pinheiro, T.**, Pimentel, A., Macedo, P., ... & Fortunato, E. Visible photoluminescent zinc oxide nanorods for label-free nonenzymatic glucose detection. *ACS Applied Nano Materials*, 2022, 5(3), 4386-4396.
- Meneses, M. J., Patarrão, R. S., **Pinheiro, T.**, Coelho, I., Carriço, N., Marques, A. C., ... & Macedo, M. P. Leveraging the future of diagnosis and management of diabetes: From old indexes to new technologies. *European Journal of Clinical Investigation*, **2023**, 53(4), e13934.

Presentations

Oral Presentations

- Tomás Pinheiro, R. Martins, M. Goreti F. Sales, Elvira Fortunato. Laser-Induced Graphene for Wearable Bioelectronics and Biochemical Sweat Sensing Systems. 10th International PhD Meeting, Dresden, Germany.
- Tomás Pinheiro, Sara Silvestre, João Coelho, Ana C. Marques, Rodrigo Martins, M. Goreti F. Sales, Elvira Fortunato. "Paper-based Laser-induced Graphene for Bioelectronic Applications and Electrochemical Sensor Production". InnoLAE 2022 - Innovations in Large Area Electronics.
- Tomás Pinheiro, Sara Silvestre, João Coelho, M. Goreti F. Sales, Elvira Fortunato, Ana C. Marques, Rodrigo Martins. "Paper-based Laser-induced Graphene for Bioelectronic Applications and Electrochemical Sensor Production". XX B-MRS Meeting 2022, Foz Iguaçu, Brazil. Presentation recipient of the Bernhard Gross student award and ACS Best Oral Presentation Prize.
- Tomás Pinheiro, Elvira Fortunato, M. Goreti F. Sales, Ana C. Marques, Rodrigo Martins. "From Disposable to Wearable Bioelectronics using Paper-derived Laser-induced Graphene". Materiais 2023 - XXI Congresso da Sociedade Portuguesa de Materiais and XII International Symposium on Materials, Guimarães, Portugal.

- Tomás Pinheiro, Elvira Fortunato, M. Goreti F. Sales, Ana C. Marques, Rodrigo Martins. "Skin-Interfaced, Graphene-based Bioelectronics for Biomedical Applications". VIII Annual Meeting i3N, 2023, Leiria, Portugal.
- Rodrigo Martins, Tomás Pinheiro, Ana C. Marques, Elvira Fortunato. "From Disposable to Wearable Bioelectronics using Paper-derived Laser-induced Graphene". MRS Spring Meeting 2023, San Franscisco, USA.
- Tomás Pinheiro, Elvira Fortunato, Henrique Almeida, Rodrigo Martins. From Disposable to Wearable Bioelectronics using Paper-derived Laser-induced Graphene. E-MRS Spring Meeting 2024, Strasbourg, France.

Poster Presentations

- Tomás Pinheiro, Sara Silvestre, André Rosa, Joana Caetano, João Coelho, Rodrigo Martins, M. Goreti F. Sales, Ana C. Marques, Elvira Fortunato. "Turning Paper into Laser-induced Graphene: Application in Electrochemical Sensors". Encontro Ciência 2022, Lisboa Portugal.
- Tomás Pinheiro, Elvira Fortunato, M. Goreti F. Sales, Ana C. Marques, Rodrigo Martins. " Paper-Based Green Laser-Induced Graphene for Disposable and Wearable Sensing Applications". IX Annual Meeting i3N, Leiria, Portugal. Recipient of Best PhD Poster Award
- Rodrigo Martins, Tomás Pinheiro, Elvira Fortunato. Paper-based Laser-induced Graphene for Disposable and Wearable Sensing Applications. MRS Fall Meeting 2023, Boston, USA.
- Rodrigo Martins, Tomás Pinheiro, Inês Cunha, Emanuel Carlos, Elvira Fortunato. Driving Flexible Electronics by Hybrid Materials. MRS Fall Meeting 2023, Boston, USA.

References

1. Ates, H. C. *et al.* End-to-end design of wearable sensors. *Nature Reviews Materials* 1–21 (2022) doi:10.1038/s41578-022-00460-x.
2. Liu, L. & Zhang, X. A Focused Review on the Flexible Wearable Sensors for Sports: From Kinematics to Physiologies. *Micromachines* **13**, 1356 (2022).
3. Hinde, K., White, G. & Armstrong, N. Wearable devices suitable for monitoring twenty four hour heart rate variability in military populations. *Sensors (Switzerland)* vol. 21 1–20 (2021).
4. Cao, M., Xie, T. & Chen, Z. Wearable Sensors and Equipment in VR Games: A Review. in *Lecture Notes in Computer Science (including subseries Lecture Notes in Artificial Intelligence and Lecture Notes in Bioinformatics)* vol. 11345 LNCS 3–12 (Springer Verlag, 2019).
5. Lee, G., Wei, Q. & Zhu, Y. Emerging Wearable Sensors for Plant Health Monitoring. *Adv. Funct. Mater.* **31**, 2106475 (2021).
6. Virginia Anikwe, C. *et al.* Mobile and wearable sensors for data-driven health monitoring system: State-of-the-art and future prospect. *Expert Syst. Appl.* **202**, 117362 (2022).
7. Yetisen, A. K. *et al.* Wearables in Medicine. *Adv. Mater.* **30**, 1706910 (2018).
8. Mitratza, M. *et al.* The performance of wearable sensors in the detection of SARS-CoV-2 infection: a systematic review. *Lancet Digit. Heal.* **4**, e370–e383 (2022).
9. Medical Enzyme Technology Market Forecast to 2028 - COVID-19 Impact and Global Analysis By Enzyme Type; Application, and Geography. https://www.researchandmarkets.com/reports/5576289/wearable-sensor-market-forecast-to-2028-covid?utm_source=GNOM&utm_medium=PressRelease&utm_code=zkthq6&utm_campaign=1701811+-+The+Worldwide+Wearable+Sensor+Industry+is+Expected+to+Reach+%245.7+Billion+by+2.
10. Wearable Medical Devices Market | Global Revenue Report, 2030. https://www.psmarketresearch.com/market-analysis/wearable-medical-devices-market.
11. Advisor, N. 1. Europe Wearable Medical Devices Market Size. https://www.novaoneadvisor.com/report/europe-wearable-medical-devices-market.
12. Hajat, C. & Stein, E. The global burden of multiple chronic conditions: A narrative review. *Prev. Med. Reports* **12**, 284 (2018).
13. Dunn, J., Runge, R. & Snyder, M. Wearables and the medical revolution. *Per. Med.* **15**, 429–448 (2018).
14. Senf, B., Yeo, W. H. & Kim, J. H. Recent Advances in Portable Biosensors for Biomarker Detection in Body Fluids. *Biosensors* vol. 10 (2020).
15. Kim, J., Campbell, A. S., de Ávila, B. E. F. & Wang, J. *Wearable biosensors for healthcare monitoring. Nature Biotechnology* vol. 37 389–406 (Nature Publishing Group, 2019).
16. Bariya, M., Nyein, H. Y. Y. & Javey, A. Wearable sweat sensors. *Nature Electronics* vol. 1 160–171 (2018).
17. Chang, E. H. Changing the tune using bioelectronics. *Bioelectron. Med.* **7**, (2021).
18. Wang, B. *et al.* Bioelectronics-Related 2D Materials Beyond Graphene: Fundamentals, Properties, and Applications. *Advanced Functional Materials* vol. 30 2003732 (2020).
19. Peres, N. M. R. Graphene, new physics in two dimensions. *Europhys. News* **40**, 17–20 (2009).
20. Cooper, D. R. *et al.* Experimental Review of Graphene. *ISRN Condens. Matter Phys.* **2012**, 1–56 (2012).
21. Zhang, F. *et al.* Recent advances on graphene: Synthesis, properties and applications. *Compos. Part A Appl. Sci. Manuf.* **160**, 107051 (2022).
22. Novoselov, K. S. *et al.* Electric field in atomically thin carbon films. *Science (80-.).* **306**, 666–669 (2004).
23. Skoda, M., Dudek, I., Jarosz, A. & Szukiewicz, D. Graphene: One material, many possibilities -

Application difficulties in biological systems. *J. Nanomater.* **2014**, (2014).
24. Wyss, K. M. *et al.* Large-Scale Syntheses of 2D Materials: Flash Joule Heating and Other Methods. *Adv. Mater.* **34**, 2106970 (2022).
25. Kumar, R. *et al.* Laser-assisted synthesis, reduction and micro-patterning of graphene: Recent progress and applications. *Coordination Chemistry Reviews* vol. 342 34–79 (2017).
26. Tran, T. S., Dutta, N. K. & Choudhury, N. R. Graphene inks for printed flexible electronics: Graphene dispersions, ink formulations, printing techniques and applications. *Adv. Colloid Interface Sci.* **261**, 41–61 (2018).
27. Lin, J. *et al.* Laser-induced porous graphene films from commercial polymers. *Nat. Commun.* **5**, 5714 (2014).
28. Krajewska, A. *et al.* Fabrication and applications of multi-layer graphene stack on transparent polymer. *Appl. Phys. Lett.* **110**, 041901 (2017).
29. Qiao, Y. *et al.* Multilayer Graphene Epidermal Electronic Skin. *ACS Nano* **12**, 8839–8846 (2018).
30. Chyan, Y. *et al.* Laser-Induced Graphene by Multiple Lasing: Toward Electronics on Cloth, Paper, and Food. *ACS Nano* **12**, 2176–2183 (2018).

2

DIRECT LASER WRITING FOR MATERIAL SYNTHESIS AND DEVICE PROCESSING

Direct Laser Writing has been increasingly selected as a microfabrication route for efficient, cost-effective, high-resolution material synthesis and conversion. Concurrently, lasers participate in the patterning and assembly of functional geometries in several fields of application, of which electronics and sensing stand out. In this chapter, recent advances and strategies based on DLW for electronics microfabrication are surveyed and outlined, based on laser material growth strategies. First, the main DLW parameters influencing material synthesis and transformation mechanisms are summarized, aimed at selective, tailored writing of laser-induced graphene (LIG). Since its discovery, significant advances have been made to obtain green LIG (gLIG) from abundant, eco-friendly, natural and organic renewable bio-based carbon sources, along with cost-effective electronic device fabrication, resulting in diverse solutions to the environmental impact caused by electronic waste (e-waste). Specifically in this chapter, state-of-the-art bioelectronics applications towards wearable devices, including electrochemical sensing, sweat biochemical analysis and electrophysiological sensing is presented, portraying which challenges and opportunities LIG has and can meet in future implementations. As portrayed by LIG, the expanded capability of lasers to participate in multiple fabrication steps at different implementation levels, from material engineering to device processing, indicates their future applicability to next-generation electronics, where more accessible, green microfabrication approaches integrate lasers as comprehensive tools.

Keywords: Lasers, laser-material processing, Direct Laser Writing, material synthesis, electronics, bioelectronics

The literature presented in this chapter is published in:

- Pinheiro, T., Morais, M., Silvestre, S., Carlos, E., Coelho, J., Almeida, H. V., ... & Martins, R. (2024). Direct Laser Writing: From Materials Synthesis and Conversion to Electronic Device Processing. *Advanced Materials*, 2402014.

- Claro, P. I., Pinheiro, T., Silvestre, S. L., Marques, A. C., Coelho, J., Marconcini, J. M., ... & Martins, R. (2022). Sustainable carbon sources for green laser-induced graphene: A perspective on fundamental principles, applications, and challenges. *Appl. Phys. Rev*, *9*(4), 041305.

2.1 Introduction to Laser Material Processing

Since the first developments in laser technologies that occurred in the 1960s [1], great advances have been made in the capability of generating these coherent, monochromatic, directional electromagnetic radiation beams with different properties, including a wide range of radiation wavelengths, pulsing capabilities, temporal, frequency and spatial characteristics and distinct energy profiles [2]. Accompanied by this progress, application areas for laser technologies also expanded, encompassing fields as distinct as communication, medical care, and analytical chemistry [3]. Concurrently, intense study on laser-material interactions has been in progress, opening new avenues for electronics microfabrication.

The ever-growing demand for electronic devices and our societal dependency on these systems and their interconnectivity are leading to novel requirements that need to be considered at different implementation levels. On the side of materials, processing paradigms require compatibility with conventional rigid conductors, semiconductors, and insulators, but also capabilities for processing mechanically flexible materials. With the increase in interconnectivity promoted by the Internet-of-Things (IoT), electronic devices need to be present in diverse settings, requiring mechanically robust, but flexible substrates, compatible materials, and manufacturing processes.[4] Even though several conventional microfabrication techniques for semiconductor devices and integrated circuits (ICs) fabrication, such as lithography techniques, chemical vapor deposition (CVD), and physical vapor deposition (PVD) methods, have shown great capabilities for flexible inorganic device manufacturing [5], they are incompatible with many emerging electronic-grade organic materials and the paradigm shift from rigid to flexible electronics, mostly due to high-vacuum and temperature requirements.[6]

Several fabrication routes capable of increasing the range of processable materials and enabling large-area production using both rigid and flexible substrates have arisen. One such alternative is solution processing for thin film technologies [7], which gives prospects for high processability and throughput, with expanded control of the composition of processable solutions, while opening up routes for low-temperature processing. Great advances have been made using solution-processable techniques, including in thin-film transistors (TFTs) [8], resistive switching (RS) devices [9], and solar cells [10] fabrication, among others. In addition, other fabrication technologies within additive manufacturing approaches have appeared as a good solution for fabricating several electronic component categories. These include batteries, solar cells, and other energy management applications [11,12], as well as communication, sensing, processing, memory, and interface components [13,14]. Such technologies overcome the dependency on subtractive processes, circumventing the need for toxic etching chemicals, photoresists, and the wastage of deposited metals and semiconductors. 3D printing and its several modalities, including extrusion-based, vat polymerization and powder bed fusion processes have allowed for manipulation of a wide range of materials, from metals to ceramics and polymers, both for layer fabrication as well as complex 3D geometries [15]. Alternatively, printed electronics have also been performed through planar printing processes, highly compatible with solution processability. Several printing modalities, including screen-printing, flexographic and gravure printing, and inkjet or aerosol printing, allow for layer-by-layer printing of conductor, semiconductor, and dielectric materials within complex planar geometries, as well as vertical layered devices [16]. Furthermore, these printing techniques can be a valuable resource for scalability, lower-cost and waste reduction, due to their compatibility with sheet-to-sheet (S2S) and roll-to-roll (R2R) manufacturing, for large-area device fabrication [6,16]. However, for complex geometric patterns, some of these techniques have drawbacks since they need masters or plates for patterning. On the other hand, while 3D printing and inkjet printing are digital and allow for patterning with complex shapes and a wide range of resolutions, complex ink formulation and rheological control of printed material are required, while in some cases, multi-step post-processing is necessary [17].

Although solution processing and additive printing technologies having occupied an important part in flexible electronics fabrication, alternative techniques that further improve versatility and efficiency in large-area processing are sought after, capable of simultaneously performing multiple fabrication steps with energy, time, and resource efficiency, within multi-material processing systems. Lasers and their high-throughput material processing capabilities have amassed a great focus of research over the years, as a comprehensive resource to complement and substitute many manufacturing paradigms for more versatile approaches. The integrated capability of laser systems to participate in several fabrication stages, from synthesis [18], doping [19], polymerization [20], and curing [21], simultaneously with patterning [22] and assembly [23], has made laser technologies an important asset in material engineering and processing.

Relying on thermal induced effects, the ablation capabilities of lasers have been extensively studied for the synthesis of nanostructures, such as metallic nanoparticles (NPs) or semiconducting quantum dots (QDs) [24]. With the further coupling of control systems capable of directing laser beams, paired with computer-aided designing, many fields have taken lasers as reliable tools for manufacturing, both in subtractive and additive frameworks [25]. Hence, Direct Laser Writing (DLW) has appeared in several fabrication settings, which include micromachining, lithographic-based techniques, and 3D printing approaches. In this context, DLW can be distinguished into three categories, depending on the desired effect promoted by the interaction between the laser beam and processable materials and substrate. Firstly, subtractive DLW (SDLW) relies on ablation and etching principle, by removing selective areas of deposited materials (**Figure 2.1a**), such as in photothermal ablation mechanisms for micromachining [26] or material drilling [27]. Secondly, additive DLW (ADLW), relies on several mechanisms aiming at synthesis and simultaneous patterning of material geometries, employing a precursor formulation (**Figure 2.1b**). This modality has been prolifically employed in 3D printing paradigms, such as in photon-induced polymerization reactions of photoinitiators and monomers, at the voxels created by focused beam paths [28]. Finally, transformative DLW (TDLW), is based on the direct irradiation of materials to transform their chemical or structural properties, without significant ablation and the need for external precursors (**Figure 2.1c**). Examples of transformative approaches include the crystallization of amorphous materials [29], laser-promoted reversible structural transformations of carbon-based materials [30], or laser doping of semiconductors [19].

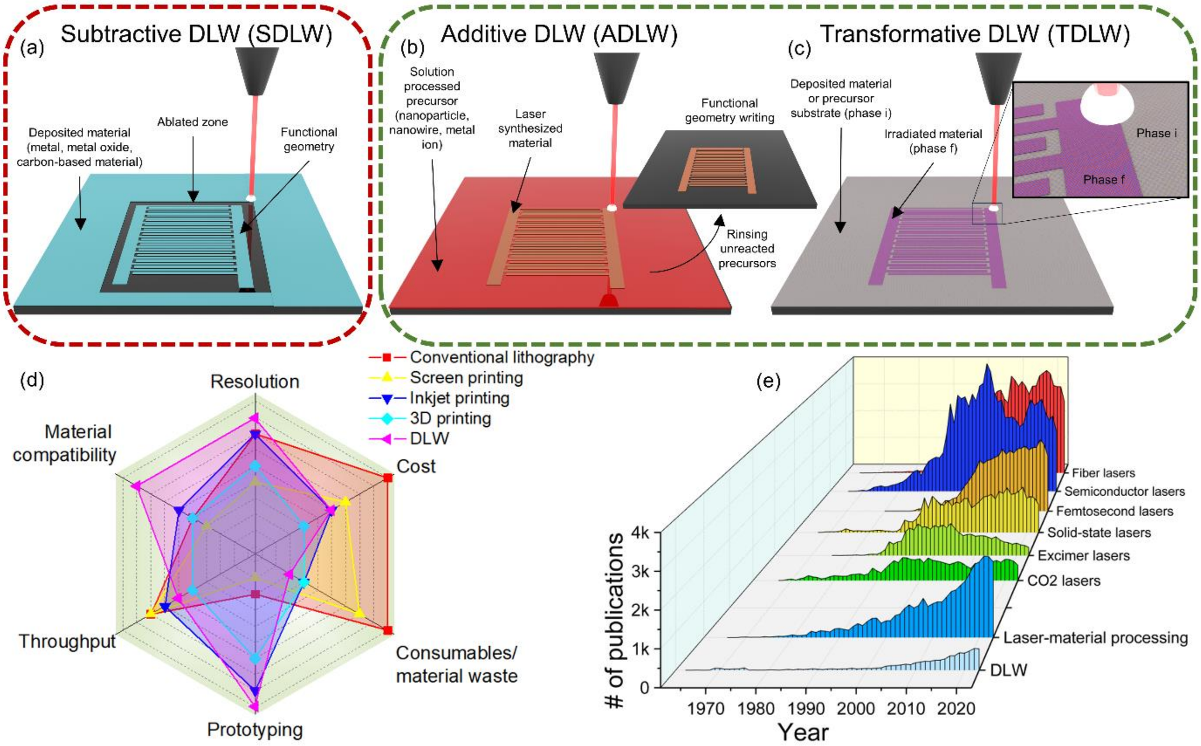

Figure 2.1 - Modalities of DLW, comparison with established microfabrication technologies and literature outlook. (a) Schematic of subtractive DLW (SDLW) for ablation-based geometry writing. (b) Schematic of additive DLW (ADLW) for simultaneous material synthesis and patterning. (c) Schematic of transformative DLW (TDLW), characterized by selective chemical and structural material transformation. (d) Spider chart comparing DLW with lithography techniques, inkjet, screen and 3D printing, in relation to key fabrication and implementation characteristics. (e) Scopus literature survey, portraying the evolution of publication for various laser systems, laser-material processing and DLW.

Some distinguishing features can be drawn between SDLW and the remaining processes. For ADLW and TDLW, the laser stimulus directly affects and dictates the resulting outcomes of irradiation over the processed substrate or precursor, in terms of its physical state, crystallinity and other properties, such as mechanical resistance and electrical or thermal conductance. For SDLW, the purpose is only to shape the geometry and architecture of solid materials with pre-defined properties and functions [31–34]. This is fundamental for several processes, including geometry definition in micromachining, but also in cutting processes used for mask manufacturing or via hole establishment [27,35]. However, other techniques must be used to synthesize and deposit materials with pre-determined properties, also generating ablation waste. Thus, ADLW and TDLW present improved degrees of freedom for material processing, since manipulated laser stimuli provide tailoring capabilities for synthesis and conversion, while the writing and patterning tasks occur simultaneously. Additionally, not only solid materials may be engineered, but also aqueous precursor formulation, liquid polymers and other material sources can be subjected to laser irradiation. Because of this versatility, ADLW and TDLW have increasingly been explored as an alternative to conventional physical and chemical deposition, as well as additive printing technologies in electronics.

The plethora of different laser types and their associated beam properties results in advantageous features when selecting microfabrication approaches, related to material processability, device prototyping, fabrication throughput, and other relevant aspects. This is outlined in **Figure 2.1d**, where a comparison is drawn between several popular microfabrication approaches and their key characteristics. Even though lithography techniques (e.g. nanoimprint lithography) present outstanding resolution in the low nanometer range, several laser systems allow for sub-micron resolution, mostly the ones promoting two-photon absorption (TPA) and polymerization processes [20]. However, DLW achieves this resolution with improved material processability, throughput and facile prototyping, due to the digital patterning capabilities. Conversely, DLW also improves some aspects when compared to printing technologies, namely the reduced consumable needs of laser systems at similar equipment costs, while also improving processability and prototyping, by incorporating several stages of fabrication in one-step processes. When studying multiparametric influences of fabrication variables in conventional fabrication strategies, such processes are strenuous and very resource and energy-consuming, while for laser systems, facile manipulation of irradiation and writing parameters is straightforward. This greatly improves the prototyping and implementation from lab to fab. Concurrently, most laser fabrication paradigms also present higher processability when compared to these printing techniques, since they are compatible with almost any type of material of interest for electronic device fabrication, from liquid precursors manipulated using solution processing, to direct solid substrate engineering. This high adaptability of lasers for very distinct tasks is represented by the immense exploration of their different configurations and capabilities in scientific literature, presented in a literature survey portrayed in **Figure 2.1e**. The development of lasers with distinct gain medium or pumping operations has been ongoing for several decades, promoting the exploration of laser-based material processing and engineering for different purposes, reflected in the increasing interest of the scientific and industrial community in DLW paradigms.

2.1.1 Early application of lasers in electronics microfabrication

Regarding laser material processing in the setting of electronics, most of the early applications were developed within conventional, high-vacuum thin film deposition and machining approaches. A timeline of important breakthroughs and representative literature advances is presented in **Figure 2.2**. Some of the earliest applications were the machining and mask patterning for IC fabrication, using laser ablation principles [36,37]. DLW also found relevant use for laser lithography in these early stages, to expose photoresist coated substrates within microfabrication processes [38]. Other relevant uses of lasers were also found for the deposition of dielectric and semiconducting films, using laser-promoted evaporation of targets under high-vacuum [39,40]. Moreover, another early application was the crystallization of semiconducting materials, including amorphous silicon, through laser annealing at lower temperatures, below the melting threshold [41–43]. Thereafter, pulsed laser annealing (PLA) and pulsed laser deposition (PLD) techniques have become very attractive for semiconducting material processing with much lower thermal budgets, capable of developing different functional homo and hetero-junctions for applications such as diodes, TFTs, and solar cells [44–47]. Then, interestingly, some works demonstrated that thorough control of laser irradiation schemes and resulting temperatures enabled solution processing frameworks with flexible polymeric substrates, such as polyimide (PI), without their thermal degradation [45,48,49], opening the door for laser processing in flexible electronics.

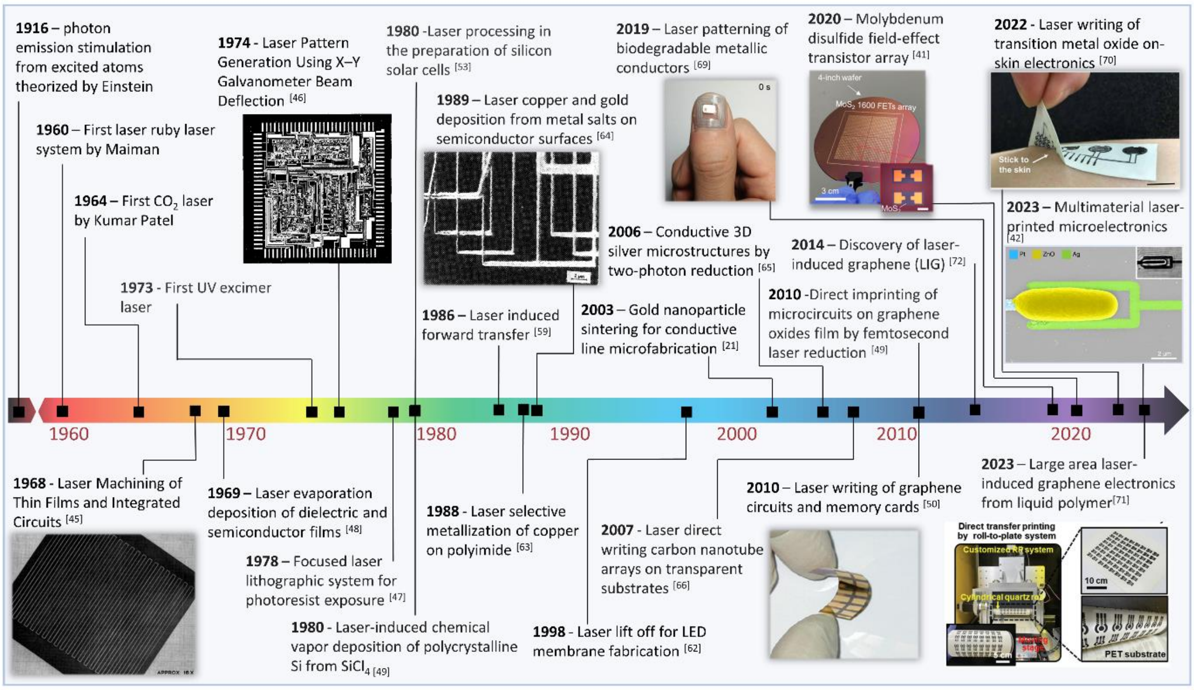

Figure 2.2 – Timeline of breakthroughs and literature advances on laser-material processing in the framework of electronics microfabrication. Image for "laser machining". Reproduced with permission [36]. Copyright 1969, Wiley-VCH. Image for "laser pattern generation". Reproduced with permission [37]. Copyright 1974, Optica Publishing Group. Image for "laser copper deposition". Reproduced with permission [50]. Copyright 1989, AIP Publishing. Image for "laser writing of graphene circuits". Reproduced with permission [51]. Copyright 2010, America Chemical Society. Image for "biodegradable conductors". Reproduced with permission [52]. Copyright 2019, American Chemical Society. Image for "wafer transistor array". Reproduced with permission [53]. Copyright 2020 American Chemical Society. Image for "laser writing of transition metal oxide". Reproduced with permission [54]. Copyright 2022, AAAS. Image for " laser printed microelectronics". Reproduced with permission [55]. Copyright 2023, Springer Nature. Image for "large-area laser-induced graphene". Reproduced with permission [56]. Copyright 2023 Wiley-VCH.I

Besides these direct material-laser interactions, aiming at selective decomposition or phase shifts, other appealing techniques based on laser-induced transfer, printing, and assembly gained preponderance in electronics microfabrication. These rely on interfacial interactions between a donor material deposited over a transparent substrate, to transfer irradiated material geometries to a receiver substrate, such as in laser-induced forward and backward transfer [57–59]. Another possibility is to use pulsed lasers with short wavelengths to perform laser lift-off techniques and separate support materials from rigid carriers, including lift-off of flexible substrates such as PI [23,60]. New paradigms of material processing for electronics have evolved over the years, taking full advantage of the capabilities of lasers for manufacturing [50,61]. Allied to their energy efficiency, lack of consumable needs and chemicals for processing, engineering of conducting, semiconducting, and insulating materials from different origins have created new opportunities to expand the range of techniques and processable materials employing more versatile approaches. An example is the production of metal lines and other geometries from metal salt precursor, by reduction mechanisms [50], that also benefited by the development of TPA processes for 3D metal microstructure printing [62]. Other important metal processing mechanisms using alternative material sources, has been laser sintering of nanomaterials, such as gold NPs [21]. The discovery of many carbon-based electronic grade materials, such as carbon nanotubes (CNTs) or graphene, opened new opportunities for flexible electronics processed by DLW, including controlled growth [63], patterned reduction for graphene oxide (GO) [64] or ablation [51].

Underpinned by these developments over the decades, recent developments on ADLW and TDLW for synthesis of distinct materials have been developed, besides metal conductors and common semiconductors beyond silicon. For carbon-based materials, the direct irradiation of polymeric substrates have created the capability for producing a vast array of carbonized and graphitized conductors and semiconductors, where the discovery of laser-induced graphene stands out [65]. At the same time, advancements are being made for the laser synthesis of multifunctional materials employed for electronic device fabrication by ADLW and TDLW, including biodegradable metallic conductors [52], transition metal dichalcogenides [53] and several metal oxide semiconductors [54,55]. These synthesis and conversion paradigms are being employed in large area fabrication, including wafer scale arrays of transistors [53] and memristors [55], as well as implementing laser processed products within R2R manufacturing [56]. This demonstrates the ongoing attempt for large-scale, mass-production implementation of laser-processed electronics, especially for flexible devices with novel architectures and more accessible material sources, crucial for the progressing IoT [4].

2.1.2 Laser systems and operating principles for DLW microfabrication

Physical and chemical phenomena governing laser beam-material interactions are complex and depend on the multiparametric characteristics of laser beams and the absorption and thermal coefficients of irradiated materials. In this section, an overview of key fabrication factors is outlined, establishing some considerations for compatible laser systems and resources for DLW microfabrication paradigms, aiming towards customizable material properties, writing resolutions, and resulting functional material designs.

2.1.2.1 Laser Setups for DLW

Laser systems are usually characterized by fundamental components in their setup. Depending on the active medium used as the radiation source, lasers can be divided into gas (e.g., CO_2 and excimer lasers), liquid (dye lasers), solid-state (e.g., fiber lasers) and semiconductor (e.g., diode) lasers [2]. Besides the laser gain medium, different configurations of pumping energy sources and resonators can be deployed (**Figure 2.3a**), to create laser beams with different characteristics, including wavelengths, energy levels, and time development. For radiation wavelengths, lasers mostly range from ultraviolet (UV) to far infrared (IR), leading to photons with corresponding energies according to Planck's equation: $E = h.\nu$ (**Figure 2.3b**). For the temporal characteristics, laser systems can be divided into two main categories, namely continuous wave (CW) and pulsed lasers. While CW lasers emit steady beams with consistent energy characteristics over time, pulsed lasers allow for a train of individual pulses to be emitted with different pulse widths and frequencies. For example, CO_2 lasers are very limited regarding

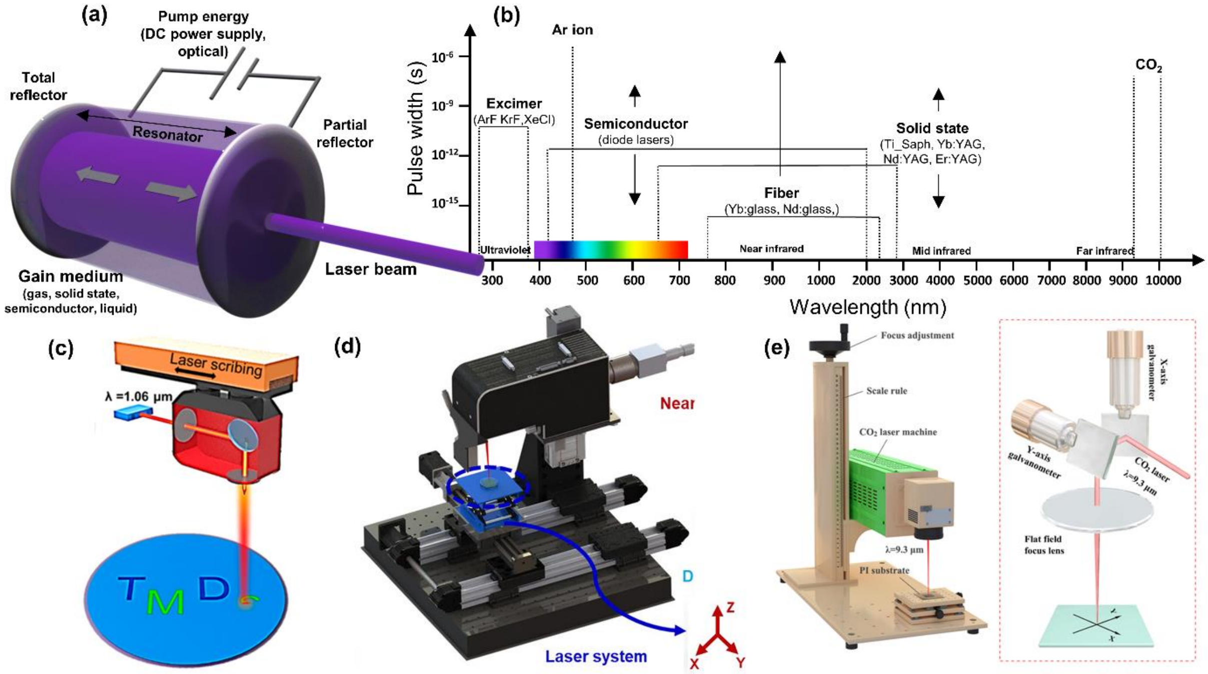

Figure 2.3 - Schematic of laser setups for DLW microfabrication tasks. (a) Representation of a generic laser source and its components. (b) Graph relating wavelength and PWof common laser sources employed for DLW and material processing, depending on their gain medium. (c) Representation of a scribing system based on moving optics system. Adapted with permission [53]. Copyright 2020, American Chemical Society. (d) Representation of a scribing system based on movable stage and static optics. Adapted with permission [76]. Copyright 2022, American Chemical Society. (e) Representation of a writing system based on the use of a galvanometer system. Adapted with permission [82]. Copyright 2021, American Chemical Society.

pulse width (PW) in the millisecond to microsecond range [66], while other laser configurations allow for very short laser pulses in the pico to femtosecond range, using different pulsing strategies such as q-switching and mode-locking [67] (**Figure 2.3b**).

For writing and patterning tasks, the optics systems that shape the laser beam must be coupled with control systems, capable of directing it at determined locations. Movable laser beams have been produced through several routes, each one relying on different hardware assemblies and their coupling with the laser source. A common approach is to integrate mirrors and lens setups with motors that move them, while computer-controlled designs dictate when the laser beam is turned on or off (**Figure 2.3c**). These motion systems are common in many commercial flatbed laser cutting and engraving machines, that have been prolifically employed in DLW tasks [68–72]. Another alternative is the assembly of servo or stepper motors in linear configurations, to build translation stages that move the irradiated substrate, while the optics system is static. (**Figure 2.3d**) [73–77]. Both these approaches result in adequate processing speeds in the meter-per-second range. Besides motion systems, a different approach is the use of scanning systems, such as galvanometers [18,78–82], that directly manipulate laser beam propagation direction towards selective locations, also allowing for higher processing speeds (**Figure 2.3e**). They can also be used to overcome some of the physical limitations of deflecting ultra-short pulse beams as well as high-frequency pulsed lasers [83]. In some cases, tilt stages are also needed in galvanometer-based configurations, to ensure a parallel irradiation surface [78,79].

2.1.2.2 Fabrication parameters for DLW microfabrication

Depending on the characteristics of a laser system, control of laser material interactions and resulting irradiation outcomes is intrinsically dependent on fabrication parameters (e.g., power or writing speed, points per inch, or defocus value, among others). In turn, these parameters control physically significant variables, that dictate the type of phenomenon occurring during irradiation, such as photon flux or heat accumulation over the laser irradiated surface. This is important since researchers can either use commercial or custom-made laser systems, digitally controlled through different fabrication parameters, that may not directly translate to physically meaningful variables (e.g., pulse power, pulse width, repetition frequency, or spot size). As such, physically meaningful fabrication parameters must be used in process-property studies, so that significant comparisons may be drawn between studies employing distinct laser systems or irradiation schemes [84]. Thus, an overview of energy, time, frequency, and spatial domain variables of laser operation and their interdependence are presented in

Figure 2.4 and are further explored in the following sections in terms of their importance in DLW fabrication tasks.

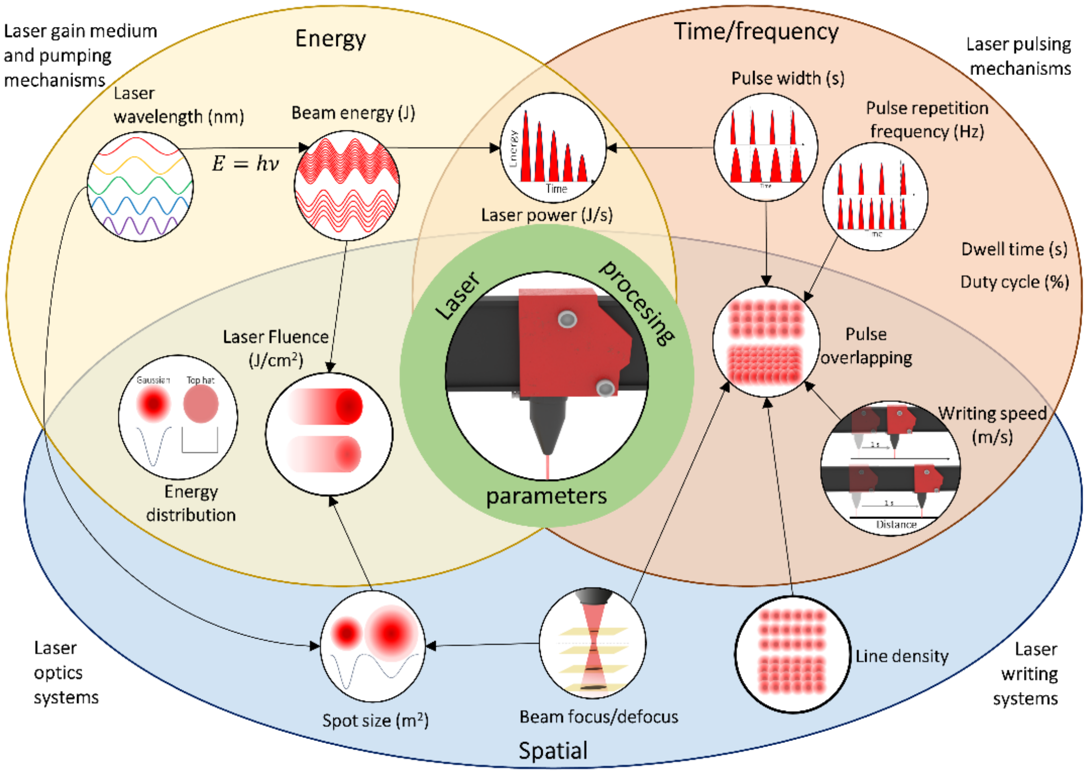

Figure 2.4 - Scheme of DLW fabrication parameters in the energy, time/frequency and spatial domains and their interdependence.

Laser wavelength.

Laser wavelength is a key feature determining the nature of reactions occurring upon irradiation of dissimilar materials. For lower wavelengths, such as in UV excimer lasers, the absorption of radiation is highly dependent on the chemical and electronic structure of irradiated materials, dictating the photochemical phenomenon occurring during irradiation. Low wavelength radiation usually presents higher absorptivity for organic materials and semiconductors, due to the resonant range of chemical bond energies or electronic band structures matching with the photonic excitation energy of the laser photons [85]. For organic materials, different phenomena can occur, including bond forming, isomerization, and breaking [86]. In the case of semiconductor materials, photon energy can differently stimulate the excitation of electrons and have other effects, including thermalization, carrier removal, and thermal and structural effects [87]. For higher wavelengths, lattice vibrations dominate the effects caused by photon energy absorption, leading to a preponderance of photothermal effects resulting in high energy accumulation and temperature increase. The promotion of phonons with high vibrational energies leads to the decomposition of several lower energy bonds while allowing for fast reorganization and structural transitions of irradiated chemical structures during thermal accumulation and after thermal relaxation [88,89].

Wavelength selection is also important to control beam penetration depth, influencing the thickness of processable materials and desired outcomes. This penetration depth (δ) is expressed by: $\delta = \frac{\lambda}{4\,\pi\,k_e}$, where k_e is the extinction coefficient of the material at a specific wavelength [87]. Generally, lower laser wavelengths lead to less penetration, increasing for higher wavelengths, although the absorptivity of materials at specific wavelengths influences these outcomes. This creates the need to optimize photon absorption by the irradiated material at distinct depths, either at the surface of the support substrate or at the surface of active irradiation layers (**Figure 2.5a**). This in turn impacts material deposition and pattern resolution. Thus, studies on the transmission or absorption of irradiated materials are usually performed, to determine the suitability of specific laser wavelengths with different target mechanisms for DLW-based synthesis. While most bulk materials, such as metals, present low absorbances at most wavelengths above the UV (**Figure 2.5b**) [90], other metal micro and nanostructures or metal salt precursors present characteristic absorption profiles due to their chemical structure or plasmonic behavior (**Figure 2.5c**). Therefore, several processes based on single and multiphoton absorption (MPA) benefit from a considerate wavelength selection for optimal reactions and patterning outcomes [55,91]. Within these absorption processes, TPA is a powerful tool within laser-based material processing and microfabrication, used for 3D photolithography and photopolymerization, using photoresists and light sensitive monomers, for high-resolution laser writing [92]. Because two photons are needed to induce efficient electron excitation of a target photosensitive material, their absorption is proportional to the square of light intensity (I^2), resulting in non-linear processes, where photons must coincide in time and space. Thus, the sum of absorbed photon energies must be sufficient to cause excitation from a ground state to an excited state. Because of this, laser wavelength and associated photon energy for two-photon DLW (TP-DLW) must be lower than the energy difference (ΔE) between the electronic states, to avoid the occurrence of single-photon absorption (SPA) processes, that are linear and diminish high-resolution capabilities of the DLW process. Furthermore, laser wavelength also influences the spatial profile of focal units, usually called voxels, manipulated to achieve sub-micrometer resolutions [93].

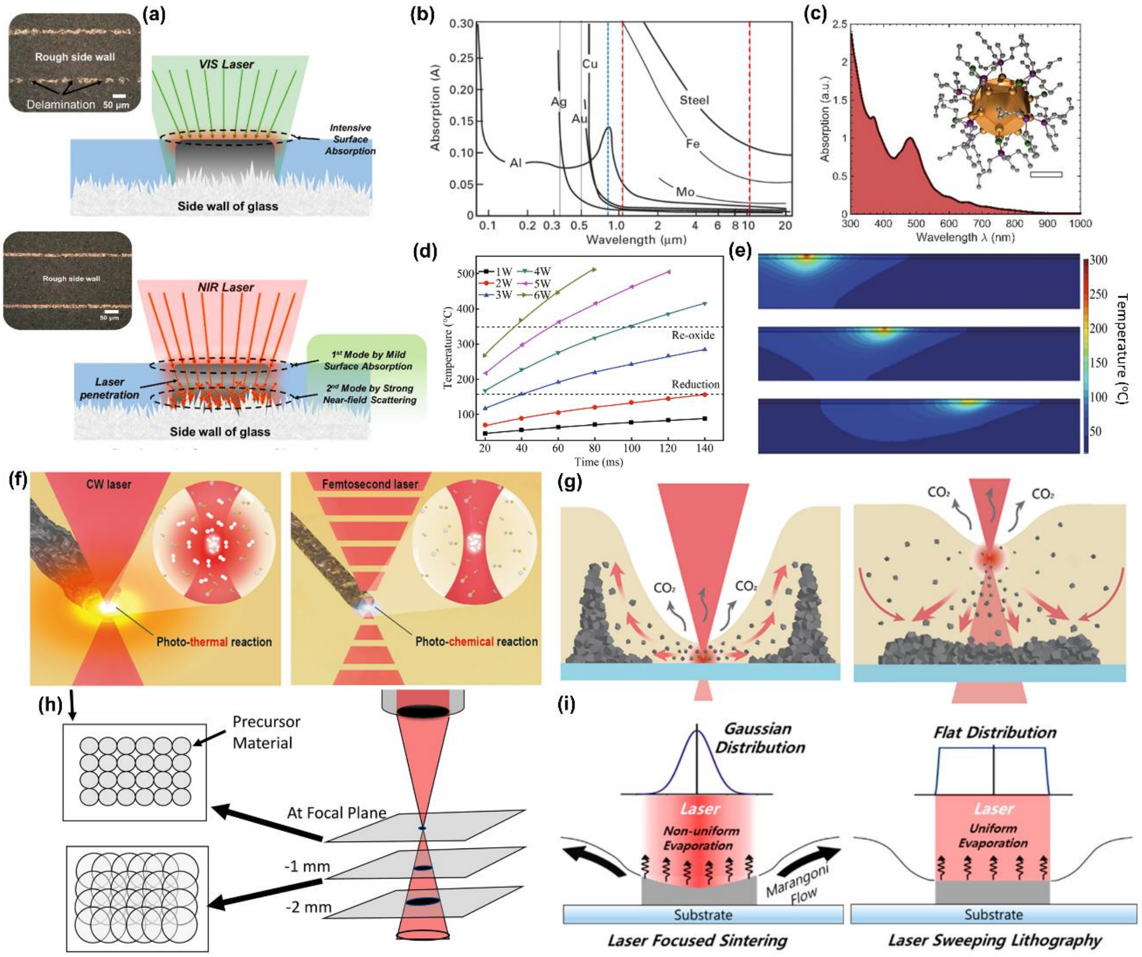

Figure 2.5 - Influence of fabrication parameters on DLW laser-material interactions. (a) Comparison of visible and NIR laser on their penetration depth, absorption and scattering on a silver NP sintering model over a glass. Adapted with permission [310]. Copyright 2020, American Chemical Society. (b) Absorption spectrum of several bulk metals at specific laser wavelengths. Adapted with permission [90]. Copyright 2021, MDPI. (c) Representative absorption spectrum of a plasmonic gold nanocluster. Reproduced with permission [311]. Copyright 2023, Wiley-VCH. (d) Influence of laser power and irradiation duration on reduction and oxidation outcomes of a copper metal ion precursor. (e) Heatmap of temperature distribution for different writing speeds. Reproduced with permission [98]. Copyright 2017, Springer Nature. (f) Schematic comparison of photothermal vs. photochemical material processing depending on CW or femtosecond pulsed laser. (g) Deposition profile of a transition metal dichalcogenide processed by DLW, depending on laser beam focus. Adapted with permission [18]. Copyright 2022, American Chemical Society. (h) Pulse spot overlapping profile of a CO2 laser, depending on laser defocus degree. Adapted with permission [114]. Copyright 2018, American Chemical Society. (i) Comparison of Gaussian and flat top beam energy distributions and effects over silver NP sintering by DLW. Adapted with permission [115]. Copyright 2018, American Chemical Society.

Laser energy and power.

Laser power (Watts – J.s-1) is usually the most used metric in the energy domain, being given by differentiating the energy (Joules – J) of the laser beam concerning time. While in many cases the laser beam power is analogically controlled in the laser system, by modulating the gain medium pumping and output beam, some laser systems control the output power by pulse width modulation (PWM) [94]. In these cases, the laser output energy is constant, and the resulting power is given by percentages of maximum power under continuous mode operation, depending on the pulse duration [94]. Thus, different energy profiles can be reached for the same absolute power output, depending on the employed laser system, and its power control mechanism.

Regarding laser-material interactions, laser power is crucial to establish the threshold at which photochemical or photothermal effects are dominant [95]. Especially for low-wavelength lasers, lower power regimens lead to a preponderance of photochemical phenomena, due to the higher photon energy. With the increase of power, higher temperatures are promoted and can lead to desirable microstructural transitions and phase changes that can be temperature dependent. Depending on the laser power and time evolution of the irradiation process, different temperature-dependent mechanisms can occur, including reduction or re-oxidation of materials, in case excessive energy is employed. (**Figure 2.5d**) [96–98]. When surpassing the melting point, adequate power can lead to sintering and annealing processes for some metallic and metal oxide materials [99], while allowing for photothermal-induced bond breaking and rearrangement in other processes, such as carbonization and graphitization [85]. If not properly controlled, high laser power can also lead to evaporation, sublimation, and ablation of irradiated materials, which in some cases is the desirable outcome for patterning [33,100]. In other cases, it can be an undesirable outcome, that indicates that excessive laser energy degraded the chemical or physical process being targeted. Hence, most process-property optimization methods report the outcomes of irradiation within power intervals against another variable of interest (e.g., writing speed, repetition frequency) to determine processing windows. Thus, laser power is not an independent variable and must be considered together with the time and spatially dependent variables that govern patterning tasks.

Laser writing speed.

Laser writing speed (m.s^{-1}) is highly dependent on the laser beam directing control systems described before, and greatly influences the accumulation of thermal effects promoted by laser irradiation. For CW lasers, writing speed dictates the fluence (J.cm^{-2}) or irradiance

(W.cm^{-2}), since it directly establishes the dwell time of the beam over a unit of area [101]. For pulsed lasers, writing speed is also crucial to determine the overlapping rate of subsequent pulses, playing a critical role in many synthesis and conversion processes, as well as in patterning resolution [102]. As such, writing speed is usually used in conjunction with laser power, to control the energy dose subjected to the irradiated material and its areal distribution, as well as the resulting heat accumulation and dissipation effects. Usually, lower speeds lead to increased temperatures at the irradiation spot and higher heat accumulation at adjacent areas and in depth, while higher speed leads to less thermal accumulation, due to energy dissipation caused by the movement of the laser spot (**Figure 2.5e**) [98]. Thus, many reports of process-property optimizations use power and speed pairs to determine useful processing windows, in opposition to undesirable outcomes such as ablation or incomplete reactions [94,103–106]. A final aspect regarding writing speed is the fabrication and production time. While writing speed has a relevant impact on photon and thermal-induced conversion and synthesis processes, it is relevant to optimize DLW processes for maximum speed, allowing for higher fabrication throughput, contingent that material performance is not compromised [107–109].

Pulse width and pulse repetition frequency.

PW (s) and pulse repetition frequency (PRF - Hz) are the two main variables in the time and frequency domains of pulsed laser irradiation and writing processes. Like writing speed, both have a great influence on photon flux and resulting energy and heat accumulation of individual pulses or subsequent pulse trains. PW can vary greatly, depending on the assembled laser system, going from milliseconds (10^{-3} s) to femtoseconds (10^{-15} s). Generally, PW dictates the time a pulse interacts with the material, and depending on this duration, the radial heat dispersion profile and penetration depth can be manipulated. This has implications not only on patterning resolution, but also in the photochemical or photothermal reactions that can occur during irradiation and their extent over the irradiated area. For CW lasers and short-pulsed lasers, energy accumulation is increased, and higher writing speeds are needed to ensure appropriate reaction conditions and microscale patterning. Ultrashort pulsed lasers allow for a more contained reaction environment, through the creation of reaction voxels [18] that promote photochemical reactions instead of thermal-induced processes (**Figure 2.5f**). More specifically, femtosecond lasers have gained great preponderance in TP-DLW micro and nano-manufacturing paradigms based on photochemical reaction mechanisms, due to the non-linear and nonequilibrium phenomenon that can occur [110]. These processes rely on spatial and temporal photon overlap, showing the non-linear, quadratic dependence of electron excitation. These are greatly promoted using ultra-short pulsed lasers, mostly femtosecond lasers, that provide high photon flux and high peak power at low average power [93], which increase the occurrence of TPA, diminish the occurrence of photothermal effects and provide higher spatial resolution over the writing process.

Usually, ultrashort laser pulses are also coupled with the capability for high PRFs, in the MHz and GHz (10^6 – 10^9 Hz), to allow for material patterning in different settings [111]. In this regard, the duty cycle is an important metric since it establishes the relation between PW and PRF in terms of relative activation time over a pulsing period, and can be used as an optimization metric [112]. This duty cycle can be expressed as a fraction or percentage and is given by the expression: $\text{Duty cycle} = \text{PW x } {}^{1}/_{PRF}$. Knowing the PRF and energy of the laser beam, average laser power can be derived, by the expression: $P_{ave} = E_P \text{ x PRF}$, where E_p is pulse energy. Inversely, pulse power is computed using pulse duration, employing the inverse relation: $P = E_P \text{ / PW}$. For some laser systems, PW and PRF may be manipulated directly in the control software. For some commonly used laser engraving systems, especially with PWM, they are expressed by pulse per distance metrics, such as pulses per inch (PPI) [68–72]. In these cases, conversions are necessary, considering writing speed. For different writing speeds, PRF must vary, to ensure the same number of pulses occur in a set writing distance. In cases where PW and PRF are similar (duty cycle approximating 100 %), there may be overlaps between subsequent pulse activations, giving rise to much higher thermal accumulation and an operation approximating a CW laser [94].

Laser beam focus and spot size.

Spot size and laser beam focusing are crucial variables in the spatial domain of laser writing processes. Laser spot size depends on two main components, namely the wavelength of laser photons and the optics system employed for beam shaping. For a Gaussian beam, laser spot size radius (ω) can be calculated by the following expression: $\omega(z) = w_0\sqrt{1 + (\frac{\lambda.z}{\pi\omega_0^2})^2}$, where ω_0 is the spot radius at focus and z is the relative distance to the focal point. It's noteworthy that spot radius at focus depends on the focal length, characteristic of the specific lens employed for beam shaping. Thus, irradiation spot size is directly controlled by the relative position of the optic lens system and the substrate surface. In a focused position, spot size is minimal, and the beam interacts with materials in its most condensed form. By varying this positioning, irradiation spot size can be manipulated and the laser beam can be focused on various positions relative to the processed material's surface or interface with a support substrate [18,113]. This, in turn, can have various effects on laser-material interactions. For example, when employing solution processing for materials synthesis from a thin precursor film, laser writing at different focal points can determine the architecture and shape of deposited materials (**Figure 2.5g**)[18].

In turn, defocusing beam incidence also results in increases of beam spot radius. This directly dictates the energy density of a laser pulse, expressed by: $\text{Laser Fluence} = {E_p}/{(\pi * \omega_z^2)}$ (J.cm^{-2}), where E_p is pulse energy and ω_z is the spot radius. An increase in spot size also promotes the increase in subsequent laser pulse overlapping, alongside other variables previously discussed. For some writing and conversion processes, overlapping can be a determining variable in the quality of converted materials, as is the case of LIG synthesis (**Figure 2.5h**) [114]. Defocus of the laser beam can also lead to either a convergent or divergent nature of laser photon paths, which can also influence laser-material interaction outcomes, even in cases of equal spot size [94]. It's also important to make some exceptions regarding alternative optic systems and their focusing capabilities. For galvanometer-based systems, the deflection of the laser beam requires lenses capable of focusing beams with different entry angles over a flat working surface. This is usually achieved using f-theta lenses [78,79], which have distinct aspects when considering spot size calculations and fluence. Another factor is the energy distribution of laser beams. While most commonly, laser beams employed in DLW present a Gaussian distribution (TEM00), specific optical hardware can be implemented to achieve alternative beam energy profiles, such as a flat top energy distribution (**Figure 2.5**i)[115]. In such cases, the beam energy is distributed differently over the laser spot area and can lead to different geometrical profiles of written patterns.

Irradiation atmosphere

Although not directly related to laser operation, irradiation atmosphere is an important variable when performing DLW synthesis and conversion tasks. Usually, a choice must be made between performing DLW under inert conditions or an ambient atmosphere. Under inert atmospheres, film and substrate contamination can be avoided, while the absence of reactive volatiles suppresses the occurrence of possible oxidation or combustion promoted by the presence of oxygen [116,117]. These inert atmospheres are usually developed by permeating the working chamber with inert gases [116] or injecting these gases through a nozzle directed at the irradiated area [118], being argon [29,117,119–121] or argon/H_2 mixture (95:5) [116,118] the most common choices. Other gases have been employed for atmosphere control in irradiation procedures, to accelerate certain reactions, for example, reduction, or to suppress plasma and exacerbated heat accumulation [87], where nitrogen flow stands out [68,71,105,122]. However, the need for gas injection systems decreases the cost-effectiveness of the laser writing microfabrication procedures. Thus, ambient atmosphere irradiation schemes have been preferred, in cases where this is not detrimental to the synthesis and conversion outcomes [52–54,123–125].

2.2 Introduction to Laser Carbonization and Graphitization

Laser carbonization and graphitization are similar mechanisms, related to the irradiation of carbon-based precursors, resulting in photothermal effects caused by lattice vibrations and heat accumulation. High temperatures promote the cleavage of chemical bonds, with the release of oxygen-rich volatiles, while most of the carbon fraction of the material reorganizes, also due to photothermal effects. This reorganization is both dependent on the imposed temperatures and heat accumulation overtime, where different irradiation schemes, irradiation atmosphere, and other factors influence the extent of reorganization of native chemical bonds onto pristine, crystalline hexagonal lattices, with minimized atomic defects (**Figure 2.6a**) [126]. This distinguishes processes that lead to carbonization and graphitization, where, more amorphous, less crystalline carbon forms are synthesized for carbonization, while the evolution of this process over time leads to structures with a higher degree of aromaticity and graphitic stacking.

Synthesis principles are similar for both mechanisms, in which carbon bonds are converted from their original hybridization to sp^2-rich chemical structures, through aromatization and condensation processes. Ultimately, this leads to the build-up of graphene lattices in organizations analogous to graphite, with similar interlayer distances (3.37 Å) (**Figure 2.6b**), but more defective atomic carbon-bond organization at the lattice level. (**Figure 2.6c**) [88]. Regarding the microstructure of carbonized and graphitized materials of different origins, the release of volatiles leads to the formation of porous 3D structures, where cross-section analysis is usually employed to determine the effect of the irradiation towards the thickness and arrangement of formed graphitic layers (**Figure 2.6d**). In the perpendicular axis, there is usually a distribution of the material accompanying the laser beam path (**Figure 2.6e**). In cases where there is the presence of other inorganic phases, carbonization processes can also promote the synthesis of metal carbide materials, with carbon fraction participating in carbothermal reduction mechanisms [127,128].

Laser carbonization of PI has been observed as far back as the 1980s [129], using argon-ion lasers. However, these techniques took traction when Dr. James Tour's research group reported, in 2014, an alternative for the synthesis of 3D porous graphene resulting from the conversion of PI when exposed to far-IR CO_2 laser irradiation [65]. Although CO_2 lasers being the tool of choice for carbonization and graphitization [65,70,128,130,131], other laser sources have shown compatibility, including UV [132–135] and visible lasers [136,137]. For these lower wavelength sources, authors report the concurrent occurrence of photochemical processes [138], although they are not sufficient to cause efficient carbonization and graphitization, which is mostly promoted by temperature-induced effects [139,140].

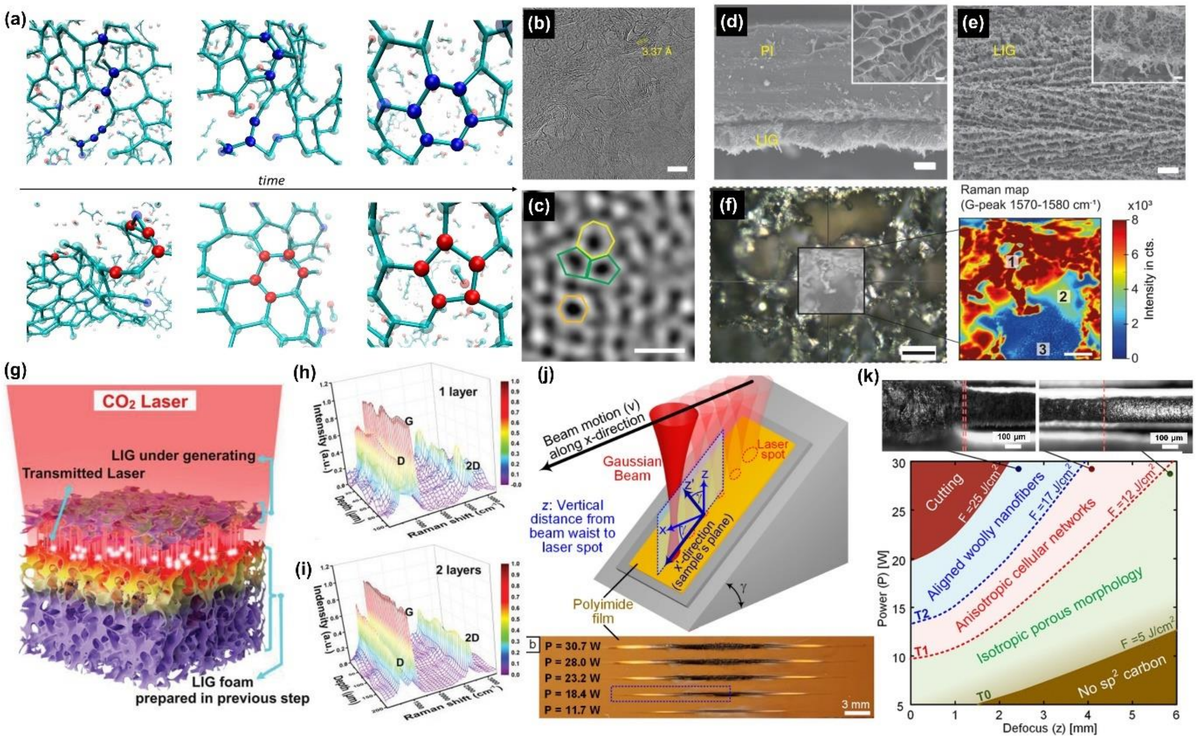

Figure 2.6 - DLW for laser-induced carbonization and graphitization. (a) ReaxFF molecular dynamics simulations of PI carbonization/graphitization over time and the distribution of pentagonal and hexagonal carbon arrangements. Reproduced with permission [126]. Copyright 2020, American Chemical Society. Transmission electron microscope images of LIG for (b) interlayer distance and (c) carbon atom lattice distribution analysis. Scanning electron microscope images of LIG (d) cross-section and (e) distribution of porous material over the laser beam irradiation path. Reproduced with permission [65]. Copyright 2014, Springer Nature. (f) Raman spectroscopy mapping of a wood derived LIG surface and the distribution of G peak intensities. Adapted with permission [128]. Copyright 2022, Springer Nature. (g) Layered synthesis of LIG from a polyether sulfone precursor and the distribution of chemical properties in depth, surveyed by Raman spectroscopy for (h) 1 precursor layer and (i) 2 precursor layers. Reproduced with permission [141]. Copyright 2023, Wiley-VCH. (j) Laser beam defocus method for spot size and laser fluence selection. (k) Dependency on laser power and defocus distance towards morphological transition levels. Adapted with permission [96]. Copyright 2021, American Chemical Society.

The resulting material was labeled LIG, although other names have been used in the literature, including laser-engraved graphene (LEG) [142] or laser-scribed graphene (LSG) [143]. Since then, tremendous progress on conversion and patterning mechanisms of PI and other precursors has occurred, regarding conversion mechanisms, material property optimization, and the multiple fields of application [144–147]. Depending on the chemical structure of precursors, different graphitization potentials result from the abundance of aromatic chemical structures within a precursor, while for substrates without aromatic chemical moieties, different modification strategies are needed to ensure efficient carbonization and graphitization strategies.

For synthetic aromatic polymers, such as PI and polyetherimide (PEI), DLW leads to direct graphitization, contingent that the laser irradiation schemes provide sufficient temperature stimuli [65,126]. For aliphatic materials, such as several abundant biopolymers, substrate modification strategies that improve thermal resistance are needed. Appropriate laser systems that present higher control of heat accumulation profiles can also be used [88]. Contingent on the chemical formulation of precursors and laser irradiation schemes, tailored properties of resulting graphitized materials are possible, aiming at improved defect densities, crystallite size, electrical conductivity, and overall morphology. Being a 3D graphitic material with significant porosity, control of the overall chemical properties of LIG throughout the irradiated area and film depth is also important, usually being surveyed in many process-property experiments. This optimization has been mainly performed using Raman spectroscopy, to determine chemical characteristics of LIG over material topography. In the work by Dreimol et al., mapping of Raman peak distribution over wood-derived LIG showed improved graphitization in more superficial areas, exposed to higher temperatures (**Figure 2.6f**). Because of these differences in depth, novel strategies have appeared in the DLW graphitization paradigm, designed to synthesize more uniform LIG in all directions. An example is the work by Song et al. [141], where the synthesis is performed in multiple steps, each focusing on a single layer of precursor (**Figure 2.6g**). A controlled thickness of precursor can be used, guaranteeing a uniform graphitization at depth for subsequent layers, surveyed by Raman spectroscopy (**Figure 2.6h-i**). Along with these outcomes, the control of the electrical conductivity of carbonized and graphitized materials has been essential in developing this field.

Although LIG is categorized as semiconducting ($\sigma < 10^3$ S.cm^{-1}), it has mostly been used due to its conductive characteristics. Contrarily to laser synthesized and patterned metal oxides and other semiconductor materials, where standardization of properties highly depends on the metal type and other variables such as oxygen content, LIG has been mainly compared by its sheet resistance. Another important consideration is the morphology of the resulting LIG, highly dependent on the coefficient of thermal expansion and melting mechanisms of the precursor and irradiation parameters. For PI, the specific manipulation of several parameters, not only related to power but also associated with spot size, beam defocus, and resulting areal energy density, allows for control of shape and topological distribution of LIG networks. More specifically, in the work by Abdulhafez et al. [96], a control of laser defocus and resulting fluence allows for the formation of distinct 3D arrangements, depending on the distance of the substrate to the beam-shaping lens (**Figure 2.6j**). The formation of isotropic pores, cellular networks, and nanofibers can be selected, at transition levels depending on the applied laser fluence regimen (**Figure 2.6k**). In addition, synergistic effects of chemical and morphological properties of LIG also influence the interaction of these graphitic materials with aqueous and liquid phases, with the possibility of controlling hydrophobicity, an important factor in several applications requiring electrolyte/electrode interactions [148,149]. For other emerging precursor materials, such process-properties studies have been explored in more specific cases and in less detail but are fundamental in the future development of DLW fabrication paradigms in several applications.

2.3 DLW of Carbon-based Materials

The manipulation of carbon-based precursors and surfaces using DLW has been explored over the years, to achieve the synthesis of varied materials or improve their functionality in different contexts. Processes that include annealing of amorphous carbon films [150], synthesis of CNTs from carbon black [63], carbon-rich SiC structures over 4H-SiC wafer, [151] and writing of diamond-like carbon materials [152] are some relevant examples. However, their expression and adoption in electronics microfabrication was not widespread, since either the materials did not provide attractive features or because they were meant to substitute established techniques and did not provide sufficient flexibility and throughput. Recently, other relevant approaches with much higher adoption have appeared, where laser synthesis and patterning of reduced graphene oxide (rGO) stand out [153]. Even though the popularity and prolific applicability of laser-based rGO synthesis, this method suffers from a key disadvantage, since there is the need for multiple preparation steps, starting with the cumbersome synthesis of GO from graphite, GO dispersion, and ink preparation, followed by the modification of the substrate material or surface with GO. However, this technique propelled the interest in laser fabrication and engineering of graphene-based electronics [154].

Contrarily, DLW applied for direct carbonization and graphitization of substrates has gained great traction, since it has shown to be compatible with a large pool of substrate sources, from synthetic to naturally sourced. Simultaneously, it allows for one-step, selective synthesis, and patterning of tailored graphene-based structures and seamless assembly of graphene architectures. To draw comparisons between several precursor substrates and resulting irradiation outcomes, an overview of LIG synthesis and properties using several emerging precursor substrates is presented in **Table 3.1**, including aromatic polymers, naturally derived precursors, and custom-made precursor formulations.

Table 2.1 - Overview of LIG synthesis from carbon-based precursors and resulting properties.

Precursor	Substrate formulation/ treatment	Atmosphere	Laser source	ID/IG	Conductivity	Ref
PI	-	Ambient	CO2 laser (10.6 µm)	0.4	15 Ω.sq-1 / 25 S.cm-1	65
Polyetherimide	3D printed PEI	Ambient	CO2 laser (10.6 µm)	-	0.3 Ω.sq-1	155
	-	Ambient	CO2 laser (10.6 µm)	0.2	15 Ω.sq-1	114
Polycarbonate/PEI blends	Different blend percentages	Ambient	CO2 laser (10.6 µm)	-	4 S.cm-1	156
Polyethersulfone	Microporous PES	Ambient	CO2 laser (10.6 µm)	0.7 – 0.3	4.1 Ω.sq-1 / 9.24 S.cm-1	141
Parylene-c	-	Ambient Nitrogen flow	CO2 laser (10.6 µm)	0.42	9.2 Ω.sq-1 178.5 Ω.sq-1	157
Polybenzimidazole ink	PBI @ DMSO coated on PET and glass	Ambient	Picosecond UV laser (355 nm)	-	8 Ω.sq-1 / 50 S.cm-1	132
Liquid crystal polymer	Aromatic block copolymer	Ambient	450 nm laser	0.58	<20 Ω.sq-1	56
Para-aramid textile (Kevlar)	Woven, non-woven and knitted textiles	Ambient	Yb-doped femtosecond fiber laser (1035 and 347.8 nm)	0.265	2.86 Ω.sq-1 5.02 Ω.sq-1	158
Meta-aramid (Nomex paper)	-	Ambient	CO2 laser (10.6 µm)	-	~20 Ω.sq-1	159
Carbon fibers	Mesophase pitch carbon fibers (pre-carbonized)	-	CW semiconductor laser (915 nm)		7.04 x 103 S.cm-1	117
	Lignin-impregnated carbon cloth	Ambient	CO2 laser (10.6 µm)	0.85	-	160
Liquid precursor	Synthetic aromatic-rich polymeric viscous precursor using benzoxazine chemistry	Ambient	CO2 laser (10.6 µm)	0.4	50 S.cm-1	70
	Furfuryl alcohol	Ambient	CO2 laser (10.6 µm)	0.7	-	120
Wood	-	Ar/H2	CO2 laser (10.6 µm)	0.48	10 Ω.sq-1	116
	-	Ambient	UV femtosecond laser (343 nm)	0.63	10 Ω.sq-1	133
	Iron-tannic acid ink treatment	Ambient	CO2 laser (10.6 µm)	-	30 Ω.sq-1 /25 S.cm-1	128
Cork	-	Ambient	CO2 laser (10.6 µm)	<1	115 Ω.sq-1	161
	Agglomerated and natural cork	-	Diode-pumped Nd:YVO4 pulsed laser (355 nm)	<1	75 Ω.sq-1	134

	Commercial cork + FR (boric acid)	Ambient	450 nm laser	1	46 Ω.sq-1	136
	Agglomerated cork + wax treatment	Nitrogen flow	Nd:YAG fiber laser (1.06 µm)	0.2	7.5 Ω.sq-1	162
	Natural cork	Ambient	450 nm laser	0.8	10.8 Ω.sq-1	163
Lignin / Lignocellulose	Lignin/PVA film	Ambient	CO2 laser (10.6 µm)	0.39	3.8 Ω.sq-1 /66.2 S.cm-1	164
	Lignin/PVA/urea film	Ambient	CO2 laser (10.6 µm)	0.33	2.8 Ω.sq-1	165
	Lignin/PEO film	Ambient	CO2 laser (10.6 µm)	1.1	363.1 Ω.sq-1	166
	Kraft lignin/PVA	Ambient	CO2 laser (10.6 µm)	0.37	4.5 Ω.sq-1	167
	DES pretreatment for lignocellulose film production	Ambient	CO2 laser (10.6 µm)	0.61	24 Ω.sq-1	69
	2-hydroxyethyl cellulose + lignosulfonate ink + FR (boric acid)	Ambient	CO2 laser (10.6 µm)	-	3.8 Ω.sq-1 / 28 S.cm-1	168
Paper	Whatman filter paper + commercial FR (ammonium sulfamate)	Ambient	CO2 laser (10.6 µm)	0.86	61.5 Ω.sq-1	169
	Filter paper + commercial FR (ammonium phosphate)	Ambient	CW CO2 laser (10.6 µm)	0.5	32 Ω.sq-1	170
	Filter paper + commercial FR (ammonium phosphate)	Ambient	Diode-pumped Nd:YVO4 UV laser (355 nm)	-	132 Ω.sq-1	135
	Cotton cellulose paper + FR (ammonium sulfamate)	Ambient	CO2 laser (10.6 µm)	1	23 Ω.sq-1	171
	Colored paper, paper cup & milk carton	-	Nd:YAG CW laser (532 nm)	0.9	105 Ω.sq-1	172
	Whatman filter paper + FR (sodium tetraborate) + coloured wax loading	Ambient with nitrogen flow	CO2 laser (10.6 µm)	0.28	5 Ω.sq-1 / 24.3 S.cm-1	130
	Hemp fiber paper + lignin-based epoxy acrilates + FR (ammonium phosphate)	Ambient	CO2 laser (10.6 µm)	0.77	3 Ω.sq-1	173
	Filter paper + lignin solution + FR	-	460 nm laser	-	52 Ω.sq-1	174
Nanocellulose	TEMPO-oxidized cellulose nanofibers	Ambient	CO2 laser (10.6 µm)	>1	60 mS.cm-1	123
	Cellulose nanofiber film	Ambient	Femtosecond laser (522 nm)	0.2	6.9 S.cm-1	75
	Cellulose nanocrystals film	Nitrogen flow	CO2 laser (10.6 µm)	>1	600 Ω.sq-1	175
Hemicellulose	Carboxymethyl Xylan + FR (ammonium phosphate)	Ambient	CW CO2 laser (10.6 µm)	-	186 Ω.sq-1	176
Chitosan	Chitosan/HCl solution	Ambient	CO2 laser (10.6 µm)	-	5.5 kΩ.sq-1	177
	Chitosan/acetic acid/glycerol solution	Ambient	3-step laser synthesis: CO2 laser (10.6 µm) and UV laser (405 nm)	1	40 Ω.sq-1 / 2.5 S.cm-1	178
	Carboxymethyl chitosan aqueous solution	Ambient	CW CO2 laser (10.6 µm)	-	2.2 kΩ.sq-1	131
	Chitosan oligosaccharide aqueous solution	Ambient	CW CO2 laser (10.6 µm)	-	33.9 Ω.sq-1	131
	Chitosan hydrochloride aqueous solution	Ambient	CW CO2 laser (10.6 µm)	-	12.7 Ω.sq-1	131
	Chitosan-borax composite film	Ambient	CO2 laser (10.6 µm)		110 Ω.sq-1	179
Chitin	Chitin nanopaper + FR (CaCl2)	-	CO2 laser (10.6 µm)	-	-	71
Alginate	Cross-linked sodium alginate (CaCl2 cross-linking agent)	-	CO2 laser (10.6 µm)	2.2	15 kΩ.sq-1	180
Agarose	Agarose + lignin hydrogel	Ambient	Femtosecond laser (522 nm)	-	150 µS	181
Elastomers	Ecoflex	Ambient	CW Verdi laser (532 nm)	-	-	137
	PDMS	Ambient	CW diode laser (405 nm)	0.8	5.0 kΩ.sq-1	182

	PDMS	Ambient	Femtosecond laser (522 nm)	0.4	0.5 S.cm-1	183
	PDMS + triethylene glycol	Ambient	CO2 laser (10.6 µm)	1.64	130 Ω.sq-1	184
Natural fabrics	Commercial woven silk fabric precarbonized before irradiation	Ambient	Fiber laser (1064 nm)	-	40 Ω.sq-1	185
Metal-organic frameworks	NiCo-MOFs/PAA films	-	Femtosecond laser (1035 nm)	0.98	45 Ω.sq-1	186

2.3.1 DLW of synthetic aromatic polymers

Since the initial report by Jian Lin et al. [65], several advancements have been made in the preparation of LIG from different aromatic polymer sources. For PI and similar polymers containing aromatic and imide repeating units, efficient graphitization is straightforward, where fine control of irradiation parameters leads to sheet resistances around 15 $\Omega.sq^{-1}$ (σ of 25 $S.cm^{-1}$) or lower. Other aspects besides conductivity have also been manipulated with great efficiency, including morphological characteristics [96], surface hydrophobicity [149], and doping of graphene crystalline structures [187]. Many process-property optimization studies targeting different characteristics of LIG materials have shown to be crucial to understanding irradiation outcomes in PI and establishing protocols for the transfer of writing principles for the graphitization of alternative polymer substrates. Several aromatic polymers have been targeted, including PEI [114,155], polyethersulfone (PES) [141], parylene-C [157], polybenzimidazole (PBI) [132], and aromatic polyamides [158,159]. In terms of the conductive characteristics of resulting LIG, similar sheet resistances are achieved to standard PI-derived LIG. Notably, PEI has shown to be a high-efficiency precursor, with sheet resistances below that of PI, with values as low as 0.3 $\Omega.sq^{-1}$ for LIG derived from 3D printed PEI surfaces [114]. This work by Gilavan et al. [114] shows the capability of integrating conductive LIG patterns on surfaces with 3D conformations. Thus, one of the main trends in aromatic polymer-based LIG has been the use of custom-made polymer formulations, in opposition to commercial forms of these materials. One example is the work by Correia et al. [157], where LIG patterning is performed on parylene-C, a biocompatible, flexible, highly inert substrate, deposited over a glass carrier through CVD. By employing ambient and nitrogen-rich irradiation atmospheres, the authors showed the relevant influence of ambient atmospheres to achieve an efficient graphitization of this aromatic polymer precursor, reaching sheet resistances values as low as 9.2 $\Omega.sq^{-1}$ for ambient atmosphere, in opposition to 178.5 $\Omega.sq^{-1}$ when employing a nitrogen-rich atmosphere.

Because of the efficient nature of DLW, novel fabrication paradigms have appeared for these high-efficiency aromatic precursors. One such breakthrough is the development of LIG from aromatic liquid precursors. In the work by Huang et al. [132], organic PBI inks were used as a graphene-forming phase and can be printed onto different substrates, including glass and PET. Attractive conductivities can be achieved using this process, employing a picosecond UV laser, with a sheet resistance of 8 $\Omega.sq^{-1}$ translating to conductivities around 50 $S.cm^{-1}$. In the work by Yu et al. [70], the authors developed a custom-made formulation of a liquid, viscous aromatic polymer precursor, made from two monomer units, that endow the precursor with its graphitizable characteristics, arising from the aromatic structure, as well as molecular flexibility, through the introduction of a long alkyl chain (**Figure 2.7a**). No detriment to the structural integrity of the graphitized patterns was caused by the liquid nature of the precursor (**Figure 2.7b**), retaining the characteristic porous nature of LIG (Figure **2.7c**). The authors performed process-property optimization studies focusing on three fabrication variables, namely spot diameter, laser power, and thickness of the precursor film. Spot size was an important variable determining the efficiency of graphitization, surveyed by Raman spectroscopy (**Figure 2.7d**),

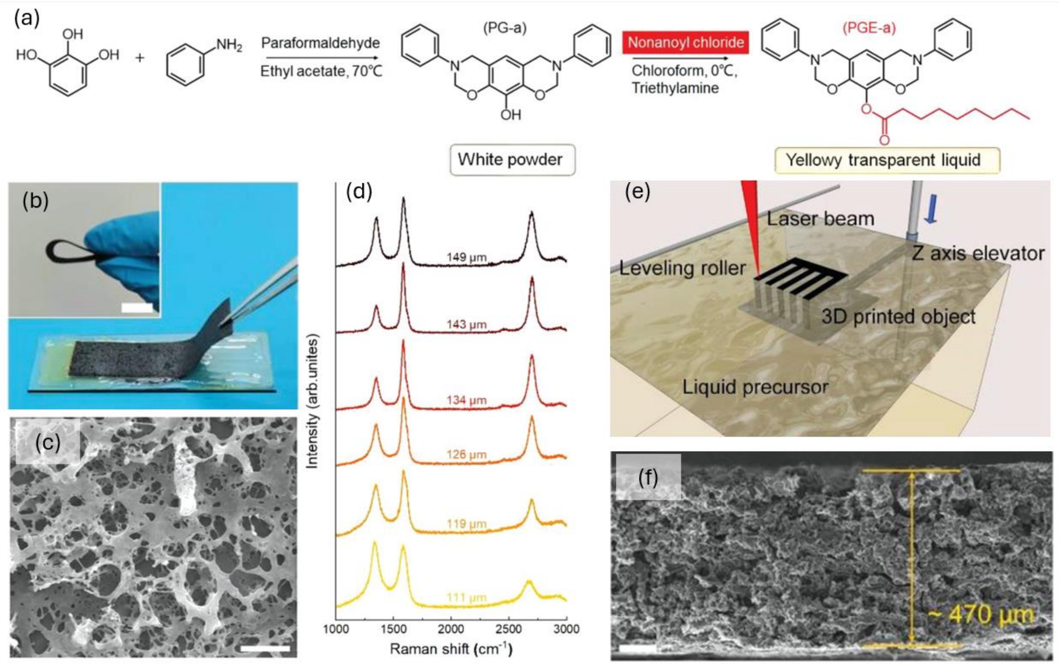

Figure 2.7- DLW processing of a liquid aromatic precursor for LIG synthesis and patterning. (a) Chemical structure of aromatic liquid precursor made from aromatic monomers and long alkyl chains (PGE-a). (b) Images of converted liquid precursor, showing mechanical stability and flexibility. (c) SEM image of porous LIG structure arising from graphitization of liquid precursor. (d) Raman spectroscopy process-property optimization of chemical properties of LIG, depending on laser spot size. (e) Printing of 3D LIG microstructures from aromatic liquid precursor and (f) resulting thickness of the LIG macrostructure. Adapted with permission [70]. Copyright 2022, Wiley-VHC.

and in conjunction with the remaining two variables, tunable conductivity and thickness of graphitization layers were achieved, showing a maximum conductivity of around 50 S.cm^{-1}. Most importantly, this liquid characteristic of the precursor allows for the printing of 3D LIG structures, by employing successive irradiation cycles and manipulating beam focus, by moving the precursor in the z-axis (**Figure 2.7e**). This is performed by moving the substrate platform at a length equal to the thickness of individual LIG layers, leading to the integration of porous, vertical layers within 3D geometries with controlled height (**Figure 2.7f**). This turns spot size into a key fabrication parameter since different positionings of the laser beam leads to varied spot sizes and possible inconsistencies of the synthesis in the vertical direction. Additive laser printing of 3D LIG structures has thus been sought after to improve the applicability of laser graphitization processes. Another proposed approach was reported by Song et al. [141], using successive porous PES layer deposition and laser graphitization. This layer-by-layer covalent growth approach allows for an efficient interconnection between subsequent LIG layers, showing not only an efficient conductivity in each layer, but also an improved cross-layer conductivity for the all-graphene macrostructures. In-plane conductivity of 9.2 S.cm^{-1} was achieved, while comparable cross-layer conductivity of 8.2 S.cm^{-1} was reported. This good isotropic conductivity was attributed to the capacity to achieve efficient covalent interconnection between LIG layers, also improving crystallinity over the macrostructure thickness. Other aromatic polymer forms were shown to be attractive LIG precursors. Notably, aramid materials have been used, either in the form of Kevlar fabrics [158,188,189] or Nomex paper [159]. In the work by Yang et al. [158] the use of a femtosecond fiber laser for the graphitization of non-woven, knit, and woven Kevlar textiles allows for the efficient synthesis of LIG with low sheet resistances of 2.86 Ω.sq^{-1}, endowing several functionalities onto these textiles for multimodal applications in smart clothing. Nomex paper sheets have also resulted in LIG with attractive sheet resistances around 20 Ω.sq^{-1}, enabling the production of double-sided surfaces employed for human-machine interfacing [159].

2.3.2 DLW of naturally sourced materials

Green LIG (gLIG) is an emerging and trendy carbon material obtained by DLW of several bio-based carbon sources and substrates, such as wood, leaves, cork, husks and cellulose (**Figure 2.8a**) [190]. The graphitization occurs by the same mechanisms as for aromatic polymer precursors, through photothermal and/or photochemical effects, upon which surface carbon atoms are converted from sp^3 to sp^2 dominated configurations, with some differences in chemical reactions depending on the aromatic or aliphatic nature and composition of the substrates.

Furthermore, different laser systems and their operational parameters influence this conversion, namely in terms of bond breaking, rearrangement and the efficiency of these processes in the synthesis of graphitic carbon forms that characterize gLIG. In this section, conversion processes and their manipulation are addressed.

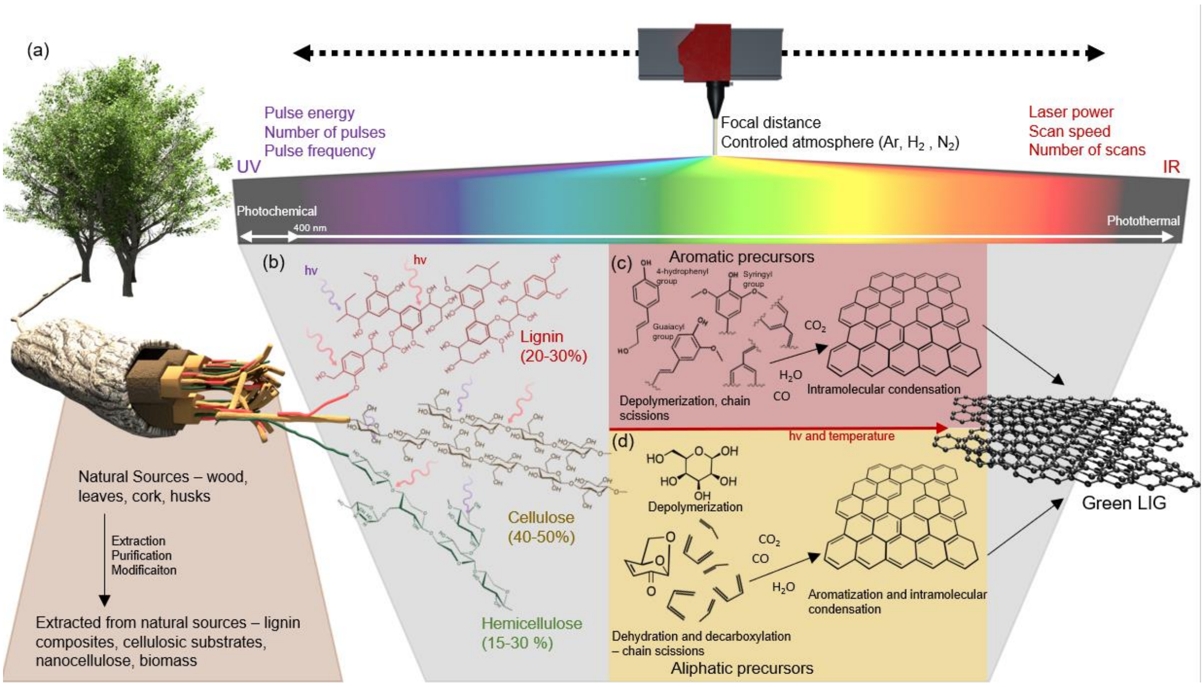

Figure 2.8 - Schematic illustration of the conversion mechanism for green LIG. (a) Sources of green LIG from raw materials and processed by-products obtained from these natural sources. (b) Macromolecule chemical structure of lignocellulose biopolymers, its composition range on natural sources. (c) Aromatic and (d) aliphatic chemical mechanism conversion to green LIG, respectively.

2.3.2.1 Aromatic lignocellulosic materials

Lignocellulosic materials found in many potential gLIG precursor substrates are the most abundant renewable sources of aromatic chemical structures [191]. This is because of the high lignin content of the natural materials, with up to 30% content depending on the biomass source. Lignin contains in its structure an abundance of benzene rings covalently bound to other functional groups, resulting in an amorphous branched aromatic polymer, constituted by three different aromatic ring substitution patterns, namely p-hydroxyphenyl, guaiacyl, and syringyl monomers (**Figure 2.7b**) [192]. When using bio-based gLIG sources that contain this aromatic macromolecule, such as wood or even engineered films composed of extracted lignin, the conversion processes and reactions into graphitic structures are based on the breaking of

C-C, C-O and C-H bonds both within and outside the aromatic structures, followed by reorganization into char-like or graphitic structures, depending on the degree of pyrolytic activity set by the laser irradiation parameters. These principles are analogous to the ones established for PI conversion into LIG, since both these precursors are rich in native aromatic structures. However, each have specificities related to the differences in their chemical structure and the distribution of aromatic moieties over the molecular structure [126,193].

When considering the photochemical degradation processes that can occur upon the laser irradiation process, specific linkages within the polymeric structures of lignin and their interaction with the incident photons must be considered. Several studies have reported the analysis of UV photodegradation of lignin in wood and kraft pulp, showing that α and β glycosidic bonds are more prone to cleavage, while carbon bonds connecting aromatic structures have resistance to UV irradiation [194]. This shows that the aromatic backbone of lignin and its connection is usually maintained, allowing for their subsequent reorganization and polymerization into graphene structures. Similar processes have been achieved using IR laser irradiation, by tuning the wavelength to specific vibrational modes of linkages within lignin, leading to depolymerization [195]. However, photochemical processes alone are not capable of inducing graphitization. For the synthesis of more aromatic dense chemical structures leading to LIG, photothermal processes are needed, to further break undesired chemical structures and promote an efficient reorganization. In most pyrolytic reactions of lignin, based on its exposure to varying temperatures and pressures, its decomposition is also based on depolymerization, by breaking of different ether linkages (C-O-C) or condensed C-C bonds, leading to the formation of volatiles and solid carbonized materials identified as chars [196]. In these cases, the increase in photothermal induced temperature leads to further degradation of chars and lignin monomers, to synthesize highly valuable, refined aromatic chemicals such as phenol or benzene, among others [191,196,197]. For some conditions, such as in fast pyrolysis, these small aromatic molecule precursors can be used for condensation, leading to the synthesis of polycyclic aromatic hydrocarbons (PAHs), with higher density of aromatic structures [198].

These pyrolysis principles serve as a model to understand the laser irradiation conversion process of gLIG from aromatic-rich lignin. For gLIG synthesis, lignin is exposed to much higher temperatures for much shorter time frames, leading to the occurrence of very fast, similar processes, that can be modeled in two distinct steps:

(i) photochemical/photothermal promoted bond cleavage and laser promoted vibration of atomic networks, resulting in high localized heating of the material, leading to depolymerization, decarboxylation and dehydration, by cleavage of C-O-C, C-O, C-C and C-H bonds and subsequent recombination of oxygen, hydrogen and some carbon into volatiles.

(ii) temperature-promoted rearrangement of aromatic compounds and other carbon chemical structures to form condensed graphitic structures dominated by sp^2 hybridized carbon (**Figure 2.8c**). In terms of the rearrangement of aromatic structures into sp^2 dominated lattices, reactions governing these phenomena are based on ring closures that define the graphitization process. Although there are several chemical processes for ring closure and stitching for synthesis of graphene nanostructures from PAHs [199], gLIG synthesis ensuing graphitization is promoted by the very fast photothermal processes caused by the laser, that induce structural changes into more energetically stable graphene lattices and their 3D stacked form.

During laser irradiation, both these sub-processes of removal of oxygen functional groups and direct conversion from sp^3 to sp^2 dominated structures coexist and are manipulated by laser operation parameters dictating the level of laser exposure or by the selected laser wavelength [200]. As such, most literature has proposed that this aromatic bio-based source can be directly converted to graphitic structures. Because of the native presence of aromatic structures in lignin, its conversion is not fully supported over additional aromatization, as opposed to other LIG precursors discussed in the following section. As such, control over the aromaticity of the synthesized structures is based on the efficiency of the laser irradiation process over the cleavage of undesirable bonds, that promote more reduced structures with less oxygen functional groups, while the degree of aromatic condensation relies upon reaching temperatures that promote efficient rearrangement of aromatic structures [201], resulting into 2D lattices composing the 3D structure of LIG. By establishing these conversion principles, more control over the resulting properties of LIG can be achieved and tailored to specific applications.

Another class of natural aromatic precursors explored for LIG synthesis have been naturally sourced polycyclic heavy hydrocarbons (PHHs), such as coal, tar, pitch and biochars [202–204]. These materials present a native abundance of aromatic carbon and sp^2 hybridized chemical structures, intercalated by some aliphatic hydrocarbon structures. By employing laser irradiation over these substrates, the aromatic content and sp^2 concentration can be tailored from amorphous into highly ordered graphitic structures with intrinsic conductive properties, characteristic of LIG. This conversion is different from lignin conversion in that laser irradiation promotes the annealing of native sp^2 structures and a decrease of C-H bonds present in the precursor material, without the need for additional aromatization.

Several sources of vegetable biomass have been used as efficient LIG precursors, due to the presence of aromatic components that endow them with graphitization potential [88]. For wood, there is a significant presence of aromatic lignin, in addition to polysaccharides such as cellulose and hemicellulose, with relative amounts dependent on the type of wood and tree species, leading to distinct graphitization potentials. This was first reported in the pioneering work by Ye et al. [116], where pine, birch, and oak wood sources were used for LIG synthesis. Because of the higher relative concentration of lignin in pine, a lower degree of defects in LIG structures is achieved, as well as attractive sheet resistance around 10 $\Omega.sq^{-1}$. However, as denoted in this work, the significant fraction of aliphatic carbon, arising from polysaccharides, diminishes the stability of the material for graphene induction. Polysaccharides tend to completely decompose upon irradiation, instead of participating in the carbonization and graphitization process. To avoid this, the authors employed an inert Ar/H_2 atmosphere, to decrease the oxidative and combustive effects. Since then, several strategies have been put forward to avoid the use of a less accessible inert atmosphere. These include the use of femtosecond lasers, that allow for an increased control of heat accumulation and resulting photothermal processes, decreasing the decomposition of aliphatic phases in wood and other materials, such as leaves [133,205]. Another approach is to perform chemical treatments of lignocellulosic precursors, including fire-retardants [114] and catalyzing inks [128]. In the work by Dreimol et al. [128], an iron-tannic acid ink, made with gum arabic and glycerol, was used to enable conversion into high-quality, conductive graphitic materials, promoted by the aromatic tannic acid and the presence of iron (**Figure 2.9a**). Iron appears as a crucial component, due to the formation of iron carbide NPs, as surveyed by TEM imaging (**Figure 2.9b-c**) The authors propose that these carbide NPs promote graphitization in opposition to the formation of amorphous carbon. This way, CO_2 lasers can be readily employed for the graphitization of wood materials, making this process much more accessible.

Besides wood, other vegetable biomass sources have appeared as highly efficient precursors. One of the most prolific has been cork, due to the abundant presence of not only lignin but also suberin, an aromatic-aliphatic cross-linked polymer, that improves the relative aromatic content in this material. Several approaches have been used for cork graphitization and pattern by DLW, using CO_2 [161], UV and [163] IR-fiber lasers [162]. The use of fire-retardant chemicals has also been attempted [136]. Sheet resistances comparable to wood have been achieved using cork substrates, with the lowest value reported in the literature of 7.5 $\Omega.sq^{-1}$ [162] using waxed cork substrates and a 1064 nm fiber laser. Inspired by the graphitization potential of lignin, isolated forms of this component have also been employed for LIG production. In most cases, lignin has been used within polymeric composite sheets, where the concentration of lignin can be studied for optimized irradiation outcomes. Such polymers include PVA [165,167,206], PES [207], poly-l-lactic acid (PLLA) [208], and polyethylene oxide (PEO) [166,209]. Several lignin sources have also been targeted, including kraft lignin [166,167], alkali lignin [208,209], and lignosulfonate [165,168,210]. Very attractive properties of resulting LIG can be achieved using such formulations, such as sheet resistances as low as 2.8 $\Omega.sq^{-1}$ [165] and conductivities as high as 66.2 $S.cm^{-1}$ [164]. Besides these polymers, other materials have been used to disperse lignin, where cellulose-based materials stand out. This way, lignocellulosic matrices can be mimicked, with the benefit of controlling the relative concentration between aromatic and aliphatic components. One example is the work by Yuan et al. [210], where lignin is dispersed in a hydroxyethyl cellulose slurry. Another similar approach was presented by Edberg et al. [168], where a similar lignin/hydroxyethyl cellulose formulation also including boric acid fire retardant is employed as a high-efficiency LIG precursor, used in conjunction with screen-printing for patterning. Low sheet resistances of 3.8 $\Omega.sq^{-1}$ are reported, translating to a conductivity of 28 $S.cm^{-1}$. Thus, lignin has turned into a valuable resource in several DLW graphitization routes, used either as the sole graphitizable element or to improve the graphitization potential and add functionality to graphitizable substrates [211].

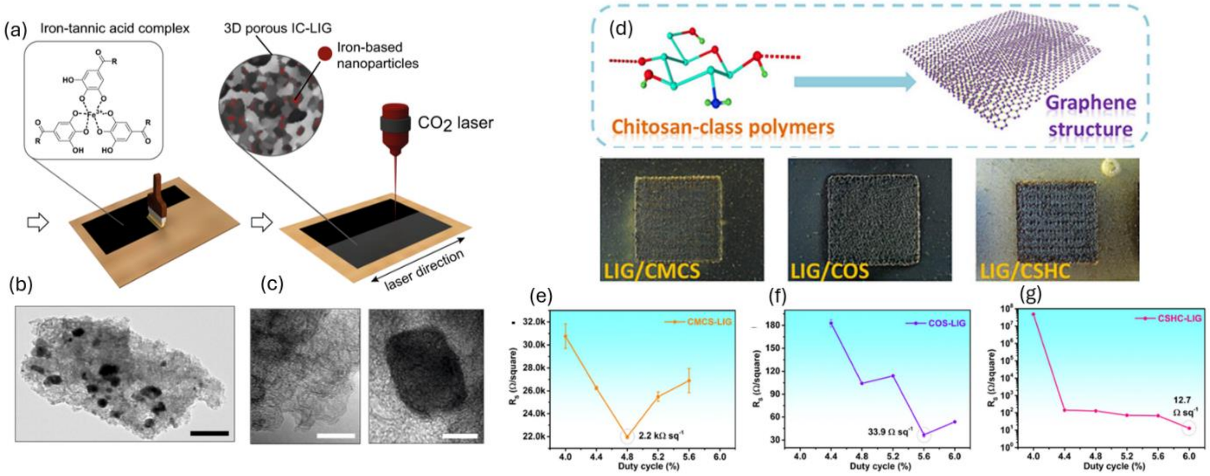

Figure 2.9 - DLW processing of a lignocellulosic and polysaccharide precursors for LIG synthesis and patterning. (g) Modification of wood with iron-tannic acid ink for improved DLW processability and LIG conversion. (h-i) TEM image of LIG and iron carbide NPs, responsible for improving graphitization potential. Adapted with permission [128]. Copyright 2022, Springer Nature. (j) DLW conversion of chitosan-class polymers: (1) carboxymethyl chitosan (CMCS), (ii) chitosan oligosaccharide and (iii) chitosan hydrochloride. (k-m) Process-property optimization of sheet resistance employing duty cycle has the fabrication parameter of study. Adapted with permission [131]. Copyright 2023, American Chemical Society.

2.3.2.2 Aliphatic polysaccharide sources

Aliphatic bio-based precursors for gLIG synthesis are mainly found in two forms, namely cellulose and hemicellulose (**Figure 2.8b**). The first one is formed by a polymeric arrangement of β-1, 4-linked glucose monomers, with relatively equal amounts of carbon and oxygen in its functional groups. These polymeric arrangements are then connected by hydrogen bonds between oxygen functional groups both at intra and intermolecular levels, to form more complex structures such as fibrils and fibers in wood biomass and other materials such as paper.[212] Similarly, hemicelluloses are composed of an arrangement of multiple sugar monomers, including glucose, galactose, mannose, xylose and other sugar residues, in heteropolymer structures with higher complexity when compared to cellulose, being found with different compositions, usually lacking the crystallinity and fibrous nature found in cellulose [213].

Regarding conversion mechanisms, laser irradiation of aliphatic precursors causes the same breaking of C-H, C-O-C and C-C bonds in their structure, through photothermal or photochemical phenomena, with rearrangement of the remaining elements depending on the imposed temperature determined by the laser fluence [190]. When compared to aromatic LIG precursors, aliphatic ones do not possess the necessary, native aromatic ring structures with sp^2 hybridized carbon bonds. Thus, different considerations are required to achieve similar degrees of graphitization reached by aromatic precursors. In complex natural materials, where there is a simultaneous presence of aromatic and aliphatic components, such as in wood, it has been reported that a single step irradiation of the substrate is sufficient for gLIG synthesis, depending on laser source and irradiation atmosphere. This is because there is a synergistic effect of the two types of precursors in the conversion, decreasing the thermal and energy barriers necessary for significant rearrangement and vacancy filling of carbon bonds into sp^2 hybridized structures.[214] The presence of aliphatic components can also be mobilized to form conjugated interconnections among aromatic sheets in the synthesized aromatic clusters, as shown in PHHs irradiation [204].

However, for substrates with high degree of aliphatic composition, such as various types of engineered paper substrates, some impediments are imposed to direct substrate graphitization. These include not only the lack of the native aromatic compounds, but also the resulting inherent thermal resistance, that does not withstand the very high localized temperatures upon laser irradiation processes. As such, authors have resorted to the application of different chemical treatments, that promote the increase of thermal resistance of the precursor material, for example using fire retardant chemicals or promoting oxidation reactions [190,215,216]. Such treatments increase the thermal resistance of substrates, introducing functional groups or external molecules, such as phosphate and boron moieties, that suffer endothermic decomposition and act as chemical heat sinks, that allow for laser induced reactions to occur at the molecular level, without ignition and ablation of the precursor materials [217,218]. If such pre-treatments are not applied, most aliphatic rich substrates suffer combustion processes that cause the formation of volatile compounds and the complete ablation of the substrates.[219] Contrarily, when such pre-treatments are applied, the aliphatic rings in cellulose will undergo photothermal-induced modification caused by the imposed laser photon energies and high temperatures, with different stages that lead to the formation of sp^2 rich carbon structures characteristic of gLIG.

For photodegradation of cellulose and hemicellulose structures, radiation with different wavelengths mainly causes depolymerization of polymeric chains, by scission of C-O-C glycosidic bonds, or photo-oxidative degradation, that can lead to the formation of reactive radicals [220]. Depending on the laser fluence, higher wavelengths near the IR can also cause cross-linking and the formation of new chemical species that possess sp^2 hybridization, such as furfural, that can have interesting properties, such as high fluorescence [220,221]. Also, the tailoring of laser photon wavelength to specific vibration modes in specific bonds can be used for their cleavage [195]. In terms of thermochemical effects arising from pyrolysis of cellulose and hemicellulose through different methodologies, the exposure of these polysaccharides to high temperatures causes depolymerization of sugar monomers and subsequent decarboxylation, aromatization and intramolecular condensation of the resulting aromatic structures [222–224]. Some pyrolysis methods have been used for the synthesis of PAHs from cellulose and hemicellulose, showing the possibility to transform the aliphatic ring structures characteristic of these polysaccharides into aromatic rich chemical structures [225,226]. These aromatization mechanisms are based on the thermal decomposition of cellulose and hemicellulose, to form intermediate species such as furan and furfural, that already contain some degree of sp^2 hybridization [227]. Further thermal decomposition also leads to the synthesis of carbon pools composed of hydrocarbons with C=C bonds, such as ethene, propylene or butene, that can take part in cyclization reactions for aromatization and recyclization for the extension of these aromatic chemical structures, ultimately leading to the synthesis of chars and graphitic structures. As such, laser irradiation processes for conversion of these precursors into LIG is modelled by the same reactions happening in the fast time frames of laser pulse irradiation, namely:

(i) photochemical and/or photothermal promoted dehydration and decarboxylation of aliphatic ring structures, that leads to depolymerization by cleavage of C-O-C glycosidic bonds into D-glucopyranose or other sugar monomers, followed by

(ii) deoxygenation and dehydration, through cleavage of C-O, C-H and C-C bonds and rearrangement of carbon atoms into sp^2 rich chemical structures, by cyclization, serving as template for aromatization and producing H_2O, CO and CO_2. Finally, the high temperatures imposed by the laser irradiation allow for

(iii) aromatization and intramolecular condensation, for rearrangement of aromatic rings into sp^2 dominated graphitic structures (**Figure 2.8d**). It is important to note that such reactions happen extremely fast when compared to other pyrolytic biomass treatment methods, due to the pulsed nature of most laser conversion methods and the very high temperatures that can be reached, being extremely hard to model how each of these steps influence the formation of gLIG structures from aliphatic precursors. In this case, it is important to select laser operational parameters able to achieve high degrees of depolymerization and aromatization, while simultaneously allowing for the necessary intramolecular condensation into aromatic-rich structures and possibly polycondensation of these structures into larger 2D lattices composing 3D LIG structures [228]. And because of the lack of native aromatic rings in these precursors, the additional aromatization step changes the dynamics of the conversion when compared to aromatic precursors. Consequently, many authors have reported that single step irradiation processes of aliphatic rich substrates leads to carbonization, forming chars with significant presence of oxygen moieties, similar to graphene oxide [190,229].

Thus, this conversion process presents underlying dynamic phenomena, that can be manipulated in many ways with the purpose of achieving tailored physical, chemical, and conductive properties. In addition, understanding the dynamics associated with both aromatic and aliphatic gLIG precursors may lead to future improvements on the development of green composite materials, that can assimilate the advantages of both types of precursors, similarly to raw materials such as wood. This would potentiate the efficiency of the discussed graphitization processes, ensuring better sp^2 hybridization yield and maximizing specific properties for different target applications.

Arising from different biomass processing chains, polysaccharides have appeared as interesting LIG precursors, due to intrinsic properties that make them attractive for degradable and biocompatible electronics. The first major polysaccharide used for this purpose was cellulose, mostly within paper substrates. Paper has gained great popularity in the field of electronics in the last decades, due to many meritorious properties. These include inherent properties such as flexibility, porous structure, capillary capabilities for fluid transportation and dielectric aspects in terms of conductivity, but also higher accessibility in terms of production cost, being biodegradable and easily disposable [230–235]. It is also compatible with various fabrication technologies for electronic element fabrication, while also presenting high adaptability, for example by the possibility of folding it or using its capillary properties for chemical modifications or development of microfluidic structures [236]. Furthermore, depending on the utility of the paper substrate, there might be variations in terms of this composition, or even variations in its physical (e.g. grammage, thickness, pore sizes) and chemical properties (e.g. presence of additives) [237,238]. However, as previously stated, laser irradiation of cellulose in wood using CO_2 lasers results in complete degradation and combustion, showing that on its own, cellulose does not present apparent graphitization potential. To circumvent this, the use of several fire retardants has been the main strategy of choice, allowing for an increase in the thermal resistance of cellulose substrates and the formation of chars and graphitized products, depending on the treatment and irradiation scheme. Fire-retardant chemicals have been employed, either commercial or custom-made formulations. These include ammonium sulfamate [169,171], ammonium phosphates [114,135,170,216], boric acid [239], and sodium tetraborate [105,106,130,240]. Depending on the fire retardant, different mechanisms may occur upon their decomposition under laser irradiation, but they commonly promote the transformation of cellulose chemical structures into char, instead of their complete degradation. As such, initial reports stated that to achieve graphitization of paper, the application of more than one laser irradiation cycle was needed, to promote an initial char formation, while subsequent laser scanning promoted the build-up of graphene lattices, characteristic of graphitization [88,169,239]. However, this process can also be replicated by manipulating laser operational conditions, such as the lasing power, pulse resolution and the laser spot size upon irradiation, to increase bond breaking efficiency and create pulse overlapping patterns that mimic multiple laser scanning [176].

As such, even with the use of fire-retardant treatments, the graphitization potential of this polysaccharide is much lower, when compared to aromatic precursors. Different works report higher sheet resistances of resulting LIG, such as the work by Park et al. [169], where the authors reached a minimum value of 61.5 $\Omega.sq^{-1}$, or the work by Kulyk et al. [170], where a minimum value of 32 $\Omega.sq^{-1}$ was reached. Similarly, other forms of cellulose have been employed, resulting in more resistive LIG, including cellulose nanofibers films [75,123] and cellulose nanocrystals [175]. Recently, novel approaches have been employed to improve conductive properties and boost the graphitization potential of cellulose-based precursors, resorting to modification with not only fire-retardants but also aromatic-rich components. One straightforward solution is the reintegration of lignin within paper, to reach compositions close to lignocellulosic materials [173,174]. Besides lignin, alternative sources can be employed for a similar effect. Dreimol et al. [128]

employed the same iron-tannic acid ink used to improve wood processability to modify paper substrates, with good prospects in improving the properties of paper-derived LIG.

Other novel polysaccharide sources have steadily been rising as compatible materials for DLW processing. The first example is hemicellulose, the remaining by-product of wood processing. In the work by Kulyk et.al [176], xylan, a common form of hemicellulose, was successfully graphitized for the formation of conductive LIG. However, like cellulose, the resulting properties show a lower potential for graphitization, with more resistive LIG films with sheet resistances of 182 $\Omega.sq^{-1}$. Maintaining the same principles of polysaccharide chemical treatments for DLW processability, chitosan has also recently appeared as a precursor of interest. Analogous to cellulose, most reports of chitosan-derived LIG show the need for an efficient control of laser irradiation schemes and resulting temperatures, to initiate char formation and subsequent graphitization [131]. As such, initial proposed experimental procedures employ multiple irradiation cycles until the chitosan precursor is efficiently graphitized [178]. Other reports show the capability for one-step induction, where the chemical structure of the chitosan precursor is a key variable to achieve maximized properties of resulting LIG. Huang et al. [131] used three chitosan derivatives, namely carboxymethyl chitosan, a chitosan oligosaccharide, and chitosan hydrochloride, successfully implemented in DLW processing schemes (**Figure 2.9d**). However, the resulting outcomes of each derivative are different, both in terms of the chemical characteristics and resulting conductive capabilities. The authors used the duty cycle as the main process-property optimization metric to assess the effect of laser irradiation over the resistivity of the chitosan-derived LIG films (**Figure 2.9e-g**). While for carboxymethyl chitosan a highly resistive film with a minimum sheet resistance of 2.2 $k\Omega.sq^{-1}$ was reached (**Figure 2.9e**), for the chitosan oligosaccharide film and chitosan hydrochloride, the sheet resistance dropped to 33.9 (**Figure 2.9f**) and 12.7 $\Omega.sq^{-1}$ (**Figure 2.9g**), respectively. This shows the great potential for this polysaccharide for biodegradable and biocompatible electronics, opening routes to explore different formulations and chemical compositions of distinct polysaccharide sources for DLW.

2.4 DLW-enabled bioelectronics applications

Because of its vast capability of synthesizing and engineering functional materials, DLW can be employed in the end-to-end prototyping and fabrication of several applications, including simple electrical interconnect designs and circuits, functional processing components (transistors and memristors), energy harvesting and storage elements and sensing devices. The production of electronic components was firstly based on clean room deposition processes. However, alternatives to these procedures have been widely explored in the past decades to shift into more time- and cost-effective processes. In this scope, DLW has gathered much attention as it offers the possibility of producing and simultaneously patterning different materials on several substrates with relatively good resolution in a short time without resorting to masks. In some application fields, DLW material synthesis and growth is still in an early stage of development and further research and breakthroughs are needed to match conventional microfabrication technologies in terms of applicability.

2.4.1 Electrochemical Sensors

Electrochemical sensors have become ubiquitous devices for the detection and measurement of several chemical and biological parameters. Using electrodes made from conductive and semiconductive materials as transducing elements, they produce electrical signals correlated with an electrochemical reaction or an underlying biological event.

The integration of electrodes within electrochemical cell assemblies can result in different electrode systems, being the two-electrode and three-electrode-based systems the most common for sensing applications [247]. In a two-electrode system, a working and reference electrode are used (**Figure 2.10a**). The reference electrode has the purpose of maintaining a stable potential to establish the operational potential at the working electrode. At the working electrode, the electrochemical reaction of interest occurs. In these two-electrode systems the reference electrode is also used to close the electrodes/analyte circuit, making it a current-carrying electrode, which can change its potential. Thus, two electrode-based systems present some drawbacks and impose limits to experimental conditions, regarding electrolyte solution, amount of current flowing in the cell and electrochemical technique used to drive the generation of electrochemical signals, so that a stable potential is kept at the reference electrode. Three-electrode systems (**Figure 2.10b**) have become mainstream when developing electrochemical sensors and biosensors, where an additional counter electrode is used as the current-carrying electrode, allowing for a stable reference electrode potential. Consequently, a constant potential between the working and counter electrode is achieved and no limitation in the current magnitude of transduced signals is needed [247]. Other systems have also been used for electrochemical transduction and sensing, such as organic field effect transistors [248].

Based on two and three-electrode systems, electrochemical sensors can be divided into different categories. The first distinction can be drawn between (i) electrochemical sensors designed for direct electroanalysis of molecules, through redox mechanism under applied

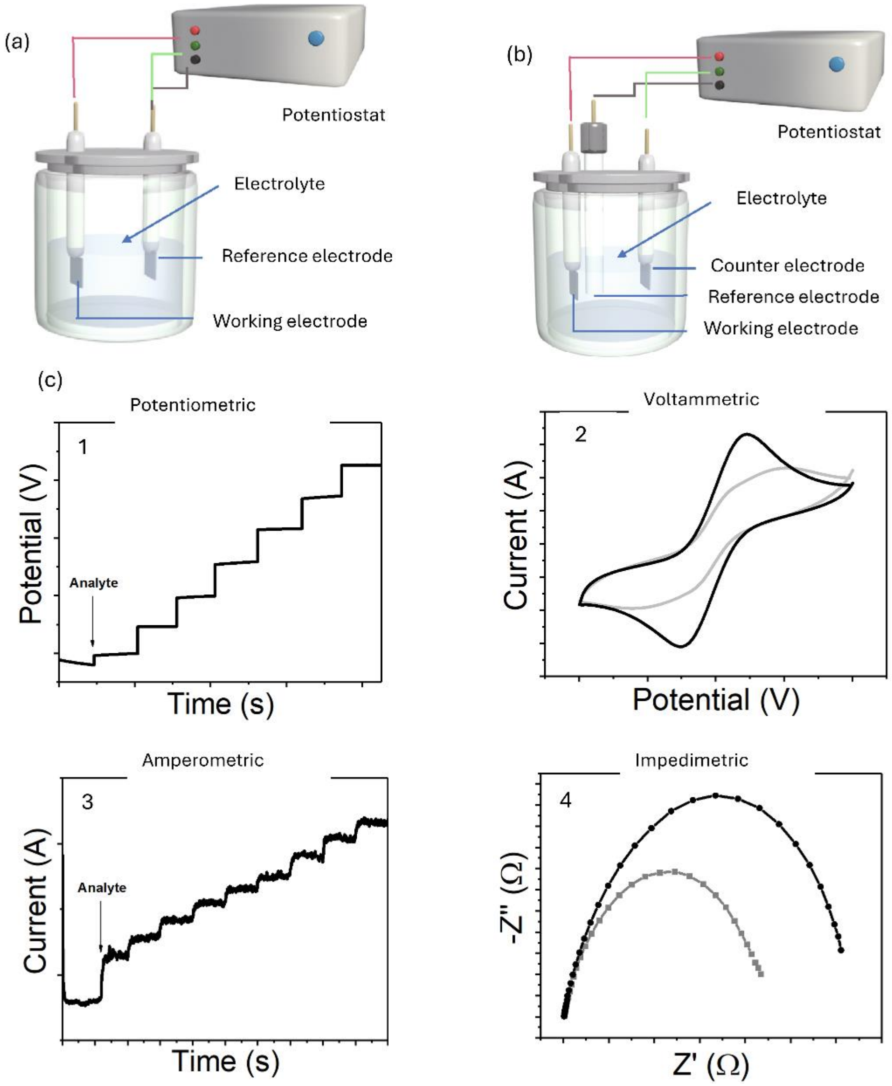

Figure 2.10 - Electrode setups and typical response curves of electrochemical sensors. Assembly of electrochemical cells based on two electrode (a) and three-electrode systems. Reproduced with permission [309]. Copyright 2020, Springer Nature. Representative electrical response curves of (a) potentiometric, (b) voltammetric, (c) amperometric and (d) impedimetric biosensors.

potentials, resulting in significant faradaic currents [249], and (ii) sensors employing recognition elements with affinity towards a target analyte, participating in its redox catalysis, generation of useful products or binding to electrode surface [250]. This second type of electrochemical sensor has been the basis for the research and development of electrochemical biosensors for detection of analytes in several fields, from environmental and food screening to medical diagnosis and prognosis [250]. In terms of operation principles, electrochemical biosensors have different categories, with the following being the most preponderant (**Figure 2.10c**):

(i) **Potentiometric biosensors** - detection of analytes by measuring changes in the potential of the electrochemical system (**Figure 2.10c-1**). Most notably, pH and electrolyte detection has been performed using potentiometric biosensors, using recognition elements such as ion-selective membranes [251].

(ii) **Voltammetric and amperometric biosensors** - detection of analytes by measuring changes in current generated in the electrochemical system. For voltammetric biosensors, currents are measured with varied applied potentials (**Figure 2.10c-2**), while amperometric biosensors detect current changes at a fixed potential (**Figure 2.10c-3**). Usually, three-electrode systems are most common when developing these biosensors, where the counter electrode is used as a current source and the recognition elements are integrated in the surface of the working electrode. The most popular sensors based on these operating principles are enzymatic sensors for the detection of different metabolites, using target-specific enzymes within different biodetection schemes [252].

(iii) **Impedimetric biosensors** - detection of analytes by measuring changes in the impedance of the electrochemical system upon a binding event (**Figure 2.10c-4**). Using electrochemical impedance spectroscopy (EIS), alternate current (AC) signals with varying frequencies are applied to the electrode system, to monitor changes in electrochemical mechanisms (e.g. adsorption, charge transfer or mass transfer) at the working electrode, depending on the presence of the analyte [253]. The most common impedimetric biosensors are formulated by modifying the working electrode with antibodies as recognition elements, to develop immunosensors to quantify protein analytes [254]. Other recognition elements, such as aptamers and molecularly imprinted polymers, are also used to detect other molecules, such as metabolites and nucleic acid strands [253,255].

Due to the great versatility of electrochemical biosensors and their operating principles, they have found applicability in different contexts, from single-use, easily disposable platforms [256], to long-term use in wearable and even implantable applications [257,258]. For that, device integration strategies regarding material use and fabrication standpoints have developed towards substituting bulk electrodes, as the ones shown in **Figure 2.10a-b,** to miniaturized, planar electrodes fabricated by subtractive and additive technologies, compatible with small sample volume analysis. Conventionally, a set of materials are used in the fabrication of bulk electrodes for electrochemical experiments. For reference electrodes, the standard hydrogen electrode (SHE) establishes the thermodynamic redox potential scale, with other alternatives, such as the saturated calomel electrode (SCE) and the silver/silver chloride (Ag/AgCl) being more commonly used. For the counter electrode, inert materials are ideal, to drive charge flow without consuming redox species in the electrolyte. Common materials used as counter electrodes are platinum wires and graphite rods. Similarly, inert materials are also preferred for the working electrode, including noble metals such as gold, and carbon electrodes, being the glassy carbon electrode the most common. To shift from bulk electrodes to other geometries and form-factors, that increase the versatility, flexibility and reach of electrochemical biosensors, microfabrication and printing technologies have become the gold-standard [259]. When biosensor integration in comprehensive, fully functional systems is envisioned, different requirements are needed, including flexible and sustainable substrates and electrode materials for disposable applications, or seamless integration, flexibility, softness, stretchability and biocompatibility when interfacing with biological soft tissue is needed. Because of these requirements, conventional techniques, such as metal electroplating or evaporation associated with lithographic techniques [260] has been progressively shifting to more accessible fabrication routes, alternative electrode materials and greener substrates. DLW has been a great asset in the fabrication and prototyping of electrodes for electrochemical sensing tasks, mainly due to the possibility for form factor-free design and organization of electrodes in the same substrate or chip platform. This ultimately decreases the steps needed from design to fabrication and implementation of an electrochemical biosensor. In this scope, LIG has been fruitfully explored as an electrode material, presenting itself as fairly inert, while showing good charge transfer capabilities for redox, faradaic analytical detection processes [143]. Since the first reports, LIG derived from several precursor sources has been explored for three-electrode systems, integrated on-chip electrochemical sensor fabrication. PI has been the main aromatic polymer of choice [261], but substrate choice has been extended to substrates such as lignin [69,165], paper [105,171,172], cork [163], or chitosan [178,179].

The first report of LIG-based, portable on-chip electrochemical cells for sensing purposes was reported by Nayak et al. [143], using the original PI sheet precursor (**Figure 2.11a**). Three-electrode cells were fabricated and characterized by cyclic voltammetry (CV) in terms of their charge transfer characteristics using both inner-sphere (ferrocyanide - $[Fe(CN)_6]^{-4}$) and outer-sphere (hexaammineruthenium - $[Ru(NH_3)_6]^{-3}$) redox probes, which present different diffusion properties and interaction with electrode surface (**Figure 2.11b-c**). Pristine LIG electrodes were compared to other graphitic materials, showing more attractive characteristics, including larger redox currents associated with faster electron transfer, along with improvements in the electrochemically active surface area for both redox probes. These on-chip electrochemical cells were used to develop simple sensors for direct electroanalysis of metabolites, including ascorbic acid, uric acid and dopamine, that can be directly oxidized at the LIG electrode surface and generate electrochemical signals. Differential pulse voltammetry was the electrochemical techniques used for the measurements of the three metabolites, achieving good sensitivity and selectivity. Simultaneous measurement of the analytes was achievable, since the metabolites present distinct oxidation potentials (**Figure 2.11d**). Furthermore, the authors also demonstrated the flexibility of the sensors, that maintained their stability when bent (**Figure 2.11e**). Another relevant work was reported by Lei et al. [165], using an alternative lignin-based precursor for the patterning of LIG-based electrodes for enzymatic sensing. Electrochemical cells with

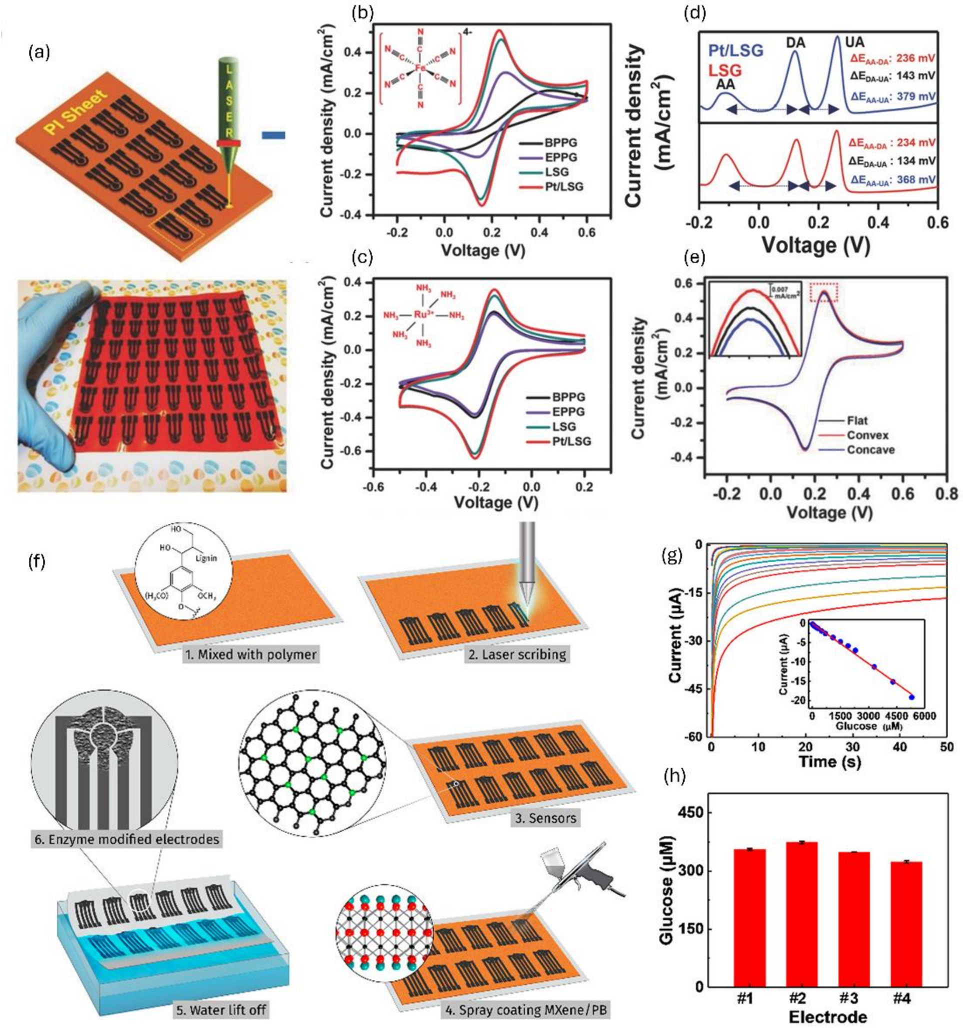

Figure 2.11 - LIG-based electrochemical sensors and biosensors. (a) LIG on-chip electrochemical sensors fabricated on polyimide sheet precursor. Cyclic voltammograms of LIG electrochemical cells using inner-sphere (a) and (b) outer-sphere redox probes. (d) Differential pulse voltammetry oxidation peaks of ascorbic acid, dopamine and uric acid. (e) Cyclic voltammograms of LIG electrochemical cells at flat and bent conformation. Reproduced with permission [143]. Copyright 2016, Wiley-VCH. (f) Schematic of lignin-derived LIG electrochemical sensors and their functionalization. (g) Chronoamperometric characterization of enzymatic glucose quantification and corresponding calibration curve. (h) Reproducibility assessment of enzymatic glucose biosensors. Reproduced with permission [165]. Copyright 2019 American Chemical Society.

five electrodes (including three working electrodes for each analyte) were patterned in the precursor film, composed of a lignin/PVA/urea mixture (**Figure 2.11f**). Subsequently, the authors further modified the working electrodes with a MXene/Prussian Blue mixture, to introduce an electrochemical mediator, followed by functionalization with target specific enzymes (glucose oxidase, alcohol oxidase and lactate oxidase). The electrochemical method used to characterize the biosensors was chronoamperometry, in an artificial sweat matrix, resulting in highly sensitive sensors detecting metabolite concentration in physiologically relevant ranges in sweat. For glucose, the biosensors presented a wide operating concentration range between 10 μM - 5.3 mM, with a sensitivity of 49.2 $\mu A.mM^{-1}.cm^{-2}$ and a detection limit of 0.3 μM (**Figure 2.11g**). The reproducibility of the assembled sensors was also tested, by selecting four sensors and testing them under the same analyte concentration condition, achieving low relative standard deviation for each individual sensor and electrode-to-electrode reproducibility (**Figure 2.11h**).

Ultimately, precursor choice, allied with the irradiation scheme and electrode designs, dictate material and device performance, regarding the resulting charge transfer capabilities and analytical performance, within specific biodetection schemes [94]. However, each specific substrate and its inherent properties may endow the resulting electrochemical biosensors with certain capabilities, related to mechanical flexibility, biocompatibility, and biodegradability.

2.4.2 Wearable biochemical sensing

The need for multifunctionality is a key factor in many bioelectronic applications, mostly the ones designed for deployment in *in vivo* scenarios. Devices such as electronic skins (e-skins), wearables for human-machine interfacing, smart wound patches, or implantable electronics, require careful material selection, accommodating form factors, and several integrated functionalities, from sensing capabilities to energy management and connectivity [263]. In terms of sensing capabilities, most advanced and commercialized wearable devices for consumer electronics have focused on the measurement of physical parameters, such as body temperature, movement and heart rate and have found acceptance by consumers as daily tools for personal tracking [264]. However, in many scenarios, such as in sports or healthcare monitoring, biochemical information is key for informed decision by a user or a healthcare provider. Thus, prolific research on the development of miniaturized, user-friendly devices is ongoing, where different strategies have been put forward, including wearable textile-based devices [265] or conformable patch and tattoo-based sensing systems [266].

Such devices have promoted a shift from using invasive blood collection and analysis or minimally invasive methods for interstitial fluid analysis, to non-invasive collection of readily available biofluids with a plethora of biochemical information (e.g. tears [267], saliva [268]) . Among these fluids, sweat has been one of the most used biofluids for noninvasive biomarker sensing, due to a set of advantages [269,270]. Firstly, sweat can be sampled over a large body area, since eccrine sweat glands are present throughout the body, allowing for continuous access to the biofluid during sweat secretion periods. Because of this, comfortable and easily placeable device architectures can be designed, aiming at sampling and analysis of low fluid volumes directly on the skin, avoiding external contamination, and immediate sensing before analyte degradation and evaporation [269]. Secondly, sweat contains a large pool of analytes of physiological relevance for healthcare purposes, from electrolytes (Na+, Cl^-, K^+), metabolites (lactate, urea, glucose), amino acids, micronutrients and hormones [271]. With the increase in interest on sweat analysis, more studies using conventional analytical techniques, as well as novel wearable devices in a research setting, are improving the level of confidence for the correlation of these analytes to their levels in blood, increasing the interest in the development and use of sweat analysis devices for personalized healthcare [270]. Thirdly, sweat can be stimulated by two methods, either actively by performing physical activity, or passively through different methods, in which iontophoresis is included. Depending on the target user, use case and sensing task to be performed, both methods have shown to be efficient in generating sweat volumes appropriate for biosensing.

2.4.2.1 Sweat sensors enabled by physical activity sweat secretion

One of the first reports of a skin-interfaced wearable device for in-situ analysis of sweat biomarkers was presented by Gao et al. [272]. This device comprised a set of electrodes for electrochemical sensing of sweat metabolites (glucose and lactate) and electrolytes (Na^+, K^+), alongside a temperature sensor, fabricated by photolithography and electron-beam metal evaporation on a PET substrate (**Figure 2.12a**). The flexible electrode array included two working electrodes modified with ion selective membranes for Na^+ and K^+ selectivity, which could also be modified with a Prussian Blue mediator layer and enzymes immobilized in a chitosan

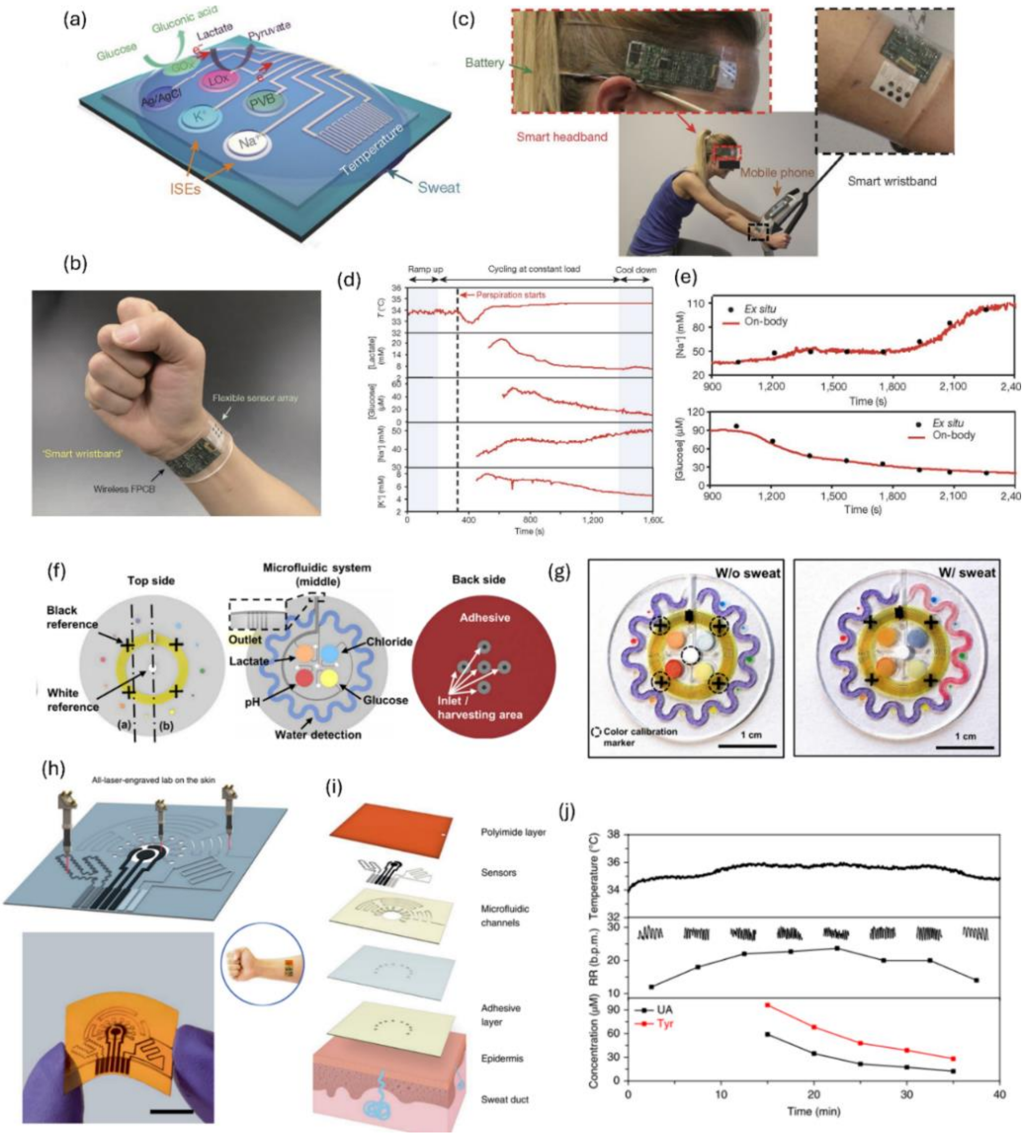

Figure 2.12 - State-of-the-art miniaturized, flexible patch-like devices for on-body sweat biochemical sensing. (a) Schematic of electrode array for metabolite (glucose and lactate) and electrolyte (Na+ and K+) sensing and (b) its implementation as a wrist worn device. (c) Real-life testing of devices as wrist and headband for exercise induced sweat sensing. (d) Continuous monitoring of physical and biochemical parameters for the exercise period. (e) External validation curves of Na+ and glucose sensors on-body sensors. Reproduced with permission [272]. Copyright 2016 Springer Nature. (f) Schematic of layer components of epifluidic devices for on-body sweat sampling, transportation and colorimetric biochemical analysis. (g) Operation of epifluidic device after sweat accumulation, inducing color changes in reaction chamber associated with analyte concentrations and within a microfluidic channel designed to assess sweat rate. Reproduced with permission [274]. Copyright 2016 American Association for the Advancement of Science. (h) Schematic of fully laser processed system for biophysical and biochemical on-body sensing integrate with epifluidics. (i) Representation of device layer components, including adhesive layer, hydrophilic membrane for epifluidic module assembly and PI-derived LIG components for sensing. (j) Long-term on body measurements of biophysical (temparature and respiration rate) and biochemical (uric acid and tyrosine) parameters. Reproduced with permission [275]. Copyright 2019 Springer Nature.

matrix, to establish the biosensing schemes for glucose and lactate detection. The sensing array was interfaced with a flexible printed circuit board with the required instrumentation for electrochemical signal analysis and transmission (**Figure 2.12b**). The complete sensing system was tested as smart head and wristbands (**Figure 2.12c**), to continuously analyze sweat during physical exercising periods (**Figure 2.12d**), using mechanically flexible components, improving user friendliness and deployment of wearable biochemical analysis tools. Furthermore, validation of measured analyte concentration with external measurements of collected sweat was also performed by the authors, to showcase the validity and accuracy of the system (**Figure 2.12e**).

However, efficient sweat sampling is usually required to achieve precise measurements in long-term operation, to minimize the influence of sweat mixing over time, which can affect measured analyte concentrations. To avoid possible contaminations or interferences, skin-interfaced microfluidic setups, or epifluidics, have been developed to sample and transport sweat for in-situ analysis, while allowing for further functionalities to be included in such wearables, including sweating rate estimation [273]. Initially, epifluidic devices were applied for colorimetric sensing and analysis of sweat, such as in the work by Koh et al. [274], where soft lithography was used to fabricate polydimethylsiloxane (PDMS) microfluidic devices capable of handling microliter volumes of sweat. The microfluidics included inlets, sweat transporting channels, containment reservoirs where colorimetric reactions occurred and outlets, to avoid back pressure impeding sweat flow (**Figure 2.12f**). Furthermore, an NFC communication system was also embedded in the microfluid device, for automatized color recording and analysis using a smartphone app system. The microfluidic device was capable of quantifying sweat glucose, lactate chloride, pH and sweat volume, by analyzing the filling of a dedicated microfluidic channel over time (**Figure 2.12g**).

Recently, the fabrication of such devices has greatly benefited from DLW, due to the capability to straightforwardly fabricate functional components with seamless interconnectivity. Using the vast capabilities of lasers, different sensing elements can be fabricated in the same substrates, aiming at multimodal detection of different physiological information, while also being capable of participating in the fabrication of other passive components, such as microfluidic networks. Yang and co-authors developed a wearable device that includes three functional components. An electrochemical sensing unit was integrated for biochemical monitoring of uric acid and tyrosine, while the remaining components were designed to detect biophysical signals, namely temperature and respiration rate [275]. The LIG-based electrochemical, temperature, and strain sensors were all patterned in the same PI substrate, being interfaced with a laser-engraved microfluidic network, designed to sample and transport sweat for on-body biochemical sensing (**Figure 2.12h**). This work introduced a straightforward approach using the same laser tool to fabricate all the required components for the integration of bio-physical and biochemical sensing units, alongside an epifluidics module for efficient sweat sampling. To produce these epifluidic components, the authors used different membranes, such as double-sided adhesives and hydrophilic films, cutting in each layer the different element of the module (**Figure 2.12i**). In the bottom layer, a set of inlets were cut on a double-sided adhesive, which was attached to a PET membrane with the same patterned inlets. This PET layer worked as the hydrophilic membrane allowing for passive sweat movement without external pumping, being attached to another double-sided adhesive layer engraved with a microfluidic network design, to transport sweat through the working area of the electrochemical sensing module and onto an outlet. Finally, this layer arrangement was attached to the PI substrate scribed with the required electrode for uric acid, tyrosine, respiration rate and body temperature sensing (**Figure 2.12j**). Furthermore, the wearable sensing chip was connected to a flexible PCB, designed to analyze and transmit the retrieved physiological information. This was a breakthrough work, that showed the applicability of LIG-based, integrated bioelectronics for sweat metabolite detection, with full functionality for autonomous operation directly in the body.

2.4.2.2 Iontophoresis-based sweat sensors

Besides active sweat stimulation through physical activity, alternative sweat induction mechanisms have been explored, so that sweat collection becomes possible in individuals unable to perform physical exercise. One such method is pharmacologically induced sweat secretion, performed by iontophoretic methods [276]. Iontophoresis is a technique in which small electric currents are applied in a localized area of the body, using a cathode and anode interfaced with the skin, connected to a current source. The generated electric field promotes electromigration and electro-osmosis of charged and neutral particles in the vicinity of the stimulated area, allowing for use in controlled and programmed transdermal drug delivery [277]. Using cholinergic agonists capable of interacting and stimulating sweat glands and delivering them to the skin by iontophoresis, controlled sweat stimulation is achieved, followed by sweat collection and analysis. These drugs mimic the action of the neurotransmitter acetylcholine and its interaction with eccrine sweat glands, binding to muscarinic, nicotinic receptors or both [278]. Different drugs have been used in iontophoretic sweat gland stimulation and sweat secretion, including acetylcholine, methacholine, pilocarpine and carbachol, each presenting different interaction mechanisms, metabolism and resulting sweat gland stimulation over time, influencing gland response time, sweat rate and sweat secretion duration [278,279].

The first widespread use case of iontophoresis-based sweat stimulation for biochemical analysis was for cystic fibrosis diagnosis in infants [280], where pilocarpine iontophoresis is performed, followed by sweat collection using the commercialized Macroduct ® sweat collection system, used until today in clinical practice. Another example is the GlucoWatch ®, a wrist worn device commercialized to monitor blood glucose levels using reverse iontophoresis [281]. Differently from iontophoresis devices for drug delivery, reverse iontophoresis aims to directly convect molecules from the skin through the applied electric field and onto the skin surface, where mounted sensors can quantify the analyte [282]. Although previously commercialized, the high current magnitudes and application time needed for glucose reverse iontophoresis caused irritation and discomfort in users, ultimately leading to its discontinuation [281]. Inspired by these products, novel iontophoresis-based system designs and implementation have been researched, aiming at bringing iontophoresis-based sweat stimulation and its potential for sweat biosensing purposes towards personalized healthcare monitoring scenarios. This trend is based on developing highly conformable, comfortable skin-interfaced devices with careful material selection and form-factors, for long-term monitoring of several analytes of interest. In the work by Emaminejad et al. [279], Au/Cr electrodes for iontophoresis and electrochemical sensing were patterned onto a PET substrate, by photolithography and thermal evaporation, to develop a wearable electrode array comprising all the components for in-situ sweat stimulation and biochemical analysis (**Figure 2.13a-b**). The authors tested different cholinergic agonist molecules within agarose hydrogels, as well as different stimulation current profiles, to determine the most suitable setup for efficient sweat stimulation. Generally, current is employed, flowing from the anode compartment, containing the cholinergic agonist, towards the cathode compartment, containing a hydrogel without the agonist (**Figure 2.13c**). The ionic promoted movement of the cholinergic agonist into the skin promotes the secretion of sweat, which is captured within the area where the electrochemical sensors are placed. Acetylcholine, the naturally occurring sweat stimulant neurotransmitter, provides efficient sweat generation. However, according to the authors, methacholine and pilocarpine stimulation provided longer secretion periods beyond 60 minutes, with methacholine providing a faster secretion onset and rates above the recommended for cystic fibrosis analysis (>100 $nL.min.cm^{-2}$).

As for the stimulation current, the authors used a 1 mA current for 10 minutes delivery time, resulting in characteristic sweat rate profiles displaying a peak rate, followed by a steady decay over time (**Figure 2.13d**). The electrochemical sensing module was designed to quantify Na^+

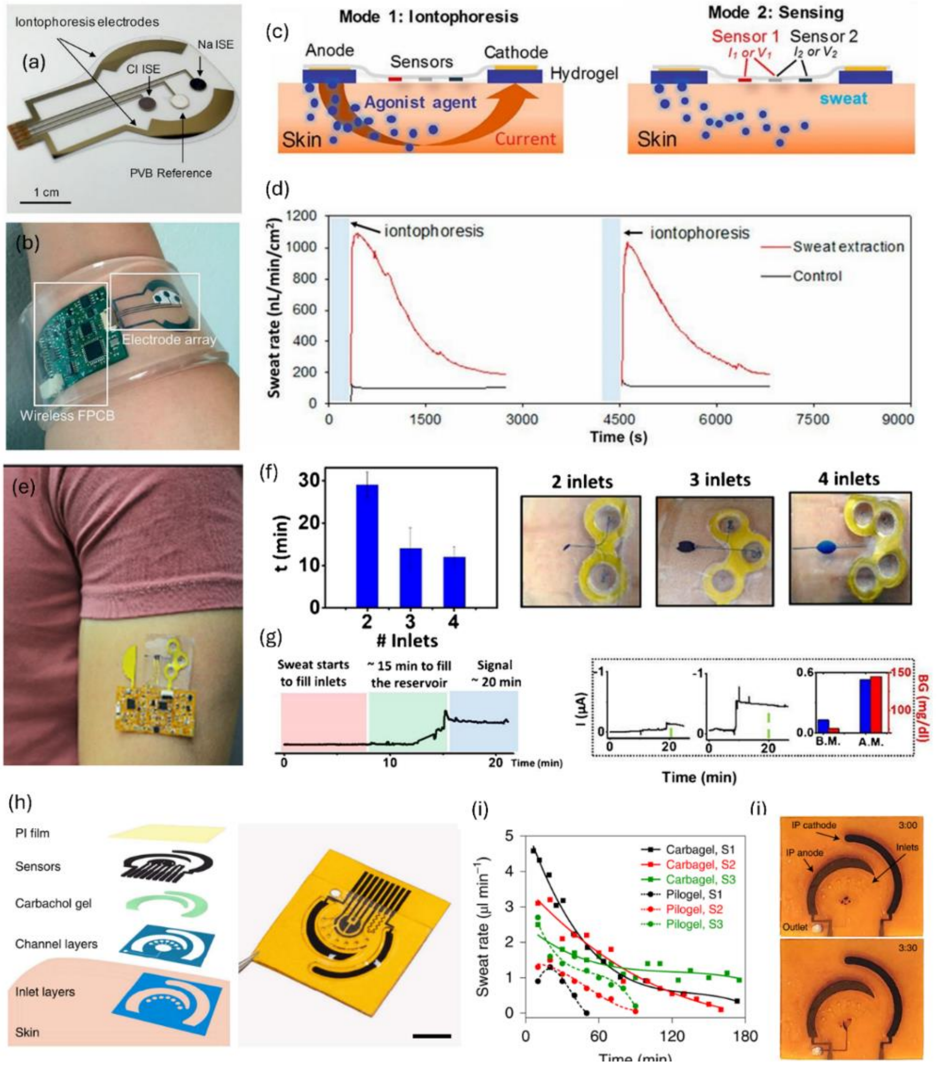

Figure 2.13 - Iontophoresis-based systems for on-body sensing of sweat analytes. (a) Schematic of electrode arrays on PET substrates that include and anode and cathode for iontophoretic delivery and an electrochemical sensing array for cystic fibrosis diagnosis. (b) Implementation of the device as a wrist-worn band for on-body sensing. (c) Schematic of iontophoresis and sensing operation of the device, starting with iontophoretic delivery of cholinergic agonist, followed by sweat secretion and capture at electrochemical sensing module. (d) Sweat rate profile of acetylcholine delivery using 10% (w/v) hydrogel vs. a control without the cholinergic agonist. Reproduced with permission [279]. Copyright 2017 National Academy of Sciences. (e) Iontophoresis-based device integrated with a PDMS-based epifluidic module for sweat sampling and transportation. (f) Study of epifluidic module features, namely inlet number and its influence on sweat filling time. (g) Profile of device operation from start of iontophoretic sweat induction, filling of microfluidic channels and interaction with electrochemical sensor for glucose monitoring, tracked before and after meals ingestion in several subjects. Reproduced with permission [283]. Copyright 2022 Springer Nature. (h) Laser processed, integrated iontophoresis, electrochemical sensing and microfluidic device. (i) Sweat-rate profile comparison of carbachol and pilocarpine delivery. (j) Images of device after stimulation, portraying the filling of the microfluidic channels over time. Reproduced with permission [285]. Copyright 2022 Springer Nature.

and Cl$^-$, aiming at cystic fibrosis diagnostics, as well as sweat glucose levels, by capturing the secreted sweat in an absorbent membrane placed between the skin and sensor surfaces. Since these initial developments of miniaturized iontophoresis devices paired with electrochemical sensing modules, different advancements have been made to further potentiate this technology. The integration of iontophoresis-based sweat stimulation with epifluidics has been a key feature, to improve the sampling of sweat and allow for continuous electroanalysis. An example is the work by Bolat et al. [283], where a PDMS microfluidic device was interfaced with the iontophoresis and sensing units, allowing for freshly generated sweat to be naturally pumped into the microfluidic channels, creating sweat flow within the device (**Figure 2.13e**). Employing pilocarpine-based iontophoresis, the authors studied the effect of the microfluidic inlet number and stimulation time to optimize the network filling time (**Figure 2.13f**). Using a 0.4 mA.cm^{-2} current density for stimulation, an optimized 13-minute filling time for three-inlet microfluidic network was observed. Sweat glucose analysis was performed within the system, capable of distinguishing glucose circulating levels before and after meals, characterized by a marked increase in the current measured in the electrochemical sensor (**Figure 2.13g**).

Although state-of-the-art pilocarpine-based iontophoresis being capable of generating relevant sweat volumes for analysis within electrochemical sensors in the tens of microliters, this cholinergic agent suffers from some disadvantages, having a shorter action period and not having full nicotinic and muscarinic receptor activity, producing shorter stimulation periods [278]. As such alternative agonists have been recently explored, where carbachol stands out, for being a longer lasting, non-selective molecule that has shown to provide longer sweat secretion periods lasting for several hours, attractive for continuous sweat monitoring [278]. In the work by Hauke et al. [284], a device integrating carbachol-based iontophoresis demonstrated the capability of generating sweat up to two hours, and was developed to monitor alcohol levels. More recently, Wang et al [285] introduced the capability of developing LIG-based electrodes for iontophoresis systems, showing the compatibility of this material within these systems, paired with carbachol delivery. Similarly to previous work from the authors' group, full laser fabrication principles were employed, by DLW patterning of LIG electrodes for sweat stimulation, electrochemical sensor electrode array and laser cut microfluidic components (**Figure 2.13h**). Regarding the iontophoretic capabilities of LIG electrodes paired with carbachol delivery, the authors compared this arrangement with pilocarpine delivery. An increased sweating period after carbachol stimulation, along with increased sweat rates were verified (**Figure 2.13i**). In addition, sweat was not limited only to the adjacent area of contact between cholinergic hydrogel and skin, but also surrounding areas, increasing the reach of sweat stimulation. In addition, these more favorable results associated with carbachol delivery are achieved with a greatly reduced stimulation current of 50-100 μA, when compared to convention values for pilocarpine delivery, situated around 1-1.5 mA, resulting in sweat secretion rates upwards of 4 $\mu L.min^{-1}$. Coupled with the iontophoresis systems, the microfluidic network was able to direct small volumes of sweat (2.36 μL volume capacity of the microfluidic module) towards sensors (**Figure 2.13j**) for the quantification of different metabolites and nutrients, including essential amino acids and vitamins, employing molecularly imprinted polymers as synthetic recognition elements. Furthermore, the authors further included in-situ sensor calibration, to minimize sweat variability effects between subjects, through temperature and electrolyte calibrations. Since then, other LIG-based wearable devices for iontophoresis-based sweat biomarker analysis have been fabricated, such as for c-reactive protein [286] detection.

2.4.3 Electrophysiological Sensing

Measurement of biopotential signals in biological systems and their stimulation are key when pursuing several functions for bioelectronic systems, such as human-machine interfaces, robotics, wearables, and implantable devices. [74,289] As such, flexible electrodes with good mechanical and electrical properties that can transport electrical stimulus are desired for applications such as the monitoring of electrophysiological signals or tissue stimulation [74]. Electrodes fabricated by DLW based on LIG and conductive polymers have been explored for this purpose, due to their good conductivity, low contact impedance, and overall biocompatibility [56,289]. Won et al. employed laser-induced phase separation processes, to improve conductivity and water-stability of PEDOT:PSS-based hydrogels and pattern neural recording and stimulation electrodes. Three electrode arrays were used to record neuronal signals on the hippocampus within a brane slice of mice, able to detect excited states of the local field potential signals of brain tissue after the delivery of an excitatory drug (bicuculline, 20 μM) (**Figure 2.14a-b**). Using low voltage, the same electrode array was used to stimulate the sciatic nerve, inducing significant leg motion [289]. Apart from neural stimulation, SiC electrodes produced by laser writing of PDMS were used to stimulate an ex-vivo isolated heart that exhibited a slow atrioventricular node rhythm without stimulation, which synchronized with the stimulation frequency during the experiments. Additionally, a sheet of smooth muscle cells was stimulated using this SiC-based platform. After synchronization, enhanced contractility was detected, suggesting a possible therapeutic application of the developed composites in sphincter contraction or vasoconstriction [290]. Several LIG-based electrodes have also been used to record electrophysiological signals, using a myriad of substrates, from liquid crystal polymers [56], Whatman Grade 1 paper

[130], and Kevlar textiles [188]. Notably, kirigami-inspired LIG electrodes were constructed from a liquid crystal aromatic polymer precursor, improving the operation of such electrodes under stretchable on-body applications (**Figure 2.14c**). The fabricated electrodes were used to monitor the EMG and ECG signals to distinguish physical activity intensities (**Figure 2.14d**) [56]. The same precursor was used to fabricate LIG three electrode arrays for in-vivo recording of cortical potentials from the whisker somatosensory barrel cortex in mice, as well as allowing for motor cortex stimulation to induce hind limb movement [56]. Additionally, copper electrodes on PDMS substrates produced by laser-induced selective metallization were used to record EMG signals to detect different finger gestures. The EMG signals were used to train a classifier, which then acted on a robot hand and allowed precise control over this tool. The results demonstrated the possibility of integrating the copper electrodes in human–machine interface applications [74]. Thus, recent developments of DLW have accessed time and cost-effective production of high-performance bioelectronic platforms for both wearable and in vivo, implantable bioelectronic applications, by engineering of low-impedance material writing on biocompatible, flexible substrate materials.

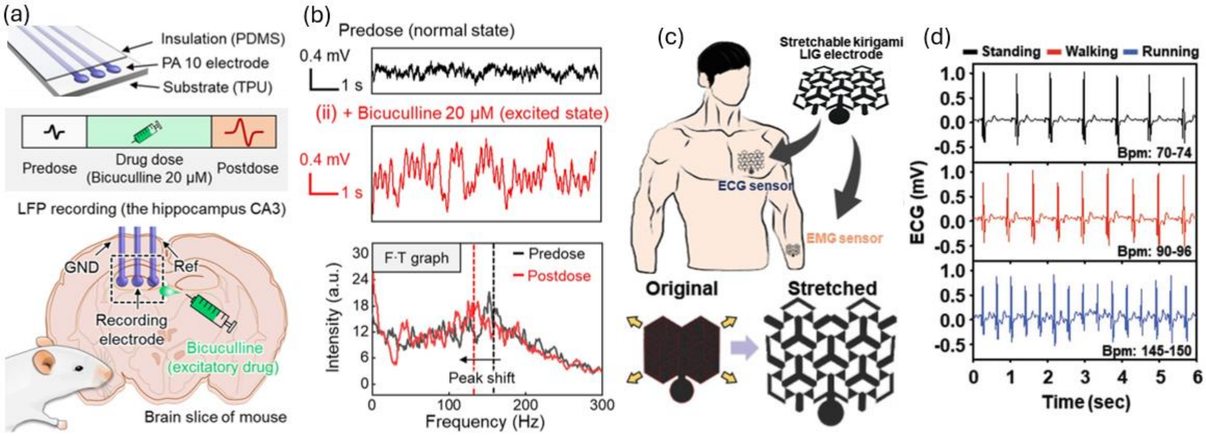

Figure 2.14 –DLW fabrication of bioelectrode for electrophysiological signal acquisition. (a) Neural recording device based on laser selective phase transformation of PEDOT:PSS and schematic in-situ recording and neural stimulation of mice brain slice hippocampus. (b) Local field potential signals of brain tissue and corresponding Fourier transform before and after stimulation with bicuculline. Reproduced with permission [289]. Copyright 2022, American Association for the Advancement of Science. (c) Kirigami-inspired LIG electrodes produced from liquid crystal polymer and its stretching characteristics for biopotential measurements. (d) ECG signals monitored for different activity states. Adapted with permission [56]. Copyright 2023, Wiley-VHC.

2.4.4 Laser-induced graphene transfer strategies for conformable bioelectronics

As presented in previous sections, LIG has been employed in the production of several forms of wearable devices for *in vivo* applications. This portrays its vast multifunctionality, along with good mechanical robustness under real application scenarios, associated with its binding with precursor polymer membranes. However, for specific applications, placement of devices in body part with high stretching motions creates motion induce stress that requires highly conformable, flexible and even stretchable materials that withstand these stresses and accompany body movements, without producing significant noise or measurement artifacts. Furthermore, the characteristic topography of different body parts requires highly conformable substrates that can robustly adhere to varying surface shapes. Common precursor polymers, such as PI or even paper, do not portray these specific capabilities, mostly lacking stretchability. To further improve the functionality of LIG for application in stretchable and highly conformable bioelectronic devices, several material transfer strategies have been proposed, to efficiently separate LIG from precursor substrates into several flexible and elastic materials, that present the ideal mechanical properties for conformable bioelectronics and reach skin-like sensing systems [291]. Several elastomeric materials have been used for LIG transferring, including PDMS [292–294], Ecoflex ® [295,296], Dragon Skin ™ [297], styrene-ethylene-buthylene-styrene (SEBS) [298] , polyurethane (PU) [299,300] and custom-made hydrogel formulation [301,302].

The main strategy for transferring based on elastomeric materials, as reported in several works [292–295,297,298,301,302], is by engraving the desired LIG patterns on the precursor, most commonly PI, followed by casting of liquid forms of the elastomeric materials, so that they penetrate the porous structure of LIG (**Figure 2.15a-b**). Subsequently, the elastomers are cured and solidify, anchoring the LIG patterns over their volume. When peel-off is performed, LIG stays within the elastomer material and is separated from the precursor surface. A simpler strategy is based on adhesive-based peel-off methods, where an adhesive material is joined to the surface of LIG patterns and the precursor substrate, followed by peeling-off the elastomeric membrane. If the binding strength of the adhesive to the LIG patterns is higher than the one between LIG and the precursor substrate, efficient separation of the patterns is achieved (**Figure 2.15c-d**). This method has been mostly applied for adhesive membranes, such as medical grade PU [299,300]. Based on these transfer strategies, several LIG-based bioelectronic applications have been explored, including biophysical signal detection (e.g. temperature, strain) [293,298,301], tactile sensors [300,303], electrophysiological signal monitoring [297,298,300–302], electrochemical potentiometric sensors [296], demonstrating the robustness of these methods in maintaining the conductive properties of LIG after transfer. However, these transfer strategies have mostly been restricted to PI-derived LIG. Thus, exploration of these transfer strategies and their compatibility with other LIG precursors or the development of novel LIG transfer mechanisms compatible with alternative precursors would be important to expand the toolbox of materials to be used for conformable bioelectronics system development.

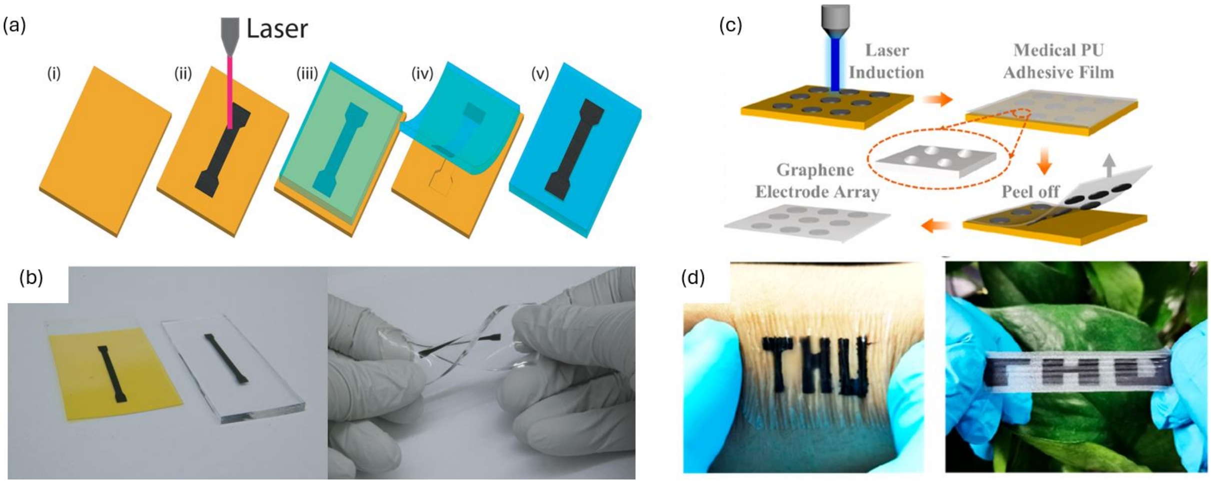

Figure 2.15 – LIG transfer strategies toward conformable applications. (a) Schematic of elastomer casting and curing for LIG transfer, using PDMS. (b) Pattern before and after transfer and bendable properties of the elastomer-LIG composite. Adapted with permission [293]. Copyright 2015, American Chemical Society. (c) Schematic of adhesive membrane peel-off transfer, using PU adhesive tape. (d) Resulting transfer patterns placed on the skin and their stretchable properties. Adapted from [300]. Copyright 2022 American Chemical Society.

2.5 Summary and outlook

As presented in this chapter, DLW has found widespread applicability in the microfabrication of bioelectronic components, needed for next-generation IoT sensing technologies. This versatility arises mostly from the distinct stimulus provided by laser beams, either photochemical or photothermal, to perform ablative, additive, and transformative material processing tasks and construct functional elements and geometries. With the focus given in this chapter to additive and transformative laser-enabled material processing, DLW-based microfabrication presents itself as a straightforward, scalable production method with very high prototyping and iterative capabilities, poised for decreasing the time from laboratory to fabrication and final implementation. Laser material processing tools have become ubiquitous both in laboratories and in industrial processes, enabling a faster process-property optimization of both resulting laser-processed material properties and material integration and assembly, to reach next-generation consumable electronic and bioelectronic applications.

Both empirical and simulation studies have provided greater understanding and control over laser-material interactions and outcomes. The straightforward adjustability of laser stimulus, by manipulation of energy (e.g. beam energy, power), time/frequency (PRF, PW), and spatial (e.g. spot size, writing speed) fabrication parameters, enables the tuning of writing resolution, material thickness, uniformity and suitability for specific functional roles. Furthermore, tunable laser-processed material composition and resulting conductive or semiconductive properties allow for selective writing of integrated geometries with distinct capabilities from a common precursor, further highlighting the effortless, seamless integration potential of ADLW and TDLW processes. Outside of wafer-scale microfabrication, large-area microfabrication of functional elements, from electrodes, current collectors, semiconducting sensing channels and others, has also benefited from the deployment of DLW, especially in the fields of energy harvesting and storage, sensors, and bioelectronics. Specifically, the capability to write multi-material electrode geometries with tailored properties and functionalities has been the most explored feature of DLW schemes. However, in this case, DLW still suffers from an important disadvantage when compared to other solution processing and printing technologies, related to the lower throughput, associated with some setups for material writing. For several printing processes, such as screen, flexographic, and gravure printing, S2S and R2R implementation for high-density fabrication of electronic components can be pursued, after optimization of printed material properties. In contrast, DLW suffers from the characteristic line-by-line patterning associated with beam-directing systems, instead of the planar modality of printing technologies. Aiming at improving the fabrication throughput of optics and stage motion systems, the integration of multi-axis and multiple lasers for synchronized and simultaneous patterning could be explored to improve throughput and compatibility with S2S and R2R processes for large-area fabrication. Furthermore, as previously pointed out, optimizing DLW tasks for high scanning speed regimens, as well as the implementation of high-speed scanning systems can drastically improve the fabrication throughput of DLW. With further development of DLW microfabrication paradigms, a synergy between the continuous study of laser-material interactions and the development of laser systems would be beneficial for future industrial implementation, because most commercial laser systems are not specifically designed for material synthesis and conversion tasks. Thus, greater fine-tuning of applied laser stimulus with specialized lasers would decrease variability in material properties and a greater overall reproducibility of DLW processes. In addition, most studies of DLW material growth focus on manipulating precursors for available lasers, and not on designing laser tools with compatible properties for maximized irradiation outputs. Some recent instances in the literature have appeared, where tailoring the laser system hardware clearly benefits the laser synthesis processes and final device performance. Thus, the final implementation of fully functional hardware for DLW setups would need to include appropriate laser sources, optics and beam directing systems, while benefiting the nature of the irradiated precursor.

In this context, DLW of carbon-based polymers for LIG engraving has been regarded as one of the most interesting methods for graphene production. Although its properties are not directly comparable to single layer graphene, LIG ease of production and handling offer many opportunities for applications that do not require the conductive and optical properties of available graphene powder. As it was described through this chapter, LIG opens the possibility for the simple, cost effective and scalable production of technological components. LIG production does not require controlled environments, expensive chemicals or equipment, thus substantially reducing production costs, while being a sustainable and environmentally friendly manufacturing approach. It virtually produces zero waste, and it can be performed in green-based biocompatible and biodegradable precursors. On the other hand, it is a one-step manufacturing process, that does not require slurry preparation or any other deposition methods, once again lowering production time and costs. Therefore, LIG represents a very interesting and promising material for solving, or at least reducing, the problems associated with toxic and harmful e-waste. Nevertheless, it is not common for new and emerging technologies to get in the market if they do not surpass the current state of the art or if they do not follow the "ten times cheaper or ten times better" rule [304]. Therefore, it is very unlikely that LIG-based devices will quickly surpass already available mature technologies, which can be produced in mass at relatively low cost. However, nanomaterials, such as graphene, exhibit clear advantages for the production and scale up of emerging flexible and wearable devices. Due to its compatibility with flexible substrates and low-cost fabrication, LIG-based electronics can bring electronic functionality to markets unfit for rigid and expensive silicon electronics.[144] The technology readiness levels (TRL) for these technologies is still low, therefore more opportunities are presented for different processing methods, materials, and products to get in the market. Along with other printing technologies, LIG may play a relevant role on the future market of flexible technologies and become fundamental for device fabrication, based on a trade-off between high performance obtained by silicon-based electronics and fast device prototyping and fabrication. Nevertheless, one of the most important advantages of LIG processing is its sustainable nature and the capability of promoting a truly greener, circular economy.

In terms of LIG applicability in electronic component fabrication, this chapter aimed at showcasing the multifunctionality of this material in multiple thin film, in-plane bioelectronic components and systems. LIG products present several advantages, such as the ability to pattern complex geometries in a one-step process, while allowing for a simultaneous tuning of surface properties, regarding conductivity, wettability and other aspects such as morphology, giving rise to its multifunctional properties. Furthermore, in-plane components can be readily designed and studied using LIG, reducing material usage and improving the efficiency when compared to non-planar geometries. However, due to the transformative nature of the laser graphitization process, LIG thin films are eventually restricted and bound to the precursor substrate, slightly restricting their application in thin film technologies where complex layer stacking may be required, a disadvantage when comparing to graphene in powder form. Another aspect relevant when developing applications with LIG is substrate compatibility and durability. Green, bio-based materials have been intensely studied in the electronics field for various purposes, such as transistor fabrication [305] and soft, flexible electronics [306], pushing several avenues for the advancement of more sustainable fabrication, with circular approaches that promote reusability, recyclability, reducing carbon footprint and energy consumption in fabrication [307]. As such, intrinsic properties of natural materials must be carefully selected, to meet the requirements of any target application, both in terms of mechanical properties, but also on the ability to be readily converted to LIG with appropriate characteristics, while preserving all the necessary sustainability aspects. Some natural substrates, such as wood and other rigid biomass, are great candidates to be used in rigid application, such as printed circuit boards, while flexible cellulose or lignin films are attractive for soft, flexible and wearable technologies. Careful engineering of natural materials' composition and resulting mechanical and thermal properties is a key aspect for their applicability in specific technologies [308]. As such, future development on natural composites, using blending and coating approaches are envisioned to improve several aspects of LIG synthesis, including precursor substrate compatibility and resulting mechanical, morphological, and conductive properties. In addition, promising work is being presented, regarding the use of new chemical treatments, such the use of non-toxic, green catalysts, which improve the efficiency and outcome of laser graphitization processes, paired with meticulous control of the laser irradiation process. With the concepts and recent developments discussed in this chapter, challenges related to devices performance and novel functionalities may be tackled, while enabling multi-level integration of different components, using other compatible fabrication technologies such as screen or inkjet printing, to produce hybrid laser engraved and printed systems. DLW microfabrication and its additive and transformative modalities are becoming adaptable, multifaceted, and auspicious tools for the manufacturing of next-generation, flexible bioelectronics for the IoT. By itself, or complementing other fabrication techniques within hybrid frameworks, alongside solution processing and printed electronics, future developments of DLW technology have the potential to impact electronics microfabrication. With the scope of different implementation levels, from material engineering, functional patterning, and system-level integration enabled by DLW, future interest in research and industrial application is anticipated, strengthened by the overview provided to readers in this chapter.

References

1. Hecht, J. A short history of laser development. *Appl. Opt.* **49**, F99 (2010).
2. Jelínková, H. & Šulc, J. Laser characteristics. in *Lasers for Medical Applications* 17–46 (Elsevier, 2013). doi:10.1533/9780857097545.1.17.
3. Affan Ahmed, S., Mohsin, M. & Zubair Ali, S. M. Survey and technological analysis of laser and its defense applications. *Defence Technology* vol. 17 583–592 (2021).
4. Zhan, Y., Mei, Y. & Zheng, L. Materials capability and device performance in flexible electronics for the Internet of Things. *J. Mater. Chem. C* **2**, 1220–1232 (2014).
5. Kim, D. H., Xiao, J., Song, J., Huang, Y. & Rogers, J. A. Stretchable, curvilinear electronics based on inorganic materials. *Advanced Materials* vol. 22 2108–2124 (2010).
6. Yin, L., Lv, J. & Wang, J. Structural Innovations in Printed, Flexible, and Stretchable Electronics. *Advanced Materials Technologies* vol. 5 2000694 (2020).
7. Eslamian, M. Inorganic and Organic Solution-Processed Thin Film Devices. *Nano-Micro Letters* vol. 9 1–23 (2017).
8. Park, J. W., Kang, B. H. & Kim, H. J. A Review of Low-Temperature Solution-Processed Metal Oxide Thin-Film Transistors for Flexible Electronics. *Advanced Functional Materials* vol. 30 1904632 (2020).
9. Carlos, E., Branquinho, R., Martins, R., Kiazadeh, A. & Fortunato, E. Recent Progress in Solution-Based Metal Oxide Resistive Switching Devices. *Advanced Materials* vol. 33 2004328 (2021).
10. Zhang, Y., Ng, S. W., Lu, X. & Zheng, Z. Solution-Processed Transparent Electrodes for Emerging Thin-Film Solar Cells. *Chemical Reviews* vol. 120 2049–2122 (2020).
11. Pang, Y. *et al.* Additive Manufacturing of Batteries. *Advanced Functional Materials* vol. 30 1906244 (2020).
12. Zhakeyev, A. *et al.* Additive Manufacturing: Unlocking the Evolution of Energy Materials. *Advanced Science* vol. 4 1700187 (2017).
13. Espera, A. H., Dizon, J. R. C., Chen, Q. & Advincula, R. C. 3D-printing and advanced manufacturing for electronics. *Progress in Additive Manufacturing* vol. 4 245–267 (2019).
14. Buga, C. S. & Viana, J. C. The role of printed electronics and related technologies in the development of smart connected products. *Flexible and Printed Electronics* vol. 7 043001 (2022).
15. Divakaran, N. *et al.* Comprehensive review on various additive manufacturing techniques and its implementation in electronic devices. *Journal of Manufacturing Systems* vol. 62 477–502 (2022).
16. Khan, Y. *et al.* A New Frontier of Printed Electronics: Flexible Hybrid Electronics. *Advanced Materials* vol. 32 1905279 (2020).
17. Yarali, E. *et al.* Recent Progress in Photonic Processing of Metal-Oxide Transistors. *Advanced Functional Materials* vol. 30 1906022 (2020).
18. Xu, Y. *et al.* Rapid In-Situ Synthesis and Patterning of Edge-Unsaturated MoS 2 by Femtosecond Laser-Induced Photo-Chemical Reaction. *ACS Appl. Mater. Interfaces* **14**, 5558–5566 (2022).
19. Tan, X. *et al.* Laser doping of 2D material for precise energy band design. *Nanoscale* **15**, 9297–9303 (2023).
20. Carlotti, M. & Mattoli, V. Functional Materials for Two-Photon Polymerization in Microfabrication. *Small* **15**, 1902687 (2019).
21. Chung, J., Ko, S., Bieri, N. R., Grigoropoulos, C. P. & Poulikakos, D. Laser curing of gold nanoparticle inks. in *American Society of Mechanical Engineers, Heat Transfer Division, (Publication) HTD* vol. 374 131–140 (American Society of Mechanical Engineers Digital Collection, 2003).
22. Zhu, C. *et al.* Direct Laser Patterning of a 2D WSe 2 Logic Circuit. *Adv. Funct. Mater.* **31**, 2009549 (2021).
23. Bian, J. *et al.* Laser Transfer, Printing, and Assembly Techniques for Flexible Electronics. *Advanced Electronic Materials* vol. 5 1800900 (2019).

24. Kim, M., Osone, S., Kim, T., Higashi, H. & Seto, T. Synthesis of nanoparticles by laser ablation: A review. *KONA Powder and Particle Journal* vol. 2017 80–90 (2017).
25. Kumar, A., Kumar, A. & Kumar, A. *Laser-based Technologies for Sustainable Manufacturing*. *Laser-based Technologies for Sustainable Manufacturing* (CRC Press, 2023). doi:10.1201/9781003402398.
26. Chen, Z., Yang, J., Liu, H., Zhao, Y. & Pan, R. A short review on functionalized metallic surfaces by ultrafast laser micromachining. *International Journal of Advanced Manufacturing Technology* vol. 119 6919–6948 (2022).
27. Kim, K.-R. *et al.* High-precision and ultrafast UV laser system for next-generation flexible PCB drilling. *J. Manuf. Syst.* **38**, 107–113 (2016).
28. Balena, A., Bianco, M., Pisanello, F. & De Vittorio, M. Recent Advances on High-Speed and Holographic Two-Photon Direct Laser Writing. *Advanced Functional Materials* 2211773 (2023) doi:10.1002/adfm.202211773.
29. Ahmadi, Z., Fathi-Hafshejani, P., Kayali, E., Beidaghi, M. & Mahjouri-Samani, M. Rapid laser nanomanufacturing and direct patterning of 2D materials on flexible substrates—2DFlex. *Nanotechnology* **32**, 055302 (2020).
30. Ge, Y. *et al.* Structural Transformation of Unconventional-Phase Materials. *ACS Nano* **17**, 12935–12954 (2023).
31. Chen, C. *et al.* Solution-processed metal oxide arrays using femtosecond laser ablation and annealing for thin-film transistors. *J. Mater. Chem. C* **5**, 9273–9280 (2017).
32. Yang, H. *et al.* Solution-Processed Organic Thin-Film Transistor Arrays with the Assistance of Laser Ablation. *ACS Appl. Mater. Interfaces* **9**, 3849–3856 (2017).
33. Ślusarz, A. M., Komorowska, K., Baraniecki, T., Zelewski, S. J. & Kudrawiec, R. Transparent Metal Mesh Electrodes Microfabricated by Structuring Water-Soluble Polymer Resist via Laser Ablation. *ACS Sustain. Chem. Eng.* **10**, 8196–8205 (2022).
34. Ravi-Kumar, S., Lies, B., Zhang, X., Lyu, H. & Qin, H. Laser ablation of polymers: a review. *Polym. Int.* **68**, 1391–1401 (2019).
35. Song, S. *et al.* Photothermal Lithography for Realizing a Stretchable Multilayer Electronic Circuit Using a Laser. *ACS Nano* **17**, 21443–21454 (2023).
36. Cohen, M. I., Unger, B. A. & Milkosky, J. F. Laser Machining of Thin Films and Integrated Circuits. *Bell Syst. Tech. J.* **47**, 385–405 (1968).
37. Raamot, J. & Zaleckas, V. J. Laser Pattern Generation Using X–Y Beam Deflection. *Appl. Opt.* **13**, 1179 (1974).
38. Becker, R. A., Sopori, B. L. & Chang, W. S. C. Focused laser lithographic system. *Appl. Opt.* **17**, 1069 (1978).
39. Hass, G. & Ramsey, J. B. Vacuum Deposition of Dielectric and Semiconductor Films by a CO_2 Laser. *Appl. Opt.* **8**, 1115 (1969).
40. Baranauskas, V., Mammana, C. I. Z., Klinger, R. E. & Greene, J. E. Laser-induced chemical vapor deposition of polycrystalline Si from SiCl4. *Appl. Phys. Lett.* **36**, 930–932 (1980).
41. Fan, J. C. C. & Zeiger, H. J. Crystallization of amorphous silicon films by Nd:YAG laser heating. *Appl. Phys. Lett.* **27**, 224–226 (1975).
42. Watanabe, H., Miki, H., Sugai, S., Kawasaki, K. & Kioka, T. Crystallization process of polycrystalline silicon by KrF excimer laser annealing. *Jpn. J. Appl. Phys.* **33**, 4491–4498 (1994).
43. Bertolotti, M. Laser annealing of semiconductors. *J. Sov. Laser Res.* **6**, 395–404 (1985).
44. Muller, J. C., Fogarassy, E., Salles, D., Stuck, R. & Siffert, P. M. Laser Processing in the Preparation of Silicon Solar Cells. *IEEE Trans. Electron Devices* **27**, 815–821 (1980).
45. Misra, N., Xu, L., Rogers, M. S., Ko, S. H. & Grigoropoulos, C. P. Pulsed laser annealing of semiconductor structures for functional devices. in *Physica Status Solidi (C) Current Topics in Solid State Physics* vol. 5 3264–3270 (John Wiley & Sons, Ltd, 2008).
46. Norton, D. P. Synthesis and properties of epitaxial electronic oxide thin-film materials. *Materials*

Science and Engineering R: Reports vol. 43 139–247 (2004).

47. Lee, S. Y., Shim, E. S., Kang, H. S., Pang, S. S. & Kang, J. S. Fabrication of ZnO thin film diode using laser annealing. *Thin Solid Films* **473**, 31–34 (2005).
48. Smith, P. M., Carey, P. G. & Sigmon, T. W. Excimer laser crystallization and doping of silicon films on plastic substrates. *Appl. Phys. Lett.* **70**, 342–344 (1997).
49. Tsagarakis, E. D., Lew, C., Thompson, M. O. & Giannelis, E. P. Nanocrystalline barium titanate films on flexible plastic substrates via pulsed laser annealing. *Appl. Phys. Lett.* **89**, 202910 (2006).
50. Nánai, L. *et al.* Laser-induced metal deposition on semiconductors from liquid electrolytes. *Appl. Phys. Lett.* **54**, 736–738 (1989).
51. Liang, J. *et al.* Toward all-carbon electronics: Fabrication of graphene-based flexible electronic circuits and memory cards using maskless laser direct writing. *ACS Appl. Mater. Interfaces* **2**, 3310–3317 (2010).
52. Feng, S., Cao, S., Tian, Z., Zhu, H. & Kong, D. Maskless Patterning of Biodegradable Conductors by Selective Laser Sintering of Microparticle Inks and Its Application in Flexible Transient Electronics. *ACS Appl. Mater. Interfaces* **11**, 45844–45852 (2019).
53. Park, S. *et al.* Layer-Selective Synthesis of MoS 2 and WS 2 Structures under Ambient Conditions for Customized Electronics. *ACS Nano* **14**, 8485–8494 (2020).
54. Zhao, G. *et al.* Laser-scribed conductive, photoactive transition metal oxide on soft elastomers for Janus on-skin electronics and soft actuators. *Sci. Adv.* **8**, 9734 (2022).
55. Yang, L. *et al.* Laser printed microelectronics. *Nat. Commun.* **14**, 1103 (2023).
56. Park, R. *et al.* Laser-Assisted Structuring of Graphene Films with Biocompatible Liquid Crystal Polymer for Skin/Brain-Interfaced Electrodes. *Adv. Healthc. Mater.* 2301753 (2023) doi:10.1002/adhm.202301753.
57. Bohandy, J., Kim, B. F. & Adrian, F. J. Metal deposition from a supported metal film using an excimer laser. *J. Appl. Phys.* **60**, 1538–1539 (1986).
58. Piqué, A. *et al.* A novel laser transfer process for direct writing of electronic and sensor materials. *Appl. Phys. A Mater. Sci. Process.* **69**, S279–S284 (1999).
59. Ur Rehman, Z., Yang, F., Wang, M. & Zhu, T. Fundamentals and Advances in Laser-Induced Transfer. *Optics and Laser Technology* vol. 160 109065 (2023).
60. Wong, W. S. *et al.* Fabrication of thin-film InGaN light-emitting diode membranes by laser lift-off. *Appl. Phys. Lett.* **75**, 1360–1362 (1999).
61. Liu, Y. S. & Cole, H. S. Laser Surface Modification for Copper Deposition on Polyimide. *MRS Proc.* **129**, 579 (1988).
62. Tanaka, T., Ishikawa, A. & Kawata, S. Two-photon-induced reduction of metal ions for fabricating three-dimensional electrically conductive metallic microstructure. *Appl. Phys. Lett.* **88**, 81107 (2006).
63. Chen, Z. *et al.* Laser direct writing carbon nanotube arrays on transparent substrates. *Appl. Phys. Lett.* **90**, 133108 (2007).
64. Zhang, Y. *et al.* Direct imprinting of microcircuits on graphene oxides film by femtosecond laser reduction. *Nano Today* **5**, 15–20 (2010).
65. Lin, J. *et al.* Laser-induced porous graphene films from commercial polymers. *Nat. Commun.* **5**, 5714 (2014).
66. Jitsuno, T. & Uno, K. CO2 Lasers. in *Handbook of Laser Micro- and Nano-Engineering* vol. 20 1–23 (Springer International Publishing, 2021).
67. Liu, X., Popa, D. & Akhmediev, N. Revealing the Transition Dynamics from Q Switching to Mode Locking in a Soliton Laser. *Phys. Rev. Lett.* **123**, 093901 (2019).
68. Bayhan, Z. *et al.* A Laser-Induced Mo2CTx MXene Hybrid Anode for High-Performance Li-Ion Batteries. *Small* 2208253 (2023) doi:10.1002/smll.202208253.
69. Zhang, H., Sun, Y., Li, Q. & Wan, C. Upgrading Lignocellulose to Porous Graphene Enabled by Deep Eutectic Solvent Pretreatment: Insights into the Role of Lignin and Pseudo-lignin. *ACS*

Sustain. Chem. Eng. **10**, 11501–11511 (2022).

70. Yu, W., Zhao, W., Wang, S., Chen, Q. & Liu, X. Direct Conversion of Liquid Organic Precursor into 3D Laser-Induced Graphene Materials. *Adv. Mater.* **35**, 2209545 (2023).
71. Yeamsuksawat, T., Zhu, L., Kasuga, T., Nogi, M. & Koga, H. CO2-laser-induced carbonization of calcium chloride-treated chitin nanopaper for applications in solar thermal heating. *RSC Adv.* **13**, 17556–17564 (2023).
72. Zang, X. *et al.* Laser-sculptured ultrathin transition metal carbide layers for energy storage and energy harvesting applications. *Nat. Commun.* **10**, 3112 (2019).
73. Li, Y. *et al.* Laser-Patterned Copper Electrodes for Proximity and Tactile Sensors. *Adv. Mater. Interfaces* **7**, 1901845 (2020).
74. Ji, Y. *et al.* Flexible Metal Electrodes by Femtosecond Laser-Activated Deposition for Human-Machine Interfaces. *ACS Appl. Mater. Interfaces* **14**, 11971–11980 (2022).
75. Morosawa, F., Hayashi, S. & Terakawa, M. Femtosecond Laser-Induced Graphitization of Transparent Cellulose Nanofiber Films. *ACS Sustain. Chem. Eng.* **9**, 2955–2961 (2021).
76. Ren, J. *et al.* Laser Direct Activation of Polyimide for Selective Electroless Plating of Flexible Conductive Patterns. *ACS Appl. Electron. Mater.* **4**, 2191–2202 (2021).
77. Wei, Y., Chen, J., Liang, L., Wang, J. & Zeng, H. Laser-Induced Optoelectronic Tuning of Perovskite Nanocrystal Films for Multicolor Pattern Displays. *ACS Appl. Nano Mater.* **2022**, 11020–11027 (2022).
78. Nam, V. B. *et al.* Highly Stable Ni-Based Flexible Transparent Conducting Panels Fabricated by Laser Digital Patterning. *Adv. Funct. Mater.* **29**, 1806895 (2019).
79. Binh Nam, V., Thi Giang, T. & Lee, D. Laser digital patterning of finely-structured flexible copper electrodes using copper oxide nanoparticle ink produced by a scalable synthesis method. *Appl. Surf. Sci.* **570**, 151179 (2021).
80. Yeo, J. *et al.* Next generation non-vacuum, maskless, low temperature nanoparticle ink laser digital direct metal patterning for a large area flexible electronics. *PLoS One* **7**, e42315 (2012).
81. Zhang, J. *et al.* Laser-Induced Selective Metallization on Polymer Substrates Using Organocopper for Portable Electronics. *ACS Appl. Mater. Interfaces* **11**, 13714–13723 (2019).
82. Zhang, J., Xu, R., Feng, J., Xie, Y. & Zhou, T. Laser Direct Writing of Flexible Heaters on Polymer Substrates. *Ind. Eng. Chem. Res.* **60**, 11161–11170 (2021).
83. Moskal, D., Martan, J. & Honner, M. Scanning Strategies in Laser Surface Texturing: A Review. *Micromachines* **14**, 1241 (2023).
84. Kumar, R. *et al.* Laser processing of graphene and related materials for energy storage: State of the art and future prospects. *Prog. Energy Combust. Sci.* **91**, 100981 (2022).
85. Devi, M., Wang, H., Moon, S., Sharma, S. & Strauss, V. Laser-Carbonization – A powerful tool for micro-fabrication of patterned electronic carbons. *Adv. Mater.* 2211054 (2023) doi:10.1002/adma.202211054.
86. Chatani, S., Kloxin, C. J. & Bowman, C. N. The power of light in polymer science: photochemical processes to manipulate polymer formation, structure, and properties. *Polym. Chem.* **5**, 2187–2201 (2014).
87. Palneedi, H. *et al.* Laser Irradiation of Metal Oxide Films and Nanostructures: Applications and Advances. *Advanced Materials* vol. 30 1705148 (2018).
88. C. Claro, P. I. *et al.* Sustainable carbon sources for green laser-induced graphene: A perspective on fundamental principles, applications, and challenges. *Appl. Phys. Rev.* **9**, 041305 (2022).
89. Song, C. *et al.* Driving forces for ultrafast laser-induced sp2 to sp3 structural transformation in graphite. *npj Comput. Mater.* **9**, 1–7 (2023).
90. Bunaziv, I., Akselsen, O. M., Ren, X., Nyhus, B. & Eriksson, M. Laser Beam and Laser-Arc Hybrid Welding of Aluminium Alloys. *Metals (Basel).* **11**, 1150 (2021).
91. Nishiyama, H., Umetsu, K. & Kimura, K. Versatile direct laser writing of non-photosensitive materials using multi-photon reduction-based assembly of nanoparticles. *Sci. Rep.* **9**, 1–10 (2019).

92. Lio, G. E. *et al.* Leveraging on ENZ Metamaterials to Achieve 2D and 3D Hyper-Resolution in Two-Photon Direct Laser Writing. *Adv. Mater.* **33**, 2008644 (2021).
93. Bougdid, Y. *et al.* Systematic λ /21 resolution achieved in nanofabrication by two-photon-absorption induced polymerization. *J. Micromechanics Microengineering* **29**, 035018 (2019).
94. Pinheiro, T. *et al.* Influence of CO2 laser beam modelling on electronic and electrochemical properties of paper-based laser-induced graphene for disposable pH electrochemical sensors. *Carbon Trends* **11**, 100271 (2023).
95. Zhang, T. *et al.* Laser ablation behavior and mechanism of polyimide by UV irradiation. *Mater. Manuf. Process.* **37**, 809–815 (2022).
96. Abdulhafez, M., Tomaraei, G. N. & Bedewy, M. Fluence-Dependent Morphological Transitions in Laser-Induced Graphene Electrodes on Polyimide Substrates for Flexible Devices. *ACS Appl. Nano Mater.* **4**, 2973–2986 (2021).
97. Zhang, J. *et al.* Light-induced irreversible structural phase transition in trilayer graphene. *Light Sci. Appl.* **9**, 174 (2020).
98. Bai, S. *et al.* Laser-assisted reduction of highly conductive circuits based on copper nitrate for flexible printed sensors. *Nano-Micro Lett.* **9**, 1–13 (2017).
99. Joe, D. J. *et al.* Laser–Material Interactions for Flexible Applications. *Adv. Mater.* **29**, 1606586 (2017).
100. Bajpai, A., Kumbhakar, P., Tiwary, C. S. & Biswas, K. Conducting Graphene Synthesis from Electronic Waste. *ACS Sustain. Chem. Eng.* **12**, 20 (2021).
101. Shahbazi, A., Koohian, A. & Madanipour, K. Effect of scanning speed on continuous wave laser scribing of metal thin films: Theory and experiment. *Laser Phys.* **27**, 016101 (2017).
102. Yang, C.-C., Hung, M.-W., Tsai, H.-Y., Chuang, W.-N. & Huang, K.-C. Planar square spiral inductor generated through indium–tin oxide film removal by using UV laser ablation. *Appl. Phys. A* **122**, 441 (2016).
103. Antolini, F., Limosani, F. & Carcione, R. Direct Laser Patterning of CdTe QDs and Their Optical Properties Control through Laser Parameters. *Nanomaterials* **12**, 1551 (2022).
104. Jones, J., Snowdon, M. R., Rathod, S. & Peng, P. Direct laser writing of copper and copper oxide structures on plastic substrates for memristor devices. *Flex. Print. Electron.* **8**, 015008 (2023).
105. Pinheiro, T. *et al.* Laser-Induced Graphene on Paper toward Efficient Fabrication of Flexible, Planar Electrodes for Electrochemical Sensing. *Adv. Mater. Interfaces* **8**, 2101502 (2021).
106. Coelho, J. *et al.* Paper-based laser-induced graphene for sustainable and flexible microsupercapacitor applications. *Microchim. Acta* **190**, 40 (2023).
107. Saha, S. K., Au, B. & Oakdale, J. S. High-Speed Direct Laser Writing of Silver Nanostructures via Two-Photon Reduction. *Adv. Eng. Mater.* **21**, 1900583 (2019).
108. Waller, E. H., Duran, S. & von Freymann, G. Direct laser writing of 3D metallic mid- and far-infrared wave components. *Nanophotonics* **12**, 1549–1555 (2023).
109. Murray, R., Burke, M., Iacopino, D. & Quinn, A. J. Design of Experiments and Optimization of Laser-Induced Graphene. *ACS Omega* **6**, 16736–16743 (2021).
110. Guo, B. *et al.* Femtosecond Laser Micro/Nano-manufacturing: Theories, Measurements, Methods, and Applications. *Nanomanufacturing Metrol.* **3**, 26–67 (2020).
111. Raciukaitis, G. Ultra-Short Pulse Lasers for Microfabrication: A Review. *IEEE J. Sel. Top. Quantum Electron.* **27**, 1–12 (2021).
112. Chen, Y.-S. *et al.* Preparation of Electroless Copper Circuit on Polycarbonate/ Acrylonitrile Butadiene Styrene (PC/ABS) Using a Laser curing of Pd complex. *Int. J. Electrochem. Sci.* **16**, 21112 (2021).
113. Greenberg, E., Armon, N., Kapon, O., Ben-Ishai, M. & Shpaisman, H. Nanostructure and Mechanism of Metal Deposition by a Laser-Induced Photothermal Reaction. *Adv. Mater. Interfaces* **6**, 1900541 (2019).
114. Chyan, Y. *et al.* Laser-Induced Graphene by Multiple Lasing: Toward Electronics on Cloth, Paper,

and Food. *ACS Nano* **12**, 2176–2183 (2018).

115. Yun, J., Yang, M. & Kang, B. Laser Sweeping Lithography: Parallel Bottom-up Growth Sintering of a Nanoseed-Organometallic Hybrid Suspension for Ecofriendly Mass Production of Electronics. *ACS Sustain. Chem. Eng.* **6**, 4940–4947 (2018).
116. Ye, R. *et al.* Laser-Induced Graphene Formation on Wood. *Adv. Mater.* **29**, 1702211 (2017).
117. Zhang, Z. *et al.* Carbon Fibers with High Electrical Conductivity: Laser Irradiation of Mesophase Pitch Filaments Obtains High Graphitization Degree. *ACS Sustain. Chem. Eng.* **8**, 17629–17638 (2020).
118. Mizoshiri, M. & Yoshidomi, K. Cu patterning using femtosecond laser reductive sintering of cuo nanoparticles under inert gas injection. *Materials (Basel).* **14**, 3285 (2021).
119. Zhang, Z., Song, L., Cheng, L., Tan, J. & Yang, W. Accelerated Graphitization of PAN-Based Carbon Fibers: K + -Effected Graphitization via Laser Irradiation. *ACS Sustain. Chem. Eng.* **10**, 8086–8093 (2022).
120. Wable, M. *et al.* CO2Laser Direct-Write Process for Micro-Gradient-Patterned Carbon Composed of Graphene-like and Disordered Carbon Forms for a Robust Anode-Free Li-Metal Battery. *ACS Appl. Energy Mater.* **5**, 10940–10951 (2022).
121. Zhang, Z. *et al.* A Laser-Processed Carbon-Titanium Carbide Heterostructure Electrode for High-Frequency Micro-Supercapacitors. *Small* **19**, 2300747 (2023).
122. Rahimi, R. *et al.* Laser-Enabled Processing of Stretchable Electronics on a Hydrolytically Degradable Hydrogel. *Adv. Healthc. Mater.* **7**, 1800231 (2018).
123. Lee, S. & Jeon, S. Laser-Induced Graphitization of Cellulose Nanofiber Substrates under Ambient Conditions. *ACS Sustain. Chem. Eng.* **7**, 2270–2275 (2019).
124. Wang, B. *et al.* Ultrafast, Kinetically Limited, Ambient Synthesis of Vanadium Dioxides through Laser Direct Writing on Ultrathin Chalcogenide Matrix. *ACS Nano* **15**, 10502–10513 (2021).
125. Bae, G. *et al.* Photon-Pen Writing for Metal Oxide-Based Versatile Nanosensors. *Adv. Funct. Mater.* **32**, 2204821 (2022).
126. Vashisth, A. *et al.* ReaxFF Simulations of Laser-Induced Graphene (LIG) Formation for Multifunctional Polymer Nanocomposites. *ACS Appl. Nano Mater.* **3**, 1881–1890 (2020).
127. Wang, H. *et al.* In Situ Synthesis of Molybdenum Carbide Nanoparticles Incorporated into Laser-Patterned Nitrogen-Doped Carbon for Room Temperature VOC Sensing. *Adv. Funct. Mater.* **31**, 2104061 (2021).
128. Dreimol, C. H. *et al.* Sustainable wood electronics by iron-catalyzed laser-induced graphitization for large-scale applications. *Nat. Commun.* **13**, 3680 (2022).
129. Raffel, J. I., Freidin, J. F. & Chapman, G. H. Laser-formed connections using polyimide. *Appl. Phys. Lett.* **42**, 705–706 (1983).
130. Pinheiro, T. *et al.* Water Peel-Off Transfer of Electronically Enhanced, Paper-Based Laser-Induced Graphene for Wearable Electronics. *ACS Nano* **16**, 20633–20646 (2022).
131. Huang, Q.-M. *et al.* Laser-Induced Graphene Formation on Chitosan Derivatives toward Ecofriendly Electronics. *ACS Appl. Nano Mater.* **6**, 10453–10465 (2023).
132. Huang, Y. *et al.* Laser Direct Writing of Heteroatom (N and S)-Doped Graphene from a Polybenzimidazole Ink Donor on Polyethylene Terephthalate Polymer and Glass Substrates. *Small* **14**, 1803143 (2018).
133. Le, T. D., Park, S., An, J., Lee, P. S. & Kim, Y. Ultrafast Laser Pulses Enable One-Step Graphene Patterning on Woods and Leaves for Green Electronics. *Adv. Funct. Mater.* **29**, 1902771 (2019).
134. Carvalho, A. F., Fernandes, A. J. S., Martins, R., Fortunato, E. & Costa, F. M. Laser-Induced Graphene Piezoresistive Sensors Synthesized Directly on Cork Insoles for Gait Analysis. *Adv. Mater. Technol.* **5**, 2000630 (2020).
135. Kulyk, B. *et al.* Laser-Induced Graphene from Paper by Ultraviolet Irradiation: Humidity and Temperature Sensors. *Adv. Mater. Technol.* **7**, 2101311 (2022).
136. Imbrogno, A. *et al.* Laser-Induced Graphene Supercapacitors by Direct Laser Writing of Cork

Natural Substrates. *ACS Appl. Electron. Mater.* **4**, 1541–1551 (2022).
137. Gao, Y. *et al.* Laser Direct Writing of Ultrahigh Sensitive SiC-Based Strain Sensor Arrays on Elastomer toward Electronic Skins. *Adv. Funct. Mater.* **29**, 1806786 (2019).
138. Carvalho, A. F. *et al.* Laser-Induced Graphene Strain Sensors Produced by Ultraviolet Irradiation of Polyimide. *Adv. Funct. Mater.* **28**, 1805271 (2018).
139. Terakawa, M. Laser-Induced Carbonization and Graphitization. in *Handbook of Laser Micro- and Nano-Engineering* vol. 2 857–878 (Springer International Publishing, 2021).
140. Chen, Y. *et al.* UV Laser-Induced Polyimide-to-Graphene Conversion: Modeling, Fabrication, and Application. *Small Methods* **3**, 1900208 (2019).
141. Song, Y. *et al.* Macro-Sized All-Graphene 3D Structures via Layer-by-Layer Covalent Growth for Micro-to-Macro Inheritable Electrical Performances. *Adv. Funct. Mater.* **33**, 2305191 (2023).
142. Wang, M., Yang, Y. & Gao, W. Laser-engraved graphene for flexible and wearable electronics. *Trends Chem.* **3**, 969–981 (2021).
143. Nayak, P., Kurra, N., Xia, C. & Alshareef, H. N. Highly Efficient Laser Scribed Graphene Electrodes for On-Chip Electrochemical Sensing Applications. *Adv. Electron. Mater.* **2**, 1600185 (2016).
144. Le, T. S. D. *et al.* Recent Advances in Laser-Induced Graphene: Mechanism, Fabrication, Properties, and Applications in Flexible Electronics. *Adv. Funct. Mater.* **32**, 2205158 (2022).
145. Vivaldi, F. M. *et al.* Three-Dimensional (3D) Laser-Induced Graphene: Structure, Properties, and Application to Chemical Sensing. *ACS Appl. Mater. Interfaces* **13**, 30245–30260 (2021).
146. Huang, L., Su, J., Song, Y. & Ye, R. Laser-Induced Graphene: En Route to Smart Sensing. *Nano-Micro Lett.* **12**, 1–17 (2020).
147. Muzyka, K. & Xu, G. Laser-induced Graphene in Facts, Numbers, and Notes in View of Electroanalytical Applications: A Review. *Electroanalysis* **34**, 574–589 (2022).
148. Li, Y. *et al.* Laser-Induced Graphene in Controlled Atmospheres: From Superhydrophilic to Superhydrophobic Surfaces. *Adv. Mater.* **29**, 1700496 (2017).
149. Dallinger, A., Steinwender, F., Gritzner, M. & Greco, F. Different Roles of Surface Chemistry and Roughness of Laser-Induced Graphene: Implications for Tunable Wettability. *ACS Appl. Nano Mater.* **6**, 16201–16211 (2023).
150. Bowden, M., Gardiner, D. J. & Southall, J. M. Raman analysis of laser-annealed amorphous carbon films. *J. Appl. Phys.* **71**, 521–523 (1992).
151. Salama, I. A., Quick, N. R. & Kar, A. Laser synthesis of carbon-rich SiC nanoribbons. *J. Appl. Phys.* **93**, 9275–9281 (2003).
152. Salama, I. A., Quick, N. R. & Kar, A. Laser direct writing and doping of diamond-like carbon, polycrystalline diamond, and single crystal silicon carbide. *J. Laser Appl.* **16**, 92–99 (2004).
153. Wan, Z. *et al.* Laser-Reduced Graphene: Synthesis, Properties, and Applications. *Adv. Mater. Technol.* **3**, 1700315 (2018).
154. You, R. *et al.* Laser Fabrication of Graphene-Based Flexible Electronics. *Adv. Mater.* **32**, 1901981 (2020).
155. Tavakkoli Gilavan, M., Rahman, M. S., Minhas-Khan, A., Nambi, S. & Grau, G. One-Step Fabrication of Low-Resistance Conductors on 3D-Printed Structures by Laser-Induced Graphene. *ACS Appl. Electron. Mater.* **3**, 3867–3875 (2021).
156. Yazdi, A. Z., Navas, I. O., Abouelmagd, A. & Sundararaj, U. Direct Creation of Highly Conductive Laser-Induced Graphene Nanocomposites from Polymer Blends. *Macromol. Rapid Commun.* **38**, 1700176 (2017).
157. Correia, R. *et al.* Biocompatible Parylene-C Laser-Induced Graphene Electrodes for Microsupercapacitor Applications. *ACS Appl. Mater. Interfaces* **14**, 46427–46438 (2022).
158. Yang, D. *et al.* Multimodal E-Textile Enabled by One-Step Maskless Patterning of Femtosecond-Laser-Induced Graphene on Nonwoven, Knit, and Woven Textiles. *ACS Nano* **17**, 18893–18904 (2023).
159. Wang, G. *et al.* Nomex paper-based double-sided laser-induced graphene for multifunctional

human-machine interfaces. *Carbon N. Y.* **193**, 68–76 (2022).

160. Sun, X., Jin, H. & Qu, W. Lignin-derived 3D porous graphene on carbon cloth for flexible supercapacitors. *RSC Adv.* **11**, 19695–19704 (2021).
161. Stanford, M. G. *et al.* Laser-Induced Graphene Triboelectric Nanogenerators. *ACS Nano* **13**, 7166–7174 (2019).
162. Silvestre, S. L. *et al.* Cork derived laser-induced graphene for sustainable green electronics. *Flex. Print. Electron.* **7**, 035021 (2022).
163. Vaughan, E. *et al.* Sustainable Laser-Induced Graphene Electrochemical Sensors from Natural Cork for Sensitive Tyrosine Detection. *Adv. Sens. Res.* 2300026 (2023) doi:10.1002/adsr.202300026.
164. Zhang, W. *et al.* Lignin Laser Lithography: A Direct-Write Method for Fabricating 3D Graphene Electrodes for Microsupercapacitors. *Adv. Energy Mater.* **8**, 1801840 (2018).
165. Lei, Y., Alshareef, A. H., Zhao, W. & Inal, S. Laser-Scribed Graphene Electrodes Derived from Lignin for Biochemical Sensing. *ACS Appl. Nano Mater.* **3**, 1166–1174 (2020).
166. Mahmood, F., Zhang, H., Lin, J. & Wan, C. Laser-Induced Graphene Derived from Kraft Lignin for Flexible Supercapacitors. *ACS Omega* **5**, 14611–14618 (2020).
167. Yang, S. *et al.* Lignin-derived porous graphene for wearable and ultrasensitive strain sensors. *J. Mater. Chem. C* **10**, 11730–11738 (2022).
168. Edberg, J. *et al.* Laser-induced graphitization of a forest-based ink for use in flexible and printed electronics. *npj Flex. Electron.* **4**, 17 (2020).
169. Park, H., Kim, M., Kim, B. G. & Kim, Y. H. Electronic Functionality Encoded Laser-Induced Graphene for Paper Electronics. *ACS Appl. Nano Mater.* **3**, 6899–6904 (2020).
170. Kulyk, B. *et al.* Laser-Induced Graphene from Paper for Mechanical Sensing. *ACS Appl. Mater. Interfaces* **13**, 10210–10221 (2021).
171. Bezinge, L. *et al.* Paper-Based Laser-Pyrolyzed Electrofluidics: An Electrochemical Platform for Capillary-Driven Diagnostic Bioassays. *Adv. Mater.* 2302893 (2023) doi:10.1002/adma.202302893.
172. Jung, Y. *et al.* Smart paper electronics by laser-induced graphene for biodegradable real-time food spoilage monitoring. *Appl. Mater. Today* **29**, 101589 (2022).
173. Zhao, N. *et al.* Direct Induction of Porous Graphene from Mechanically Strong and Waterproof Biopaper for On-Chip Multifunctional Flexible Electronics. *Small* 2300242 (2023) doi:10.1002/smll.202300242.
174. Shen, L., Zhou, S., Gu, B., Wang, S. & Wang, S. Highly Sensitive Strain Sensor Fabricated by Direct Laser Writing on Lignin Paper with Strain Engineering. *Adv. Eng. Mater.* **25**, 2201882 (2023).
175. Claro, P. I. C. *et al.* Tuning the Electrical Properties of Cellulose Nanocrystals through Laser-Induced Graphitization for UV Photodetectors. *ACS Appl. Nano Mater.* acsanm.1c01453 (2021) doi:10.1021/ACSANM.1C01453.
176. Kulyk, B. *et al.* Conversion of paper and xylan into laser-induced graphene for environmentally friendly sensors. *Diam. Relat. Mater.* **123**, 108855 (2022).
177. Zikulnig, J., Neumaier, L., Lenzhofer, M., Carrara, S. & Kosel, J. Laser-Induced Graphene on Chitosan: An Enabling Technology for Sustainable Resistive Humidity Sensors. *IEEE Sensors Lett.* **2**, 1–4 (2023).
178. Larrigy, C. *et al.* Porous 3D Graphene from Sustainable Materials: Laser Graphitization of Chitosan. *Adv. Mater. Technol.* **8**, 2201228 (2023).
179. Vaughan, E. *et al.* Direct Laser Writing of Chitosan–Borax Composites: Toward Sustainable Electrochemical Sensors. *ACS Sustain. Chem. Eng.* **11**, 13574–13583 (2023).
180. Vićentić, T. *et al.* Laser-induced graphene on cross-linked sodium alginate. *Nanotechnology* (2023) doi:10.1088/1361-6528/ad143a.
181. Miyakoshi, R., Hayashi, S. & Terakawa, M. Direct Patterning of Conductive Structures on Hydrogels by Laser-Based Graphitization for Supercapacitor Fabrication. *Adv. Electron. Mater.* **9**, 2201277 (2023).

182. Zhu, Y., Cai, H., Ding, H., Pan, N. & Wang, X. Fabrication of Low-Cost and Highly Sensitive Graphene-Based Pressure Sensors by Direct Laser Scribing Polydimethylsiloxane. *ACS Appl. Mater. Interfaces* (2019) doi:10.1021/acsami.8b17085.
183. Hayashi, S., Morosawa, F. & Terakawa, M. Laser Direct Writing of Highly Crystalline Graphene on Polydimethylsiloxane for Fingertip-Sized Piezoelectric Sensors. *Adv. Eng. Mater.* **23**, 2100457 (2021).
184. Zaccagnini, P. *et al.* Laser-Induced Graphenization of PDMS as Flexible Electrode for Microsupercapacitors. *Adv. Mater. Interfaces* **8**, 2101046 (2021).
185. Li, Z. *et al.* Preparation of Laser-Induced Graphene Fabric from Silk and Its Application Examples for Flexible Sensor. *Adv. Eng. Mater.* **23**, 2100195 (2021).
186. Li, Y. *et al.* Multifunctional metal–organic frameworks nanoengineered laser-induced graphene for health electronics. *Chem. Eng. J.* **475**, 146330 (2023).
187. Khandelwal, M., Tran, C. Van & In, J. Bin. Nitrogen and phosphorous Co-Doped Laser-Induced Graphene: A High-Performance electrode material for supercapacitor applications. *Appl. Surf. Sci.* **576**, 151714 (2022).
188. Wang, H. *et al.* Laser Writing of Janus Graphene/Kevlar Textile for Intelligent Protective Clothing. *ACS Nano* **14**, 3219–3226 (2020).
189. Kim, Y. J. *et al.* Direct-laser-conversion of Kevlar textile to laser-induced-graphene for realizing fast and flexible fabric strain sensors. *CIRP Ann.* **71**, 473–476 (2022).
190. Chyan, Y. *et al.* Laser-Induced Graphene by Multiple Lasing: Toward Electronics on Cloth, Paper, and Food. *ACS Nano* **12**, 2176–2183 (2018).
191. Meng, Q. *et al.* Sustainable production of benzene from lignin. *Nat. Commun.* **12**, 4534 (2021).
192. Wang, L., Wang, Z., Bakhtiyari, A. N. & Zheng, H. A Comparative Study of Laser-Induced Graphene by CO2 Infrared Laser and 355 nm Ultraviolet (UV) Laser. *Micromachines* **11**, 1094 (2020).
193. Zhang, H. *et al.* Probing laser-induced structural transformation of lignin into few-layer graphene. *Green Chem.* **26**, 5921–5932 (2024).
194. Cogulet, A., Blanchet, P. & Landry, V. Wood degradation under UV irradiation: A lignin characterization. *J. Photochem. Photobiol. B Biol.* **158**, 184–191 (2016).
195. Kawasaki, T. *et al.* Degradation of Lignin by Infrared Free Electron Laser. *Polymers (Basel).* **14**, 2401 (2022).
196. Kawamoto, H. Lignin pyrolysis reactions. *J. Wood Sci.* **63**, 117–132 (2017).
197. Alherech, M. *et al.* From Lignin to Valuable Aromatic Chemicals: Lignin Depolymerization and Monomer Separation via Centrifugal Partition Chromatography. *ACS Cent. Sci.* **7**, 1831–1837 (2021).
198. Zhou, H. *et al.* Polycyclic Aromatic Hydrocarbon Formation from the Pyrolysis/Gasification of Lignin at Different Reaction Conditions. *Energy & Fuels* **28**, 6371–6379 (2014).
199. Wang, X.-Y., Yao, X. & Müllen, K. Polycyclic aromatic hydrocarbons in the graphene era. *Sci. China Chem.* **62**, 1099–1144 (2019).
200. Wan, Z., Nguyen, N.-T., Gao, Y. & Li, Q. Laser induced graphene for biosensors. *Sustain. Mater. Technol.* **25**, e00205 (2020).
201. Wiedemeier, D. B. *et al.* Aromaticity and degree of aromatic condensation of char. *Org. Geochem.* **78**, 135–143 (2015).
202. Zhang, C., Xie, Y., Zhang, C. & Lin, J. Upgrading coal to multifunctional graphene-based materials by direct laser scribing. *Carbon N. Y.* **153**, 585–591 (2019).
203. Zang, X. *et al.* Laser-engineered heavy hydrocarbons: Old materials with new opportunities. *Sci. Adv.* **6**, 1–10 (2020).
204. Zang, X., Ferralis, N. & Grossman, J. C. Electronic, Structural, and Magnetic Upgrading of Coal-Based Products through Laser Annealing. *ACS Nano* **16**, 2101–2109 (2022).
205. Le, T. D. *et al.* Green Flexible Graphene–Inorganic-Hybrid Micro-Supercapacitors Made of Fallen Leaves Enabled by Ultrafast Laser Pulses. *Adv. Funct. Mater.* 2107768 (2021)

doi:10.1002/adfm.202107768.

206. Lei, Y. *et al.* Three-Dimensional Ti 3 C 2 T x MXene-Prussian Blue Hybrid Microsupercapacitors by Water Lift-Off Lithography. *ACS Nano* acsnano.1c06552 (2022) doi:10.1021/acsnano.1c06552.
207. Sun, X., Liu, X. & Li, F. Sulfur-doped laser-induced graphene derived from polyethersulfone and lignin hybrid for all-solid-state supercapacitor. *Appl. Surf. Sci.* **551**, 149438 (2021).
208. Funayama, R., Hayashi, S. & Terakawa, M. Laser-Induced Graphitization of Lignin/PLLA Composite Sheets for Biodegradable Triboelectric Nanogenerators. *ACS Sustain. Chem. Eng.* **11**, 3114–3122 (2023).
209. Mahmood, F. *et al.* Transforming lignin into porous graphene via direct laser writing for solid-state supercapacitors. *RSC Adv.* **9**, 22713–22720 (2019).
210. Yuan, M. *et al.* Smart wearable band-aid integrated with high-performance micro-supercapacitor, humidity and pressure sensor for multifunctional monitoring. *Chem. Eng. J.* **453**, 139898 (2023).
211. Yuan, M. *et al.* Laser direct writing O/N/S Co-doped hierarchically porous graphene on carboxymethyl chitosan/lignin-reinforced wood for boosted microsupercapacitor. *Carbon N. Y.* **202**, 296–304 (2023).
212. Wohlert, M. *et al.* Cellulose and the role of hydrogen bonds: not in charge of everything. *Cellulose* **29**, 1–23 (2022).
213. Bajpai, P. Wood and Fiber Fundamentals. in *Biermann's Handbook of Pulp and Paper* 19–74 (Elsevier, 2018). doi:10.1016/B978-0-12-814240-0.00002-1.
214. Ye, R. *et al.* Laser-Induced Graphene Formation on Wood. *Adv. Mater.* **29**, 1702211 (2017).
215. Claro, P. I. C. *et al.* Tuning the Electrical Properties of Cellulose Nanocrystals through Laser-Induced Graphitization for UV Photodetectors. *ACS Appl. Nano Mater.* **4**, 8262–8272 (2021).
216. Yao, Y. *et al.* One-step process for direct laser writing carbonization of NH4H2PO4 treated cellulose paper and its use for facile fabrication of multifunctional force sensors with corrugated structures. *Cellulose* **26**, 7423–7435 (2019).
217. Nine, M. J., Tran, D. N. H., Tung, T. T., Kabiri, S. & Losic, D. Graphene-Borate as an Efficient Fire Retardant for Cellulosic Materials with Multiple and Synergetic Modes of Action. *ACS Appl. Mater. Interfaces* **9**, 10160–10168 (2017).
218. Nagieb, Z. A., Nassar, M. A. & El-Meligy, M. G. Effect of Addition of Boric Acid and Borax on Fire-Retardant and Mechanical Properties of Urea Formaldehyde Saw Dust Composites. *Int. J. Carbohydr. Chem.* **2011**, 1–6 (2011).
219. Chyan, Y., Cohen, J., Wang, W., Zhang, C. & Tour, J. M. Graphene Art. *ACS Appl. Nano Mater.* **2**, 3007–3011 (2019).
220. Kolar, J., Strlic, M., Pentzien, S. & Kautek, W. Near-UV, visible and IR pulsed laser light interaction with cellulose. *Appl. Phys. A* **71**, 87–90 (2000).
221. Clark, K. M. *et al.* Fluorescent patterning of paper through laser engraving. *Soft Matter* **16**, 7659–7666 (2020).
222. Xin, S. *et al.* Chemical structure evolution of char during the pyrolysis of cellulose. *J. Anal. Appl. Pyrolysis* **116**, 263–271 (2015).
223. Zhou, X., Li, W., Mabon, R. & Broadbelt, L. J. A Critical Review on Hemicellulose Pyrolysis. *Energy Technol.* **5**, 52–79 (2017).
224. Cheng, F. & Li, X. Preparation and Application of Biochar-Based Catalysts for Biofuel Production. *Catalysts* **8**, 346 (2018).
225. McGrath, T. E., Chan, W. G. & Hajaligol, M. R. Low temperature mechanism for the formation of polycyclic aromatic hydrocarbons from the pyrolysis of cellulose. *J. Anal. Appl. Pyrolysis* **66**, 51–70 (2003).
226. Yang, Y., Luo, Z., Li, S., Lu, K. & Wang, W. Catalytic pyrolysis of hemicellulose to produce aromatic hydrocarbons. *BioResources* **14**, 5816–5831 (2019).
227. Hidalgo-Carrillo, J., Marinas, A. & Urbano, F. J. Chemistry of Furfural and Furanic Derivatives. in *Furfural: An Entry Point of Lignocellulose in Biorefineries to Produce Renewable Chemicals,*

Polymers, and Biofuels 1–30 (World Scientific Publishing Co., 2018). doi:10.1142/9781786344878_0001.

228. Yang, H. *et al.* Cellulose Pyrolysis Mechanism Based on Functional Group Evolutions by Two-Dimensional Perturbation Correlation Infrared Spectroscopy. *Energy and Fuels* **34**, 3412–3421 (2020).
229. Park, H., Kim, M., Kim, B. G. & Kim, Y. H. Electronic Functionality Encoded Laser-Induced Graphene for Paper Electronics. *ACS Appl. Nano Mater.* **3**, 6899–6904 (2020).
230. Fortunato, E. *et al.* High-Performance Flexible Hybrid Field-Effect Transistors Based on Cellulose Fiber Paper. *IEEE Electron Device Lett.* **29**, 988–990 (2008).
231. Pereira, L. *et al.* The influence of fibril composition and dimension on the performance of paper gated oxide transistors. *Nanotechnology* **25**, 094007 (2014).
232. Martins, R. *et al.* Write-erase and read paper memory transistor. *Appl. Phys. Lett.* **93**, 203501 (2008).
233. Ferreira, I. *et al.* Self-Rechargeable Paper Thin-Film Batteries : Performance and Applications. *J. Disp. Technol.* **6**, 332–335 (2010).
234. Nathan, A. *et al.* Complementary Metal Oxide Semiconductor Technology With and On Paper. *Adv. Mater.* **23**, 4491–4496 (2011).
235. Gaspar, D. *et al.* Planar Dual-Gate Paper/Oxide Field Effect Transistors as Universal Logic Gates. *Adv. Electron. Mater.* **4**, 1–8 (2018).
236. Khan, S. M., Nassar, J. M. & Hussain, M. M. Paper as a Substrate and an Active Material in Paper Electronics. *ACS Appl. Electron. Mater.* **3**, 30–52 (2021).
237. Shen, J., Song, Z., Qian, X. & Ni, Y. A review on use of fillers in cellulosic paper for functional applications. *Ind. Eng. Chem. Res.* **50**, 661–666 (2011).
238. Niskanen, K. *Mechanics of paper products*. (Walter de Gruyter, 2011).
239. Chyan, Y., Cohen, J., Wang, W., Zhang, C. & Tour, J. M. Graphene Art. *ACS Appl. Nano Mater.* **2**, 3007–3011 (2019).
240. Reynolds, M. *et al.* Laser-engraved ammonia sensor integrating a natural deep eutectic solvent. *Microchem. J.* **157**, 105067 (2020).
241. Žemgulytė, J. *et al.* Effects of different manufacturing techniques on the performance of planar antennas. *Sci. Rep.* **13**, 22510 (2023).
242. Clement, B. *et al.* Recent Advances in Printed Thin-Film Batteries. *Engineering* **13**, 238–261 (2022).
243. Li, H. & Liang, J. Recent Development of Printed Micro-Supercapacitors: Printable Materials, Printing Technologies, and Perspectives. *Adv. Mater.* **32**, 1805864 (2020).
244. Delipinar, T., Shafique, A., Gohar, M. S. & Yapici, M. K. Fabrication and Materials Integration of Flexible Humidity Sensors for Emerging Applications. *ACS Omega* **6**, 8744–8753 (2021).
245. Singh, K. *et al.* Significance of nano-materials, designs consideration and fabrication techniques on performances of strain sensors - A review. *Mater. Sci. Semicond. Process.* **123**, 105581 (2021).
246. Jeroish, Z. E., Bhuvaneshwari, K. S., Samsuri, F. & Narayanamurthy, V. Microheater: material, design, fabrication, temperature control, and applications—a role in COVID-19. *Biomed. Microdevices* **24**, 3 (2022).
247. Saputra, H. A. Electrochemical sensors: basic principles, engineering, and state of the art. *Monatshefte fur Chemie* **154**, 1083–1100 (2023).
248. Kotlowski, C. *et al.* Electronic biosensing with flexible organic transistor devices. *Flex. Print. Electron.* **3**, 034003 (2018).
249. Li, Z. *et al.* Advances of Drugs Electroanalysis Based on Direct Electrochemical Redox on Electrodes: A Review. *Crit. Rev. Anal. Chem.* **54**, 269–314 (2024).
250. Sumitha, M. S. & Xavier, T. S. Recent advances in electrochemical biosensors – A brief review. *Hybrid Adv.* **2**, 100023 (2023).
251. Mou, J., Ding, J. & Qin, W. Modern Potentiometric Biosensing Based on Non-Equilibrium Measurement Techniques. *Chem. – A Eur. J.* **29**, e202302647 (2023).

252. Gupta, U., Gupta, V., Arun, R. K. & Chanda, N. Recent advances in enzymatic biosensors for point-of-care detection of biomolecules. *Biotechnol. Bioeng.* **119**, 3393–3407 (2022).
253. Bahadır, E. B. & Sezgintürk, M. K. A review on impedimetric biosensors. *Artif. Cells, Nanomedicine, Biotechnol.* **44**, 248–262 (2016).
254. Leva-Bueno, J., Peyman, S. A. & Millner, P. A. A review on impedimetric immunosensors for pathogen and biomarker detection. *Med. Microbiol. Immunol.* **209**, 343–362 (2020).
255. Shah, N. S. *et al.* Picomolar or beyond Limit of Detection Using Molecularly Imprinted Polymer-Based Electrochemical Sensors: A Review. *Biosensors* **12**, 1107 (2022).
256. J., M., D., D. & R., A. R. Review—Current Trends in Disposable Graphene-Based Printed Electrode for Electrochemical Biosensors. *J. Electrochem. Soc.* **167**, 067523 (2020).
257. Zhu, B., Li, X., Zhou, L. & Su, B. An Overview of Wearable and Implantable Electrochemical Glucose Sensors. *Electroanalysis* (2021) doi:10.1002/ELAN.202100273.
258. Zheng, Z., Zhu, R., Peng, I., Xu, Z. & Jiang, Y. Wearable and implantable biosensors: mechanisms and applications in closed-loop therapeutic systems. *J. Mater. Chem. B* (2024) doi:10.1039/D4TB00782D.
259. Wu, J., Liu, H., Chen, W., Ma, B. & Ju, H. Device integration of electrochemical biosensors. *Nat. Rev. Bioeng.* **1**, 346–360 (2023).
260. Baracu, A. M. & Dinu Gugoasa, L. A. Review—Recent Advances in Microfabrication, Design and Applications of Amperometric Sensors and Biosensors. *J. Electrochem. Soc.* **168**, 037503 (2021).
261. Lahcen, A. A. *et al.* Electrochemical sensors and biosensors using laser-derived graphene: A comprehensive review. *Biosens. Bioelectron.* **168**, 112565 (2020).
262. Kang, S. J. & Pak, J. J. Synthesis of Laser-Induced Cobalt Oxide for Non-Enzymatic Electrochemical Glucose Sensors. *ChemElectroChem* **9**, e202200328 (2022).
263. Luo, Y. *et al.* Technology Roadmap for Flexible Sensors. *ACS Nano* **17**, 5211–5295 (2023).
264. Niknejad, N., Ismail, W. B., Mardani, A., Liao, H. & Ghani, I. A comprehensive overview of smart wearables: The state of the art literature, recent advances, and future challenges. *Eng. Appl. Artif. Intell.* **90**, 103529 (2020).
265. Shi, Y., Zhang, Z., Huang, Q., Lin, Y. & Zheng, Z. Wearable sweat biosensors on textiles for health monitoring. *J. Semicond.* **44**, 021601 (2023).
266. Zhu, X., Liu, W., Shuang, S., Nair, M. & Li, C.-Z. Intelligent tattoos, patches, and other wearable biosensors. in *Medical Biosensors for Point of Care (POC) Applications* 133–150 (Elsevier, 2017). doi:10.1016/B978-0-08-100072-4.00006-X.
267. Wang, Z. *et al.* An artificial intelligence-assisted microfluidic colorimetric wearable sensor system for monitoring of key tear biomarkers. *npj Flex. Electron.* **8**, 35 (2024).
268. Swetha, P., Balijapalli, U. & Feng, S.-P. Wireless accessing of salivary biomarkers based wearable electrochemical sensors: A mini-review. *Electrochem. commun.* **140**, 107314 (2022).
269. Heikenfeld, J. Non-invasive Analyte Access and Sensing through Eccrine Sweat: Challenges and Outlook circa 2016. *Electroanalysis* **28**, 1242–1249 (2016).
270. Childs, A. *et al.* Diving into Sweat: Advances, Challenges, and Future Directions in Wearable Sweat Sensing. *ACS Nano* **18**, 24605–24616 (2024).
271. Baker, L. B. & Wolfe, A. S. Physiological mechanisms determining eccrine sweat composition. *Eur. J. Appl. Physiol.* **120**, 719–752 (2020).
272. Gao, W. *et al.* Fully integrated wearable sensor arrays for multiplexed in situ perspiration analysis. *Nature* **529**, 509–514 (2016).
273. Choi, J., Ghaffari, R., Baker, L. B. & Rogers, J. A. Skin-interfaced systems for sweat collection and analytics. *Sci. Adv.* **4**, (2018).
274. Koh, A. *et al.* A soft, wearable microfluidic device for the capture, storage, and colorimetric sensing of sweat. *Sci. Transl. Med.* **8**, 366ra165-366ra165 (2016).
275. Yang, Y. *et al.* A laser-engraved wearable sensor for sensitive detection of uric acid and tyrosine in sweat. *Nat. Biotechnol.* **38**, 217–224 (2020).

276. Baker, L. B. Sweating Rate and Sweat Sodium Concentration in Athletes: A Review of Methodology and Intra/Interindividual Variability. *Sport. Med.* **47**, 111–128 (2017).
277. Priya, B., Rashmi, T. & Bozena, M. Transdermal iontophoresis. *Expert Opin. Drug Deliv.* **3**, 127–138 (2006).
278. Simmers, P., Li, S. K., Kasting, G. & Heikenfeld, J. Prolonged and localized sweat stimulation by iontophoretic delivery of the slowly-metabolized cholinergic agent carbachol. *J. Dermatol. Sci.* **89**, 40–51 (2018).
279. Emaminejad, S. *et al.* Autonomous sweat extraction and analysis applied to cystic fibrosis and glucose monitoring using a fully integrated wearable platform. *Proc. Natl. Acad. Sci. U. S. A.* **114**, 4625–4630 (2017).
280. Webster, H. L. & Rundell, C. A. Laboratory Diagnosis of Cystic Fibrosis. *CRC Crit. Rev. Clin. Lab. Sci.* **18**, 313–338 (1982).
281. Huang, J., Zhang, Y. & Wu, J. Review of non-invasive continuous glucose monitoring based on impedance spectroscopy. *Sensors Actuators A Phys.* **311**, 112103 (2020).
282. Rao, G. *et al.* Reverse Iontophoresis: Noninvasive Glucose Monitoring in Vivo in Humans. *Pharm. Res. An Off. J. Am. Assoc. Pharm. Sci.* **12**, 1869–1873 (1995).
283. Bolat, G. *et al.* Wearable soft electrochemical microfluidic device integrated with iontophoresis for sweat biosensing. *Anal. Bioanal. Chem.* **414**, 5411–5421 (2022).
284. Hauke, A. *et al.* Complete validation of a continuous and blood-correlated sweat biosensing device with integrated sweat stimulation. *Lab Chip* **18**, 3750–3759 (2018).
285. Wang, M. *et al.* A wearable electrochemical biosensor for the monitoring of metabolites and nutrients. *Nat. Biomed. Eng.* **6**, 1225–1235 (2022).
286. Tu, J. *et al.* A wireless patch for the monitoring of C-reactive protein in sweat. *Nat. Biomed. Eng.* **7**, 1293–1306 (2023).
287. Torrente-Rodríguez, R. M. *et al.* Investigation of Cortisol Dynamics in Human Sweat Using a Graphene-Based Wireless mHealth System. *Matter* **2**, 1–17 (2020).
288. Torrente-Rodríguez, R. M. *et al.* SARS-CoV-2 RapidPlex: A Graphene-Based Multiplexed Telemedicine Platform for Rapid and Low-Cost COVID-19 Diagnosis and Monitoring. *Matter* **3**, 1981–1998 (2020).
289. Won, D. *et al.* Digital selective transformation and patterning of highly conductive hydrogel bioelectronics by laser-induced phase separation. *Sci. Adv.* **8**, 3209 (2022).
290. Nair, V. *et al.* Laser writing of nitrogen-doped silicon carbide for biological modulation. *Sci. Adv.* **6**, (2020).
291. Xu, K. *et al.* Toward Integrated Multifunctional Laser-Induced Graphene-Based Skin-Like Flexible Sensor Systems. *ACS Nano* (2024) doi:10.1021/acsnano.4c09062.
292. Lamberti, A., Clerici, F., Fontana, M. & Scaltrito, L. A Highly Stretchable Supercapacitor Using Laser-Induced Graphene Electrodes onto Elastomeric Substrate. *Adv. Energy Mater.* **6**, 1600050 (2016).
293. Rahimi, R., Ochoa, M., Yu, W. & Ziaie, B. Highly Stretchable and Sensitive Unidirectional Strain Sensor via Laser Carbonization. *ACS Appl. Mater. Interfaces* **7**, 4463–4470 (2015).
294. Huang, L. *et al.* Wearable Flexible Strain Sensor Based on Three-Dimensional Wavy Laser-Induced Graphene and Silicone Rubber. *Sensors* **20**, 4266 (2020).
295. Wang, W. *et al.* Fingerprint-Inspired Strain Sensor with Balanced Sensitivity and Strain Range Using Laser-Induced Graphene. *ACS Appl. Mater. Interfaces* **14**, 1315–1325 (2022).
296. Rahimi, R. *et al.* Highly Stretchable Potentiometric pH Sensor Fabricated via Laser Carbonization and Machining of Carbon-Polyaniline Composite. *ACS Appl. Mater. Interfaces* **9**, 9015–9023 (2017).
297. Sun, B. *et al.* Gas-Permeable, Multifunctional On-Skin Electronics Based on Laser-Induced Porous Graphene and Sugar-Templated Elastomer Sponges. *Adv. Mater.* **30**, 1804327 (2018).
298. Zhang, S. *et al.* On-skin ultrathin and stretchable multifunctional sensor for smart healthcare

wearables. *npj Flex. Electron.* **6**, 11 (2022).

299. Dallinger, A., Keller, K., Fitzek, H. & Greco, F. Stretchable and Skin-Conformable Conductors Based on Polyurethane/Laser-Induced Graphene. *ACS Appl. Mater. Interfaces* **12**, 19855–19865 (2020).
300. Xu, J. *et al.* Electrooculography and Tactile Perception Collaborative Interface for 3D Human–Machine Interaction. *ACS Nano* **16**, 6687–6699 (2022).
301. Lu, Y. *et al.* Stretchable graphene–hydrogel interfaces for wearable and implantable bioelectronics. *Nat. Electron.* **7**, 51–65 (2023).
302. Zhao, L. *et al.* Robust, stretchable bioelectronic interfaces for cardiac pacing enabled by interfacial transfer of laser-induced graphene via water-response, nonswellable PVA gels. *Biosens. Bioelectron.* **261**, 116453 (2024).
303. Lu, Y. *et al.* Machine Learning-Enabled Tactile Sensor Design for Dynamic Touch Decoding. *Adv. Sci.* **10**, 2303949 (2023).
304. Pinilla, S., Coelho, J., Li, K., Liu, J. & Nicolosi, V. Two-dimensional material inks. *Nat. Rev. Mater. 2022 79* **7**, 717–735 (2022).
305. Torricelli, F. *et al.* Green Materials and Technologies for Sustainable Organic Transistors. *Adv. Mater. Technol.* **7**, 2100445 (2022).
306. Gao, D., Lv, J. & Lee, P. S. Natural Polymer in Soft Electronics: Opportunities, Challenges, and Future Prospects. *Adv. Mater.* **34**, 2105020 (2022).
307. Tarazona, N. A. *et al.* Opportunities and challenges for integrating the development of sustainable polymer materials within an international circular (bio)economy concept. *MRS Energy Sustain.* **9**, 28–34 (2022).
308. Zhu, H. *et al.* Wood-Derived Materials for Green Electronics, Biological Devices, and Energy Applications. *Chem. Rev.* **116**, 9305–9374 (2016).
309. Lv, H., Pan, Q., Song, Y., Liu, X.-X. & Liu, T. A Review on Nano-/Microstructured Materials Constructed by Electrochemical Technologies for Supercapacitors. *Nano-Micro Lett.* **12**, 118 (2020).
310. Kwon, S. G., Kang, J., Back, S. & Kang, B. Rapid Electronic Interconnection across the Glass Boundary Edge for Sustainable and Lean Electronics Manufacturing. *ACS Sustain. Chem. Eng.* **8**, 11348–11357 (2020).
311. Geladari, O. *et al.* Nanometer Sized Direct Laser-Induced Gold Printing for Precise 2D-Electronic Device Fabrication. *Small Methods* **7**, 2201221 (2023).

3

LASER-INDUCED GRAPHENE PLANAR ELECTRODES FOR ELECTROCHEMICAL SENSING

Laser irradiation to induce networks of graphene-based structures towards cost effective, flexible device fabrication has been a highly pursued area, with applications in various polymeric substrates. In this work, we report the application of this approach towards commonly available, eco-friendly, low-cost substrates, namely chromatographic and office papers. Through an appropriate chemical treatment with sodium tetraborate as a fire-retardant agent, photothermal conversion to porous laser-induced graphene (LIG) on paper was achieved. Raman peaks were identified, with I_{2D}/I_G and I_D/I_G peak ratios of 0.616 ± 0.095 and 1.281 ± 0.173, showing the formation of multi-layered graphitic material, exhibiting sheet resistances as low as 56.0 $\Omega.sq^{-1}$. Co-planar, LIG-based, three-electrode systems (working, counter and reference electrodes) were produced and characterized, showing high current faradaic oxidation and reduction peaks, translating in high electrochemical active area, doubling the geometric area. Good electron transfer kinetics performed exclusively with on-chip measurements were reached, with k_0 values as high as 7.15×10^{-4} $cm.s^{-1}$. Proof-of-concept, amperometric, enzymatic glucose biosensors were developed, exhibiting good analytical performance in physiologically relevant glucose levels, with results pointing to the applicability of paper-based LIG towards efficient, disposable electrochemical sensor development, increasing their sustainability and accessibility, while simplifying their production and reducing their cost.

Keywords: laser-induced graphene, cellulose, paper substrates, fire-retardant agents, electrochemical sensors, glucose

The literature presented in this chapter is published in:

- Pinheiro, T., Silvestre, S., Coelho, J., Marques, A. C., Martins, R., Sales, M. G. F., & Fortunato, E. (2021). Laser-induced graphene on paper toward efficient fabrication of flexible, planar electrodes for electrochemical sensing. *Advanced Materials Interfaces*, 8(22), 2101502.

3.1 Introduction

Biosensors are currently one of the most pursued fields of research, with several applications finding important use in our society, from food to environmental monitoring [1,2], forensics [3,4] and healthcare [5] , by introducing devices with little complexity, low cost of production, easy operation and higher user friendliness [6,7]. Biosensors mostly distinguish themselves through their detection methodologies, where electrochemical ones stand out, due to their high analytical performance in terms of sensitivity, selectivity and response time, paired with low-cost and portability [8,9], being highly recognized by several decades of advances in glucometers [10].

For electrochemical biosensor production, the use of lithography or screen-printed electrodes (SPEs) prevails, due to advantages regarding their sensitivity in small currents (picoamperes to nanoamperes), reduced ohmic loss in electric potential, low response times to variations in applied potential and other analytical advantages, including small sample volume requirements [11]. The use of easily available and low-cost carbon-based materials for their production, such as graphene, carbon nanotubes and other carbon nanostructures, has transformed biosensor development, further improving the analytical characteristics of these systems, due to their exceptional electron transfer capability and high surface-to-volume ratio [12–14]. However, devices produced with these technologies need intricate and time-consuming manufacturing processes, making them harder to develop and increasing their overall cost. Furthermore, they are less flexible for exploring different device architectures or multifunctional platform development, raising the need for alternative microfabrication techniques [15].

Since the first report on the production of porous graphene films from polymeric substrates through laser irradiation, introduced by Tour and co-workers [16], new systems based on this laser-induced graphene (LIG) have been developed and reported. Most commonly, the use of polyimide tapes and films for photothermal conversion of the polymer into a three-dimensional, porous graphene structure has been employed for the production of a myriad of applications [17], ranging from chemical and physical biosensors [18–21], UV sensors [22], energy storage devices [23,24] to paper electronics [25], offering a mask-less, high-resolution, scalable and inexpensive approach for carbon-based electrode development. Using this method for graphene production, graphitic structures with tailored properties can be synthesized, based on the native polymeric substrate, from synthetic polymers such as PI or polysulfones [26] to natural materials such as wood [27], paper and coal [28] and on experimental laser conditions being applied [16], maintaining most of the advantages offered by conventionally fabricated electrodes. Furthermore, it introduces the possibility of easily exploring different electrode configurations, with different system architectures in terms of electrode size and their disposition in the substrate, readily fabricated in a single-step approach in the same support material. Moreover, the applicability that has been proven in laser-enabled techniques for LIG production in flexible substrates such as PI and paper, has given the possibility to apply these approaches in flexible electronics. Besides the direct synthesis of materials in which LIG is included, other laser-based approaches for substrate microprocessing [29] and surface treatment are achievable, in an abundant list of materials, including polymers [30], graphene [31] or metallic surfaces and nanoparticles [32], for patterning and fabrication of active electronic elements and to potentiate the electric and conductive properties of many materials. Powered by these laser processing techniques, LIG has shown promising properties to complement such approaches, as well as conventional printing techniques, including screen-printing[33] and inkjet printing [34], to develop active elements in flexible electronics for application in bioelectronic systems, such as conductive films [35], supercapacitors [36] and biofuel cells [37] that can be integrated with biosensors for comprehensive, multifunctional, self-sustainable applications.

In this work, we show the versatility of laser irradiation technique for three-electrode system development for use as electrochemical biosensors, using cellulosic substrates such as chromatography and commercial office paper. The development of paper-based electrochemical analytical devices has risen in previous years, [38] due to the advantageous properties of paper as an abundant, low-cost, flexible and easily disposable material, with improved sustainability, being commercialized in various engineered forms that present multiple properties in terms of porosity, thickness or the presence of additives [39]. The production of LIG using various cellulosic substrates has been previously presented. Because of inherent mechanical and chemical properties, some higher grammage papers (e.g. paperboard)[40] or paper composites (e.g. phenolic paper)[41], have been readily employed for graphitization through laser irradiation and subsequent application as electrochemical sensors. However, other more common, commercial and easily available cellulosic substrates have impediments for direct application for laser scribing. These substrates, such as kraft, chromatography or standard office papers, do not withstand the power of laser cutters used to induce graphitization in other polymeric substrates, because they mainly consist of cellulose, not directly converting to LIG, but to amorphous carbon materials such as char. [42] To reduce the thermal degradation and ablation usually observed when these substrates are submitted to laser irradiation and allow for direct conversion to graphene, fire-retardant chemical treatments have been proposed for application in these substrates, using specific chemicals such as commercial, phosphate-based fire-retardants [25,42] and boron derivatives, such as boric acid [42] and sodium tetraborate (Borax). [43] More specifically, these boron-based, inorganic metal-hydrate chemicals, such as Borax, have been extensively explored, to mitigate thermal degradation of natural fibers such as cellulose [44], while acting as chemical heat sinks during laser induced combustion, because they undergo endothermic decomposition processes that can prevent ignition of the substrate [45]. Adaptation of these approaches opens the possibility for new LIG precursor materials to be used and manipulated for graphene-based material synthesis, where eco-friendly, abundant and lower-cost paper substrates present themselves as ideal solutions for more accessible device development, that may take part in meeting the goals proposed by the UN for sustainable development, using more responsible and sustainable production methods and reducing waste, by creating new functionalities for mundane paper substrates. [46]

In this scope, we present, for the first time, the application of such approaches towards the fabrication of co-planar, three-electrode systems for electrochemical sensor development using such paper substrates. By manipulation of laser operation parameters for LIG synthesis optimization and its subsequent characterization in terms of morphology, surface chemistry and electric properties, high-throughput, easily adaptable, disposable electrochemical sensors were fabricated and characterized in terms of their electrochemical capabilities, for simple, enzymatic, amperometric glucose sensor development, resulting in a novel approach for electrochemical sensor development using more sustainable, less-costly materials and fabrication techniques, with potential for application in bioelectronics and wearable devices.

3.2 Experimental Section

Reagents and materials

During this work, ultrapure Milli-Q water laboratory grade (conductivity < 0.1 µS cm^{-1}) was used to prepare all solutions. Sodium tetraborate decahydrate, potassium chloride, phosphate buffered saline (PBS), Glucose oxidase (GOx) from *Aspergillus niger*, horseradish peroxidase (HRP), D-trehalose, D-glucose, ascorbic acid, fructose, bovine serum albumin (BSA) and uric acid were purchased from Sigma**,** potassium hexacyanoferrate (III) ($K_3[Fe(CN)_6]$) and potassium hexacyanoferrate (II) trihydrate ($K_4[Fe(CN)_6] \cdot 3H_2O$) were purchased from Roth. All reagents were used as received, without further purification. Whatman chromatography paper grade 1 (Whatman International Ltd., Floram Park, NJ, USA) and commercial office paper (Xerox Colotech+ 220 g m^{-2}) were used for laser irradiation and LIG formation.

LIG synthesis on paper

Firstly, paper sheets of each paper type were cut into A5 standard size (148x210 mm) and chemically treated as previously described,[43] by soaking the paper sheets in sodium borate solution (0.1 mol.L^{-1}) for 10 minutes and subsequently allowing them to dry at room temperature, overnight. After this treatment, the paper sheets were submitted to wax printing, using a Xerox ColorCube wax printer, followed by heating of the paper sheet at 120 °C for 2 minutes, with the purpose of inducing hydrophobicity through its volume. For LIG formation at the paper substrates, a computer-controlled CO_2 laser cutting machine (VLS 3.50, Universal Laser Systems), with a 10.6 μm wavelength, beam diameter of 0.127 mm was used. By varying laser parameters, more specifically laser power and laser scan speed, the effect of the laser towards the paper substrates was assessed, in terms of its ability to produce LIG, in opposition to ablation of paper fibers or no LIG formation.

Paper-based LIG characterization

LIG formed in the paper substrates was characterized by SEM (Hitachi TM 3030Plus Tabletop) to have a visual image of three-dimensional LIG networks. Electrical sheet resistance (R_{sh}, Ω.sq^{-1}) was determined by measurements in Van der Pauw geometry (5x5 mm square architecture, with 1 mm circular silver conductive ink contacts at each corner) with a Biorad HL 5500 four-point probe equipment. These measurements were performed in triplicates for all LIG samples. Raman measurements were made with a Renishaw® inVia™ Qontor® confocal Raman microscope (Gloucestershire, UK) equipped with a Renishaw Centrus 2957T3 detector. The laser beam was focused through a 50x Olympus objective lens. Measurements were performed with a 633 nm laser with 10 s exposure time and 3 accumulations as measurement parameters, with a laser power of 16 mW. Ten measurements were performed in each sample, in pre-determined areas of the LIG film area. X-ray photoelectron spectroscopy (XPS, Kratos Axis Supra, UK) equipped with a monochromated Al Kα radiation (1486.6 eV).

Paper-based LIG electrochemical sensor production

For paper-based LIG electrochemical sensor fabrication, a vector image software (Adobe Illustrator, Adobe Systems software, Ireland) was used to design three-electrode systems comprised of a working electrode (WE) with 4 mm in diameter, counter electrode (CE) and reference electrode (RE), engraved using the optimized laser parameters. Following engraving, the devices were encapsulated in plastic sheets incorporated with an adhesive tape mask, using a commercial laminator. These sheets were previously cut, using the same CO_2 laser machine, to have an open area for electrodes and conductive tracks. Lastly, silver conductive ink (AG-510 silver ink, surface resistivity: <0015 Ω/square/mil, Conductive Compounds, Inc., Hudson, NH) was used to establish conductive tracks and Ag/AgCl ink (AGCL-675, Conductive Compounds, Inc., Hudson, NH) was used to pattern the RE, followed by a curing process in a hot plate (50 °C, 1 hour) and removal of the adhesive mask.

For unmediated enzymatic glucose sensing, the WEs were modified by drop-casting 10 μL of a solution containing GOx (3 $mg.mL^{-1}$), peroxidase (6.5 $mg.mL^{-1}$) and D-trehalose (113 mg. mL^{-1}, to stabilize enzymes and their activity [47]) in its surface, followed by drying overnight at 4 °C. For mediated glucose biosensors, the WEs were modified by drop-casting a mixture of GOx and potassium ferricyanide as the mediator, at different concentrations. For miniaturized test strips, a double-sided adhesive and a glass fiber absorbent membrane were laser cut and placed over the working area of the test strip, as sample uptake layer. Waxed paper was also laser cut with a sample entrance for the introduction and wicking of samples and attached to the sample uptake layer, to finalize the test strip construction.

Electrochemical characterization

Sensors were submitted to electrochemical characterization, to determine experimental parameters and draw a comparison between LIG sensors produced using the paper substrates under study. Electrochemical measurements were performed using PalmSens 4.0 Potentiostat (PalmSens Compact Electrochemical Interfaces). Prior to characterization, an electrochemical pre-treatment step was performed on the electrodes, as previously described, [48] by CV scanning a potential window from -2 to 2 V at a scan rate of 100 mV s^{-1}, using the supporting electrolyte (0.1 $mmol.L^{-1}$ KCl). After pre-treatment, electrochemical systems were left to dry in air. CV assays were carried with a potential window from -0.3 to 0.7 V, at scan rates from 10 to 150 $mV.s^{-1}$. EIS was carried with a pulse of 5 mV in amplitude, 50 data points, over a frequency range from 10.000 to 0.1 Hz. The electrochemical measurements both by CV and EIS were performed using a redox probe solution of 5.0 $mmol.L^{-1}$ $[Fe(CN)_6]^{3-}$ and $[Fe(CN)_6]^{4-}$, prepared in the supporting electrolyte. To measure the response of unmediated glucose sensors towards the presence of glucose, the amperometric response of the sensors towards solutions with different glucose content (0.5 to 15 mM in PBS) was followed by chronoamperometry, using an applied potential of 1 V. Continuous measurements were carried by applying 50 μL of testing solution to the working area of the electrode, while carrying a single chronoamperometry measurement at 1 V applied potential. Every 100 seconds, 25 µL were extracted and 25 µL solution of glucose with double the testing concentration was added to monitor the current increases with increasing addition of glucose. Testing of selectivity for un-mediated enzymatic system was carried out using the same method, to monitor current changes and the influence of ascorbic acid (0.1 mM), uric acid (0.1 mM) and fructose (1 mM). For the mediated sensor, chronoamperometry was also employed for signal generation, with different applied voltages depending on sensor construction (0.7 V for regular test strips and 0.3 V for the miniaturized test strips).

3.3 Paper-based LIG Synthesis and Characterization

3.3.1 Laser Parameter Optimization for LIG synthesis

Chemical treatment with sodium borate (0.1 mol.L^{-1} in deionized water) was performed on the paper substrates, as represented in **Figure 3.1a**. This is a crucial step when using these natural polymeric substrates for laser irradiation, since they improve the resistance of fibers to heat accumulation caused by laser, acting as chemical heat sinks, reducing thermal degradation. This effect was verified and shown in Figure A1, where untreated paper suffered complete fiber ablation without conversion to graphitic materials. Following chemical pre-treatment, paper was modified with wax, for impermeabilization of the substrate and further use in electrochemical sensor production, as seen in **Figure 3.1b**. All further characterization and experiments were carried out with wax treated paper substrates. The synthesis of LIG on paper substrate was performed by determining the effects of two different laser parameters, laser power (P) and laser scan speed (S) percentage towards the paper substrates, in terms of the laser ability to induce the production of noticeable graphitic materials. Laser power varied from 3% to 10% of maximum operational value (1.5 to 5 W, respectively), with the same percentages being applied to laser scan speed (38.1 cm.s^{-1} to 127 cm.s^{-1}, respectively).

An 8x8 matrix of S and P coordinates was constructed, to establish which power and speed pairs could be applied for LIG synthesis and characterization. Matrices for chromatography and office paper are presented in **Figure 3.1c-d**. LIG synthesis occurred at a regimen where S and P have similar percentage values or at a low-speed regimen, where laser power is the dominant variable. In this low-speed regimen, power percentages need be restricted, to avoid complete paper ablation or marked alterations to the natural cellulose network. For low power regimen (P coordinate lower than S), there is less effect of the laser over the paper

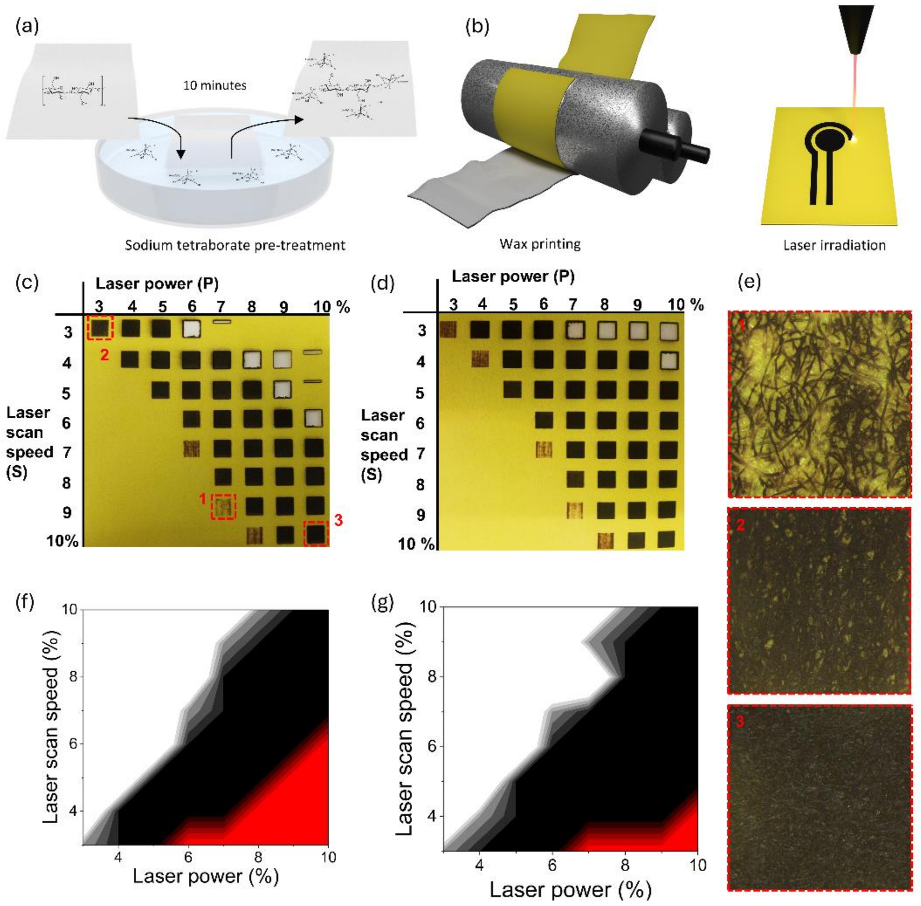

Figure 3.1 - Laser operation parameter optimization conducing towards LIG formation. (a) Chemical treatment imposed to paper substrates, with sodium borate acting as fire-retardant. (b) Wax printing for modification of paper substrates for laser irradiation and LIG synthesis. Matrices of laser operation parameters (P - power, S – scan speed) for chromatography paper (c) and office paper (d). (e) Different LIG coverage areas for three different laser operation coordinates (1- P7S9, 2- P3S3, 3- P10S10). Heatmaps of laser irradiation effect towards chromatography paper (f) and office paper (g), in terms of laser ability to produce LIG, in opposition to paper ablation or absence of conversion.

substrate, leading to mild LIG formation only at superficial paper fibers, as shown in **Figure 3.1e1**. For regimens conducing to LIG, P and S operation coordinates show some differences relating to LIG area coverage. For some coordinates, LIG synthesis is more superficial (**Figure 3.1e2**), in opposition to higher surface coverage (**Figure 3.1e3**), due to laser reaching internal fibers, with more in-depth LIG synthesis, caused by the increase in laser operation coordinates. Heatmaps of laser influence in the paper were constructed, based on the optimization matrices and are shown in **Figures 3.1f-g**. The heatmaps show the laser parameters necessary for LIG synthesis for each paper type. A comparison shows that for office paper, higher power can be used to produce LIG, as this paper presents an increased grammage and the presence of additives, taking a higher laser power to cause complete paper ablation.

3.3.2 Paper-based LIG characterization

Thorough physico-chemical characterization of LIG produced on these paper substrates was performed, to retrieve information about its chemical, electrical and morphological properties. Taking the previously presented matrices as reference, three power and speed coordinates were selected for characterization, to establish a comparative study regarding the effect of increasing laser operation parameters and the properties of the graphitic materials produced from paper-based laser irradiation. The selected conditions were matching power and speed percentages of 6, 8 and 10 %. The reason for this selection was that for lower P and S percentages, LIG did not establish a fully connected network, capable of transporting current and serving as electrodes for electrochemical sensor production. For higher values, the laser would increase the thermal degradation of the formed material or cause ablation of fibers, which ultimately impairs the possibility of using the paper substrate as a sensor, due to leakage of solutions used in sensor operation.

A morphological study of the produced paper based LIG was performed by SEM, to understand the effect of different laser operation conditions towards the surface of cellulose fibers. Results are presented in **Figure 3.2**. Inspection of both paper types showed different fiber architecture of these paper substrates, with chromatography paper presenting much more defined and round fibers, with higher pore size, while office paper presents thinner fibers with lower pore sizes. Furthermore, additives used in office paper fabrication can be clearly identified, with large salt agglomerates of calcium carbonate ($CaCO_3$). When laser modification is imposed, fibers suffer an apparent ablation or decomposition, that is more intense when laser power and speed coordinates are increased. For chromatography paper (**Figure 3.2a-b**), cellulose fibers' structure is preserved, with higher porosity and structural decomposition being induced for higher laser power. For office paper (**Figure 3.2c-d**), the same trend is observed. However, for laser coordinates P10S10, more intense ablation of superficial fibers is observed, with some loss of the natural network structure of the substrate. It is also visible that the laser does not seem to remove the presence of other materials in this paper type ($CaCO_3$ and other binders or fillers used in its production), which may lead to less uniform LIG coverage. For laser coordinates P10S10, more intense ablation appears to induce some coral like structures within the fibers, inducing increased porosity in the topography of paper based LIG surface. The

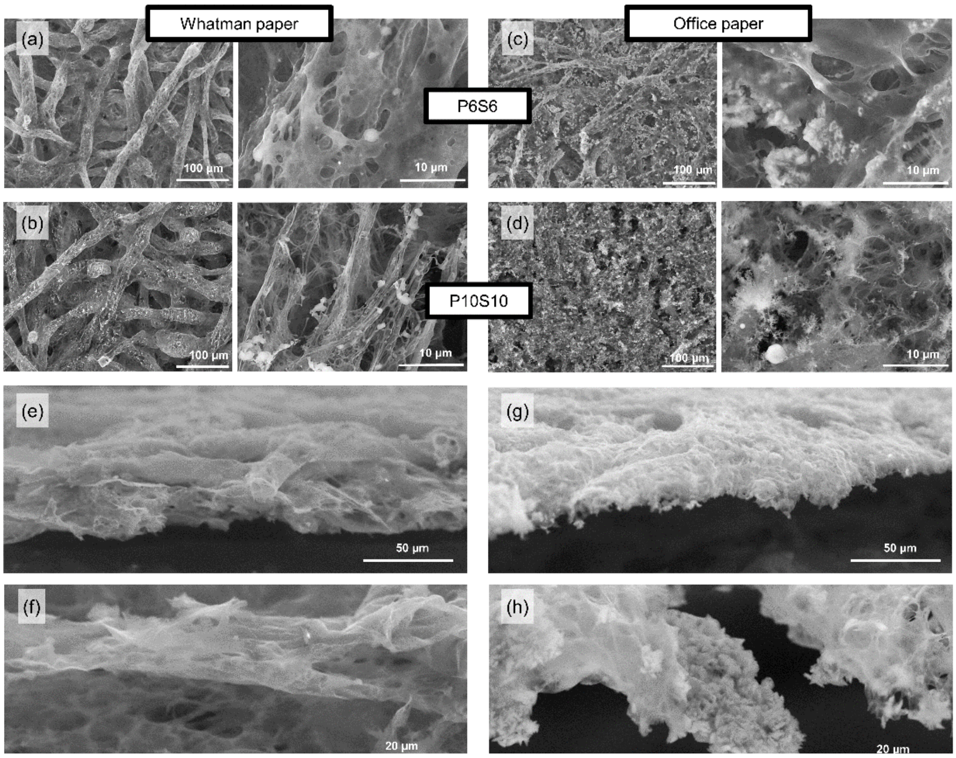

Figure 3.2 - Scanning electron microscopy study of surface morphology of laser treated paper for LIG synthesis. LIG synthesized using chromatography paper at operational laser parameter (a) P6S6, (b) P10S10. LIG synthesized using office paper at operational laser parameters (c) P6S6, (d) P10S10. Cross-sectional analysis of LIG structures for Whatman paper (e-f) and office paper (g-h).

implications of the observed morphological alterations caused by laser scanning for LIG production indicate that a compromise is required between using higher laser coordinates, leading to more efficient graphitization, while not increasing these coordinates to a point where ablation becomes the dominant phenomenon. When this happens, higher porosity is induced due to excessive destruction of the native fiber structures, leading to an increase in the capillary transportation properties. Thus, even though this paper-based LIG presents hydrophobic properties (Figure A2), this increased capillarity leads to leakage of any sample used in the produced electrodes (that can reach contact areas and cause short-circuits) and reduce the effective conductive networks responsible for electron flow, thus affecting the electrochemical properties of the produced electrochemical cell systems. Cross-section images were also taken from peeled off LIG structures produced using P10S10 coordinates. For chromatography paper (**Figures 3.2e-f**), it is visible that the natural fiber configuration is maintained in the formed LIG network, in opposition to irradiated office paper (**Figures 3.2g-h**). These LIG structures showed varying thickness, related to the width of converted fibers, ranging from 10 to 30 µm.

Raman spectroscopy was used to study and identify the presence of LIG after laser treatment. Both paper substrates were analyzed, with comparative spectra being presented in **Figure 3.3a** and **Figure 3.3b** for chromatography and office paper, respectively. Three distinct peaks were identified in the Raman spectra, at around 1324, 1582 and 2644 cm^{-1}, corresponding to D, G and 2D peaks characteristic of carbon-based structures. [49] The D band is attributed to defects of sp^2 carbon hybridization in hexagonal sheets of carbon atoms. In this case, the D peak is the most prominent peak, independent of laser operation coordinates or substrate used for synthesis, except in LIG synthesized in chromatography paper using laser operation coordinates P10S10 (**Figure 3.3c**), where some LIG structures showed a more intense G peak. G peak, resulting from first-order inelastic processes attributed to bond stretching of sp^2 hybridized carbon atoms in the graphitic structure, mostly shows a lower intensity when compared to the D peak, for the remaining laser operation conditions analyzed. The peak showing a more pronounced dependence from laser parameters and paper substrate was the 2D peak, attributed to second-order, two-phonon resonance process dependent on excitation laser frequency. For both chromatography and office papers, this peak showed an increase in its intensity when laser operation coordinates increased, indicating that structures with fewer layers

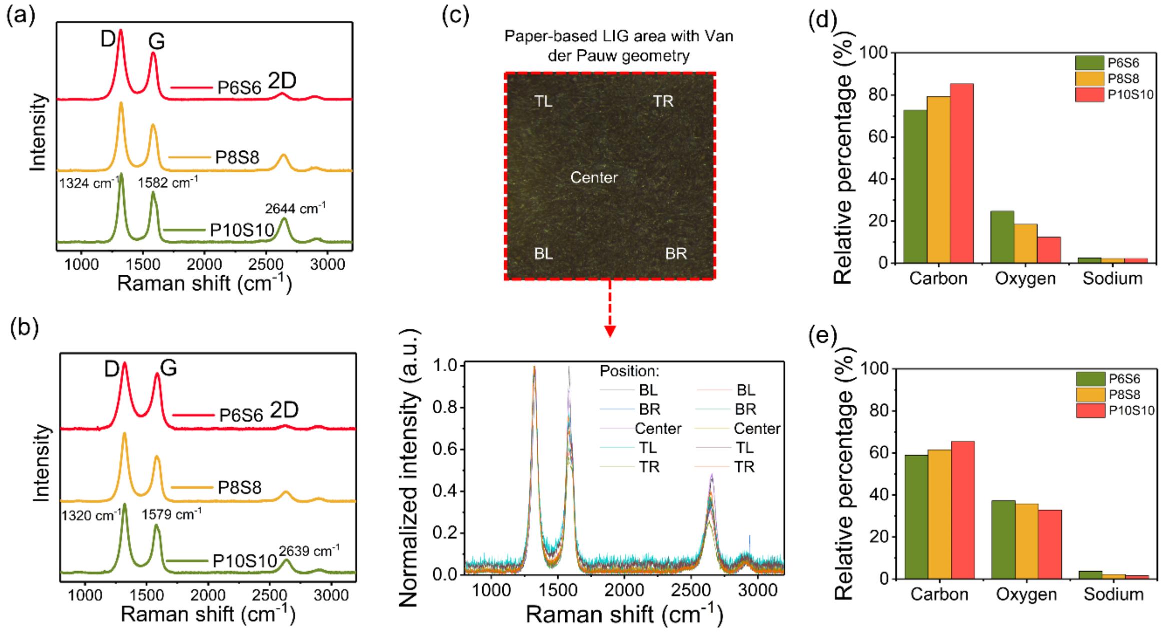

Figure 3.3 - Chemical characterization of paper-based LIG for different laser operational parameter coordinates. (a) Raman spectra of LIG produced using chromatography paper. (b) Raman spectra of LIG produced using office paper. (c) Distribution of 10 measure at LIG sample with Van der Pauw geometry (TL – top left, TR – top right, BL – bottom left, BR – bottom right) and corresponding Raman spectra, using P10S10 operation coordinates. Relative element composition for LIG samples for each laser operation coordinate set for (d) Whatman paper and (e) office paper, from EDS measurements.

were being formed. When comparing both paper types, the intensity of this peak is characteristically higher for chromatography paper. Considering the area under the peaks, the order and disorder properties of the synthesized LIG were studied, by following the trends in I_{2D}/I_G and I_D/I_G peak ratios.

The results are presented in Table A1, showing the values of these ratios for all LIG synthesis conditions. The I_{2D}/I_G ratio, which gives a measure on the layered nature of produced graphitic structures, showed an increase in value associated with the increase in laser operation coordinates, varying from 0.132 ± 0.085 to 0.616 ± 0.173 for chromatography paper and 0.073±0.037 to 0.269 ± 0.113 for office paper, explained by the increase in 2D peak intensity. These values indicate that LIG produced from these paper-substrates is multi-layered, with the highest I_{2D}/I_G ratio value being 0.749 using laser operation coordinates P10S10 in chromatography paper. The opposite behavior was observed for the I_D/I_G peak ratio, which slightly decreased its value in association with the increase in laser operation coordinates. For chromatography paper, it varied from 1.580 ± 0.142 to 1.281 ± 0.173, while for office paper, this decrease is not so significant. The lowest value obtained for the I_D/I_G ratio was also for laser operation coordinates P10S10, applied to chromatography paper, resulting in a value of 0.987, indicating that in some cases, more pristine, less defect dense LIG was synthesized. This can be seen in **Figures 3.3c**, showing the distribution of 10 measures used to study each sample and the variability in chemical structure along the sample. In fact, because paper presents a highly porous and heterogeneous structure, the effect of the laser will differ depending on the depth of the fiber it reaches, ultimately synthesizing LIG with varying characteristics on the same sample. Thus, there is some intra-sample variation regarding the chemical properties of the synthesized LIG. To also monitor the chemical constitution of LIG samples, EDS was used to track the alterations in relative elemental composition (namely carbon and oxygen), related to laser operation parameters (**Figure 3.3d-e** and Table A1). Native chromatography paper has surface composition in which carbon and oxygen are present at similar relative percentages [50]. Upon laser irradiation, carbon content in LIG samples increased significantly (upwards of 70 % for chromatography paper and 60 % for office paper), paired with a decrease in oxygen content, highlighting the graphitization of the irradiated substrate, which is in accordance with previous reports on similar processes on cellulose-based materials processed by laser irradiation.[51,52] Moreover, increase in laser operation coordinates also leads to higher carbon content in the samples, indicating a better conversion of the cellulose into LIG. XPS was also used to confirm this conversion, with spectra presented in Figure A3. C1s spectra showed the presence of sp^2 domain for irradiation of both paper substrates, in opposition to the precursor substrate, confirming the formation of LIG structures in the irradiated paper. Regarding electrical and conductive characteristics of paper based LIG, sheet resistance (R_{sh}) measures were taken from each synthesis condition previously presented, with results being presented in Table A1. For both types of paper substrates, R_{sh} suffered a decrease associated with an increase in laser operations coordinates. Similarly to Raman peak ratios, R_{sh} showed more desirable and lower values for chromatography paper, varying from 329 ± 60.0 $\Omega.sq^{-1}$ (n=3) for P6S6 laser operation coordinates to 56.0 ± 12.3 $\Omega.sq^{-1}$ (n=3) for P10S10 coordinates. For office paper, LIG produced with P6S6 coordinates did not show measurable conductive properties, probably because a full LIG network, covering the laser treated area and establishing conductive paths wasn´t achieved with these conditions. For subsequent laser coordinates, R_{sh} varied from 387.7 ± 135.6 and 217 ± 21.8 $\Omega.sq^{-1}$ (n=3). Thus, R_{sh} values presented an approximate 4-fold decrease for P10S10 coordinates applied to chromatography paper for the same synthesis conditions. The lowest R_{sh} value was obtained for these operation coordinates, with a value as low as 46.8 $\Omega.sq^{-1}$ being reached. Some constraints are present when analyzing the resistivity of this material due to the porous characteristics of the native paper substrates, that lead to LIG films with the same fibrous morphology, as shown in **Figure 3.2**. Thus, it is not possible to measure the exact thickness of films, which are dependent on individual fibers' thickness, inhibiting the calculation of absolute resistivity and conductivity of the films. However, R_{sh} measurements portray the good conductive properties of the synthesized paper based LIG.

In **Table 3.1**, a literature survey focusing on chemical and electrical properties of laser engraving approaches applied to different substrates is presented, to draw a comparison between the presented results and LIG derived from various polymeric materials. The results obtained by this paper based LIG synthesis approach show that chemical properties are similar to LIG obtained from other laser irradiated substrates, although LIG synthesized from natural polymers such as cellulose tend to present higher I_D/I_G ratios, indicating higher defect density. In terms of conductive properties, this paper based LIG showed similar R_{sh} values to LIG obtained from other substrates, including different paper substrates and polyimide. However, these properties are greatly influenced by laser operation variables, indicating that their manipulation and study can lead to the production of higher quality LIG derived from these paper substrates.

Table 3.1 - Comparison of chemical properties obtained by Raman characterization and electrical properties of LIG produced from different substrates.

Substrate	I_D/I_G	I_{2D}/I_G	R_{sh} (Ω sq^{-1})	Ref.
PI	0.44	0.88	15	[16]
PI	0.6	0.6	n.a.	[53]
PI	<1	>0.2	85	[54]
PEI	0.2	0.65	83.76	[42]
PI/PDMS	0.72	0.61	80	[55]
KL/PEO	0.50	0.40	363.1	[24]
Cork	0.41	0.37	75	[56]
Coal	0.78	0.92	12	[28]
Paperboard	0.71	n.a.	n.a.	[40]
Paperboard	1.2	n.a.	n.a.	[43]
Phenolic paper	0.88	n.a.	n.a.	[41]
Watercolor paper	1	n.a.	40	[57]
Chromatography paper	0.88	0.84	83	[25]
Chromatography paper	0.5	n.a.	32	[58]
Chromatography paper	1.28	0.62	56.0	This work
Office paper	1.33	0.27	217.7	This work

PI – polyimide; PEI – poly(ether imide); PDMS – polydimethylsiloxane; KL/PEO – kraft lignin/poly(ethylene oxide)

3.4 Paper-based LIG Electrode Fabrication and Electrochemical Characterization

After characterization of paper based LIG, laser operation coordinates P10S10 were selected for electrode fabrication, as these conditions presented more appealing chemical and electrical properties. Electrodes were patterned by laser irradiation in the same paper sheet (**Figure 3.4a1**), to establish the architecture of the WE, CE and RE. The following step aimed to establish a passivation layer for the electrodes, using plastic laminating sheet pouches covered with an adhesive tape layer, to serve as mask for conductive track introduction and establish a working area for the system (**Figure 3.4a2**). Subsequently, conductive tracks were established using a silver conductive ink, and the RE was manually patterned, using an Ag/AgCl ink, painted on top of the LIG area corresponding to the RE (**Figure 3.4a3**). After all the fabrication steps, the electrochemical behavior of the devices was characterized using 0.5 mmol.L^{-1} $Fe(CN)_6^{3-}$/ $Fe(CN)_6^{4-}$ (solution as a standard redox probe prepared in 0.1 mol.L^{-1} KCl supporting electrolyte) (**Figure 3.4a4**).

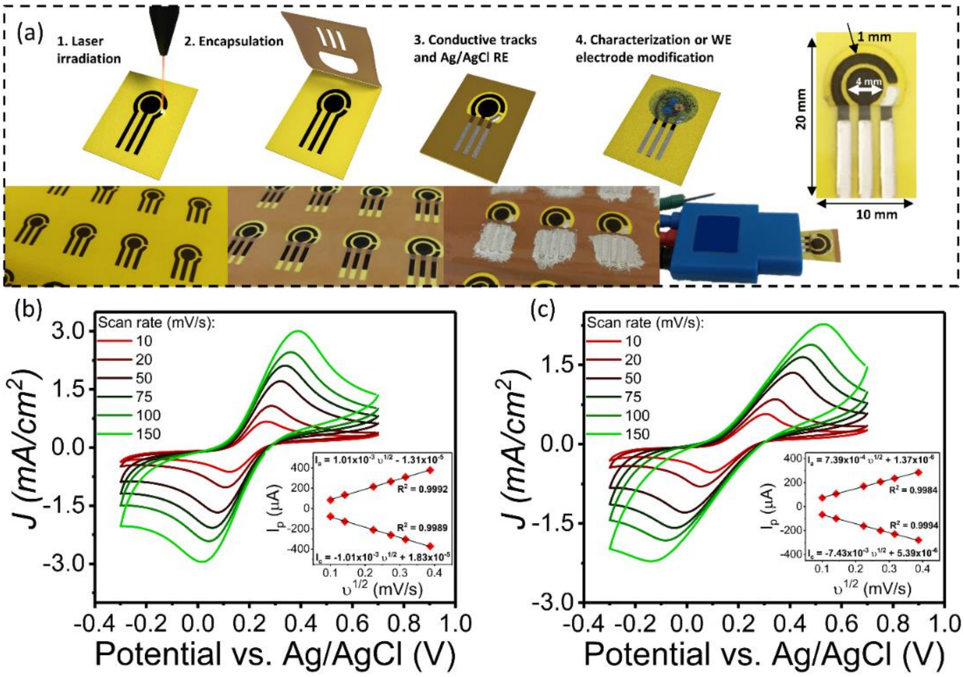

Figure 3.4 - Electrochemical sensor production and cyclic voltammogram characterization. (a) Schematic representation of fabrication workflow used to produce paper-based LIG 3-electrode systems and resulting device architecture. Cyclic voltammograms obtained for (b) chromatography paper and (c) office paper for scan rates from 10 to 150 mV.s^{-1} using 5 mM $Fe(CN)_6^{3-}$/ $Fe(CN)_6^{4-}$ as redox probe (inset shows the plot of peak currents vs. square root of corresponding scan rate).

Prior to electrochemical characterization, electrochemical pre-treatment of the electrodes was performed using the supporting electrolyte, as presented in Figure A4. After electrochemical pre-treatment, sequences of cyclic voltammograms in the range -0.3 to 0.7 V were conducted, as shown in **Figure 3.4b-c**, for a set of 4 electrodes for both chromatography and office paper. Faradaic currents corresponding to cathodic and anodic redox peaks for the electrochemical redox couple can be clearly seen in the voltammograms, for all applied scan rates under study (10 to 150 mV s^{-1}). These results portrayed the electron transfer between the LIG electrodes and redox mediator that was expected for this system. The electrochemical behavior of the electrodes showed peak potentials dependent on scan rate, with peaks located at approximately -0.11 V and 0.25 V for chromatography paper and -0.09 V and 0.31 V for office paper, at a scan rate of 10 mV s^{-1}. As scan rate increased, peak potential separation (ΔE_p) followed the same trend, showing that these carbon-based electrodes promote a quasi-reversible electrochemical behavior, since ΔE_p had different values than 0.059/n (n being the number of electrons transferred between electroactive probes), the theoretical value for a fully reversible electrochemical charge transfer. This behavior is usually attributed to limitations on the charge transfer processes arising from the porosity of the material comprising the electrodes, as is the case with this paper based LIG. From the CVs, the dependence of anodic and cathodic peak currents towards the scan rate was followed using the Randles-Sevcik equation, described in equation 3.1:[59]

$$i_p = 2.69 \text{ x } 10^5 A\, D^{1/2}\, n^{3/2}\, v^{1/2}\, C \qquad (3.1)$$

where A is the electrochemical active surface area of the WE, D is the diffusion coefficient of the redox probe (D = 6.40x10^{-6} cm^2.s^{-1} for $[Fe(CN)_6]^{4-}$, in 0.1 M KCl [60]), n is the number of electrons participating in the charge transfer process (n=1), v is the scan rate and C is the concentration of the redox probe molecule (in mol.cm^{-3}). The plot of anodic and cathodic peak current vs. square root of scan rate are presented in inset **Figures 3.4b** and **Figures 3.4c**. As it is visible, current increases linearly with scan rate, portraying an electrochemical process ruled by diffusion of the analyte from the bulk solution towards electrode surface. Also, it is visible that for Whatman paper, current densities upwards of 3 mA.cm^{-2} (taking the geometric area of electrodes, A_g = 12.56 mm2) were achieved at 150 mV.s^{-1} scan rate, while for office paper, maximum current densities of 2.2 mA.cm^{-2} were reached for the same scan rate. From the current vs. scan rate plots, the electrochemical active area (A_e) was calculated, using the anodic peak dependency on scan rate, for two sets of four electrochemical systems for both paper types. Results are summarized in **Table 3.2**, with additional CVs and complementary plots presented in Figures A5 and A6. Results show that A_e increased when compared to the A_g. For chromatography paper, a mean A_e of 28.59 mm^2 was reached, while for office paper, a mean A_e of 20.15 mm^2 was achieved. This resulted in an increase of the activity ratio (A_e/A_g) of more than two-fold for chromatography paper, probably related to the natural fiber network structure of paper allowing for greater LIG surface area to form. This aspect also relates to the morphology of the resulting LIG networks for both paper types, where SEM analysis showed a greater preservation of the natural fiber structure being maintained for Whatman paper, that may lead to this increase in active electrochemical material at the electrodes.

Regarding the electron transfer kinetics, a comparison between ΔE_p for the studied scan rates and both paper types is presented in **Figure 3.5a**. As evidenced, lower ΔE_p are characteristic for chromatography paper, with values varying from 146 mV for 10 mV.s^{-1} scan rate to 370 mV for 150 mV.s^{-1} scan rate, producing a total variation of 224 mV. For office paper, ΔE_p for 10 mV s^{-1} scan rate is approximately 220 mV, increasing to upwards of 700 mV for 150 mV.s^{-1} scan rate. This indicates that electron transfer kinetics for office paper electrodes is poorer when compared to chromatography paper-based electrodes, which is also in agreement with LIG

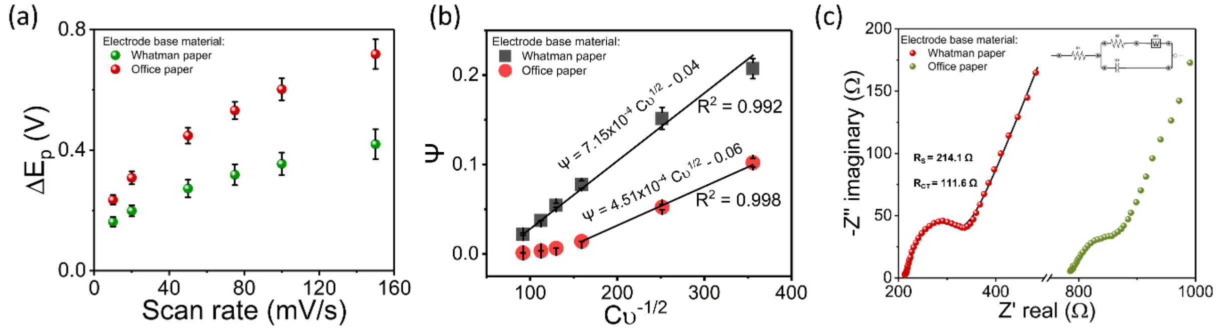

Figure 3.5 - Electron transfer characterization and impedance spectroscopy characterization of paper-based electrochemical systems. (a) Plot of ΔEp vs. corresponding scan rate, for paper substrate under analysis. (b) Dependency of ΔEp toward scan rate, using the dimensionless kinetic parameter Ψ, for calculation of HET rate. (c) Nyquist plots obtained from impedance spectroscopy analysis for both paper substrates under study, with fitting of Nyquist plot for Whatman paper with Randles modified circuit (inset).

characterization previously presented, that showed that LIG synthesized from office paper presented less desirable chemical and electric characteristics for the same applied synthesis conditions. To better understand these electron transfer kinetic mechanisms, the Nicholson method [61] and its extension, introduced by Lavagnini et al. [62], were used to determine the heterogeneous electron transfer (HET) rate (k_0) parameter. This method relates the dimensionless kinetic parameter Ψ with ΔE_p and the corresponding scan rate by the relation presented in Equation 3.2:

$$\Psi = k_0 \left(\frac{D_O}{D_R}\right)^{\alpha/2} \sqrt{\frac{R\,T}{\pi\, n\, F\, D_O\; v}} \tag{3.2}$$

where D_O/D_R are the diffusion coefficients for oxidized and reduced species, α is the transfer coefficient, n is the number of electrons participating in the reaction, R is the universal gas constant (8.314 $J.K^{-1}.mol^{-1}$), T is the absolute temperature and F is the Faraday constant (96 489 $C.mol^{-1}$). To use this dependency, there is the assumption for this quasi-reversible system that diffusion coefficients are approximately equal and that redox kinetics are symmetrical ($\alpha \approx 0.5$), which was confirmed by the Laviron equation, where $\alpha = \frac{\delta_{pa}}{\delta_{pa} + \delta_{pc}}$ (δ_{pa} and δ_{pc} being the slope of the curves for anodic and cathodic peak currents vs log of scan rate) [48], with values presented in **Table 3.2**. Then Equation 2 simplifies to Equation 3.3,

$$\Psi = k_0 \sqrt{\frac{R\,T}{\pi\, n\, F\, D\; v}} = C\, k_0\, v^{-1/2} \quad \left(C = \sqrt{\frac{RT}{\pi\, n\, F\, D}} = 35.56,\ D = 6.40 * 10^{-4}\ cm^2/s\right) \tag{3.3}$$

The dimensionless kinetic parameter is also related to ΔEp by Equation 3.4:

$$\Psi = \ 2.18\, [\alpha/\pi]^{1/2} \exp\left[-\left(\frac{\alpha^2 F}{RT}\right) n\, \Delta E_p\right] \tag{3.4}$$

Using equations 3 and 4, k_0 can be determined by the slope of Ψ vs. C.$v^{-1/2}$. Representative plots for this dependency are presented in **Figure 3.5b**, corresponding to the cyclic voltammograms presented in **Figure 3.4**. From the slopes of the curves presented in **Figure 3.5b**, k_0 presents a much higher value of 7.15 x 10^{-4} cm.s^{-1} for chromatography paper, confirming the improved charge transfer properties of LIG produced from this paper source. For office paper, this value was obtained from the slope of the linear segment of the plot, where ΔE_p values not exceeding 500 mV were considered (quasi-reversibility is maintained),[62] with k_0 dropping to 4.49 x 10^{-4} cm.s^{-1} for the CV curve presented in **Figure 3.4c**. To confirm this trend and test the reproducibility of the electrochemical behavior of these electrochemical chips, this parameter was analyzed for the additional set of electrochemical systems, with results presented in **Table 3.2**. An average k_0 value of 6.85 x 10^{-4} cm.s^{-1} (RSD = 3.7%) was reached for chromatography paper, whilst for office paper, this value decreased to 4.08 x 10^{-4} cm.s^{-1} (RSD = 12.9%), showing less reproducibility in devices produced using this substrate.

EIS was also used to characterize the electrodes and have a comparison between charge transfer resistance (R_{CT}) and solution resistance (R_S) obtained from fitting of Nyquist plots presented in **Figure 3.5c**. Solution resistance was different for the two electrode base materials, with characteristically lower values of R_S obtained for chromatography paper-based systems. For chromatography paper, an R_S value of 214.6 ± 10.6 Ω (n=4) was achieved, increasing to 830 ± 39 Ω for office paper. Since R_S is dependent on electrode area and its geometry, the differences previously presented in SEM characterization may explain the marked difference in this parameter. For R_{CT}, fitting with the Randles circuit, including a constant phase element replacing the double layer capacitor, resulted in a value of 101.5 ± 9.8 Ω (n=4) for chromatography paper as base material. For office paper no significant information was retrieved from this fitting, as this parameter showed great variation for the produced electrochemical systems. Overall, these results indicated that LIG electrodes produced from chromatography paper could be employed for impedimetric sensor development, but more in-depth study of these properties should be carried out to test their suitability. Furthermore, reproducibility of the chip sensors could be studied in terms of the mechanistic properties of the produced LIG, so that it could be tailored to more specific and accurate application in sensing and bioelectronics.

Table 3.2 - Stochastic electrochemical parameters for electrochemical systems produced from chromatography and office papers.

	Chromatography paper			Office paper		
Electrodes	A (mm^2)	α	k_0 (10^{-4} cm.s^{-1})	A (mm^2)	α	k_0 (10^{-4} cm.s^{-1})
#1	29.81	0.499	7.15	21.72	0.499	4.51
#2	27.24	0.499	6.97	20.60	0.497	4.45
#3	30.12	0.491	6.68	19.14	0.490	3.98
#4	27.18	0.498	6.61	19.15	0.494	3.37
Average	28.59	0.497	6.85	20.15	0.495	4.08
RSD (%)	5.6	0.8	3.7	6.2	0.8	12.9

3.5 Proof-of-Concept Amperometric Biosensors

3.5.1 Unmediated glucose biosensor

After electrochemical characterization of the paper-based LIG three-electrode systems, simple, disposable electrochemical sensors based on enzyme catalyzed reaction of glucose using GOx and HRP were produced. WEs were modified by simple drop-casting method, to allow for adsorption of enzymes into the paper-based LIG surface. CV was used to determine if there was any alteration in current caused by the introduction of glucose standard solutions with different concentrations, related to the catalytic reactions of the bi-enzymatic system applied for electron transfer pathways at electrode surface, without any electrochemically active mediator [63].

$$\mathrm{Glucose} + \mathrm{O_2} \xrightarrow{\mathrm{GOx}} \mathrm{Gluconolactone} + \mathrm{H_2O_2} \tag{1}$$

$$\mathrm{H_2O_2} + \mathrm{Peroxidase_{red}} \longrightarrow \mathrm{Peroxidase_{ox}} + \mathrm{H_2O} \tag{2}$$

$$\mathrm{Peroxidase_{ox}} + 2e^- \longrightarrow \mathrm{Peroxidase_{red}} \tag{3}$$

Results presented in **Figure 3.6a** indicate an increase in anodic current resulting from increasing glucose concentrations introduced into the system. This in accordance with H_2O_2 oxidation by peroxidase in PBS medium [64], and was used to establish the amperometric measurements. This anodic current appears to increase more intensely for potentials above 0.5 V, so a measure potential of 1 V was established to guarantee that glucose-induced current changes could be detected (this parameter was not fully studied, although it is important to establish optimized sensitivity and detection range). In **Figure 3.6b**, the chronoamperometric response of the modified electrode is presented, showing the current increase related to the increase in glucose sample concentration. Baseline current of 12.9 ± 2.7 µA for PBS buffer with no glucose was achieved after a stabilization period of 50 seconds, increasing until 119.4 ± 6.7 µA for 15 mM glucose concentration. The obtained current values after a stabilization period of 50 seconds were used for calibrating the sensor, presented in **Figure 3.6c**. The sensitivity range showed two regimens, with the first linear range (0 to 1 mM) showing a higher sensitivity of 27.24 $\mu A.mM^{-1}$, with a limit of detection of 0.13 mM (calculated as 3σ/S), and the second

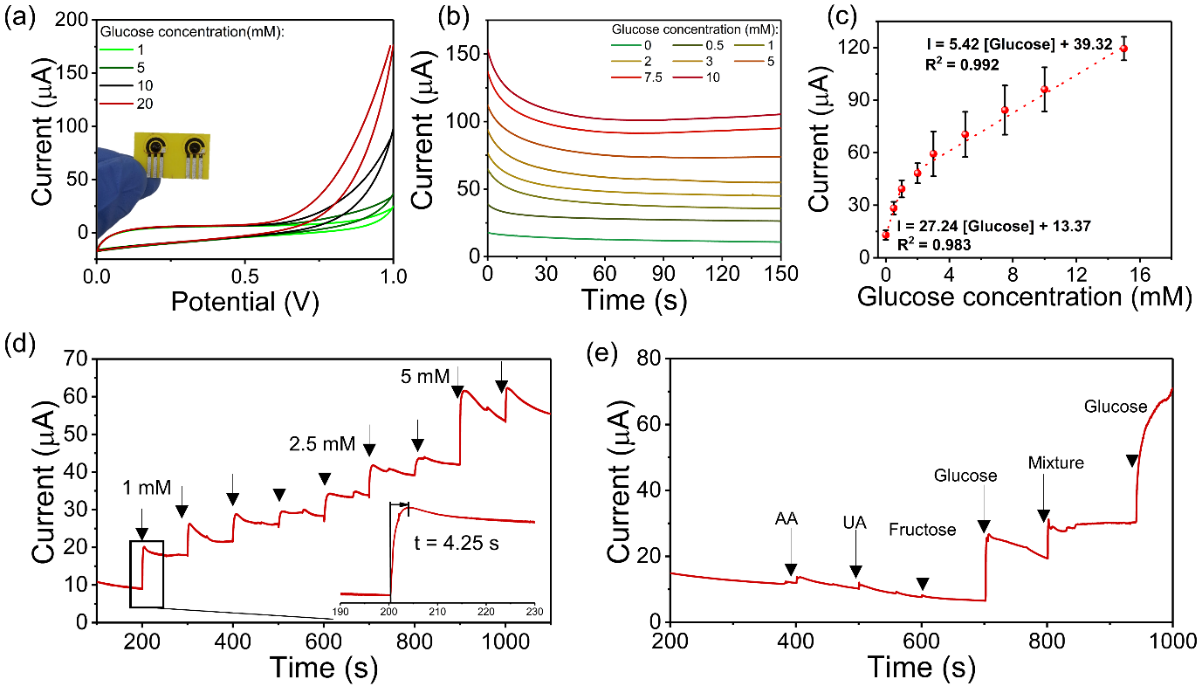

Figure 3.6 - Paper-based LIG three-electrode systems applied as unmediated enzymatic, amperometric glucose biosensor. (a) CVs for different amounts of glucose in PBS buffer. (b) Chronoamperometric sensor response to different glucose concentrations (0 to 15 mM), measured at 1V applied potential. (c) Resulting calibration curve from chronoamperometric response 150 seconds after glucose introduction. (d) Continuous amperometric sensor response to the introduction glucose (inset showing the first current increase step). (e) Selectivity of enzymatic biosensing strategy towards glucose, assessed by monitoring current response to the introduction of ascorbic acid (AA), uric acid (UA), fructose and a mixture of glucose and interfering metabolites.

linear range having a lower sensitivity of 5.42 μA.mM^{-1}. To study the sensor response to the introduction of glucose as a continuous measurement, the amperometric response was followed for successive additions of glucose in the working area of the sensor. Results are presented in **Figure 3.6d**, showing the current step related to introduction of 1.0 to 5.0 mM glucose, with inset showing one of the current steps in more detail. The current increase upon glucose introduction has a variation with the amount of glucose, taking less time for lower glucose concentrations. To confirm that the amperometric response of the bi-enzymatic reaction started with glucose introduction, selectivity was monitored by studying if possible interfering metabolites (ascorbic acid, uric acid and fructose in PBS buffer) could induce current response in the sensor, with results in **Figure 3.6e** showing that significant current increases occurred only in the presence of glucose. These results show that paper-based LIG three-electrode systems can be adapted for disposable, electrochemical sensor development using amperometric signals for correlation with glucose levels, that could be further improved in terms of enzyme immobilization approaches for better performance.

3.5.2 Mediated glucose biosensor

The second generation of glucose biosensors is portrayed as mediated enzymatic sensors, where there is the use of non-physiological redox mediators capable of transporting electrons towards the electrode surface. [65] Most test strips from commercial glucometer systems involve modifying the reaction zone (WE) with an appropriate enzyme with affinity for glucose and an electrochemical mediator that changes its redox state due to the biological recognition reaction between the enzyme and analyte. **Table 3.3** shows various combinations of enzymes and mediators used in various commercial test strips, serving as a source for selection of an appropriate enzyme-mediator pair.

Table 3.3 - Enzyme/mediator combinations employed in commercial test strips. Adapted from [66].

Test strip	Enzyme	Mediator
One Touch Ultra	GOx	Ferricyanide
Arkray	PQQ-GDH	Hexaammineruthenium (III)
Ascencia Contour	FAD-GDH	Ferricyanide
BD Test Strip	GOx	Ferricyanide
FreeStyle	PQQ-GDH	Osmium complex
Precision Xtra	NAD-GDH	Phenanthroline quinone
TrueTrack Smart System	GOx	Ferricyanide
Accuchek Aviva	PQQ-GDH	Proprietary

GOx - Glucose oxidase; PQQ-GDH - glucose dehydrogenase pyrroloquinoline quinone; FAD-GDH - flavin adenine dinucleotide-dependent glucose dehydrogenase; NAD-GDH - nicotinamide glucose dehydrogenase

The most common approach has been the combination of GOx as the biological recognition element and potassium ferricyanide ($K_3[Fe(CN)_6]$), an electroactive compound also used throughout the work to characterize the faradaic charge transfer capabilities of LIG-based electrochemical systems. This biodetection mechanism is based on the selectivity of the GOx enzyme for the glucose oxidation reaction, which leads to the reduction of the enzyme's cofactor (FAD to $FADH_2$)) (**Figure 3.7a**). After this reaction, the enzyme is regenerated through the reduction of the mediator, induced by the electron acceptor cofactor. After this cascade of reactions, the reduced form of the mediator (potassium ferrocyanide - $K_4[Fe(CN)_6]$) accumulates. The application of an appropriate potential induces an electrochemical reaction, which regenerates the mediator to its initial form, leading to the capture of an electron referring to the oxidation of the accumulated mediator in its reduced form, producing an electrical response, directly proportional to the initial concentration of glucose.

LIG-based electrochemical cells were used to develop mediated glucose sensors by modifying the working electrode with a solution containing GOx and the iron mediator. From a

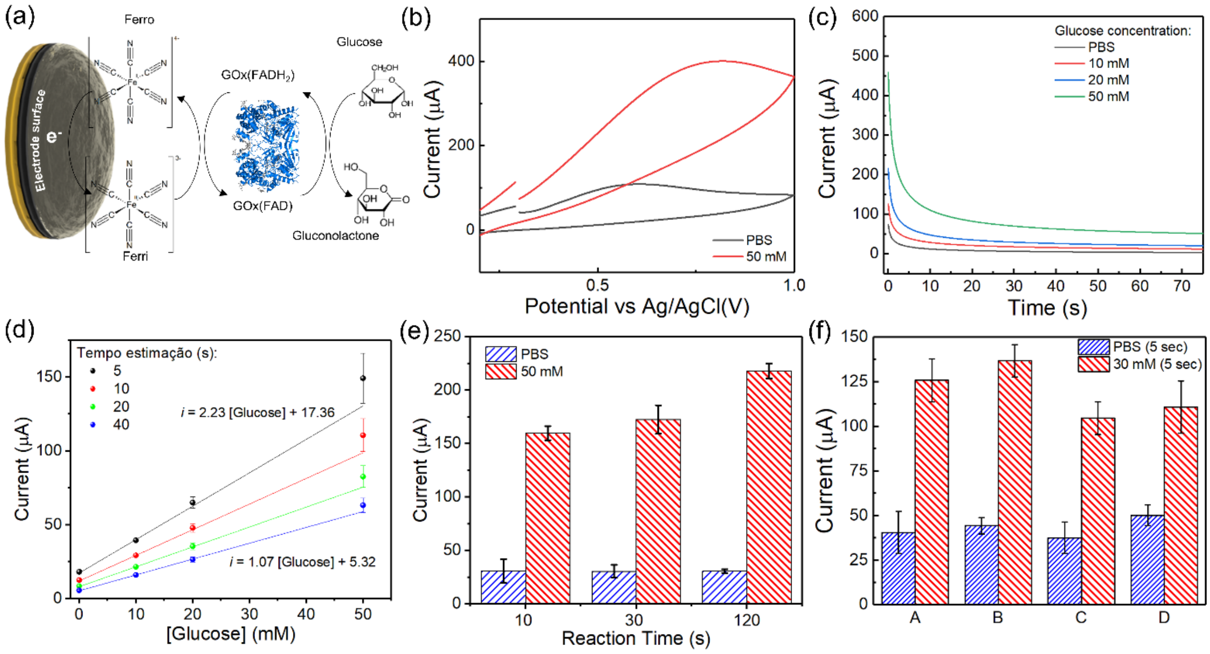

Figure 3.7 - LIG-based mediated enzymatic glucose biosensor. (a) Biodetection mechanisms and reaction cascade for mediated glucose detection using GOx and $Fe(CN)_6^{+3}$. (b) CV response of sensors in the absence and presence of glucose. (c) Chronoamperometry response of for increasing concentrations of glucose. Influence on estimation time (d), reaction time (e) and enzyme/mediator concentrations (f) on sensor response (n=3 for each concentration condition).

literature survey, the initial concentration levels for the enzyme and mediator were set at 5 mg/mL and 100 mM, correspondingly [67,68]. Given this survey, these concentration values can vary up to unit values for the enzyme and higher concentration values for the mediator, depending on the electrode materials and configuration. It is therefore necessary to study the response of this system applied to electrodes made from laser-induced graphene [67–70]. Having set an initial value for the concentration of enzyme and mediator, the biodetection scheme was tested in a standard test matrix, without the presence of interferents. This matrix consists of a 0.1 M PBS solution. The results show that the sensors respond well to the presence of glucose, using the proposed scheme. CV was used to identify the potential regions where an electrical response associated with this reaction occurs. Based on the results shown in **Figure 3.7b**, a measuring potential of 0.7 V was established, with which the amperometric analysis was carried out, shown in **Figure 3.7c**. Three repetitions (n=3) were carried out for each concentration, from which the average response curve for each concentration was obtained. From the time profile of the response curves, it is possible to select the estimation time, to derive the system's calibration curve, as shown in **Figure 3.7d**. As can be seen, the estimation time influences the magnitude of the signal current, as well as the sensitivity of the system, and is an important parameter when carrying out point-of-care tests, in terms of the time taken between carrying out the test and obtaining the result. For an estimation time of 5 seconds, resulting sensitivity of 2.2 $\mu A.mM^{-1}$, with a limit of detection (LOD) of 2.3 mM was observed, while for an estimation time of 40 seconds, the sensitivity reaches 1.1 $\mu A.mM^{-1}$ with an LOD of 2.2 mM.

Two important aspects in the measurement protocol were also studied, namely the reaction time given for accumulation of the enzyme-promoted reduced mediator and the concentration of enzyme and mediator used to modify the WE. For the reaction time, three time periods were surveyed (10, 30 and 120 seconds). As shown in **Figure 3.7e**, no alterations are detected in the baseline current observed for the PBS buffer. However, for a concentration of 50 mM, an increase in current associated with increased reaction time is observed, indicating that higher reaction times allow for a more efficient reduction of the ferricyanide mediator, impacting the final current signal. However, it is relevant to limit this reaction time, since it impacts the total test time when such test strips are implemented in a commercial system, which usually displays few seconds to get a result after a finger prick blood sample is introduced in the strip. For enzyme and mediator concentrations two alternative values for enzyme (2.5 and 10 $mg.mL^{-1}$) and mediator (50 and 200 mM) and their combinations were tested. The results indicate that increased enzyme concentration results in higher magnitude of measured current (comparison between conditions A to C and B to D, **Figure 3.7f**) in response to glucose.

For the same enzyme concentration condition, the variation of mediator concentration appears to influence the measured current, although not so significantly as for enzyme concentration. Thus, this simple analysis shows that enzyme concentration appears to be the key factor in glucose test strips and resulting sensitivity, due to the kinetics associated with its role in glucose oxidation and subsequent reaction cascade, resulting in the measured current signals.

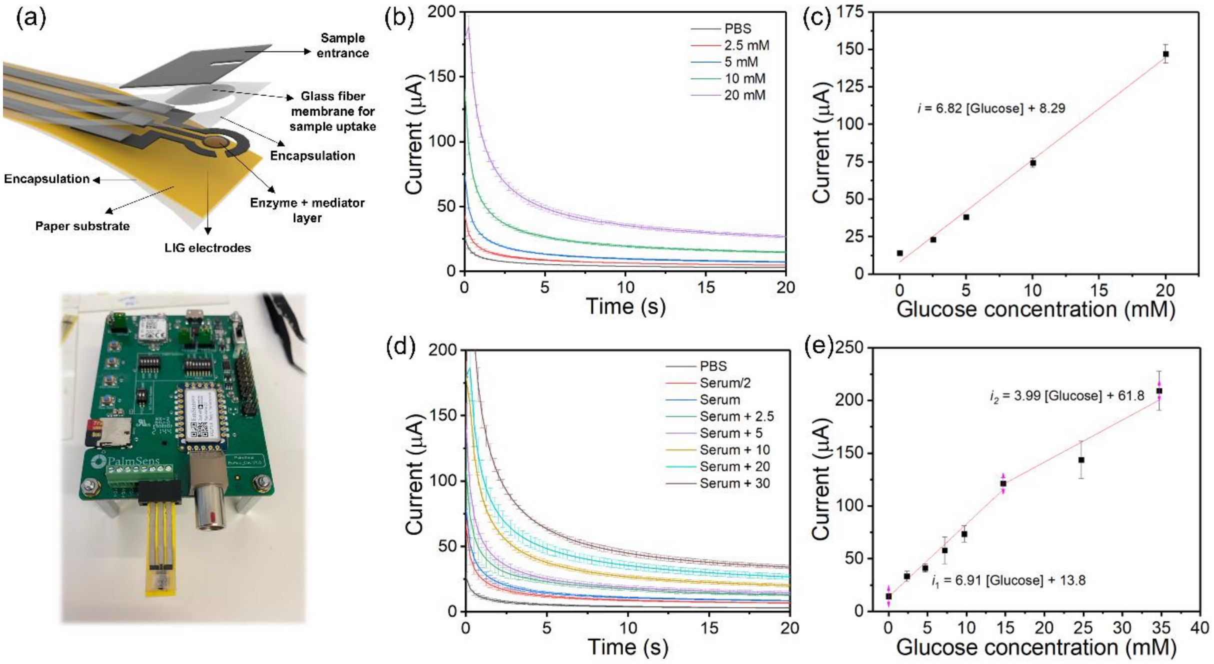

Figure 3.8 - LIG-based, miniaturized mediated glucose biosensor. (a) Scheme of miniaturized glucose test strips and its components. (b) Chronoamperometry response of miniaturized glucose test strips for increasing glucose concentrations in PBS matrix. (c) Calibration curve for the analytical response of sensors in PBS matrix. (d) Chronoamperometry response of miniaturized glucose test strips for increasing glucose concentrations in human serum matrix. (e) Calibration curve for the analytical response of sensors in PBS human serum matrix (n=3 for each concentration condition).

In this way, a working window was established for the development of the final form of the test strip, compatible with small test volumes of commercial glucometers (<5 µL) obtained through finger-prick blood extraction. **Figure 3.8a** shows the architecture of the test strip, manufactured using laser material processing principles. The main features of this test strip are its miniaturization and the inclusion of components capable of automatically collecting a blood sample after a finger prick. Additionally, because of the miniaturization, the reference electrode in this test strip is not modified with Ag/AgCl, as in previous experiments. In addition, a commercial miniaturized potentiostat unit was employed (PalmSens Emstat Pico Development Kit) to automatize the measurement protocol.

Various analytical tests were carried out with these test strips, to study their compatibility with the glucose detection processes. Measurements were initially carried out in PBS, with some changes to the electrode modification and measurement protocol, namely: (i) 2 µL of enzyme (25 mg/mL) and mediator (0.5 M) mixture deposited over the WE (ii) 4 µL volume of testing solution inserted in the sensor inlet zone, (iii) 15 seconds of enzyme reaction time after sample introduction, followed by chronoamperometric measurement at 0.3 V and (iv) current estimation time of 0.5 seconds. **Figure 3.8b** shows comparable results to the ones obtained using the first sensor prototype with PBS, with some distinction. There is an increase in the magnitude of the measured currents in relation to the smaller electrode area, due both to the increase in the concentration of enzyme/mediator and to the reduction in estimation time. Regarding the analytical performance of this miniaturized sensor conformation, (**Figure 3.8c**) there was an increase in sensitivity, to a value of 6.82 µA/mM, which has advantages in better discrimination of concentration values. In addition, an LOD of 0.9 mM (n=3) (approximately 16 mg/dL) was calculated, as well as a linear variation regime up to 20 mM (360 mg/dL). The LOD is well below the values expected by patients with hypoglycemia, which demonstrates a first technical validation of the sensors for measuring clinically significant glucose concentration, as well as the linear variation limit including the values necessary for the efficient detection of hyperglycemia.

Subsequently, a complex human serum matrix (Cormay Serum HN), very similar to blood samples, was used as a test matrix. This solution contains a concentration of glucose, previously determined by the manufacturer, of 4.71 mM (84.8 mg/dL), within the normoglycemic range. The standard addition method was used, introducing known amounts of glucose to this serum sample, to analyze the response of the sensors independently of the matrix effects of the solution. Only two test conditions did not follow this method, namely the calibration solution (PBS) and the diluted serum analysis condition (Serum 50%). The chronoamperometry results shown in **Figure 3.8d** consist of additions of known amounts of glucose (2.5 to 30 mM) to the same serum matrix. As expected, the same types of descending curves are obtained with this matrix, with a shift towards higher current densities associated with increased glucose concentrations. In addition, the current magnitudes obtained with these samples are very similar to those measured with standard samples in PBS, which underlines the compatibility of this biodetection scheme with more complex biological matrices. Regarding the analytical performance of the sensor, a slightly different behavior was observed, namely the appearance of two linearity regions with different measurement sensitivities (**Figure 3.8e**). The first shows a very similar sensitivity to the system tested in PBS, at 6.91 µA/mM, once again validating the system's compatibility for measuring complex samples. However, above a concentration of approximately 15 mM, the sensitivity drops to 3.99 µA/mM. This may be due to less efficient mass transport and diffusion of accumulated ferrocyanide at higher glucose concentrations, associated with the presence of high molecular weight interferent, such as proteins, that can block electrode surface. Because more ferrocyanide is being produced after the enzymatic oxidation of glucose, it starts accumulating beyond the electrode surface. Because of the smaller area of the WE, mass transport becomes more prevalent to move these reduced mediator molecules towards the electrode surface, decreasing the measured currents. The calculated LOD was 4 mg/dL, which demonstrates the good detection capacity in extended ranges. However, despite the upper limit of the first linearity range being 15 mM (270 mg/dL), detection of hyperglycemic states is still possible, maintaining the compatibility of use for glucose quantification.

Finally, the analytical performance was also analyzed in relation to the applicability of the measurements in the context of diabetes diagnosis and prognosis, using the Parkes consensus error grid and the ISO15197:2013 standard (n=32). The first analysis using the Parkes error grid (**Figure 3.9a**) aims to detail how many of the measurements fall within a correct diagnosis (area A), compared to the possibility of misdiagnoses, that could influence therapy to varying degrees of severity (areas B to E). Results using miniaturized test strips and serum samples with known concentration show that most measurements were within zone A, referring to correct diagnosis, with no influence on clinical action. Six of the measurements were in zone B (18.75 %), indicating a variability of the strips that could lead to cases of altered clinical action, but with a negligible effect on the clinical outcome of patients. Of the 32 strips used in these measurements, none were found in any of the other zones, in relation to possible clinical decisions that could lead to risks for patients. The same results were also analyzed using the Bland-Altman precision graph (**Figure 3.9b**), which shows the difference obtained between the tested measurement method and a standard measurement or, in this case, by the standard addition method. According to ISO 15197:2013, 95% of the samples must be within a stipulated range of variation. Up to 100 mg/dL, the strips may not show a variability of more than 15 mg/dL, while above 100 mg/dL, a variation of 15% in relation to the correct value is tolerable. According to these criteria, the sensors show an accuracy of 72% (9 samples outside the tolerance

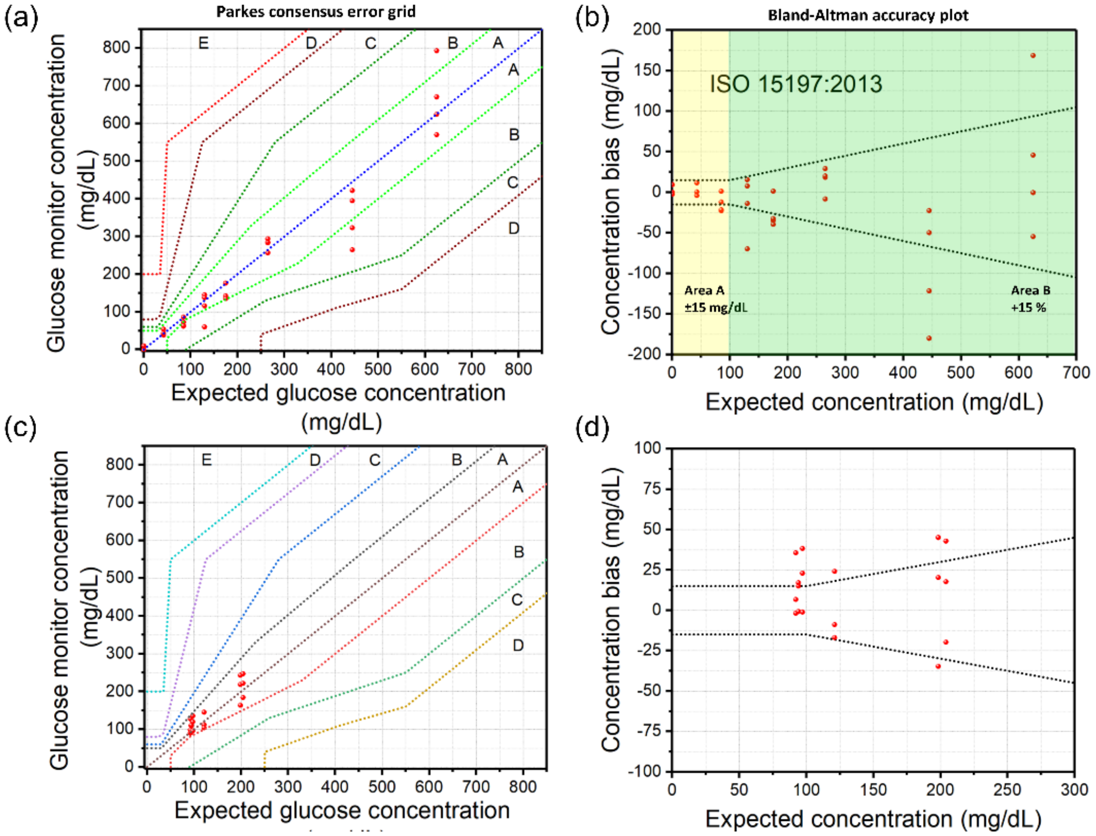

Figure 3.9 - Validation of miniaturized test strips using human serum samples. (a) Parkes consensus error grid and (b) Bland-Altman accuracy plot for testing with human serum samples using the standard addition method. Parkes consensus error grid (c) and Bland-Altman accuracy plot for testing under simulated real environment.

range). This result falls short of what is needed to fully validate this technology but demonstrates a Technology Readiness Level (TRL) of laboratory demonstration and simulated application environment.

A final validation of the test strips was carried out in a simulated real environment, in collaboration with NOVA-NMS, through real tests with blood samples collected using the standard blood prick method. At the same time, these samples were measured both with a commercial glucose meter (Contour Next, Bayer) and with the test strips. This initial validation was carried out with two volunteer subjects, using an Oral Glucose Tolerance Test (OGTT) protocol. In this protocol, fasting blood glucose is measured, followed by the ingestion of a controlled amount of glucose. A new measurement is then taken after 30 minutes to determine the participant's ability to metabolize glucose. Furthermore, two stored plasma samples collected from individuals with diabetes mellitus were also tested with the LIG-based test trips. A summary of the results is shown in **Table 3.4**.

Table 3.4 - Results obtained in the validation test of the system developed with real blood samples obtained in a laboratory environment (NOVA-NMS).

Samples	Commercial glucometer (mg/dL)	LIG test strips (mg/dL) (n=3)
Subject 1 - fasting	92	105.5 ± 16.0
Subject 1 – after 30 min	121	120.5 ± 17.8
Subject 2 - fasting	94	104.5 ± 7.9
Subject 2 – after 30 min	97	117.0 ± 16.2
Stored plasma samples		
#1	198.3	205.6 ± 33.3
#2	204.0	217.6 ± 25.7

An analysis of the results indicates some discrepancy between the values obtained with the commercial glucometer and the LIG test strips, with blood glucose values measured with LIG-based strips showing higher concentrations. Several reasons can explain this situation, including (1) the fact that the calibrations and measurements were made with different batches, manufactured at different times. But the main one is related to (2) the use of a calibration curve obtained with a different matrix (human serum). This may indicate possible matrix effects, indicating that there may be interference from other blood components and biomarkers in the magnitude of measured concentrations. To resolve this situation, more robust validation studies would be needed, where the calibration used to extrapolate measured blood glucose values would have to be done only with blood samples, to understand how much these interferents might affect the effectiveness of the system.

However, the system functioned well in its ability to keep up with the upward trend in blood glucose associated with the oral tolerance test. After oral consumption of glucose (30-minute measurement), the concentration values increase for both participants, which would be expected. It should be noted, however, that for participant 2, the blood glucose values measured at both times did not show a significant increase, which was attributed to some measurement error associated with the commercial system. In addition, two stored blood plasma samples (provided by NOVA-NMS, donor data remained anonymous in the experiment) were also measured, with values characteristic of hyperglycemia. Once again, the system's ability to follow the trend of increasing concentrations was demonstrated, with similar concentration values for both systems around 200 mg/dL. The results are also encapsulated in **Figure 9.3c-d**, which shows Clarke's error grid and the precision graph according to the ISO15197:2013 standard. Regarding the clinical relevance of the measurements according to Clarke's grid, all the measurements are in zone A. However, the evidence presented above is more strongly reflected in the precision grid, where a high number of measurements fall above the measurement tolerance levels

3.6 Conclusions

This work showed that LIG is a powerful and versatile material, displaying compatibility with scalable, flexible and efficient fabrication of electronic devices for multiple applications. With this work, we showed its applicability towards common, commercial cellulosic substrates, namely chromatography paper and office paper, chemically modified with sodium borate as fire retardant chemical, that aids in the graphitization of cellulose into multilayer, laser-induced graphitic material. This paper based LIG was fully characterized in terms of its surface chemistry, with Raman spectra showing the characteristic D, G and 2D peaks of carbon-based, with I_D/I_G ratio as low as 0.987 showing less defect dense graphitic material being synthesized when higher laser power and scan speed are employed, while increasing I_{2D}/I_G values as high as 0.749, portraying the multi-layered nature of the material. This paper based LIG also presented good electrical properties, with R_{sh} as low as 56.0 $\Omega.sq^{-1}$. Using standard redox mediator $Fe(CN)_6^{3-/4-}$ for electrochemical characterization of planar electrodes in a three-electrode architecture, quasi-reversible electron transfer was demonstrated, with high electrochemical surface area. Electron transfer kinetics of these LIG-based electrochemical sensors was also characterized, showing good results considering that all measurements were performed on chip, with no external electrodes of conventional size, thereby allowing the use of small sample volumes. Based on this characterization, simple, enzymatic glucose biosensors were tested to determine the applicability of this paper based LIG towards amperometric sensor development.

Overall, it may be said that simple, disposable, inexpensive biosensors can be developed using this laser irradiation approach for electrode fabrication, with improved sustainability. With further study and optimization of other laser parameters towards LIG synthesis, the possibility of performing compatible electrochemical treatments towards electrodes and introducing other enzyme immobilization and electrode modification strategies, promising, high-efficiency biosensors can be developed with improved sustainability, lower-cost and higher accessibility for multiple analytes of interest.

References

1. Amine, A., Mohammadi, H., Bourais, I. & Palleschi, G. Enzyme inhibition-based biosensors for food safety and environmental monitoring. *Biosensors and Bioelectronics* vol. 21 1405–1423 (2006).
2. Arduini, F. *et al.* Origami multiple paper-based electrochemical biosensors for pesticide detection. *Biosens. Bioelectron.* **126**, 346–354 (2019).
3. Yáñez-Sedeño, P., Agüí, L., Campuzano, S. & Pingarrón, J. M. What Electrochemical Biosensors Can Do for Forensic Science? Unique Features and Applications. *Biosensors* **9**, 127 (2019).
4. Shaw, L. & Dennany, L. Applications of electrochemical sensors: Forensic drug analysis. *Current Opinion in Electrochemistry* vol. 3 23–28 (2017).
5. Costa, M. N. *et al.* A low cost, safe, disposable, rapid and self-sustainable paper-based platform for diagnostic testing: lab-on-paper. *Nanotechnology* **25**, 094006 (2014).
6. da Silva, E. T. S. G. *et al.* Electrochemical Biosensors in Point-of-Care Devices: Recent Advances and Future Trends. *ChemElectroChem* **4**, 778–794 (2017).
7. Zhang, D. & Liu, Q. Biosensors and bioelectronics on smartphone for portable biochemical detection. *Biosensors and Bioelectronics* vol. 75 273–284 (2016).
8. Arduini, F. *et al.* Electrochemical biosensors based on nanomodified screen-printed electrodes: Recent applications in clinical analysis. *TrAC - Trends in Analytical Chemistry* vol. 79 114–126 (2016).
9. Kucherenko, I. S., Soldatkin, O. O., Kucherenko, D. Y., Soldatkina, O. V. & Dzyadevych, S. V. Advances in nanomaterial application in enzyme-based electrochemical biosensors: a review. *Nanoscale Advances* vol. 1 4560–4577 (2019).
10. Teymourian, H., Barfidokht, A. & Wang, J. Electrochemical glucose sensors in diabetes management: an updated review (2010–2020). *Chem. Soc. Rev.* **49**, 7671–7709 (2020).
11. Rackus, D. G., Shamsi, M. H. & Wheeler, A. R. Electrochemistry, biosensors and microfluidics: a convergence of fields. *Chem. Soc. Rev.* **44**, 5320–5340 (2015).
12. Power, A. C., Gorey, B., Chandra, S. & Chapman, J. Carbon nanomaterials and their application to electrochemical sensors: A review. *Nanotechnology Reviews* vol. 7 19–41 (2018).
13. Ramnani, P., Saucedo, N. M. & Mulchandani, A. Carbon nanomaterial-based electrochemical biosensors for label-free sensing of environmental pollutants. *Chemosphere* **143**, 85–98 (2016).
14. Song, Y. *et al.* Recent advances in electrochemical biosensors based on graphene two-dimensional nanomaterials. *Biosens. Bioelectron.* **76**, 195–212 (2016).
15. Chang, T. L., Chen, Z. C. & Tseng, S. F. Laser micromachining of screen-printed graphene for forming electrode structures. *Appl. Surf. Sci.* **374**, 305–311 (2016).
16. Lin, J. *et al.* Laser-induced porous graphene films from commercial polymers. *Nat. Commun.* **5**, 5714 (2014).
17. Ye, R., James, D. K. & Tour, J. M. Laser-Induced Graphene: From Discovery to Translation. *Advanced Materials* vol. 31 (2019).
18. Nayak, P., Kurra, N., Xia, C. & Alshareef, H. N. Highly Efficient Laser Scribed Graphene Electrodes for On-Chip Electrochemical Sensing Applications. *Adv. Electron. Mater.* **2**, 1600185 (2016).
19. Cardoso, A. R. *et al.* Molecularly-imprinted chloramphenicol sensor with laser-induced graphene electrodes. *Biosens. Bioelectron.* **124–125**, 167–175 (2019).
20. Marques, A. C., Cardoso, A. R., Martins, R., Sales, M. G. F. & Fortunato, E. Laser-Induced Graphene-Based Platforms for Dual Biorecognition of Molecules. *ACS Appl. Nano Mater.* **3**, 2795–2803 (2020).
21. Carvalho, A. F. *et al.* Laser-Induced Graphene Strain Sensors Produced by Ultraviolet Irradiation of Polyimide. *Adv. Funct. Mater.* **28**, 1805271 (2018).
22. Samouco, A., Marques, A. C., Pimentel, A., Martins, R. & Fortunato, E. Laser-induced electrodes towards low-cost flexible UV ZnO sensors. *Flex. Print. Electron.* **3**, 044002 (2018).

23. Peng, Z., Lin, J., Ye, R., Samuel, E. L. G. & Tour, J. M. Flexible and stackable laser-induced graphene supercapacitors. *ACS Appl. Mater. Interfaces* **7**, 3414–3419 (2015).
24. Mahmood, F., Zhang, H., Lin, J. & Wan, C. Laser-Induced Graphene Derived from Kraft Lignin for Flexible Supercapacitors. *ACS Omega* **5**, 14611–14618 (2020).
25. Park, H., Kim, M., Kim, B. G. & Kim, Y. H. Electronic Functionality Encoded Laser-Induced Graphene for Paper Electronics. *ACS Appl. Nano Mater.* **3**, 6899–6904 (2020).
26. Singh, S. P., Li, Y., Zhang, J., Tour, J. M. & Arnusch, C. J. Sulfur-Doped Laser-Induced Porous Graphene Derived from Polysulfone-Class Polymers and Membranes. *ACS Nano* **12**, 289–297 (2018).
27. Han, X. *et al.* Laser-Induced Graphene from Wood Impregnated with Metal Salts and Use in Electrocatalysis. *ACS Appl. Nano Mater.* **1**, 5053–5061 (2018).
28. Zhang, C., Xie, Y., Zhang, C. & Lin, J. Upgrading coal to multifunctional graphene based materials by direct laser scribing. *Carbon N. Y.* **153**, 585–591 (2019).
29. Qin, R. *et al.* Flexible Fabrication of Flexible Electronics: A General Laser Ablation Strategy for Robust Large-Area Copper-Based Electronics. *Adv. Electron. Mater.* **5**, 1900365 (2019).
30. Rodriguez, R. D. *et al.* Ultra-Robust Flexible Electronics by Laser-Driven Polymer-Nanomaterials Integration. *Adv. Funct. Mater.* **31**, 2008818 (2021).
31. You, R. *et al.* Laser Fabrication of Graphene-Based Flexible Electronics. *Adv. Mater.* **32**, 1901981 (2020).
32. Liu, S. *et al.* Laser Sintering of Liquid Metal Nanoparticles for Scalable Manufacturing of Soft and Flexible Electronics. *ACS Appl. Mater. Interfaces* **10**, 28232–28241 (2018).
33. Li, D., Lai, W.-Y., Feng, F. & Huang, W. Post-Treatment of Screen-Printed Silver Nanowire Networks for Highly Conductive Flexible Transparent Films. *Adv. Mater. Interfaces* **8**, 2100548 (2021).
34. Cheng, T. *et al.* Inkjet-Printed High-Performance Flexible Micro-Supercapacitors with Porous Nanofiber-Like Electrode Structures. *Small* **15**, 1901830 (2019).
35. Li, D., Lai, W. Y., Zhang, Y. Z. & Huang, W. Printable Transparent Conductive Films for Flexible Electronics. *Advanced Materials* vol. 30 1704738 (2018).
36. Cheng, T. *et al.* Conductive Hydrogel-Based Electrodes and Electrolytes for Stretchable and Self-Healable Supercapacitors. *Adv. Funct. Mater.* **31**, 2101303 (2021).
37. Rao, L. T., Dubey, S. K., Javed, A. & Goel, S. Laser induced graphene electrodes enhanced with carbon nanotubes for membraneless microfluidic fuel cell. *Sustain. Energy Technol. Assessments* **45**, 101176 (2021).
38. Noviana, E., McCord, C. P., Clark, K. M., Jang, I. & Henry, C. S. Electrochemical paper-based devices: Sensing approaches and progress toward practical applications. *Lab Chip* **20**, 9–34 (2019).
39. Gebretsadik, T. *et al.* Recent advances in and potential utilities of paper-based electrochemical sensors: Beyond qualitative analysis. *Analyst* vol. 144 2467–2479 (2019).
40. de Araujo, W. R. *et al.* Single-Step Reagentless Laser Scribing Fabrication of Electrochemical Paper-Based Analytical Devices. *Angew. Chemie - Int. Ed.* **56**, 15113–15117 (2017).
41. Mendes, L. F., de Siervo, A., Reis de Araujo, W. & Longo Cesar Paixão, T. R. Reagentless fabrication of a porous graphene-like electrochemical device from phenolic paper using laser-scribing. *Carbon N. Y.* **159**, 110–118 (2020).
42. Chyan, Y. *et al.* Laser-Induced Graphene by Multiple Lasing: Toward Electronics on Cloth, Paper, and Food. *ACS Nano* **12**, 2176–2183 (2018).
43. Reynolds, M. *et al.* Laser-engraved ammonia sensor integrating a natural deep eutectic solvent. *Microchem. J.* **157**, 105067 (2020).
44. Nine, M. J., Tran, D. N. H., Tung, T. T., Kabiri, S. & Losic, D. Graphene-Borate as an Efficient Fire Retardant for Cellulosic Materials with Multiple and Synergetic Modes of Action. *ACS Appl. Mater. Interfaces* **9**, 10160–10168 (2017).
45. Nagieb, Z. A., Nassar, M. A. & El-Meligy, M. G. Effect of Addition of Boric Acid and Borax on Fire-

Retardant and Mechanical Properties of Urea Formaldehyde Saw Dust Composites. *Int. J. Carbohydr. Chem.* **2011**, 1–6 (2011).

46. the United Nations. Take Action for the Sustainable Development Goals – United Nations Sustainable Development. *United Nations sustainable development* https://www.un.org/sustainabledevelopment/sustainable-development-goals/ (2020).
47. Olsson, C., Jansson, H. & Swenson, J. The Role of Trehalose for the Stabilization of Proteins. *J. Phys. Chem. B* **120**, 4723–4731 (2016).
48. Carneiro, M. C. C. G., Moreira, F. T. C., Dutra, R. A. F., Fernandes, R. & Sales, M. G. F. Homemade 3-carbon electrode system for electrochemical sensing: Application to microRNA detection. *Microchem. J.* **138**, 35–44 (2018).
49. Childres, I., Jauregui, L. A., Park, W., Caoa, H. & Chena, Y. P. Raman spectroscopy of graphene and related materials. *New Dev. Phot. Mater. Res.* 403–418 (2013).
50. Guo, J. *et al.* Photoluminescent Hybrids of Cellulose Nanocrystals and Carbon Quantum Dots as Cytocompatible Probes for in Vitro Bioimaging. *Biomacromolecules* **18**, 2045–2055 (2017).
51. Lee, S. & Jeon, S. Laser-Induced Graphitization of Cellulose Nanofiber Substrates under Ambient Conditions. *ACS Sustain. Chem. Eng.* **7**, 2270–2275 (2019).
52. Zhao, P. *et al.* Replacing the metal electrodes in triboelectric nanogenerators: High-performance laser-induced graphene electrodes. *Nano Energy* **75**, 104958 (2020).
53. Li, Y. *et al.* Laser-Induced Graphene in Controlled Atmospheres: From Superhydrophilic to Superhydrophobic Surfaces. *Adv. Mater.* **29**, 1700496 (2017).
54. Burke, M. *et al.* Fabrication and Electrochemical Properties of Three-Dimensional (3D) Porous Graphitic and Graphenelike Electrodes Obtained by Low-Cost Direct Laser Writing Methods. *ACS Omega* **5**, 1540–1548 (2020).
55. Parmeggiani, M. *et al.* PDMS/Polyimide Composite as an Elastomeric Substrate for Multifunctional Laser-Induced Graphene Electrodes. *ACS Appl. Mater. Interfaces* **11**, 33221–33230 (2019).
56. Carvalho, A. F., Fernandes, A. J. S., Martins, R., Fortunato, E. & Costa, F. M. Laser-Induced Graphene Piezoresistive Sensors Synthesized Directly on Cork Insoles for Gait Analysis. *Adv. Mater. Technol.* **5**, 2000630 (2020).
57. Chyan, Y., Cohen, J., Wang, W., Zhang, C. & Tour, J. M. Graphene Art. *ACS Appl. Nano Mater.* **2**, 3007–3011 (2019).
58. Kulyk, B. *et al.* Laser-Induced Graphene from Paper for Mechanical Sensing. *ACS Appl. Mater. Interfaces* **13**, 10210–10221 (2021).
59. Bard, A. J. & Faulkner, L. F. *Electrochemical methods: Fundamental and Applications. Wiley* (2001).
60. Moldenhauer, J., Meier, M. & Paul, D. W. Rapid and Direct Determination of Diffusion Coefficients Using Microelectrode Arrays. *J. Electrochem. Soc.* **163**, H672–H678 (2016).
61. Nicholson, R. S. Theory and Application of Cyclic Voltammetry for Measurement of Electrode Reaction Kinetics. *Anal. Chem.* **37**, 1351–1355 (1965).
62. Lavagnini, I., Antiochia, R. & Magno, F. An extended method for the practical evaluation of the standard rate constant from cyclic voltammetric data. *Electroanalysis* **16**, 505–506 (2004).
63. Xu, S., Qi, H., Zhou, S., Zhang, X. & Zhang, C. Mediatorless amperometric bienzyme glucose biosensor based on horseradish peroxidase and glucose oxidase cross-linked to multiwall carbon nanotubes. *Microchim. Acta* **181**, 535–541 (2014).
64. Şahin, S. A simple and sensitive hydrogen peroxide detection with horseradish peroxidase immobilized on pyrene modified acid-treated single-walled carbon nanotubes. *J. Chem. Technol. Biotechnol.* **95**, 1093–1099 (2020).
65. Adeel, M. *et al.* Recent advances of electrochemical and optical enzyme-free glucose sensors operating at physiological conditions. *Biosensors and Bioelectronics* vol. 165 112331 (2020).
66. Heller, A. & Feldman, B. Electrochemical glucose sensors and their applications in diabetes management. *Chemical Reviews* vol. 108 2482–2505 (2008).

67. Sharma, D., Lim, Y., Lee, Y. & Shin, H. Glucose sensor based on redox-cycling between selectively modified and unmodified combs of carbon interdigitated array nanoelectrodes. *Anal. Chim. Acta* **889**, 194–202 (2015).
68. Ramli, N. I., Abd-Wahab, M. F. & Salim, W. W. A. W. Characterization of enzymatic glucose biosensor in buffer solution, in artificial saliva, and in potassium ferricyanide by linear sweep voltammetry. in *AIP Conference Proceedings* vol. 2031 020037 (American Institute of Physics Inc., 2018).
69. KAWAGURI, M., YOSHIOKA, T. & NANKAI, S. Disposable Glucose Sensor Employing Potassium Ferricyanide as a Mediator. *Denki Kagaku oyobi Kogyo Butsuri Kagaku* **58**, 1119–1124 (1990).
70. Arslan, F. & Beskan, U. An amperometric biosensor for glucose detection from glucose oxidase immobilized in polyaniline–polyvinylsulfonate–potassium ferricyanide film. *Artif. Cells, Nanomedicine, Biotechnol.* **42**, 284–288 (2014).

4

INFLUENCE OF CO_2 LASER-BEAM MODELLING ON ELECTRONIC AND ELECTROCHEMICAL PROPERTIES OF LASER-INDUCED GRAPHENE

Laser-induced graphene (LIG) allows for the fabrication of cost-effective, flexible electrodes on a multitude of recyclable and sustainable substrates, for implementation within electrochemical biosensors. This work expands on current LIG research, by experimentally modelling the effects of several CO_2 laser irradiation variables towards resulting conductive and electrochemical properties of paper-derived LIG. Instead of relying on the established paradigm of manipulating power and scan speed of the laser irradiation process for optimized outcomes, modelling of underlying laser operation principles for pulse modulation, regarding pulse repetition frequencies, pulse duration and defocus are presented as the key aspects dominating graphitization processes of materials. This approach shows that graphitization is dominated by appropriate pulse durations, dictating the time the substrate is exposed to each laser pulse, with laser fluence and irradiation defocus influencing the resulting conductive properties, with sheet resistances as low as 14 $\Omega.sq^{-1}$. Similarly, fabrication settings controlled by these parameters have a direct influence on the properties of LIG-based electrochemical three-electrode systems, with optimized fabrication settings reaching electrochemically active surface area as high as 35 mm^2 and heterogeneous electron transfer rates of 3.4×10^{-3} $cm.s^{-1}$. As a proof-of-concept, the production of environmentally friendly, accessible, and biocompatible pH sensors is demonstrated, employing riboflavin as a pH-sensitive element.

Keywords: laser-induced graphene, CO_2 laser, paper electronics, electrochemical sensors, pH, sustainable production

The literature presented in this chapter is published in:

- Pinheiro, T., Rosa, A., Ornelas, C., Coelho, J., Fortunato, E., Marques, A. C., & Martins, R. (2023). Influence of CO_2 laser beam modelling on electronic and electrochemical properties of paper-based laser-induced graphene for disposable pH electrochemical sensors. *Carbon Trends*, 11, 100271.

4.1 Introduction

The use of distinct carbon-based materials, such as carbon nanotubes, graphene, and other graphene-related materials in electrochemical sensing approaches has been a key research focus [1,2]. Their use is based on relative chemical inertness, simultaneously allowing for wide potential windows in aqueous electrolytes, with low background currents, while improving charge transfer processes due to excellent conductivity and high specific surface areas [3]. More specifically, graphene and graphene-based nanocomposites have demonstrated great significance and applicability to produce electrochemical devices and sensors with improved analytical performance, serving as an important building blocks within sensor architectures.[4] By themselves, these materials have been employed for modification of disk electrodes [5], paste electrodes [6] and have also been employed for the fabrication of electrode architectures by printing methods.[7] Recently, a new class of graphene-like materials synthesized by laser irradiation approaches have appeared, more specifically, laser-induced graphene (LIG) [8]. Distinctively to printing approaches, LIG can be simultaneously synthesized and patterned, without the need for catalysts, ink formulations, and masks, increasing the prototyping potential of carbon-based electrode geometries. Concurrently, the use of different precursor materials and laser irradiation schemes allows for tailoring of material properties, in terms of morphological, chemical and electric conductivity outcomes [9]. The first material employed for this purpose was polyimide (PI), a petroleum-based polymer, used prolifically for electrochemical biosensor development as an electrode material in different conformations [10]. However, due to its petroleum-based origin, it raises some concerns in terms of accessibility and sustainability when developing disposable biosensors. This has led to the study of different precursor materials, mainly derived from vegetable biomass or other natural polysaccharide sources, and their suitability for electrode fabrication in different electronic applications [11].

In terms of LIG synthesis mechanisms, these are mainly based on photothermal processes that lead to the breaking of more susceptible bonds within the precursors' chemical structure, followed by a thermally induced reorganization of remaining carbon into graphene lattices composing this 3D graphitic material [9]. As such, these dynamic processes have been manipulated by different approaches, taking advantage of the high-throughput, fast prototyping nature of these direct laser writing techniques. For PI, several studies have focused on studying the effect of several laser fabrication parameters on the resulting outcomes of laser irradiation. Such simulation and empirical studies have focused on determining the tolerance of the substrate to different energy levels, determined by exposure to different power, irradiation duration, and areal energy density [12,13]. For single-pulsed conversion, pulse duration is a key variable, determining the distribution of amorphous or conductive carbon materials within the irradiated pulse area, as well as its overall shape [13]. When moving to raster processes for patterning, the movement of the laser beam introduces different variables that take a key role in the conversion dynamics, namely pulse frequency and the degree of overlapping between adjacent pulses, that allow for control of thermal accumulation and possible improvements on the photothermal graphitization processes [12,14]. Besides these, other variables that can alter pulse superposition patterns have also been studied, namely laser beam defocus [15]. Defocusing the laser creates different beam spot diameters, that allow for manipulation of laser fluence, while increasing pulse superposition. These principles are key when investigating these dynamic processes and resulting morphological characteristics of LIG structures [15], as well as the distribution of graphene and its Raman profile over the irradiated area [13], which influence the resulting electrical conductivity of LIG patterns and electrodes [16]. Similar approaches can also be explored to optimize electrode performance in several applications, based on exploring the effects of fabrication settings towards device performance, including for electrochemical biosensors [17].

For lignocellulosic and cellulosic precursor substrates, several considerations must be taken when attempting to graphitize these materials, related to the dominant presence of aliphatic carbon structures and decreased thermal resistance [11]. The main approaches to achieve graphitization in these substrates have been the introduction of fire-retardants [18] or the use of ultra-short laser pulse systems [19]. Fire retardants increase the thermal resistance of the precursor material, allowing for the molecular conversion processes to occur without significant ablation of precursor chemical structures [20]. For ultra-short laser pulse systems, mostly femtosecond lasers, thermal accumulation occurs at much more controlled heat ramps, that minimize the thermal degradation of aliphatic structures, while allowing for controlled bond breaking and rearrangement. Thus, specific treatments or irradiation atmospheres are not needed, as is the case when employing CO_2 laser sources [21]. However, LIG-based applications using several cellulosic substrates synthesized with CO_2 lasers have recently appeared [22], being of interest to study laser beam and material interactions, to better understand the dynamics underlying resulting material properties. Although many reports have been presented for simulation and empiric modeling of laser-induced PI graphitization, the surge of new precursor substrates brings the need to perform such studies on materials that present distinct chemical compositions, thermal resistances, and morphologies, including paper substrates.

In this study, experimental modeling of pulsed operation characteristics of CO_2 laser beam and resulting conductive and electrochemical properties of paper-based LIG is performed, to determine the key fabrication settings influencing the conversion of this precursor substrate. Fire-retardant and wax-modified paper is employed for irradiation [20] aiming at process-properties optimization towards the fabrication of disposable electrochemical biosensor strips. Instead of the approach of studying the influence of power and scan speed, commonly employed when using CO_2 lasers, this study focuses on the pulse modulation set by these variables, in terms of pulse frequency and duration. In addition, the influence of defocus and additional irradiation cycles are assessed, in terms of their influence over pulse superposition and areal energy density towards graphitization outcomes. The same approach is also employed in the fabrication of planar electrochemical cells, to determine the effect of distinct fabrication settings on the charge transfer capabilities of these devices. Optimized fabrication settings are then employed to develop voltametric pH sensors. Taking advantage of the appealing characteristics of paper substrates in terms of their accessibility, recyclability and easy disposal, high-performance electronic elements and sensors can be fabricated and easily discarded, with much less carbon footprint, when compared to conventional consumer electronics [23].

4.2 Experimental Section

Reagents and Materials

All solutions were prepared using ultrapure laboratory grade Milli-Q water. Britton-Robinson (BR) buffers were comprised of a mixture of acetic (CH_3COOH), phosphoric (H_3PO_4), and boric acid (H_3BO_3), purchased from Sigma-Aldrich. Sodium tetraborate decahydrate ($Na_2B_4O_{7.10}H_2O$) and riboflavin (vitamin B2) were also attained from Sigma. Potassium hexacyanoferrate (III) ($K_3[Fe(CN)_6]$), and potassium hexacyanoferrate (II) trihydrate ($K_4[Fe(CN)_6].3H_2O$) were acquired from Roth. Sodium hydroxide (NaOH) was purchased from Labkem. All chemicals were used without any further purification. Whatman chromatography paper grade 1 (Whatman International Ltd., Florham Park, NJ, USA) was utilized as the substrate for LIG production and subsequent electrode fabrication after a wax pre-treatment using a Xerox ColorQube printer. A6 glossy plastic laminating pouches (Staples Europe BV., The Netherlands) were used to seal and encapsulate the paper-based sensors. Silver conductive ink (AG-510 silver ink, Conductive Compounds, Inc., Hudson, NH) was used to coat the electrical contacts, and Ag/AgCl ink (AGCL-675, Conductive Compounds, Inc., Hudson, NH) was implemented in the fabrication of the reference electrode (RE) of all sensors.

Paper substrate pre-treatment

Before the lasing procedure, Whatman paper grade 1 was chemically pre-treated. First, paper sheets were cut into A6 standard size (105 × 148 mm). Then, the sheets were soaked in sodium tetraborate decahydrate solution (0.1 M), for 10 minutes on each side, and left to dry overnight. Next, the paper was submitted to a wax coating, running the sheet through a Xerox ColoQube wax printer. The waxed paper was placed on a hot plate for 2 minutes at 120 °C, allowing the wax to melt and become embedded within the cellulose fibers. Wax treatment waterproofs the paper substrate, which is required for electrochemical sensor testing. All subsequent experiments and characterization steps were performed using pre-treated paper as a model precursor substrate.

LIG Synthesis and Properties Optimization

For the conversion of treated paper substrates, a VLS3.50 Universal Laser Systems CO_2 laser system was employed. This laser system generates a pulsed beam with 10.6 µm photon wavelength, the maximum power output of 50 W, and allows for a raster process with a maximum scan speed of 127 $cm.s^{-1}$. For pulse density manipulation, this system allows for the selection of points per inch (PPI) until a maximum of 1000 PPI (393 points per cm). As such, for different raster speed settings, the laser pulses operate at distinct frequencies. This pulse repetition frequency (PRF) is given by equation 4.1, in function of raster speed setting:

$$\text{PRF (Hz)} = \%\ \text{Speed} * \text{Max speed} * \text{PPI} \tag{4.1}$$

Depending on the power and scan speed parameter settings, the power output of the laser beam pulses is manipulated to match the corresponding power percentage, by changing the pulse width (PW).

$$\text{PW (s)} = (1/\text{PRF}) * \%\ \text{power} \tag{4.2}$$

This dictates the duty cycle and how long the laser pulse is activated during each pulse cycle time. With a rise and fall time of 120 µs, each total laser pulse duration is given by the sum of PW and a total rise and fall time of 240 µs. As such, control of PRF and PW can lead to two distinct operation modes. For PRF below 4000 Hz, the laser operates as a pulsed laser. For higher PRF, pulse operations overlap, leading to an irradiation closer to a continuous wave laser. As such, this study was performed for power and speed percentages between 1 and 8 %, to ensure a pulsed laser operation.

Additionally, two more variables were studied, namely laser beam defocus and number of laser irradiation cycles for patterning. This laser system allows for the manipulation of the laser stage and the z-axis, allowing for defocus irradiation that manipulates laser beam spot size. With a knowledge of PW, laser pulse fluence was calculated based on this parameter and the maximum laser power and the selected defocus spot area:

$$\text{Laser fluence} = (\text{Power} * \text{PW}) / (\pi * \omega_z^2) \tag{4.3}$$

Where the power is constant at 50 W (J.s-1) and ω_z is the beam spot radius for a specific z defocus. To perform process-properties optimization of these fabrication variables, LIG square patterns with 5x5 mm dimensions were fabricated. For sheet resistance measures, silver contacts were painted in the corners of the square patterns. Measures were performed using BioRad HL5500 four-point probe equipment. Assessment of chemical characteristics of the material was performed, using a Renishaw® inVia™ Qontor® confocal Raman microscope (Gloucestershire, UK) equipped with a Renishaw Centrus 2957T3 detector and 532 nm laser. Besides, X-ray photoelectron spectroscopy (XPS, Kratos Axis Supra, UK) equipped with a monochromated Al Kα radiation (1486.6 eV) was also performed.

Electrochemical sensor fabrication

Three-electrode sensors consisting of one working electrode (WE), counter electrode (CE), and RE were designed in Adobe Illustrator and lased onto a pre-treated paper substrate. Then they were placed and sealed in plastic laminating pouches with previously laser-cut electrical contact and working area openings, establishing a passivation layer. The plastic sheets were previously covered with adhesive tape to serve as masks in the contact painting process. The conductive tracks were established by painting with silver conductive ink over the respective openings of the passivation layer. Ag/AgCl ink was applied over the LIG area corresponding to the RE. After curing on a hotplate for 1 h at 50 ºC, adhesive masks were removed, and the sensors were ready for testing.

Before characterization, electrochemical pre-treatment was applied by running 5 CV cycles, from -2.0 to 2.0 V, at a scan rate of 150 mV.s^{-1} with 60 µL of KCl (0.1 M) as the supporting electrolyte. After pre-treatment, electrochemical performance was studied with CV scans, from -0.3 to 0.7 V, at a scan rate from 10 to 150 mV.s^{-1}, 6 cycles for each scan rate. Standard redox probe solution composed of $Fe(CN)_6^{3-}$ / $Fe(CN)_6^{4-}$ (5 mM) in supporting electrolyte was used in the experiments.

pH Sensor fabrication and testing

pH sensors were fabricated by modifying the WE with riboflavin. Riboflavin modification was performed by drop-casting 15 µL of riboflavin solution (3.2 mM) [24]. pH measurements with riboflavin modified WE were carried out using Square-Wave Voltammetry (SWV), from -2.00 to 2.00 V, amplitude of 0.25 V and frequency of 20 Hz. Testing was performed with in BR buffer solutions at different pHs, made with equal parts of previously prepared acetic, boric, and phosphoric acids solutions, all with a concentration of 0.4 M. NaOH (1.75 M) and HCl (0.70 M) were added to adjust the pH levels of the BR buffer solution.

4.3 Results and Discussion

4.3.1 Laser Parameter Optimization for LIG Fabrication on Paper

4.3.1.1 Modelling of CO2 laser system operation and fabrication parameters

A series of systematic studies were conducted to optimize the conductive properties of LIG patterns, exploring several variables in laser fabrication. The variables that can be directly defined in the laser control software were laser irradiation power percentage (P), raster scan speed percentage (S), and the defocus (z). In addition, for all the tested conditions, a defined PPI setting of 500 was used. This allows for the control of the laser fluence imposed over the substrates, and of different pulse profiles, set by speed and power percentage settings. **Figure 4.1a** shows a schematic of the laser beam control system and the pulse profiles that can be achieved with the used system. By manipulating the speed percentage parameters, kept between 1 and 8%, PRFs between 250 to 2000 Hz can be set for pulse repetition. From then on, variation of power percentage setting leads to differences in PW. For a speed percentage of

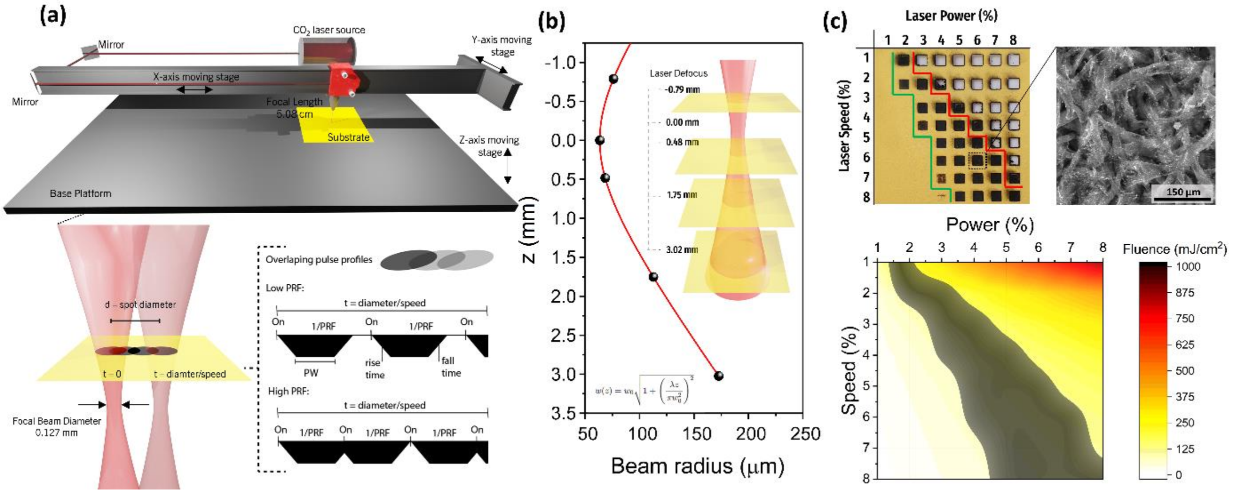

Figure 4.1 - CO$_2$ laser operation for LIG synthesis. (a) Schematic of laser beam and resulting pulse profiles manipulated by PRF and PW. (b) Calculation of laser beam spot radius for tested irradiation defocus z values. (c) LIG film matrix and fluence heatmap identifying graphitization region and its distribution in different fluence levels.

1%, power variation between 1 and 8% lead to PW between 40 to 320 µs, while for a speed percentage of 8%, PW varies between 5 and 40 µs. Considering the time it takes the laser lens to move the distance corresponding to one pulse diameter, the degree of overlapping can be determined, by taking the period between pulses (1/PRF) and total pulse time. Lower PRFs allow for complete pulse separation between subsequent pulses, leading to less thermal accumulation. In opposition, higher PRFs lead to the overlap of subsequent rise and fall of laser pulses, leading to higher energy and thermal accumulation between subsequent pulses. As previously shown, this thermal accumulation is an important consideration for LIG synthesis, allowing for higher temperatures to be reached, leading to more efficient bond breaking and rearrangement into graphene lattices [12]. For PRFs above 4000 Hz, not only the rise and fall times can overlap, but also the on-stage of beam operation, leading to a regimen approximating a continuous wave laser.

Besides pulse repetition and overlap profiles, the effect of laser spot size was also assessed, by performing the synthesis with different defocus conditions. By changing the irradiation plane, different beam spot radius and areas can be used, to manipulate the laser fluence and the degree of areal overlapping between subsequent pulses, to determine their effect over the conversion and LIG properties. **Figure 4.1b** shows the determination of beam radius (ω_z) for different irradiation planes, taking into consideration a Gaussian beam shape (**Table B1**). At focus, the beam has a radius ω_z = 63.5 µm. The laser system allows for the work stage to get close to the lens, creating a negative defocus, to a maximum distance from the focus plane of

$z = -0.79$ mm, corresponding to $\omega_z = 76$ µm. For the opposite direction, the z axis can move to larger distances, with the farthest tested positive defocus corresponding to $z = 3.02$ mm, reaching $\omega_z = 172$ µm. For each of the tested defocus distances, a matrix of power vs. speed percentages was constructed, to identify the graphitization region. **Figure 4.1c** shows the fabrication matrix for $z = -0.79$ mm, where the three distinct outcomes of ablation, absence of visual laser effects and graphitization can be distinguished. From this matrix, a heatmap of resulting laser fluence for the set beam area was constructed, overlapping with the identified graphitization zone. As visible, graphitization can occur at different fluence levels, as previously reported [15], leading to morphological transitions related to the response of the precursor material to the different imposed temperatures. Thus, it is visible that laser fluence is not the main variable responsible for the onset of graphitization. The same matrices and heatmaps were constructed for the remaining irradiation planes (**Figure B1**). A comparison shows that the graphitization regions have alterations in profile, shrinking in width for increasing positive defocus levels.

4.3.1.2 Pulse Modulation Influence on LIG Synthesis Outcomes

To better understand these effects, the relation between PRF and PW and the onset of carbonization and graphitization was further studied. To do so, heatmaps of irradiation outcomes for different PRFs and PWs were plotted for different irradiation planes, presented in Figure **4.2a-c**. These heatmaps were constructed by attributing a value to each of the laser irradiation outcomes (no effect = 0, graphitization = 1 and ablation = 2), as seen in the optimization matrices in **Figure 4.1c** and **Figure B1**. Then, these values were plotted vs. the corresponding values of PRF and PW resulting from the employed power and speed percentages. As can be seen for each heatmap, the graphitization regions span all the tested PRFs, that are directly related to the scanning speed employed in the raster process. However, the same does not occur for PW, since this parameter is dependent both on the speed and power percentages set in the operation. Thus, when speed percentage and corresponding PRF is determined, PW will be set depending on both this operation frequency and on the desired laser power output. This way, single pulses with the same PW, independent of the operational frequency, will result in the same output energy and substrate exposure time to the laser beam. Interestingly, it is then visible that for different PRFs, similar values of PW are needed for graphitization to occur. More specifically, for every tested irradiation plane, all carbonization and graphitization conditions occur between narrow values of PW between 20 and 60 µs. For $z = -0.79$ mm, the maximum PW values leading to graphitization without significant degradation of LIG structures

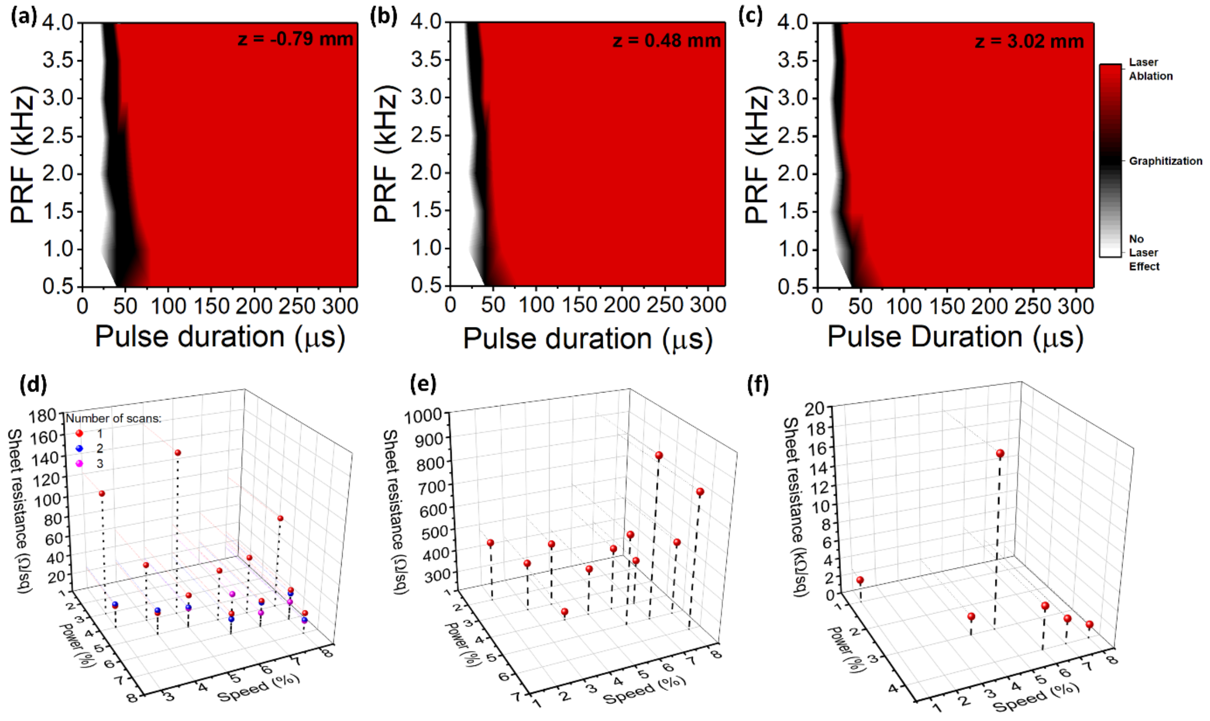

Figure 4.2 - Influence of fabrication settings on graphitization onset and conductivity. Heatmaps of laser irradiation outcomes as a function of PRF and PW for (a) z = -0.79 mm, (b) z = 0.48 mm and (c) z = 3.02 mm. Resulting sheet resistance values of LIG films synthesized at (d) z = -0.79 mm, (d) z = 0.48 mm and (e) z = 3.02 mm.

situates at 60 μs (PRF of 500 Hz), while for the remaining irradiation planes, there is a shift towards lower PWs. For z = 0.48 mm, only values equal or below 40 μs lead to carbonization and graphitization, while for z = 3 mm, 40 μs PW only leads to carbonization and graphitization for lower PRFs. For higher PW, excessive degradation and ablation of LIG chemical structures occur (zones depicted in red), rendering the films unusable. In terms of minimum PW values leading to carbonization and graphitization, the lowest pulse duration for z = - 0.79 mm corresponds to 25 μs, while for the remaining planes, it situates at 20 μs. In these cases of lower PW values, LIG is synthesized in conditions of elevated PRF, above 1500 Hz, where pulse overlap becomes more significant. These values and corresponding heatmaps were obtained with the same resolution of **Figure 4.1c**, based on a variation of 1% power and speed between samples. Thus, it is possible that graphitization may occur for intermediate values in the interface between graphitization and the remaining outcomes of ablation or absence of laser effects. However, increasing this resolution leads to a steep increase in the number of samples for analysis, so the 8x8 matrices were kept throughout the study.

The main finding of these experiments is that substrate exposure time to the laser beam, set by PW, is the dominant factor leading to graphitization. This laser system is a pulsed wave laser with 50 W maximum power, where the pulse output power is set by pulse width modulation and resulting duty cycle of each individual laser pulse. As such, the modified paper substrate only converts to LIG when exposed to 50 J for specific pulse duration intervals. Furthermore, this leads to the diagonal pattern of graphitization distribution present in **Figure 4.1c**, since for increasing PRF, higher power percentages are needed to place PW at this tolerance interval. When within this interval, other factors come into play when attempting to manipulate irradiation outcomes, for example laser fluence and laser beam spot area, resulting in distinct properties of LIG films, as visible in sheet resistance testing.

Figure 4.2d-f presents the results of sheet resistances measurements for all the resulting combinations of power and speed employed in this study. Results are only presented for conditions where sheet resistance was measurable, since for many fabrication combinations, there was excessive degradation of LIG films or visible carbonization, but the film was not conductive enough for the measure. This was mostly visible for the irradiation focal plane z = 1.75 mm. All measurements are reported in Table B2. As can be seen, relevant differences appear for the conductive properties of LIG films synthesized in different irradiation planes. For z = - 0.79 mm, sheet resistance varies from 160 ± 27.25 to 22 ± 1.9 $\Omega.sq^{-1}$, while for the remaining planes, there are substantial increases in measured sheet resistances. For z = 0.48 mm, sheet resistance varies between 248 ± 36.0 $\Omega.sq^{-1}$ and 918 ± 65.0 $\Omega.sq^{-1}$, while for z = 3.02 mm, there is a steep increase in sheet resistance to the $k\Omega.sq^{-1}$ range, with the lowest values achieved being of 2043 ± 171.88 $\Omega.sq^{-1}$. Two differences can be identified between the irradiation schemes for each set of planes, namely the fluence regimens dictated by the laser beam spot area and the convergent or divergent nature of the laser beam, depending on the negative and positive defocus. In terms of defocus, the laser beam area increases for both directions, meaning that similar laser fluences can be achieved by the same |z| defocus, leading to the same fluence regimens. However, it is visible that even in these cases, for example by comparing z = - 0.79 and z = 0.48 mm, where beam radiuses are ω_z = 76 and 68 µm, respectively, large differences in conduction are observed. Thus, it is visible that laser spot size and the resulting pulse overlapping profiles do not solely predict the resulting conductive nature of LIG films. On the other hand, it has been observed in many laser material processing applications, that positive and negative defocus have an effect on the interactions between the laser beam and the irradiated material [25]. For a negative defocus, there is a convergent nature of laser beam photons, that increases penetration efficiency. On the other hand, for positive defocus, the divergent beam nature diminishes this effect and can lead to different cross-sectional energy distributions [26], related to the larger path the beam has to travel to reach the substrates. Thus, the interaction of the laser beam and resulting temperature and depth conversion of the paper substrate is affected by the type of defocus, leading to different graphitization efficiencies. As such, it is visible that positive and negative defocus have great influence in paper-based LIG synthesis process using this laser system, dictating not only morphological and chemical characteristics, as previously reported for other materials, [15,27] but impacting the resulting conductive nature of the material. Interestingly, reports for laser irradiation of other materials has shown opposite effects of improvement in conduction for positive defocus, for example PI [15] and PEI [18], indicating that such phenomena related to the nature of defocus depends on the irradiated material and the characteristics of different laser systems.

Another interesting approach for improving the conductive properties of LIG films is performing multiple raster scans in the same irradiated area, to create subsequent graphitization cycles that can promote a more efficient bond rearrangement of pre-carbonized and graphitized material. As shown in **Figure 4.2d** and Table B3, for some fabrication combinations, performing two and even three cycles can progressively decrease the sheet resistance of LIG films, to levels on par with PI-derived LIG. For two irradiation cycles, the lowest obtained sheet resistance is situated at 14.78 ± 0.26 $\Omega.\ sq^{-1}$ for power and speed percentages of 7 and 8%, respectively. For three irradiation cycles, a larger pool of lower sheet resistance films can be created, but at the cost of higher patterning time and possible excessive degradation and ablation of LIG films. The lowest obtained sheet resistance was 14.00 ± 1.5 $\Omega.sq^{-1}$, for the same power and speed settings.

4.3.1.3 Chemical Characterization of Paper-Based LIG Films

Chemical characterization of LIG films synthesized at different irradiation planes was performed. Power and speed percentage settings that led to film engraving in all the studied irradiation planes were selected, more specifically 4 % power and 6 % speed. **Figure 4.3a** shows the Raman spectra obtained for LIG films synthesized using these parameters tested defocus levels. As visible, there are some alterations regarding peak intensity and peak ratios, presented in **Figure 4.3b**. Results present high defect density for all conditions, with some improvements for planes closer to the laser focal plane, namely for z = 0.48 mm. For this plane, there is a decrease in the I_D/I_G ratio and increase in I_{2D}/I_G ratio, ultimately reflecting the most conductive condition. For z = -0.79 and z = 1.75 mm, the LIG films did not present measurable conductivity, while for z = 3 mm, it presented a sheet resistance of 4742 $\Omega.sq^{-1}$. **Figure 4.3c** shows the effect of increasing laser power and resulting PW for constant speed of 6% (PRF = 1500 Hz), at the

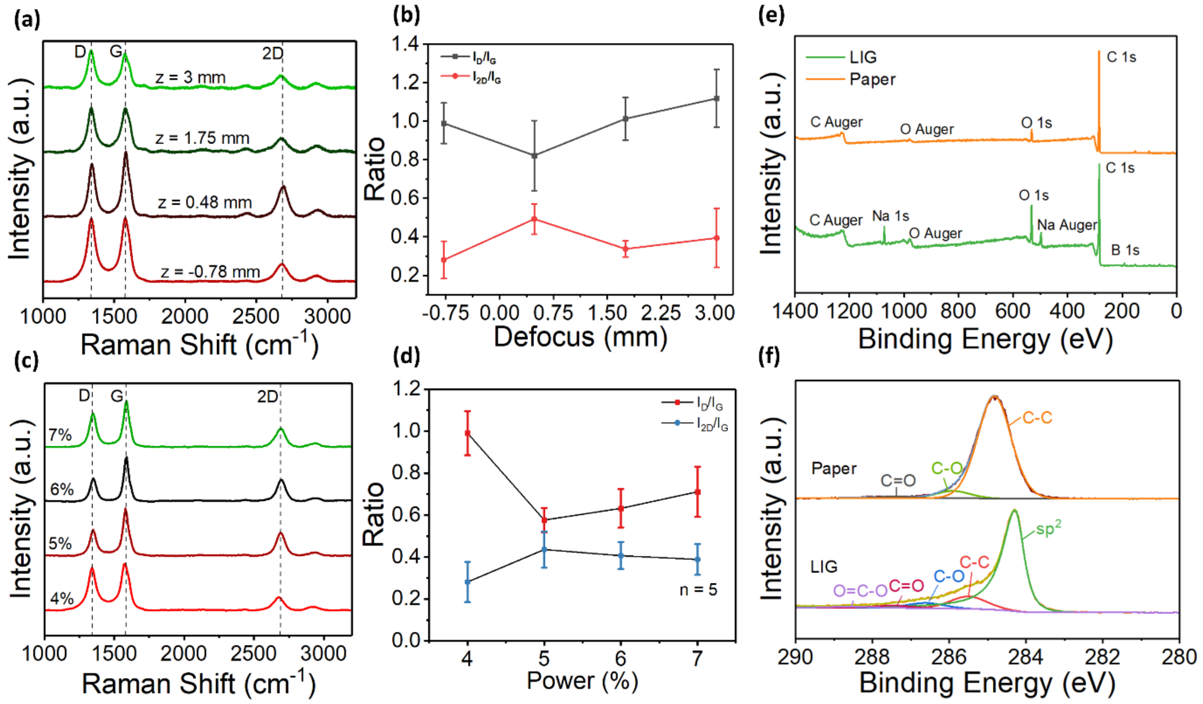

Figure 4.3 - Chemical characterization of LIG films depending on operational parameters. (a) Raman spectra of films synthesized with 4% power and 6% speed at different defocus levels and (b) corresponding Raman peak ratios. (c) Raman spectra of films synthesized at z = - 0.79 mm and 6% scanning speed and varying power percentages and (d) corresponding Raman peak ratios. (e) Wide XPS spectra and (f) C1s deconvoluted spectra comparison between paper and LIG synthesized using 6% power and speed settings at z = - 0.79 mm.

irradiation plane z = -0.79 mm. Results show that within the selected power interval, there is an optimal value of power that achieves the most attractive chemical properties. This is visible in **Figure 4.3d**, showing the plot of I_D/I_G and I_{2D}/I_G ratios. For a 5% power (PW = 33.3 µs), there is a minimum value of 0.58 ± 0.06 for the I_D/I_G ratio and a maximum value of 0.44 ± 0.09 for the I_{2D}/I_G ratio. For other power values, there is variations in both these ratios. All the results of Raman peak ratios are summarized in **Table B4. Figure 4.3e-f** present the comparative XPS spectra of the most conductive LIG film, synthesized employing 6 % power and speed. As visible, there is the appearance of peaks related with the fire-retardant modification in the wide XPS spectra, namely B1s and Na1s peaks. Regarding the C1s spectra, the appearance of the peak related to sp^2 hybridization within graphene lattices confirms the efficient graphitization of the modified paper substrate.

4.3.2 Influence of Fabrication Setting on Electrochemical Properties of LIG Three-Electrode Planar Cells

After understanding the dynamics governing the irradiation of the selected paper substrate and resulting conductive properties, their effect on the electrochemical properties of LIG-based three-electrode systems were studied. To do so, a fixed irradiation plane $z = -0.79$ mm was selected for electrode patterning, since this defocus resulted in the least resistive LIG chemical structures, important in efficient electrochemical diffusion and charge transfer processes [28]. CV studies were conducted on fabricated planar cells composed of three electrodes, presented in **Figure 4.4a**. The characteristics of the porous LIG electrode material and its conductivity have an impact in the mass transfer and subsequent diffusion of oxidized and reduced electrochemical species participating in electrochemical reactions, from the bulk electrolyte solution to the electrode surface. Thus, it is interesting to assess the influence of fabrication parameters and resulting conductive properties of the electrode materials towards these mass transport, surface diffusion and electron transfer processes, depicted in **Figure 4.4a**, that shape the resulting faradaic anodic and cathodic currents measured through CV.

Two distinct electrochemical parameters of the system were studied, namely the electrochemically active surface area - A_e , and the HET rate constant – k_0. CVs of electrochemical three electrode planar cells fabricated using 6 % power and speed setting were taken, using 1 and 2 scanning cycles for patterning, as an example. Voltammograms are shown in **Figure 4.4b-c**. As visible, faradaic cathodic and anodic peak currents for the reduction and oxidation of the ferri/ferrocyanide probes are present in the graphs. Two distinct differences can be seen from the comparison of the voltammograms at different scan rates. Besides the expected quasi-reversible behavior of the systems, characterized by the increase in cathodic and anodic peak separation (ΔE_p) with scan rate, an increase in peak currents and decrease in ΔE_p is reached when an additional patterning scan is employed. Using the Randles-Sevcik equation, that details the relationship between peak current, scan rate, and electrochemically active area, an A_e of 29.1 mm^2 was computed for a single patterning scan and 35.0 mm^2 for double scanning (**Figure 4.4d**). Employing the Nicholson method [29], detailing the relation between ΔE_p, scan rate and k_0, an electron transfer rate of 24.5×10^{-4} cm.s^{-1} for a single scan and 34.3×10^{-4} cms^{-1} for double scanning (**Figure 4.4e**) were achieved.

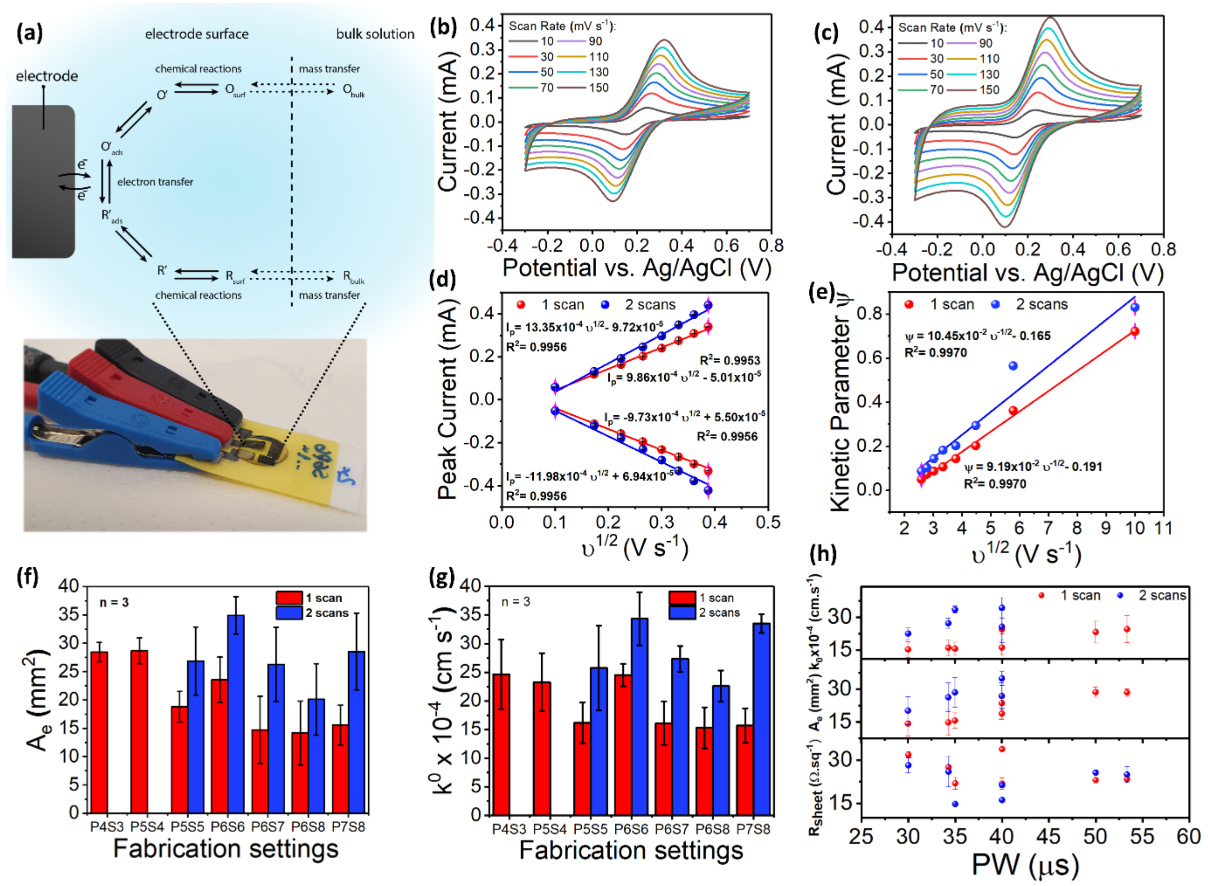

Figure 4.4 - Influence of fabrication settings on electrochemical properties of planar LIG electrochemical cells. (a) LIG-based planar electrochemical cells and potential-induced electrochemical mechanisms associated with faradaic redox current signals. Cyclic voltammograms of cells produced employing 6% power and speed settings for (b) 1 patterning scan and (c) 2 patterning scans. (d) Plots of anodic and cathodic peak currents and kinetic parameter Ψ derived from CVs, for calculation of electrochemically active surface area and k_0. Distribution of (e) electrochemically active surface area and (f) k_0 for different fabrication settings. (g) Plot of LIG sheet resistance, A_e and k_0 in function of fabrication setting PW.

The same analysis was performed for all the fabrication settings leading to conductive LIG and are presented in Figures **4.4f-g**. Unreported fabrication settings arise from the fact that LIG electrodes presented excessive degradation and ablation in their structure, leading to unwanted capillary movement of electrolyte toward silver contacts, rendering the cells unusable. Three repetitions (n=3) in stand-alone cells were performed for each fabrication setting, to compute mean A_e and k_0. As visible, most settings lead to improvements in both parameters when an additional patterning scan is performed, showing the more attractive electrochemical properties related to the improvement in electrode material conductivity. For fabrication settings P4S3 and P5S4, double patterning scans led to excessive degradation of electrodes, also rendering them unusable. From these results, two fabrication settings result in the most attractive properties, namely P6S6 and P7S8. **Figure 4.4h** reports the plot of A_e, k_0, and sheet resistance vs. PW for the reported fabrication settings. As visible, a symmetrical behavior appears around a PW of 40 µs, where the most interesting electrochemical performance is obtained for P6S6 employing single scanning. For double scanning, conditions leading to a decrease in sheet resistance are associated with an increase in the electrochemical capabilities of the electrodes, while for conditions where sheet resistance increases (P4S3 and P5S4), excessive thermal degradation of LIG structures led to unusable devices. Thus, it is visible that fabrication parameters employed in the patterning of these functional architectures have an important influence on the resulting electrochemical capabilities of devices, associated with the previously presented conductivity properties. However, several other variables, such as electrode distances, layout, and laser-derived morphological characteristics of electrode surfaces play an important role in the electrochemical diffusion and charge transfer processes described here, being of relevance in future studies of LIG-derived electrochemical sensors from distinct precursor materials.

4.3.3 Disposable Paper-based LIG Electrodes for pH Detection

Riboflavin is a pH-sensitive organic compound, previously employed in pH-sensing devices, ideal for single-measurement tasks [24]. For riboflavin modified WE, the voltametric response was surveyed through SWV, resulting in the appearance of a peak related to riboflavin oxidation reaction, where deprotonation and electron transfer occurs (**Figure 4.5a**). For a pH of 2.65, this peak has its maximum current at a potential of -409 mV, shifting towards a negative potential for higher pH values. For the highest tested pH of 9.29, the peak shifts to a potential of -938 mV, showing that the potential at which riboflavin oxidation occurs is pH dependent. Taking the peak potentials for the tested pH values, a calibration can be established for the system (**Figure 4.5b**), showing a linear response over a physiologically relevant 2-8 pH range, resulting in a sensitivity of 81.9 mV.pH^{-1}. This linear variation range is in accordance with literature on riboflavin-based pH sensors, associated with the redox behaviors of riboflavin. These are limited by very low acidic pH, leading to the decrease in oxidation currents [30]. Similarly, very high alkaline pH values around 9 also lead to limitations in the deprotonation and charge transfer for electrochemical redox reactions of riboflavin [31]. Compared to the standard Nernstian behavior of pH sensors, with a maximum sensitivity of 59.16 mV.pH^{-1}, the resulting sensor shows a super-Nernstian behavior, reported in several pH-sensing applications [32]. Reproducibility was also tested by performing pH measurements in 8 distinct sensors (**Figure 4.5c** and

Table B5). The same linear behavior was reached, resulting in a mean sensitivity of 78.2 ± 3.37 mV.pH^{-1}. In terms of operational stability over time, experiments were carried out by immerging the riboflavin-based pH sensor in a buffer solution for an extended period (16 hours). Every hour, SWV measurements were taken, and the peak potential was recorded. As seen in **Figure 4.5d**, a stable potential is measured over time, with little drift, matching with the calibration curve established for the sensor, with a pH around 5.5.

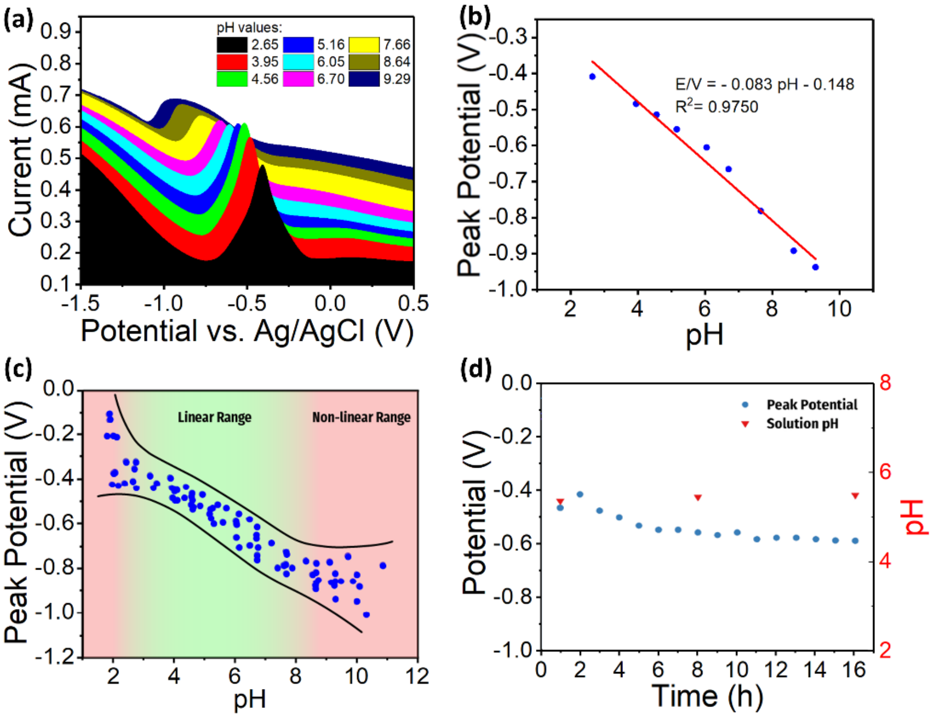

Figure 4.5 - LIG riboflavin-based electrochemical pH sensor performance. (a) SWV response of the sensor at different pH levels. (b) Resulting calibration curve of peak potential positions vs. pH. (c) Measurements distribution of 8 sensors and (d) sensor stability testing over a period of 16 hours.

4.4 Conclusions

The growing exploration of LIG derived from different carbon-based precursors in several contexts in electronics has led to several distinct applications, that require specific material characteristics. Although laser irradiation processes of polyimide have been extensively studied and modeled, such studies are still lacking when other materials are employed, including paper substrates. From this study, experimental modeling of the interactions and outcomes between CO_2 laser and modified paper substrate was assessed, resulting in some key considerations when employing these types of laser systems on cellulosic material. Instead of implementing the conventional paradigm of studying the influence of laser power vs. scan speed, underlying pulse modulation operational principles of the used laser system are highlighted and empirically studied, to understand their significance in the laser graphitization phenomenon of paper substrates. Based on the pulse modulation operation of the employed CO_2 laser system, it was found that the onset of graphitization is associated with the specific thermal tolerance of the material, associated with appropriate PW, that exposes the material to the laser beam for appropriate durations. For PW leading to graphitization, the outcomes of the conversion are then influenced by the laser fluence and employed defocus, allowing to change the sheet resistance of LIG films from 14 $\Omega.sq^{-1}$ to 18 $k\Omega.sq^{-1}$. Similar behaviors are also observed for the electrochemical properties of this material when employed within three-electrode electrochemical cells, where fabrication settings leading to higher material conductivities result in more attractive properties when measuring faradaic electron transfer processes. With appropriate fabrication settings, high-performance, disposable paper-based electrodes employing paper-based LIG can be fabricated, being employed for the voltametric sensing of pH.

References

1. Joshi, P., Mishra, R. & Narayan, R. J. Biosensing applications of carbon-based materials. *Current Opinion in Biomedical Engineering* vol. 18 100274 (2021).
2. Kirchner, E. M. & Hirsch, T. Recent developments in carbon-based two-dimensional materials: synthesis and modification aspects for electrochemical sensors. *Microchim. Acta* **187**, 1–21 (2020).
3. Fang, Y. & Wang, E. Electrochemical biosensors on platforms of graphene. *Chem. Commun.* **49**, 9526–9539 (2013).
4. Reddy, Y. V. M. *et al.* Strategies, advances, and challenges associated with the use of graphene-based nanocomposites for electrochemical biosensors. *Adv. Colloid Interface Sci.* **304**, 102664 (2022).
5. Bai, Y., Xu, T. & Zhang, X. Graphene-Based Biosensors for Detection of Biomarkers. *Micromachines 2020, Vol. 11, Page 60* **11**, 60 (2020).
6. Sawkar, R. R., Shanbhag, M. M., Tuwar, S. M., Mondal, K. & Shetti, N. P. Sodium Dodecyl Sulfate–Mediated Graphene Sensor for Electrochemical Detection of the Antibiotic Drug: Ciprofloxacin. *Materials (Basel).* **15**, 7872 (2022).
7. Tuantranont, A. *et al.* Printed graphene-based electrochemical sensors. *Graphene Sci. Handb.* **1–6**, 147–161 (2016).
8. Lin, J. *et al.* Laser-induced porous graphene films from commercial polymers. *Nat. Commun.* **5**, 5714 (2014).
9. Le, T. S. D. *et al.* Recent Advances in Laser-Induced Graphene: Mechanism, Fabrication, Properties, and Applications in Flexible Electronics. *Adv. Funct. Mater.* **32**, 2205158 (2022).
10. Wan, Z., Nguyen, N. T., Gao, Y. & Li, Q. Laser induced graphene for biosensors. *Sustain. Mater. Technol.* **25**, e00205 (2020).
11. C. Claro, P. I. *et al.* Sustainable carbon sources for green laser-induced graphene: A perspective on fundamental principles, applications, and challenges. *Appl. Phys. Rev.* **9**, 041305 (2022).
12. Singh, A. K. *et al.* Parametric investigation on laser interaction with polyimide for graphene synthesis towards flexible devices. *J. Phys. D. Appl. Phys.* **56**, 015305 (2022).
13. Ruan, X., Wang, R., Luo, J., Yao, Y. & Liu, T. Experimental and modeling study of CO2 laser writing induced polyimide carbonization process. *Mater. Des.* **160**, 1168–1177 (2018).
14. Liu, M., Wu, J. N. & Cheng, H. Y. Effects of laser processing parameters on properties of laser-induced graphene by irradiating CO2 laser on polyimide. *Sci. China Technol. Sci.* **65**, 41–52 (2022).
15. Abdulhafez, M., Tomaraei, G. N. & Bedewy, M. Fluence-Dependent Morphological Transitions in Laser-Induced Graphene Electrodes on Polyimide Substrates for Flexible Devices. *ACS Appl. Nano Mater.* **4**, 2973–2986 (2021).
16. de la Roche, J., López-Cifuentes, I. & Jaramillo-Botero, A. Influence of lasing parameters on the morphology and electrical resistance of polyimide-based laser-induced graphene (LIG). *Carbon Lett.* **1**, 1–9 (2022).
17. Behrent, A., Griesche, C., Sippel, P. & Baeumner, A. J. Process-property correlations in laser-induced graphene electrodes for electrochemical sensing. *Microchim. Acta* **188**, 1–14 (2021).
18. Chyan, Y. *et al.* Laser-Induced Graphene by Multiple Lasing: Toward Electronics on Cloth, Paper, and Food. *ACS Nano* **12**, 2176–2183 (2018).
19. Le, T. D., Park, S., An, J., Lee, P. S. & Kim, Y. Ultrafast Laser Pulses Enable One-Step Graphene Patterning on Woods and Leaves for Green Electronics. *Adv. Funct. Mater.* **29**, 1902771 (2019).
20. Pinheiro, T. *et al.* Laser-Induced Graphene on Paper toward Efficient Fabrication of Flexible, Planar Electrodes for Electrochemical Sensing. *Adv. Mater. Interfaces* **8**, 2101502 (2021).
21. Ye, R. *et al.* Laser-Induced Graphene Formation on Wood. *Adv. Mater.* **29**, 1702211 (2017).
22. Ismail, Z. Laser writing of graphene on cellulose paper and analogous material for green and sustainable electronic: a concise review. *Carbon Lett. 2022 325* **32**, 1227–1245 (2022).

23. Cantarella, G. *et al.* Laser-Induced, Green and Biocompatible Paper-Based Devices for Circular Electronics. *Adv. Funct. Mater.* **33**, 2210422 (2023).
24. Barber, R. *et al.* Laser induced graphene sensors for assessing pH: Application to wound management. *Electrochem. commun.* **123**, 106914 (2021).
25. Metelkova, J. *et al.* On the influence of laser defocusing in Selective Laser Melting of 316L. *Addit. Manuf.* **23**, 161–169 (2018).
26. Gao, W. *et al.* Effect of defocus manner on laser cladding of Fe-based alloy powder. *Surf. Coatings Technol.* **248**, 54–62 (2014).
27. Lee, S., Jang, H., Lee, H., Yoon, D. & Jeon, S. Direct Fabrication of a Moisture-Driven Power Generator by Laser-Induced Graphitization with a Gradual Defocusing Method. *ACS Appl. Mater. Interfaces* **11**, 26970–26975 (2019).
28. Wijeratne, K. *et al.* Bulk electronic transport impacts on electron transfer at conducting polymer electrode–electrolyte interfaces. *Proc. Natl. Acad. Sci. U. S. A.* **115**, 11899–11904 (2018).
29. Lavagnini, I., Antiochia, R. & Magno, F. An extended method for the practical evaluation of the standard rate constant from cyclic voltammetric data. *Electroanalysis* **16**, 505–506 (2004).
30. Sharma, A., Khosla, A. & Arya, S. Synthesis of SnO2 nanowires as a reusable and flexible electrode for electrochemical detection of riboflavin. *Microchem. J.* **156**, 104858 (2020).
31. Berchmans, S. & Vijayavalli, R. Surface Modification of Glassy Carbon by Riboflavnn. *Langmuir* **11**, 286–290 (1995).
32. Madeira, G. D. M., Hugo, H. J., Faleiros, M. C. & Mulato, M. Model improvement for super-Nernstian pH sensors: the effect of surface hydration. *J. Mater. Sci.* **56**, 2738–2747 (2021).

5

ONE-STEP LASER SYNTHESIS OF COPPER NANOPARTICLES AND LASER-INDUCED GRAPHENE IN A PAPER SUBSTRATE FOR NON-ENZYMATIC GLUCOSE SENSING

The synergy resulting from the high conductivity of graphene and catalytic properties of metal nanoparticles has been a resource to improve activity and functionality of electrochemical sensors. This work focuses on the simultaneous synthesis of copper nanoparticles (CuNPs) and laser-induced graphene (LIG) derived from paper, through a one-step laser processing approach. A chromatography paper substrate with drop-casted copper sulfate was used for the fabrication of this hybrid material, characterized in terms of its morphological, chemical, and conductive properties. Appealing conductive properties are achieved, with sheet resistance of 170 $\Omega.sq^{-1}$ being reached, while chemical characterization confirms the simultaneous synthesis of the conductive carbon electrode material and metallic copper nanostructures. Using optimized laser synthesis and patterning conditions, LIG/CuNPs-based working electrodes were fabricated within a three-electrode planar cell, and their electrochemical performance was assessed against pristine LIG electrodes, demonstrating good electron transfer kinetics appropriate for electrochemical sensing. The sensor's ability to detect glucose through a non-enzymatic route was optimized, to assure good sensing performance in standard samples and in artificial sweat complex matrix.

Keywords: laser-induced graphene, copper nanoparticles, one-step synthesis, glucose, non-enzymatic sensors.

The literature presented in this chapter is published in:

- Pinheiro, T., Caetano, J., Fortunato, E., Sales, M. G. F., Almeida, H., & Martins, R. (2024). One-Step Laser Synthesis of Copper Nanoparticles and Laser-Induced Graphene in a Paper Substrate for Non-Enzymatic Glucose Sensing. *Advanced Sensor Research*, 2400052.

5.1 Introduction

Electrochemical sensors experienced tremendous progress over the last decades and are currently one of the most common detection methods within medical, environmental, food safety, and pharmaceutical sensing devices [1]. Several advantages, such as miniaturization, portability, rapid response, high sensitivity, and selectivity, make electrochemical sensing a more attractive alternative to other detection techniques [2]. These sensors integrate electrodes capable of measuring electrically transduced signals, with the majority of the existing mechanisms including modified electrodes that provide high reactivity, affinity, and specificity to the target analyte. [3,4] Regarding the fabrication methods, printing technologies have received tremendous attention in recent years, including screen-printing [5], inkjet printing [6] and other additive methods[7] . These allow for the production of electrodes on any substrate of interest, including paper [8], using accessible conductive inks, including carbon-based inks [9]. Printed carbon electrodes, more specifically SPEs, exhibit excellent electrochemical performance and assure good reproducibility, while showing compatibility to several categories of recognition elements, either biological or synthetic, making them appealing for electroanalysis [10]. However, the need for synthesis steps for active ink materials and careful ink formulation prior to printing reduces the fast prototyping capabilities of these printing processes, while some of these techniques are resource consuming and need additional components, such as masters and plates for patterning of electrode geometries [11]. DLW has emerged has an alternative to these fabrication processes, where lasers can be used to synthesize conductive materials from and embedded in substrates of interest while functional electrode patterning occurs simultaneously [11]. Several materials can be synthesized by DLW, with laser-induced graphene (LIG) standing out has a conductive carbon-based material with compatibility for electrochemical sensor fabrication [12]. LIG is synthesized by irradiation of carbon-based polymers, leading to photothermal reactions that promote the cleavage of bonds and reorganization of carbon into graphene lattices, analogous to graphite [13].

For electrochemical sensor production based on LIG, polyimide (PI) has been the most commonly used polymer [14]. However, other carbon polymers have been successfully used for LIG synthesis and electrochemical sensor production, including paper [15–17]. Although cellulose being an aliphatic polymer with less graphitization potential when compared to aromatic polymers such as PI, modification with fire-retardant agents allows for an efficient patterning of LIG, with properties useful for electroanalysis, while exploiting paper's advantageous features, including its natural origin, facile disposability, controlled porosity, capillarity for fluid transportation and overall improved sustainability for disposable electrochemical platforms [18].

For the modification of printed electrodes, the use of additional techniques is needed to introduce recognition materials capable of specifically recognizing the target analyte. In the case of modification with metallic and metal-oxide nanostructures, used in non-enzymatic sensing, chemical methods such as electrochemical deposition is a well-established strategy for synthesis and is thus often selected by the scientific community to produce these composites on a previously fabricated conductive surface [19–21]. However, such methods require additional equipment, and their multi-step nature and individualized treatment of electrodes hinders mass production and scalability, increases manufacturing cost and diminishes the potential application in commercial devices. With these aspects in mind, DLW recently emerged as a promising method for fabricating these modified electrodes, capable of reducing the fabrication steps, equipment and material usage needed for device prototyping. This method has been explored in recent years to simultaneously synthesize LIG as well as other functional materials such as metal and metal oxide nanostructures (e.g. Co_3O_4, MnO_2, Fe_3O_4) through laser irradiation of a precursor-coated substrate[22] . Literature reports that the synergy between the high conductivity of graphene and catalytic properties of certain metallic nanoparticles, such as copper [23,24], improves the performance of electrochemical sensors in different settings, including for non-enzymatic glucose detection [25]. This fourth generation of glucose biosensors provide several advantages, by removing the need for biological, organic recognition elements, providing higher current densities and improved sensitivity, also increasing the potential for miniaturization of such biosensing platforms [26]. Several materials have been used for non-enzymatic glucose oxidation, where transition metals, more specifically copper, stand out.

Generally, glucose oxidation using copper nanomaterials within electrochemical biosensors requires an alkaline medium and copper oxide species that are capable of oxidizing glucose and generate the current response proportional to the amount of glucose in an analyte. For copper-based non-enzymatic sensor fabrication, most common approaches have been electrochemical deposition, solution-based processing and hydrothermal synthesis methods [26]. Several studies have reported the fabrication of LIG/CuNPs nanocomposites by DLW, although few describe their synthesis through laser irradiation. One example is the work done by D. Xu et al. [27], using $CuCl_2$ as the precursor for Cu and Cu_2O nanoparticles. After dissolving the precursor in ethyl alcohol, the solution was spin-coated onto a polyimide film and submitted to the laser beam to form the CuNPs/graphene nanocomposites. Lastly, the composites were transferred to a nickel foam surface to produce a graphene/CuO_x-based electrode for electrochemical water splitting. In 2022, J. Lee et al. [28] reported a similar methodology to fabricate copper oxide nanoparticles on LIG, using the same copper precursor, but this time with a two-step laser irradiation. Firstly, polyimide was irradiated with a laser beam to synthesize porous LIG. Then, a $CuCl_2$ solution was drop-casted onto the LIG patterns, and a subsequent laser scan promoted the formation of CuOx nanoparticles. Similarly, Li et al. proposed a two-step sensor fabrication protocol [29]. Firstly, a Cu precursor film is coated onto PI and irradiated with a 405 nm visible laser for copper reduction. Secondly, the same laser is used to graphitize the surface of PI, melt and sinter the copper into particles anchored onto the surface of the conductive LIG. This LIG/CuO surface was employed for the fabrication of flexible, high-sensitivity non-enzymatic glucose sensors. Besides copper, other metal nanostructures have also been synthesized employing laser irradiation techniques alongside LIG, targeting glucose sensing, such as Co_3O_4 [30].

However, the inability to fully embed metallic salt precursors within PI leads to the need for additional techniques for nanoparticle precursor coating, such as spin or blade coating, further increasing the multi-step aspect of these methodologies. On the other hand, alternative LIG precursors that allow for soaking with nanoparticle precursor solutions toward homogeneous embedding are ideal to decrease preparation steps and equipment usage and improve high-throughput and fast prototyping. Organic biomass, such as wood, has been successfully employed for this purpose, where different metallic salts are reduced to elemental metals embedded in the converted wood-derived LIG [31]. Another substrate that presents ideal properties for this purpose is paper, where its capillary properties allow for an efficient embedding of metallic salt precursors. Here, an efficient and straightforward mechanism to simultaneously synthesize LIG/CuNPs nanocomposites on a paper substrate was developed, through a one-step laser irradiation approach. The absorbent property of paper enables drop casting of a copper sulfate solution onto a pre-treated Whatman paper surface that is further converted to LIG with anchored CuNPs, when submitted to the laser beam. As proof of concept, this technique was applied to develop non-enzymatic glucose sensors with a planar three-electrode architecture, operating within low concentration regimens, promising for glucose sensing in alternative biofluids with lower glucose circulating concentrations, such as sweat.

5.2 Experimental Section

Synthesis of LIG/CuNPs composites

Firstly, the Whatman paper was submersed in a fire-retardant solution of 0.1 M sodium tetraborate decahydrate for 10 min, to prevent the substrate's chemical degradation when submitted to laser irradiation. After drying, wax printing was performed using a Xerox ColorQube wax printer. Open squares of 4x4 mm dimension (16 mm^2 area) were patterned by wax printing, followed by drop-casting of different copper sulfate precursor solution volumes for further study and optimization. The solution was then allowed to dry at room temperature. For LIG/CuNPs synthesis, a VLS 3.50, Universal Laser Systems CO_2 laser, with a 10.6 µm wavelength, beam size of 0.127 mm diameter, maximum power of 50 W, and raster speed of 127 cm.s^{-1} was employed, using different power and speed settings to achieve optimized synthesis parameters for subsequent electrode fabrication.[15]

Characterization of LIG/CuNPs composites

The morphology and chemical composition of the composites was analyzed using a SEM/EDS system (Hitachi Regulus SU8220). Raman measurements were made with a Renishaw® inVia™ Qontor® confocal Raman microscope (Gloucestershire, UK) equipped with a Renishaw Centrus 2957T3 detector. The laser beam was focused through a 50x Olympus objective lens. Measurements were performed with the 532 nm laser with 10 s exposure time and 3 accumulations as measurement parameters, with a laser power of 16 mW. X-ray photoelectron spectroscopy (XPS, Kratos Axis Supra, UK) equipped with a monochromated Al Kα radiation (1486.6 eV) was used. Biorad HL 5500 four-point probe equipment allowed to determine the sheet resistance (square geometry of side length 5 mm, with deposited silver conductive ink contacts at each corner).

LIG/CuNPs electrode fabrication and characterization

Empty circular areas (2 mm diameter) were wax printed, to be filled with the copper precursor and correspond to the active area of the WE (2.5 mm diameter). Then, 80 mM copper sulfate precursor solution was drop-casted over the empty circles and dried at room temperature. Sensor fabrication was performed as in previously presented in Chapters 3 and 4. [15,16] For the sensor fabrication, a three-electrode architecture was previously designed in Adobe Illustrator, and the substrate under optimized lasing with 4% laser power and 4% raster scan speed.

Next, a passivation layer was laser cut to protect the sensors from handling by encapsulating them with a lamination pouch with cut openings for the sensor working area and conductive tracks. Finally, the RE was painted with silver/silver chloride ink (AGCL-675, Conductive Compounds, Inc., Hudson, NH), and conductive tracks were established with silver ink (AG-510 silver ink, Conductive Compounds, Inc., Hudson, NH). All electrochemical measurements were recorded using a PalmSens4 Potentiostat, and pretreatment was initially performed with a scan rate of 150 mV.s^{-1}, ranging from -2 to 2 V and using the supporting electrolyte (0.1 mM KCl). For the determination of A_e and k_0 parameters, electrochemical assays were performed using 5 mM ferri/ferrocyanide, $[Fe(CN)_6]^{3-/4-}$ as the redox probe, prepared in the supporting electrolyte, at multiple scan rates varying from 10 to 150 mV.s$^{-1,}$ with potentials scanned from –0.3 to +0.7 V for LIG sensors and –0.2 to +0.6 V for LIG/CuNPs sensors.

Nonenzymatic glucose sensing protocol

The non-enzymatic glucose sensing performance was evaluated using chronoamperometry. For the experimental setup, a retort stand, and a three-claw clamp were used to hold the sensor, which was immersed in a beaker containing 50 mL of 0.1 M NaOH as the supporting electrolyte. Sensors were tested by addition of different volumes of a stock glucose solution, under continuous stirring and different applied potentials. For the selectivity tests, the response of sensors to sodium chloride, ascorbic acid, uric acid, fructose, galactose, lactose and sucrose was monitored, with all the interferents at a concentration of 0.1 mM and an applied glucose concentration of 0.2 mM.

Glucose determination in artificial sweat samples

For glucose measurements in a sweat matrix, commercial artificial eccrine sweat (Pickering Laboratories, 1700-0020) containing several metabolites, minerals and amino acids in physiological concentrations was used. The pH of the artificial sweat was altered by diluting NaOH to a concentration of 0.1 M, to provide the necessary alkaline pH for sensor operation. After this, the same glucose measurement protocol was employed, by immersing the sensor in 20 mL of artificial sweat and introducing volumes of an artificial sweat stock solution with glucose, to reach varying glucose concentrations in contact with the sensor.

5.3 Results and Discussion

5.3.1 Morphological, chemical, structural and electrical characterization of LIG/CuNPs composites

The first stage for assessing the ability to synthesize paper-derived LIG/CuNPs composites was to study different fabrication parameters and their influence on the properties of the resulting hybrid materials. Firstly, a study was performed to determine the optimal volume of copper sulfate precursor for modification of the paper substrate. By using wax printing, versatile patterning of hydrophilic areas with different geometries can be fabricated to standardize the distribution of copper precursor over the paper substrate. An open capillary area of 200 mm^2 was patterned through wax printing, and different volumes and concentrations of copper sulfate were employed (**Figure 5.1a**). Concentrations between 8 and 800 mM of copper sulfate were employed, at different volumes, from 50 to 200 µL. These volumes were normalized into volume-to-area (VA) ratios so that for different wax-patterned geometries, a uniform volume distribution can be compared, independent of the shape of the modification area. As seen, a concentration of 800 mM leads to excessive copper salt accumulation and the appearance of a significant coffee ring effect, for the VA ratio of 0.25 µL/mm^2. Contrarily, a concentration of 8 mM leads to incomplete coverage of the copper precursor over the modified paper area, which was undesirable. As such, a concentration of 80 mM was selected as the appropriate for modification, since for all VA ratios a consistent and uniform distribution of the copper precursor over the paper substrate is achieved. SEM images were taken of the paper modified with 80 mM copper sulfate at a VA ratio of 1 µL/mm^2 (**Figure 5.1b**), showing the uniform distribution of copper sulfate crystals over the fibrous structure of the paper substrate. EDS was also performed, showing the relative abundance of oxygen, carbon, copper and sulfur arising from the presence of $CuSO_4$ over the cellulose fibers (Figure C1). As visible, there is abundance of oxygen arising from both cellulose and $CuSO_4$, while the relative atomic weight percentage for the remaining elements is less pronounced. To note the relative percentage of copper and sulfur, with copper showing around twice the relative atomic weight percentage when compared to sulfur. Taking the atomic mass of the elements into consideration, the expected relation in terms of the stoichiometry of $CuSO_4$ is reflected in the relative atomic weight percentages, since the atomic mass of copper is approximately twice the one for sulfur. After determining an appropriate copper sulfate concentration for use, irradiation with different fabrication parameters was employed, to determine the morphological, chemical, and conductive features

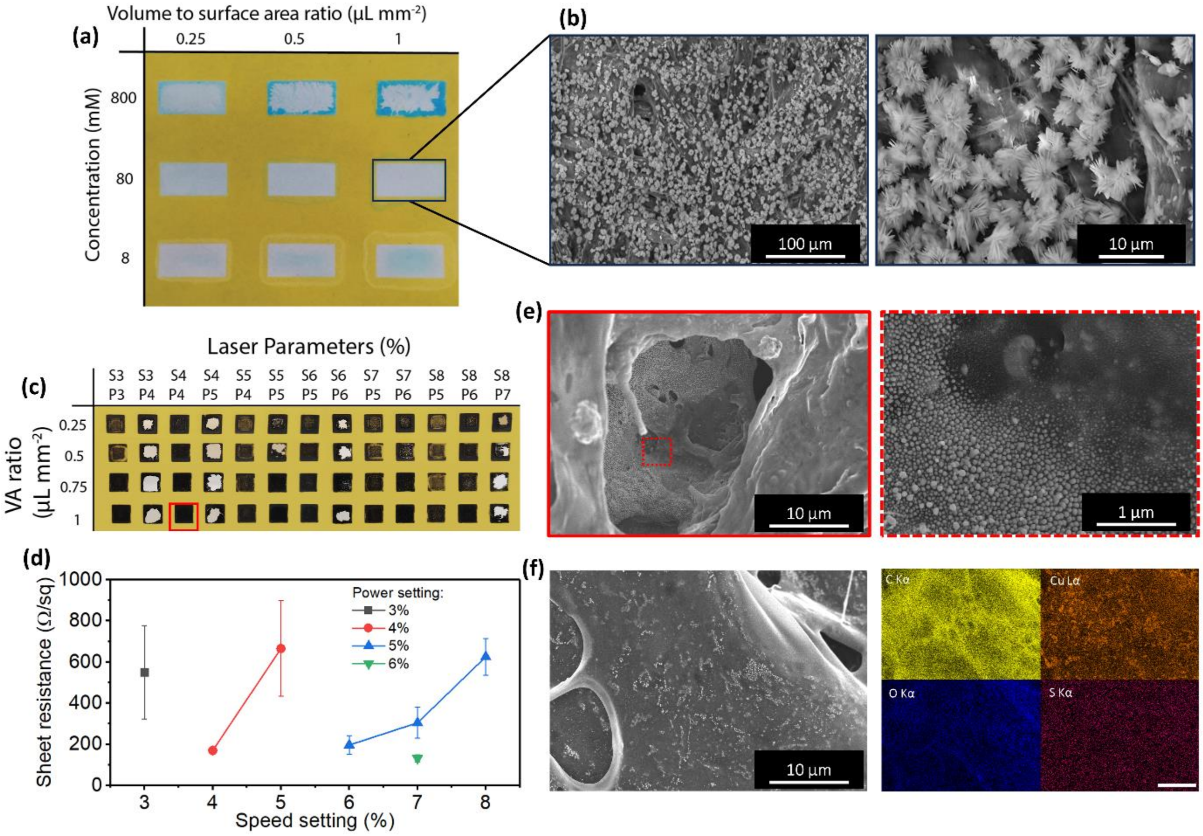

Figure 5.1 - Process optimization for copper sulfate precursor deposition and synthesis of LIG/CuNPs composites. (a) Optimization of modification volume and concentration of copper sulfate precursor for homogeneous distribution over the paper surface. (b) Morphological study of pre-treated paper substrate with copper precursor before laser irradiation, showing $CuSO_4·5H_2O$ crystals. (c) Matrix of power/speed laser setting and outcomes of irradiation for different VA ratios. (d) Analysis of sheet resistance for irradiation conditions leading to resistive films (n=3). (e) Morphological analysis of LIG/CuNPs composites. (f) Morphological and elemental analysis of inverted surface of exfoliated LIG/CuNPs films.

(**Figure 5.1c**). Different laser power and speed percentage settings were employed, to determine the effect caused by the laser irradiation over the substrate. The aim was to reach parameters that allowed for a non-destructive effect, with a homogeneous distribution of graphitized material, that serves as the conductive, transducing platform for the electrochemical sensors. Some of the tested laser conditions lead both to an ablative outcome (e.g., speed and power percentages of 3 % and 4 %, respectively), that damages the irradiated surface and renders it unusable for the purposes of electrochemical sensor fabrication and use with aqueous electrolytes. On the other hand, some conditions lead to visible conversion areas where copper precursor is deposited, showing inhomogeneous distribution of LIG, with a marked interface between the area with prior presence of $CuSO_4$ and the remaining area where only LIG is present (e.g., speed and power percentages of 8 % and 5 %, respectively). From this pool of laser irradiation settings, electrical characterization was performed through four-point probe sheet resistance measurements [16]. Results are presented for conditions conducive for resistivity measurements (e.g., conditions with no excessive ablations and cracks over the irradiated surface) (**Figure 5.1d**). Overall, results show LIG/CuNPs films with high resistivity, varying with the employed irradiation settings. Three fabrication parameter combinations (P4S4, P5S6 and P6S7) presented the lowest sheet resistances, the lowest being 132.5 ± 17.5 $\Omega.sq^{-1}$ (n=3) for a power of 6 % and scanning speed of 7 %. Furthermore, for some conditions, high variability in resistivity is observed, depending on the VA ratio employed for modification. For example, for laser settings of P4S5, a mean sheet resistance of 665.8 ± 232.6 $\Omega.sq^{-1}$ (n=3) was reached. Using these conditions, a VA ratio of 0.25 shows a minimum sheet resistance of 354 $\Omega.sq^{-1}$, while for a VA ratio of 0.5, a maximum value of 1010 $\Omega.sq^{-1}$ is observed, indicating the influence of the amount of copper sulfate on the efficiency of LIG synthesis. Comparing these values with pristine LIG reported in **Chapter 4**, a significant increase is visible in the resistivity of samples. For pristine paper LIG, values around 58 $\Omega.sq^{-1}$ are characteristic (4% power and 4% speed settings) [32], while for the same conditions, LIG/CuNP films present higher sheet resistances around 170 ± 10.4 $\Omega.sq^{-1}$ (n=3). One possible explanation is that since the CuNPs and LIG are simultaneously synthesized, the energy emitted by the IR laser will be used for both paper graphitization and synthesis of CuNPs. As in a situation of exclusive LIG formation, all the laser output energy is used to graphitize the paper fibers, while in this case, the substrate is covered with a precursor, decreasing the effectiveness in converting paper into LIG.

Fabrication settings of 4% laser power and 4% laser scan speed were selected for further characterization based on the lower resistivity and variability, accounting for different VA ratios. Morphological analysis by SEM was performed on the paper after the laser scanning with these conditions and a VA ratio of 1 $\mu L.mm^{-2}$ (**Figure 5.1e**). The results show that at superficial LIG surfaces, the presence of copper nanostructures is less dense, suggesting that the temperatures leading to graphitization also promote a full decomposition of the copper sulfate precursor and less reduction of the precursor onto copper nanostructures. However, when surveying LIG fibers at higher depths, there is the presence of dense clusters of nanoparticles, with spherical shapes and varying sizes. This indicates the hypothesis that CuNPs are formed by thermal-induced effects at depths where heat dissipation is greater and there is less direct irradiation of the laser beam. In these cases, copper ions are reduced to CuNPs loaded onto the surface of LIG fibers. Accompanying SEM analysis, EDS measures (Figure C2) show a steep increase in the relative carbon composition of the lasered surface (70 %), while the relative copper percentage remains close to the one prior to the laser scribing. Regarding oxygen and sulfur, there are significant decreases in their relative percentage, associated both with the graphitization of cellulose fibers and conversion of $CuSO_4$ to copper nanostructures, leading to the release of oxygen and sulfur-rich volatiles. To further analyze the distribution of CuNPs, a LIG/CuNPs film was exfoliated from the paper substrate, according to a protocol presented in the following **Chapter 6** [33], and its inverted surface was analyzed by SEM/EDS (**Figure 5.1f**). This surface represents the greatest depth at which the temperature induced by the laser irradiation causes graphitization of the cellulose substrate. As shown, at this depth, there is a greater spreading of synthesized CuNPs and many particle clusters are visible. Simultaneously, these clusters are anchored at the surface of LIG fibers, showing that heat accumulation during the laser irradiation process is sufficient to stimulate the synthesis of CuNPs at varying depths. EDS elemental mapping further indicates the presence of CuNP clusters, clearly distinguished in the Cu Lα mapping.

Regarding the chemical characterization of LIG/CuNPs composite, three prominent peaks located at 1346, 1586, and 2691 cm^{-1} were identified in the Raman spectrum (**Figure 5.2a**), corresponding to the D, G, and 2D bands characteristic peaks of graphitic structures. [34] Calculating the two ratios used to characterize LIG, an I_{2D}/I_G ratio of 0.67 was obtained, suggesting that the fabricated LIG presents a multilayer structure. In contrast, the I_D/I_G ratio of 1.03 indicates that during the laser induction, defective carbon-based structures are being formed. These results were compared to bare LIG synthesized without the copper precursor, presented in **Chapter 4** (I_{2D}/I_G=0.58 and I_D/I_G=0.63), showing that the presence of copper sulfate solution leads to a more defective LIG fraction within the LIG/CuNPs composite, caused by the less efficient energy utilization for the graphitization of the paper substrate, also observed for resistivity outcomes.

XRD was used to access the crystalline structure of the copper nanostructures on the paper substrate with deposited $CuSO_4$ solution before and after the laser irradiation (**Figure 5.2b**). Regarding the sample irradiated with the laser beam, three major peaks at 43.3, 50.5, and 74.1° are indexed to the (111), (200), and (220) planes of metallic copper [36]. The appearance of these diffraction peaks shows that due to laser irradiation, a change in the initial oxidation state of copper is promoted, resulting in the formation of nanoparticles arranged in an ordered crystalline arrangement characteristic of metallic copper. Further chemical characterizations were performed by XPS. XPS spectrum of LIG/CuNPs composites (**Figure 5.2c**) indicates the presence of carbon, oxygen, copper, and sodium. The detection of sodium is related to the

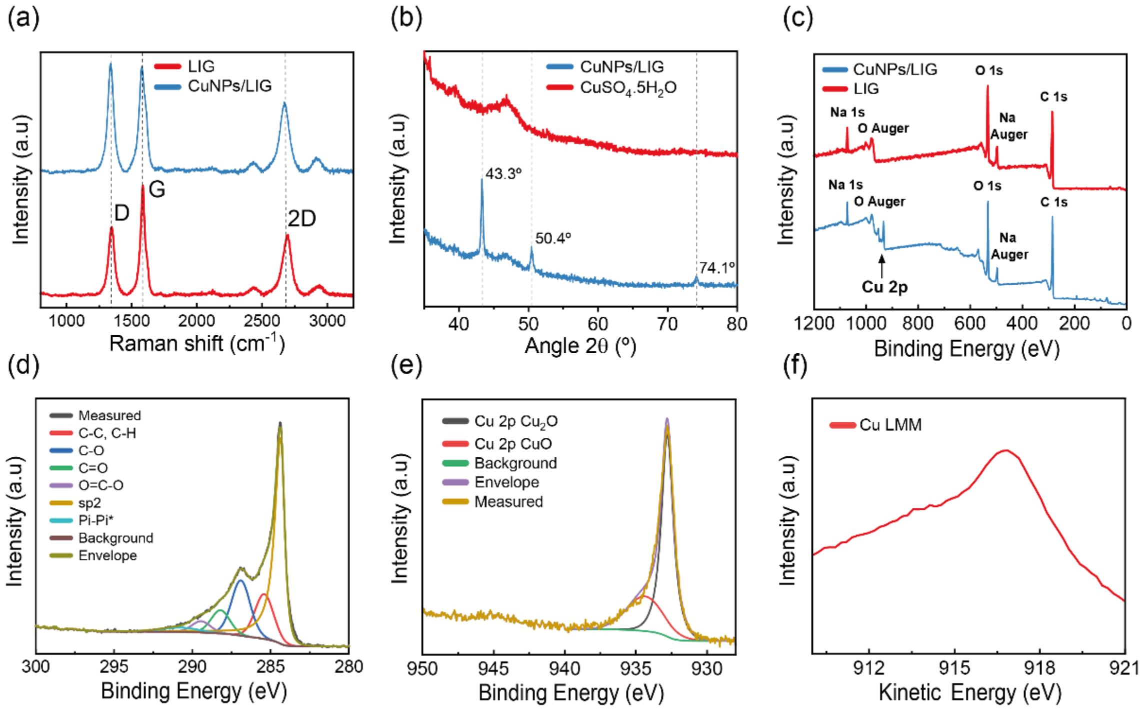

Figure 5.2 - Chemical characterization of LIG and LIG/CuNPs composite. (a) Raman spectra of LIG and LIG/CuNPs. (b) XRD analysis of the substrate with copper precursor before and after laser irradiation. (c) Survey XPS spectra of LIG and LIG/CuNPs composites. XPS spectrum of (d) C1s and (e) Cu2p peaks of LIG/CuNPs. (f) Cu LMM Auger spectrum of LIG/CuNPs.

paper treatment with the fire-retardant. The high-resolution spectrum of C1s (**Figure 5.2d**) revealed the presence of six different carbon bonds at the following binding energies: C=C (sp^2) at 284.3 eV, C–C (sp3) at 285.5 eV, C–O at 286.6 eV, C=O at 287.5 eV, O=C–O at 288.6 eV, and π–π* satellite at 290.7 eV. Since the dominant peak corresponds to the sp^2 hybridized carbon atoms, the presence of LIG is confirmed [37]. To further investigate the valence state distribution of copper in the sample, the high-resolution Cu2p spectrum was surveyed (**Figure 5.2e**). This spectrum shows that two copper species with different chemical states are present in the sample. The peak located at 934.4 eV can be assigned to CuO (or Cu(II)), [38] while the peak with the binding energy of 932.8 eV could not be identified by simply analyzing the Cu2p XPS spectrum. Since the Cu(0) and Cu(I) species have similar binding energies, they can be distinguished through the Auger parameter (calculated through the sum of the Cu LMM kinetic energy and the Cu $2p^{3/2}$ binding energy). Cu LMM Auger spectrum (**Figure 5.2f**), shows a dominant peak located at 916.89 eV. The determined Auger parameter of 1849.4 eV is characteristic of Cu_2O (or Cu(I)). [39] The presence of copper oxide species may arise by superficial oxidation of copper when exposed to the air after laser synthesis. Thus, XRD and XPS results show that the nanoparticles anchored on the LIG surface consisted of a mixture of copper and superficial copper oxides.

5.3.2 Electrochemical characterization of LIG/CuNPs electrodes

The electrochemical performance of LIG/CuNPs-based electrodes was evaluated by performing sequences of voltammograms in the presence of 5 mM $[Fe(CN)_6]^{3-/4-}$ as redox probe. The voltammograms (**Figure 5.3a**) show two well-defined cathodic and anodic peaks, corresponding to the reduction and oxidation of the electroactive species, respectively. The voltammogram shows a slight increase in the peak-to-peak separation as the scan rate increases, which means that this reaction is considered quasi-reversible. In Table C1 the obtained electrochemically active surface area (A_e) and HET rate constant (k_0) calculated for LIG/CuNPs sensors are presented (calculated from CV curves presented in Figure C3). The average A_e value was calculated to be 13.70 mm^2 (RSD = 9.61 %, n=3), which reflects an increase of 2.79 times the geometric area (A_g) of the WE. Regarding electron transfer kinetics, a mean k_0 of 8.57×10^{-3} cm.s^{-1} (RSD = 5.30 %, n=3) was determined. A comparison against electrochemical cells based on bare cellulose-based LIG was also drawn, using cyclic voltammetry. It can be noticed that bare LIG without CuNPs shows increased current densities in both anodic and cathodic peaks, as well as a smaller peak-to-peak separation, which correlates well with the presented chemical and conductive characterization presented before (**Figure 5.3b**). Comparing the

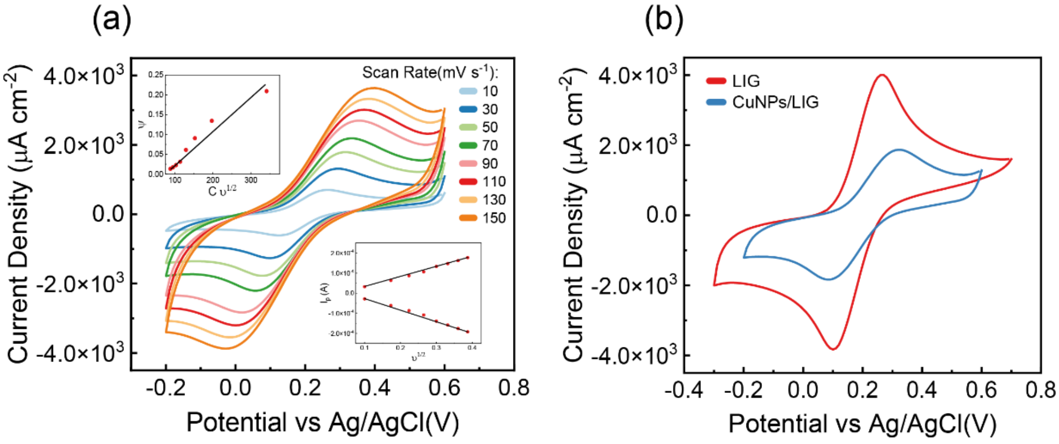

Figure 5.3 - Electrochemical performance of LIG/CuNPs and LIG electrodes. (a) Cyclic voltammograms of LIG/CuNPs sensor obtained for a scan rate range of 10 to 150 mV.s^{-1}, using 5 mM $[Fe(CN)_6]^{3-/4-}$ as redox probe. Both insets represent auxiliary plots for the determination of the kinetic parameters: the right graph is a plot of peak currents vs. square root of corresponding scan rate and the left one is a plot of kinetic parameter Ψ vs. C.v$^{-1/2}$. (b) Comparison between the plots obtained for the LIG/CuNPs and the LIG electrodes, at a scan rate of 50 mV.s^{-1}.

electrochemical parameters of LIG/CuNPs sensors with those of bare cellulose-based LIG sensors (A_e = 21.27 mm^2, RSD = 5.00 % and k_0 = 20.06×10^{-3} cm.s^{-1}, RSD = 2.76 %, n=4 detailed in Figure C4) a small deterioration on electrochemical performance and charge transfer capabilities is observed when CuNPs are present. Although literature evidences that the incorporation of CuNPs leads to enhanced electron transfer efficiency, [27,40] those studies report a separated method for the CuNPs formation after LIG synthesis. As mentioned before, in this case, the laser energy will have to be distributed by substrate graphitization and nanostructure synthesis within the one-step laser induced synthesis process, which results in less graphitized fractions and, ultimately, lower charge transfer capabilities of the electrode system. In addition, in the area used for drop-casting of $CuSO_4$ precursor, no wax is present during the laser synthesis protocol. As shown in the following chapter [16,33], wax loading used for impermeabilization of the paper substrates also promotes higher graphitization potential and improves yield of LIG synthesis, directly influencing the charge transfer properties of electrochemical cells. Thus, the diminished charge transfer capabilities resulting from the patterned WE over paper modified with $CuSO_4$ are in accordance with previous findings. Nevertheless, electrochemical performance shows suitable charge transfer potential features for use in sensing, where the presence of CuNPs can participate in the catalytic oxidation of glucose molecules in alkaline medium.

5.3.3 Nonenzymatic Glucose Sensor Performance

The ability of the fabricated LIG/CuNPs sensors for glucose detection was assessed. Firstly, chronoamperometric measures of the LIG/CuNPs sensors were taken to monitor the current response to the addition of increasing glucose concentrations. Three different electrode potentials (0.4, 0.5, and 0.6 V vs printed Ag/AgCl) were employed to determine the response of the electrodes to the addition of glucose (**Figure 5.4a**). It can be noticed that for an applied potential of 0.4 V, well-defined steps corresponding to the addition of lower glucose concentrations are observed. Therefore, 0.4 V potential was selected in subsequent experiments. The respective calibration plot (**Figure 5.4b**) exhibits a linear range from 20 µM to 1.51 mM and the sensitivity was 87.6 µA.mM^{-1}.cm^{-2}. Error bars were included using the standard deviation, and the limit of detection (LOD) was 14 µM (3σ/S). Figure C5 shows the method employed to calculate and extract current magnitudes associated with glucose additions, used to establish sensor calibrations. The LIG/CuNPs sensor was once again tested based on a chronoamperometric technique by adding successive 0.1 mM of glucose (**Figure 5.4c**). The measured current was linearly correlated to glucose, at a concentration range from 50 µM to 1.79 mM

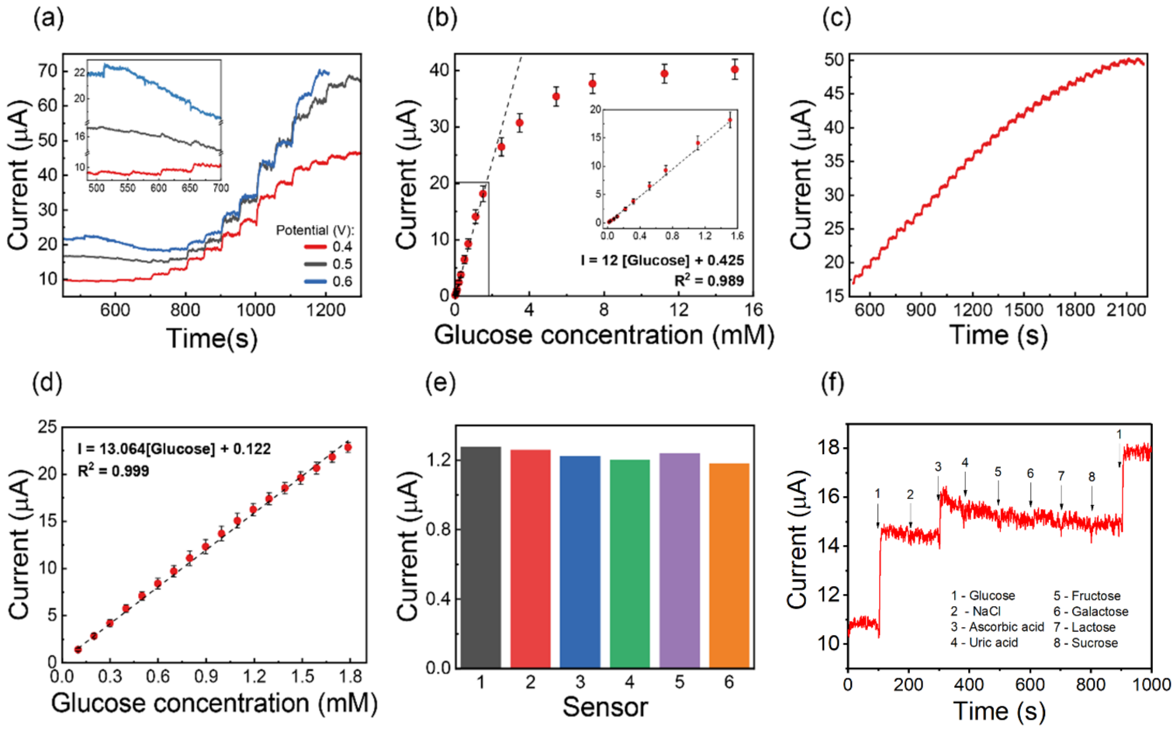

Figure 5.4 - Glucose sensing performance of LIG/CuNPs based sensor. (a) Continuous amperometric sensor response to different glucose concentrations using applied potentials of 0.4, 0.5, and 0.6 V. The inset shows the magnified section for the additions of the two lowest glucose concentrations. (b) Corresponding calibration curve for the 0.4 V potential. The inset shows the magnified section considered for a linear range response. (c) Sensor response to successive additions of 0.1 mM glucose using an applied potential of 0.4 V. (d) Corresponding calibration curve. (e) Reproducibility tests performed on six LIG/CuNPs sensors. (f) Selectivity study for the addition of 0.2 mM glucose in the presence of interfering species (each 0.1 mM).

(**Figure 5.4d**). The sensor sensitivity toward glucose was determined to be 95.3 μA.mM^{-1}.cm^{-2}. Comparing the two obtained sensitivities based on the different glucose addition protocols, it can be said that the obtained values are very approximate, which corroborates sensor viability. An LOD of 11 μM was determined. Reproducibility tests using six LIG/CuNPs sensors prepared with the same conditions were performed (**Figure 5.4e**). The amperometric responses were measured during the addition of 0.1 mM glucose, showing a mean response of 1.23 μA. The relative standard deviation of 2.84 % was calculated, suggesting that the developed sensors have good glucose-sensing reproducibility. Selectivity testing was carried out by measuring the sensor response to the addition of interferents that can influence the catalytic oxidation of glucose by CuNPs. **Figure 5.4f** presents the response of the LIG/CuNPs sensor for the consecutive addition of 0.2 mM glucose, 0.1 mM NaCl, ascorbic acid, uric acid, fructose, galactose, lactose and sucrose. The results show that the presence of NaCl and uric acid interfering species produce negligible current responses, as well as for other sugars. Considering the ascorbic acid interference, a slight increase in the sensor current response can be observed in the graph, although not significant when compared to the glucose additions, with the signal returning to the baseline current associated with the presence of glucose. Therefore, LIG/CuNP composites display good selectivity features for nonenzymatic glucose sensing

A comparison with other reports of carbon-based electrochemical sensors employing Cu nanostructures for glucose sensing and their performance metrics is drawn in **Table 5.1**, encompassing different synthesis and nanostructure deposition methods. Overall, this work is the single one proposing a single step for graphitization and copper reduction on paper substrates, offering a low-cost and efficient process of electrode fabrication, with significant advantages when scale-up is intended.

Table 5.1 - Performance comparison of several copper nanostructure-based glucose sensors.

Materials	Nanostructure synthesis/ deposition method	Linear Range	LOD (µM)	Sensitivity (µA.mM^{-1}.cm^{-2})	Reference
CuNPs, LIG, polyimide	Substrate-assisted electroless deposition	1 µM – 6 mM	0.39	495	[41]
CuNPs, graphite sheet	Hydrothermal	0.1 – 3.4 mM	1.05	7254	[42]
CuO NPs, LIG, polyimide	Focused sunlight	1 µM – 5 mM	0.1	-	[43]
CuNCs, LIG, polyimide	Electrodeposition	25 µM – 4 mM	0.025	4532	[44]
CuNPs, LIG, polyimide	Electrodeposition	1 µM – 0.5 mM	-	84	[35]
CuONPs, LIG, polyimide	Laser induction/synthesis	0-8 mM	0.049	619.43	[29]
CuNPs, LIG, paper	Laser induction/synthesis	20 µM – 1.79 mM	11	95.3	This work

5.3.4 Glucose Sensing in Artificial Sweat

Although the stable and sensitive performance of the developed nonenzymatic LIG/CuNPs sensors, testing in a complex matrix portraying real sweat environment is of significance to determine the suitability of the sensors to measure physiologically relevant glucose levels in sweat. The sensors were tested in an artificial sweat matrix, with a suitable alkaline pH by dissolving 0.1 M NaOH. Calibration of the sensors were repeated using this complex matrix

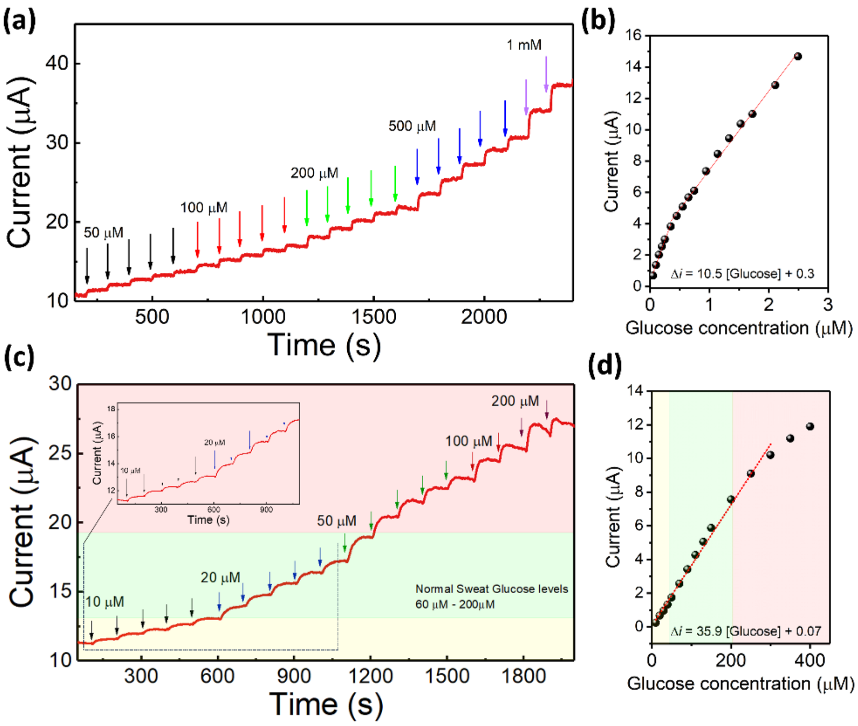

Figure 5.5 - LIG/CuNPs sensor operation with artificial eccrine sweat matrix. (a) Continuous amperometric sensor response in artificial sweat matrix and (b) corresponding calibration curve at 0.4 V. (c) Sensor response after electrochemical oxidation of CuNPs and (d) corresponding calibration curve.

(**Figure 5.5**). Addition of volume fractions of sweat sample with glucose to the sensor environment leads to the expected current step response of the sensor in continuous operation, showing the suitability of the LIG/CuNPs active surface for detection of glucose in this complex sample environment (**Figure 5.5a**). The resulting calibration (**Figure 5.5b**) shows a similar response of the sensors, but a slightly decreased sensitivity of 76.6 μA.mM^{-1}.cm^{-2} and a LOD of 26 μM, which may be attributed to the presence of other interferents in the sweat matrix, including amino acids and ions. Regular sweat glucose levels are correlated with blood glucose levels, but situate at more than one order of magnitude lower, varying from 10 to 200 μM [45]. To reliably detect glucose in real sweat samples within physiologically relevant levels, the LIG/CuNPs sensors require higher sensitivity and lower LOD. Generally, the catalysis of glucose oxidation is attributed to the presence CuOx species [26]. As shown in the literature, the degree of oxidation directly influence the sensitivity of sensors towards glucose oxidation and corresponding current density [29]. As seen in the XPS characterization of LIG/CuNPs there is oxidation of the CuNPs synthesized by the laser irradiation protocol. To further increase oxidation levels of CuNPs and increase sensor sensitivity, electrochemical oxidation of CuNPs was further promoted, by employing a chronoamperometry cycle at 0.7 V for 1 hour with 0.1 M NaOH electrolyte, prior to measurement. Subsequently, sensor response was assessed (**Figure 5.5c**), showing an improvement in the response at lower glucose concentrations. After oxidation, the sensor could reliably present current increases at low concentration of 10 μM and present a steady current step increase at physiologically relevant glucose concentrations in sweat. The calibration (**Figure 5.5d**) shows an increase in sensitivity, at 262 $\mu A.mM^{-1}.cm^{-2}$and a LOD of 3.3 μM. Using the standard deviation of background current of the sensor response instead of current response associated with glucose addition, the detection limit is as low as 338 nM. With the one-step synthesis of LIG/CuNPs modified electrodes and employing strategies to improve the presence of oxidized copper, the sensors present potentiality for further development and inclusion into wearable sensing systems for sweat glucose sensing.

5.4 Conclusions

This work focused on the development of a new method for the synthesis of LIG/CuNPs composites on paper. DLW technique was used for the simultaneous synthesis of LIG and CuNPs, which provided a simple and rapid method for the fabrication of electrodes for non-enzymatic glucose detection. The morphological, chemical, and structural properties of the fabricated composites were analyzed. LIG/CuNPs-based sensors were fabricated, and their charge transfer capabilities were assessed, reflecting good electrochemical performance. Moreover, sensors' ability to detect glucose was tested, and this non-enzymatic sensor exhibited good sensitivity and reproducibility. With careful sensor construction and methods to promote the oxidation of CuNPs within the composite, sensor response can be further improved, to show good sensitivity and detection limits for glucose determination in complex sweat matrix. These findings have potential for developing flexible bioelectronics economically and sustainably, allowing for sensor scalability and commercialization. Ultimately, by pointing out the potential of this new approach to synthesize LIG and CuNPs on paper for the non-enzymatic detection of glucose, this work brings up new possibilities for the biosensing field, translatable for the synthesis of other active metallic nanostructures.

References

1. Karimi-Maleh, H., Karimi, F., Alizadeh, M. & Sanati, A. L. Electrochemical Sensors, a Bright Future in the Fabrication of Portable Kits in Analytical Systems. *Chemical Record* vol. 20 682–692 (2020).
2. Grieshaber, D., MacKenzie, R., Vörös, J. & Reimhult, E. Electrochemical Biosensors - Sensor Principles and Architectures. *Sensors* **8**, 1400–1458 (2008).
3. Tonelli, D., Scavetta, E. & Gualandi, I. Electrochemical deposition of nanomaterials for electrochemical sensing. *Sensors (Switzerland)* vol. 19 1186 (2019).
4. Behrent, A., Griesche, C., Sippel, P. & Baeumner, A. J. Process-property correlations in laser-induced graphene electrodes for electrochemical sensing. *Microchim. Acta* **188**, 1–14 (2021).
5. Singh, S., Wang, J. & Cinti, S. Review—An Overview on Recent Progress in Screen-Printed Electroanalytical (Bio)Sensors. *ECS Sensors Plus* **1**, 023401 (2022).
6. Moya, A., Gabriel, G., Villa, R. & Javier del Campo, F. Inkjet-printed electrochemical sensors. *Current Opinion in Electrochemistry* vol. 3 29–39 (2017).
7. Cardoso, R. M. *et al.* Additive-manufactured (3D-printed) electrochemical sensors: A critical review. *Analytica Chimica Acta* vol. 1118 73–91 (2020).
8. Tortorich, R., Shamkhalichenar, H. & Choi, J.-W. Inkjet-Printed and Paper-Based Electrochemical Sensors. *Appl. Sci.* **8**, 288 (2018).
9. González-Sánchez, M. I., Gómez-Monedero, B., Agrisuelas, J., Iniesta, J. & Valero, E. Highly activated screen-printed carbon electrodes by electrochemical treatment with hydrogen peroxide. *Electrochem. commun.* **91**, 36–40 (2018).
10. Beitollahi, H., Mohammadi, S. Z., Safaei, M. & Tajik, S. Applications of electrochemical sensors and biosensors based on modified screen-printed electrodes: A review. *Anal. Methods* **12**, 1547–1560 (2020).
11. Pinheiro, T. *et al.* Direct Laser Writing: From Materials Synthesis and Conversion to Electronic Device Processing. *Adv. Mater.* 2402014 (2024) doi:10.1002/adma.202402014.
12. Gao, J., He, S. & Nag, A. Electrochemical detection of glucose molecules using laser-induced graphene sensors: A review. *Sensors* vol. 21 2818 (2021).
13. Le, T. S. D. *et al.* Recent Advances in Laser-Induced Graphene: Mechanism, Fabrication, Properties, and Applications in Flexible Electronics. *Adv. Funct. Mater.* **32**, 2205158 (2022).
14. Wan, Z., Nguyen, N. T., Gao, Y. & Li, Q. Laser induced graphene for biosensors. *Sustain. Mater. Technol.* **25**, e00205 (2020).
15. Pinheiro, T. *et al.* Laser-Induced Graphene on Paper toward Efficient Fabrication of Flexible, Planar Electrodes for Electrochemical Sensing. *Adv. Mater. Interfaces* **8**, 2101502 (2021).
16. Pinheiro, T. *et al.* Influence of CO2 laser beam modelling on electronic and electrochemical properties of paper-based laser-induced graphene for disposable pH electrochemical sensors. *Carbon Trends* **11**, 100271 (2023).
17. Bezinge, L. *et al.* Paper-Based Laser-Pyrolyzed Electrofluidics: An Electrochemical Platform for Capillary-Driven Diagnostic Bioassays. *Adv. Mater.* 2302893 (2023) doi:10.1002/adma.202302893.
18. Bhattacharya, G. *et al.* Disposable Paper-Based Biosensors: Optimizing the Electrochemical Properties of Laser-Induced Graphene. *ACS Appl. Mater. Interfaces* **14**, 31109–31120 (2022).
19. Lin, S. H., Lefeuvre, E., Tai, C. H. & Wang, H. Y. Fabrication of high-performance non-enzymatic sensor by direct electrodeposition of nanomaterials on porous screen-printed electrodes. *J. Taiwan Inst. Chem. Eng.* **137**, 104386 (2022).
20. Pérez-Fernández, B., Martín-Yerga, D. & Costa-García, A. Galvanostatic electrodeposition of copper nanoparticles on screen-printed carbon electrodes and their application for reducing sugars determination. *Talanta* **175**, 108–113 (2017).
21. Fei, J., Dou, W. & Zhao, G. A sandwich electrochemical immunosensor for Salmonella pullorum and Salmonella gallinarum based on a screen-printed carbon electrode modified with an ionic liquid and electrodeposited gold nanoparticles. *Microchim. Acta* **182**, 2267–2275 (2015).

22. Ye, R. *et al.* In Situ Formation of Metal Oxide Nanocrystals Embedded in Laser-Induced Graphene. *ACS Nano* **9**, 9244–9251 (2015).
23. Zhang, Q. *et al.* Self-Assembly of Graphene-Encapsulated Cu Composites for Nonenzymatic Glucose Sensing. *ACS Omega* **3**, 3420–3428 (2018).
24. Jiang, D. *et al.* Enhanced non-enzymatic glucose sensing based on copper nanoparticles decorated nitrogen-doped graphene. *Biosens. Bioelectron.* **54**, 273–278 (2014).
25. Adeel, M. *et al.* Recent advances of electrochemical and optical enzyme-free glucose sensors operating at physiological conditions. *Biosensors and Bioelectronics* vol. 165 112331 (2020).
26. Aun, T. T., Salleh, N. M., Ali, U. F. M. & Manan, N. S. A. Non-Enzymatic Glucose Sensors Involving Copper: An Electrochemical Perspective. *Crit. Rev. Anal. Chem.* **53**, 537–593 (2023).
27. Xu, D., Chan, K. C., Guo, H., Zhong, H. & Lu, L. One-step fabrication of a laser-induced forward transfer graphene/Cu: XO nanocomposite-based electrocatalyst to promote hydrogen evolution reaction. *J. Mater. Chem. A* **9**, 16470–16478 (2021).
28. Lee, J. U. *et al.* Green Synthesis of Laser-Induced Graphene with Copper Oxide Nanoparticles for Deicing Based on Photo-Electrothermal Effect. *Nanomaterials* **12**, 960 (2022).
29. Li, Q. *et al.* Highly Sensitive and Flexible Copper Oxide/Graphene Non-Enzymatic Glucose Sensor by Laser Direct Writing. *Adv. Sens. Res.* **2**, 2200067 (2023).
30. Zhao, J. *et al.* Co3O4 nanoparticles embedded in laser-induced graphene for a flexible and highly sensitive enzyme-free glucose biosensor. *Sensors Actuators B Chem.* **347**, 130653 (2021).
31. Han, X. *et al.* Laser-Induced Graphene from Wood Impregnated with Metal Salts and Use in Electrocatalysis. *ACS Appl. Nano Mater.* **1**, 5053–5061 (2018).
32. Coelho, J. *et al.* Paper-based laser-induced graphene for sustainable and flexible microsupercapacitor applications. *Microchim. Acta* **190**, 40 (2023).
33. Pinheiro, T. *et al.* Water Peel-Off Transfer of Electronically Enhanced, Paper-Based Laser-Induced Graphene for Wearable Electronics. *ACS Nano* **16**, 20633–20646 (2022).
34. Lin, J. *et al.* Laser-induced porous graphene films from commercial polymers. *Nat. Commun.* **5**, 5714 (2014).
35. Juska, V. B. & Juska, G. Copper-nanostructure-modified laser-scribed electrodes based on graphitic carbon for electrochemical detection of dopamine and glucose. *J. Chem. Technol. Biotechnol.* **96**, 1086–1095 (2021).
36. Peng, P. *et al.* One-step selective laser patterning of copper/graphene flexible electrodes. *Nanotechnology* **30**, 185301 (2019).
37. Kulyk, B. *et al.* Laser-Induced Graphene from Paper for Mechanical Sensing. *ACS Appl. Mater. Interfaces* **13**, 10210–10221 (2021).
38. Zhou, H. *et al.* Copper nanoparticles modified nitrogen doped reduced graphene oxide 3-D superstructure for simultaneous determination of dihydroxybenzene isomers. *Sensors Actuators, B Chem.* **249**, 405–413 (2017).
39. Whelan, C. M., Ghijsen, J., Pireaux, J. J. & Maex, K. Cu adsorption on carboxylic acid-terminated self-assembled monolayers: A high-resolution X-ray photoelectron spectroscopy study. *Thin Solid Films* **464–465**, 388–392 (2004).
40. Luo, J., Jiang, S., Zhang, H., Jiang, J. & Liu, X. A novel non-enzymatic glucose sensor based on Cu nanoparticle modified graphene sheets electrode. *Anal. Chim. Acta* **709**, 47–53 (2012).
41. Chen, Z. *et al.* Rapid and Sensitive Detection of anti-SARS-CoV-2 IgG, Using Lanthanide-Doped Nanoparticles-Based Lateral Flow Immunoassay. *Anal. Chem.* **92**, 7226–7231 (2020).
42. Alam, M. M. & Howlader, M. M. R. Nonenzymatic electrochemical sensors via Cu native oxides (CuNOx) for sweat glucose monitoring. *Sens. Bio-Sensing Res.* **34**, 100453 (2021).
43. Prabhakaran, A. & Nayak, P. Surface Engineering of Laser-Scribed Graphene Sensor Enables Non-Enzymatic Glucose Detection in Human Body Fluids. *ACS Appl. Nano Mater.* **3**, 391–398 (2020).
44. Tehrani, F. & Bavarian, B. Facile and scalable disposable sensor based on laser engraved graphene for electrochemical detection of glucose. *Sci. Rep.* **6**, 1–10 (2016).

45. Bariya, M., Nyein, H. Y. Y. & Javey, A. Wearable sweat sensors. *Nature Electronics* vol. 1 160–171 (2018).

6

WATER PEEL-OFF TRANSFER OF ELECTRONICALLY ENHANCED, PAPER-BASED LASER-INDUCED GRAPHENE FOR WEARABLE SENSING

Laser-induced graphene (LIG) has gained preponderance in recent years, as a very attractive material for the fabrication and patterning of graphitic structures and electrodes, for multiple applications in electronics. Preponderantly, polymeric substrates, such as polyimide, have been used as precursor materials, but other organic, more sustainable, and accessible precursor materials have emerged as viable alternatives, including cellulose substrates. However, these substrates lack the conductive and chemical properties achieved by conventional LIG precursor substrates and have not been translated into fully flexible, wearable scenarios. In this work, the conductive properties of paper-based LIG are expanded, by boosting the graphitization potential of paper, through the introduction of external aromatic moieties and meticulous control of laser fluence. Colored wax printing over the paper substrates introduces aromatic chemical structures, allowing for the synthesis of LIG chemical structures with sheet resistances as low as 5 $\Omega.sq^{-1}$, translating to an apparent conductivity as high as 28.2 $S.cm^{-1}$. Regarding chemical properties, I_D/I_G ratios of 0.28 showcase low defect densities of LIG chemical structures and improve on previous reports on paper-based LIG, where sheet resistance has been limited to values around 30 $\Omega.sq^{-1}$, with more defect dense, less crystalline chemical structures. With these improved properties, a simple transfer methodology was developed, based on a water-induced peel-off process that efficiently separates patterned LIG structures from the native paper substrates to conformable, flexible substrates, harnessing the multifunctional capabilities of LIG towards multiple applications in wearable electronics. Proof-of concept electrodes for electrochemical and strain sensors were patterned, transferred, and characterized, using paper as a high-value LIG precursor for multiples scenarios in wearable technologies, for improved sustainability and accessibility of such applications.

Keywords: Laser-induced graphene, paper, transfer methodologies, wearable electronics, electrochemical sensors, strain sensors

The literature presented in this chapter is published in:

❖ Pinheiro, T., Correia, R., Morais, M., Coelho, J., Fortunato, E., Sales, M. G. F., ... & Martins, R. (2022). Water peel-off transfer of electronically enhanced, paper-based laser-induced graphene for wearable electronics. *ACS Nano*, *16*(12), 20633-20646.

6.1 Introduction

Ever since its discovery, laser-induced graphene (LIG) has established itself as a very attractive material for electrode fabrication. For LIG, the straightforward fabrication stands on the need for minimal infrastructure and precursor materials, in a maskless, catalyst-free, non-toxic synthesis route, allowing for low-cost, high-throughput patterning of graphitic structures with very high selectivity and localized conversion, within fully customizable geometries [1]. This brings advantages when comparing to conventional graphene synthesis methods, such as graphite exfoliation, chemical vapor deposition (CVD) or crystal epitaxy, that require expensive and complex manufacturing equipment and processes [2]. As such, LIG has found space in the production of planar microelectronic devices, due to the resulting porous nature of the three-dimensionally stacked 2D lattices of the converted graphene structures, that circumvent some cumbersome processes of single layer graphene transfer, patterning and stacking for the production of functional architectures [3,4]. As a consequence, LIG has been used in many applications, ranging from energy harvesting and storage devices, such as triboelectric nanogenerators (TENGs) and microsupercapacitors (MSCs) [5], photovoltaics [6], electrophysiological signal monitoring [7], biophysical sensors and actuator systems [8] and electrochemical sensing[9]. Most of these applications have been developed on plastic polymers, mainly polyimide (PI), resulting in LIG with very attractive intrinsic properties, such as high specific areas (around 340 $m^2.g^{-1}$), good thermal stability (>900 ºC) and attractive electrical properties (5-25 $S.cm^{-1}$) [10]. More recently, other precursor substrates have been put forward to improve on the accessibility and environmental impact of such petroleum-based substrates [11]. These include wood [12], leaves [13] and other organic biomass such as cork [14]. Besides these, other more refined forms of extracted precursor materials have been used, including aromatic-rich lignin composite films [15] and cellulose rich substrates, such as cardboard [16] and paper sheets [17]. Natural organic substrates can achieve very good electrical properties, with sheet resistances as low as 10 $\Omega.sq^{-1}$, contingent on the presence of aromatic precursors, namely lignin, that can serve as a template for graphitization[12]. However, aliphatic-rich cellulosic substrates, such as paper, lacked in these electrical properties, since they do not possess the intrinsic aromatic carbon structures that aid in this graphitization process. With cellulose being the most abundant polymer in the world, its inclusion in fabrication chains in electronics is of interest, including as a high-value LIG precursor.

Another important aspect of LIG is its application in flexible microelectronic elements. This is empowered by the native flexible properties of the used plastic polymers or organic substrates, that lead to bound LIG microstructures that retain the mechanical properties of the selected native substrate. As such, many applications have been developed, targeting flexible, wearable electronics and bioelectronics [18]. However, these native substrates have some shortcomings when envisioning stretchable, fully conformable applications, due to low elasticity of commercial forms of these materials [19,20]. Hence, many authors have developed different transfer techniques, to move LIG microstructures into elastomeric polymers, that can add to this improved flexibility and conformability. These transfer techniques can be inspired by scotch-tape exfoliation of graphite, where adhesives are used to anchor LIG architectures to the transfer substrate [21,22]. Alternative approaches have been presented, by casting elastomer polymers over the scribed LIG structures, to produce elastomeric films that can anchor the bulk LIG volume. Such methods have been translated to use with a range of elastomers, including PDMS and other silicone elastomers [7,23], polymethyl methacrylate (PMMA) [24], Ecoflex [25] and substrates with other properties, such as biodegradable starch films [26], concrete or epoxy resins [27]. Another approach has been the embedding of LIG precursors into elastomeric films, that are then submitted to laser irradiation and patterning. Such approach has been applied for the fabrication of MSCs in PDMS embedded with PI [28] and pressure sensors from lignin embedded PDMS [29]. Using these methodologies, very attractive electronic elements can be fabricated. However, presently, none of these approaches have been adapted to the use of more accessible substrates such as paper and other cellulosic materials. This may be attributed to some technical drawbacks. Paper has high adhesion to adhesive glues, because they can incorporate its porous structure, inhibiting a direct peel-off. The same is observed for casting of elastomeric polymers over paper, ultimately hindering the peel-off without ripping the fibrous paper structure.

In this work, we expand the conductive properties of paper-based LIG, through a set of modifications that improve the conversion efficiency of cellulosic substrate into conductive graphitic structures, paired with meticulous control of laser operational parameters. Furthermore, a simple transfer method is developed, to harness these enhanced capabilities into flexible, conformable substrates, targeting applications for wearable electronics. The modifications imposed on the paper substrate are based on the introduction of aromatic carbon chemical structures, that promote a more efficient rearrangement of cleaved carbon bonds upon the laser irradiation process. The imposed treatment on the paper substrates is divided into two stages, firstly by the introduction of fire-retardant chemicals, that increase thermal resistance of the cellulose fibers, hindering their decomposition and ablation. Boron-based chemicals, such as Borax, suffer endothermic decomposition and release additional bound water molecules, acting as chemical heat sinks [30,31], that help dissipate the very high localized temperatures upon laser irradiation. Secondly, the paper substrates are treated with colored paraffin wax, to introduce aromatic compounds that can serve as templates for more efficient reorganization and intramolecular condensation upon the buildup of graphene lattices within the synthesized LIG. As previously shown for other substrates, such as wood, the amount of aromatic components, in this case lignin, is paramount to obtain improved chemical and conductive properties in the synthesized LIG structures [12]. As such, the control over the amount of colored wax used to modify the paper substrates is a simple way to control the efficiency of the laser induction and tailor the conductive properties of LIG patterns. In addition, a thorough control of the laser fluence applied to the substrate was employed, to study and optimize the outcomes upon the conversion process, by manipulating key variables including laser source power, lasing scan speed, focus of the laser beam and the number of lasing scans, used to increase the graphitization efficiency [32,33]. With such control over the conversion of wax-modified paper substrates, the conductive and chemical properties reached in this work are on par with LIG synthesized using aromatic-rich plastic polymers, such as PI and organic materials such as wood. Single-digit sheet resistance, low defect density and high degree of crystallinity of the obtained lattices is attainable with this modification, introducing paper into the toolbox of high efficiency LIG precursor materials. With these enhanced properties, versatile, simple transfer methodologies for paper-based LIG patterns are of interest, to target more comprehensive applications in flexible and wearable technologies. In this case, patterned and transferred electrodes for electrochemical and strain sensors were developed, showing the applicability and multifunctionality of this material, while improving on aspects of accessibility and cost reduction, within many sustainable production and fabrication frameworks, such as the United Nations Sustainable Development Goals or the European Union Green Deal.

6.2 Experimental Section

Reagents and Materials

During this work, ultrapure Milli-Q water laboratory grade (conductivity < 0.1 $\mu S.cm^{-1}$) was used to prepare all solutions, unless otherwise specified. Sodium tetraborate decahydrate ($Na_2B_4O_7$ $10H_2O$), potassium chloride (KCl), chroroplatinic acid hexahydrate (H_2PtCl_6 $6H_2O$), sulfuric acid (H_2SO_4) and 30% wt hydrogen peroxide solution were purchased from Sigma. Potassium hexacyanoferrate (III) ($K_3[Fe(CN)_6]$) and potassium hexacyanoferrate (II) trihydrate ($K_4[Fe(CN)_6]$. $3H_2O$) were purchased from Roth. All reagents were used as received, without further purification. Whatman chromatography paper grade 1 (Whatman International Ltd., Floram Park, NJ, USA) was used for laser irradiation and LIG formation. As transfer substrate models, Leukoplast Fixomull medical grade polyurethane tape, Hypafix polyester wound dressing tape, polydimethylsiloxane (PDMS) and 3M Transpore polyester fixing tape were used.

LIG Synthesis on Wax-modified substrates and peel-off transfer

Paper sheets were cut into A6 size (105x148 mm) and were submitted to a boron-based fire-retardant chemical treatment, as reported in previous chapters [34]. The paper sheets were dipped into a 0.1 M solution of sodium tetraborate solution for 20 minutes, followed by drying at room temperature. Following this treatment, paper sheets were submitted to wax printing, using a Xerox Colorqube printer, using commercial yellow wax printing cartridges compatible with the printer. These cartridges are composed of paraffin wax (CAS#8002-74-2) and a proprietary yellow pigment. To control the degree of paraffin and yellow pigment loaded into the paper sheets, the number of printing cycles varied, from 2 to 5. Each printing cycle consists of printing a superficial layer of wax, followed by heating the substrate over a hot plate, to permeate the wax throughout the volume of the paper. The loading capacity of the selected paper substrate was limited to 5 layers, since a complete pore filling is achieved and for higher cycle numbers, there is a leakage of wax ink outside the paper structure.

After substrate treatment and modification, the paper sheets were put over a glass substrate and fixed with adhesive tape, to secure a flat paper surface for irradiation. A CO_2 Universal Laser System with a 10.6 µm wavelength, 50 W maximum power and 127 $mm.s^{-1}$ maximum scan speed was used for substrate irradiation and LIG synthesis. Some laser operational parameters were fixed during this process. The number of points per inch (PPI) was set at 500 and the defocus between the substrate and focal point was fixed at -0.79 mm. Besides these variables, the laser source power, scanning speed and number of lasing scans were varied, to study the graphitization outcomes upon laser irradiation. In addition, the irradiation processes were performed under a nitrogen rich atmosphere.

After irradiation and patterning of LIG, the paper substrate was removed from the glass slide support and the transfer substrate was fixed to the same support. To transfer the irradiated patterns, the paper substrate is submitted to a wetting step, where both surfaces are submerged in water. Following this wetting step, the patterned paper surface is placed on top of the adhesive surface of the transfer substrate with slight pressure, for 10 seconds. After the complete area of the paper surface is put into contact with the adhesive surface, the paper substrate is peeled off, leaving behind the patterned paper-based LIG.

LIG Characterization

SEM characterization was performed using a Hitachi Regulus SU8220 system. Raman spectroscopy was performed in a Renishaw inVia Reflex micro-Raman spectrometer equipped with an air-cooled CCD detector and a HeNe laser. The laser beam was focused through a 50x Olympus objective lens. Measurements were performed with a 532 nm laser with 10 s exposure time and 3 accumulations as measurement parameters, with a laser power of 16 mW. X-ray photoelectron spectroscopy was performed using a Kratos Axis Supra, equipped with mono-chromated Al Kα radiation (1486.6 eV). Chemical composition was also studied through EDS mounted in an SEM (Hitachi TM 3030Plus Tabletop). Electrical sheet resistance was determined by Hall effect measurements in Van der Pauw geometry in a Biorad HL 5500 equipment at room temperature.

Fabrication and Characterization of Electrochemical Sensors

Three-electrode electrochemical cells were constructed by patterning LIG-WE and LIG-CE elements over wax-modified paper substrates and their subsequent transfer into the desired substrate. After transfer of these two elements, a mask was cut over a glassine paper to manually pattern an Ag/AgCl RE and silver contacts. After patterning, the glassine paper is removed and the cell is encapsulated, leaving open areas for the electrodes and contacts. Electrochemical measurements were performed using a PalmSens 4.0 Potentiostat (PalmSens Compact Electrochemical Interfaces). Prior to characterization, an electrochemical pre-treatment cleaning step was performed on the electrodes, by CV scanning a potential window from -2 to 2 V at a scan rate of 100 mV.s^{-1}, using the supporting electrolyte (0.1 mM KCl). After pre-treatment, electrochemical cells were rinsed with water and left to dry in air. CV assays were carried with a potential window from -0.3 to 0.7 V, at scan rates from 10 to 200 mV.s^{-1}. EIS was carried with a pulse of 5 mV in amplitude, 50 data points, over a frequency range from 10.000 to 0.1 Hz. The electrochemical measurements both by CV and EIS were performed using a redox probe solution of 5.0 mM $[Fe(CN)_6]^{3-}$ and $[Fe(CN)_6]^{4-}$, prepared in the supporting electrolyte. For PtNPs electrodeposition, CV technique was employed, by scanning a potential window between -0.2 and 0.7 V at 50 mV.s^{-1} for 20 cycles, using a 2.5 mM platinum salt solution in 60 mM H_2SO_4. Chronoamperometry measurements were performed by immersing the PtNPs modified sensors in 200 µL phosphate buffered saline (PBS) buffer (0.1 M, pH 7.4) and subsequently remove and add 10 µL of H_2O_2 solution in PBS buffer, to make the desired concentration.

Fabrication and Characterization of Strain Sensors

Serpentine-shaped patterns based on previous literature [35] were patterned over wax-modified paper and subsequently transferred into a desired substrate. After transfer, silver tracks were patterned using a glassine paper mask, followed by encapsulation of the sensor, so that LIG is not in contact with skin for biophysical signal monitoring. Characterization of strain sensors was performed using a custom build bending apparatus controlled by an Arduino, allowing for the control of bending radius and resulting applied strain and bending frequency. To monitor the signal arising from bending stimulus and radial artery pulse, a PalmSens 4.0 Potentiostat was used, operating in chronopotentiometry mode. For CP, a constant current of 10 µA was applied, to monitor the potential changes and compute the variations in pattern resistance towards the applied mechanical stimuli.

6.3 Results and Discussion

6.3.1 Boosting the properties of paper-based LIG through colored paraffin and laser fluence control

Paper substrates can be directly converted to LIG by DLW, using commercial CO_2 laser sources, after appropriate fire-retardant chemical treatments that increase their thermal resistance [33]. The aliphatic carbon rings within the polymeric structure of cellulose are cleaved and reorganized into graphitic structures, with the degree of aromaticity and resulting graphenization dependent on the imposed fluence over the substrate. However, due to the absence of aromatic carbon chemical arrangements in its composition, that are more prone to graphenization [12], the efficiency of these laser conversion processes have been inferior when compared to other substrates, such as PI or wood, resulting in less attractive conductive and chemical properties of the synthesized, paper-based LIG. As such, the introduction of aromatic chemical structures is proposed as a means of improving the graphenization process upon DLW of paper substrates, paired with a thorough control of laser fluence, dictated by laser operational parameters. The mechanism for the synthesis of electrically enhanced paper-based LIG is schematically illustrated in **Figure 6.1a**. Using a 10.6 µm CO_2 laser source with a 50 W maximum power, paraffin wax-treated paper substrates are irradiated under specific conditions, to achieved LIG patterns with single-digit sheet resistance (R_{sh}) and improved chemical properties, showcased by Raman profiles with improved defect densities. Firstly, the modified paper substrates are irradiated with a specific distance from the laser beam exit nozzle of 0.79

mm, to control the laser spot size and energy density imposed over the substrate by unit of area, as presented in **Chapter 4**. Using different spot size focus profiles has been shown to improve the efficiency of laser-induced conversion processes, by creating laser spot superposition patterns that act as if the same area is multiply lased, boosting the continuity of the patterned material both within a single raster line and consecutive lines [11]. Upon this irradiation, the aliphatic carbon rings within cellulose chemical structures and the hydrocarbon and aromatic structures present in the paraffin and in the yellow pigment used to color the paraffin wax suffer laser-induced pyrolysis, with photothermal cleavage of C-O-C, C-C and C-O bonds, causing depolymerization, deoxygenation and dehydration of the native chemical structures. This pyrolysis process creates a carbon pool that serves as a template for reorganization and aromatization, leading to the necessary graphitization of the substrate and LIG production, aided by the presence of increased amounts of aromatic chemical structures. In this case, this commercial form of paraffin wax contains two benzene structures bound with straight chain hydrocarbons and is mixed with resin and yellow dye [36], that can also contain aromatic carbon rings within their chemical structures. Dyes and pigments usually possess conjugated systems where there are alternating double and single bonds within aromatic structures, that have resonance of electrons giving rise to absorption in specific wavelengths of the visible spectrum

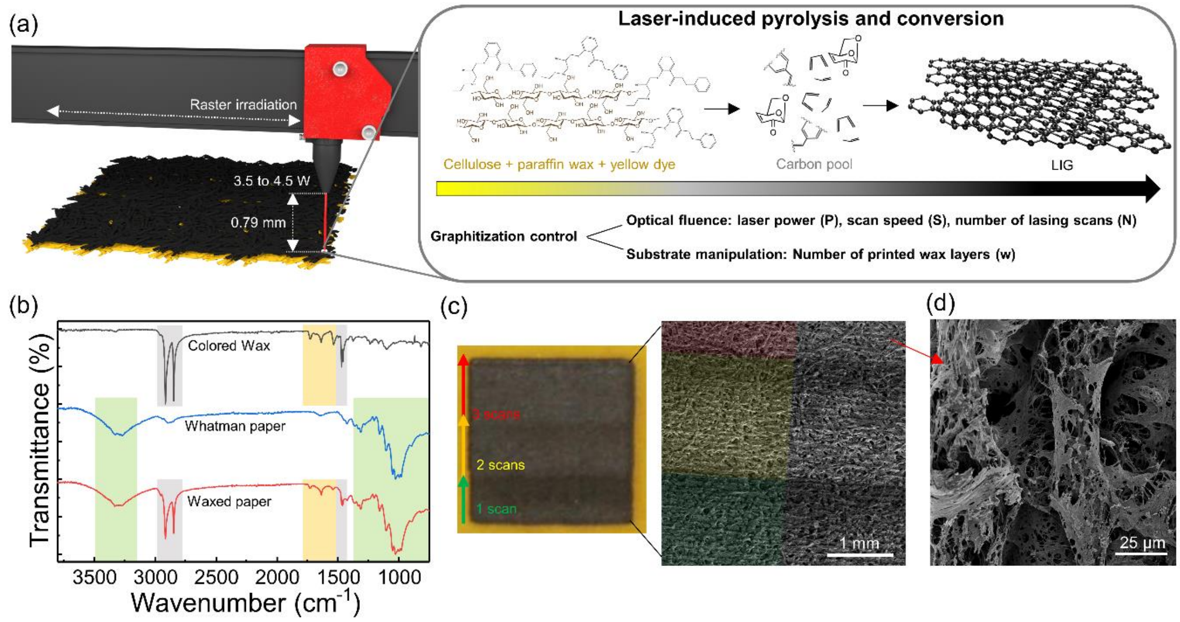

Figure 6.1 - Synthesis of LIG from wax-modified chromatography paper. (a) Schematic representation of conversion mechanism. (b) FTIR spectra of LIG precursor materials, showing the introduction of aromatic moieties into the volume of paper substrate from colored paraffin wax. (c) Optical image of converted LIG square with three distinct regions, corresponding to the number of lasing scans and the resulting SEM micrograph. (d) SEM micrographs of converted LIG after three lasing scans.

[37]. The paper substrates and modified paper substrates were studied with Fourier Transform Infrared spectroscopy (FTIR), to identify the chemical bonds within their structure, presented in **Figure 6.1b**. As can be seen, some of the characteristic peaks for paraffin wax can be identified in the FTIR spectrum of this colored wax (highlighted in gray), namely carbon-hydrogen stretching and bending bands from its -CH3 and -CH2 groups (719, 1463, 2849 and 2917 cm^{-1}) [38]. Besides these peaks, there are different overtones, from 1500 to 1750 cm^{-1}, some of them could be attributed to C=C aromatic rings and their stretching [39], arising from the aromatic components in paraffin and the yellow dye contained in it (highlighted in yellow). Although the specific pigment used for this wax printing formulation is not disclosed by the manufacturer, a thorough survey of chemical structures associated with pigments and dyes shows the abundance of aromatic-rich chemistry in these components [40]. When printing wax layers over the paper substrate, the resulting spectra contains all these components associated with colored paraffin wax, besides the ones associated with the aliphatic ring arrangements of the polymeric structure of cellulose, such as the peaks associated with C-O-C and C-O bonds around 1000 cm^{-1} (highlighted in green). As such, it is seen that the aromatic moieties contained in the paraffin wax are introduced in the volume of the paper substrate, with their density able to be controlled by the number of printing cycles (Figure D1). Furthermore, the use of more wax printing cycles leads to a more complete filling of paper porosity, turning the distribution of the modifying wax more uniform, until a maximum point reached at 5 wax layers (Figure D2).

To control the degree of graphitization of the modified substrate upon laser irradiation, the fluence applied to the substrates was manipulated, by imposing distinct laser powers, raster scan speeds and number of patterning scans to the substrate, treated with varying layers of colored paraffin wax. In **Figure 6.1c**, a square patterned within a paper substrate treated with 4 wax layers and using 4 W laser power is presented, with three different regions patterned with different number of lasing scans. In region 1, single lasing was performed with a scan speed of 15.2 $cm.s^{-1}$, while in region 2, double lasing is imposed, maintaining the same scan speed for the first scan and decreasing the scan speed to 12.7 $cm.s^{-1}$ for the second scan. In the third region, three lasing cycles are imposed, maintaining the same conditions of region 2 and performing the third scan with a scan speed of 10.2 $cm.s^{-1}$. The rationale for decreasing the scan speed for subsequent lasing scans is based on the increased conversion efficiency observed for lower speeds, caused by an increased fluence [41]. Thus, the first scan serves as a first carbonization step, with higher speed that minimizes damage to the substrate, followed by scans with lower scanning speeds, for increased cleavage and reorganization of bonds. The SEM micrograph of the patterned square is presented, showing marked differences between each region.

With the increase in the number of lasing scans, the overall coloration of the LIG surface changes and tends to become more metalized, a first indication that the pattern may become more conductive. Furthermore, it is possible to observe the effect of raster scans over the substrate, with the expected horizontal line patterns, that do not destroy the native fibrous architecture of the paper substrate. In terms of the architecture of individual fibers after the irradiation process, presented in **Figure 6.1d,** it is possible to discern that additional porosity is imposed over the substrate, caused by decomposition of organic chemical structures of the treated paper substrate and consequent release of volatiles. Furthermore, it is visible that wax previously filling paper pores is removed after irradiation, indicating that improvements in conductivity are not imposed by the presence of additional conductive material, but by more efficient graphitization of cellulose fiber templates. In addition, irradiation of paper composites with distinct amounts of wax does not lead to significant structural and morphological changes, in terms of the fibrous nature of the material, besides slightly smoother fiber surfaces for higher printing cycles. No results are presented for unmodified paper as reference, since without the inclusion of the solid wax ink, the described irradiation regimens lead to complete ablation of paper, even with the presence of a fire retardant. This shows how the proposed modification scheme further increases the thermal resistance, allowing for the application of higher power regimens and resulting temperatures for carbonization and graphitization.

When it comes to the resulting chemical and conductive properties of LIG synthesized using these conditions, characterization was performed using Raman spectroscopy, Energy Dispersive X-Ray spectroscopy (EDS), X-ray photoelectron spectroscopy (XPS) and 4-point probe electrical measurements for R_{sh} assessment. **Figure 6.2a** presents normalized Raman spectra of LIG patterned on paper modified with four wax layers, 4 W imposed power and varying number of lasing scans. From the analysis of the spectra, it is possible to see that the synthesized LIG has a low defect density, characterized by low intensity D peaks, and good crystallinity, characterized by intense 2D peaks. Furthermore, a comparison of the spectra shows how the use of multiple lasing scans is a simple strategy to improve the chemical properties of LIG. In this case, both I_D/I_G and I_{2D}/I_G ratios indicate an improvement in these properties when more lasing scans are imposed. For a single scan approach, the I_D/I_G has a value of 0.63, decreasing to a value of 0.39 for triple lasing scan. Contrarily, the I_{2D}/I_G ratio increases from 0.48 to 0.58, showing a more crystalline, ordered LIG. This improvement in the Raman profiles of LIG is paired with an increase in the superficial, relative carbon content of LIG films, demonstrated by EDS measurements presented in **Figure 6.2b**. For a single scan patterning, a C/O ratio of 28.8 is achieved, tripling the relative carbon content for three lasing scans, with a C/O

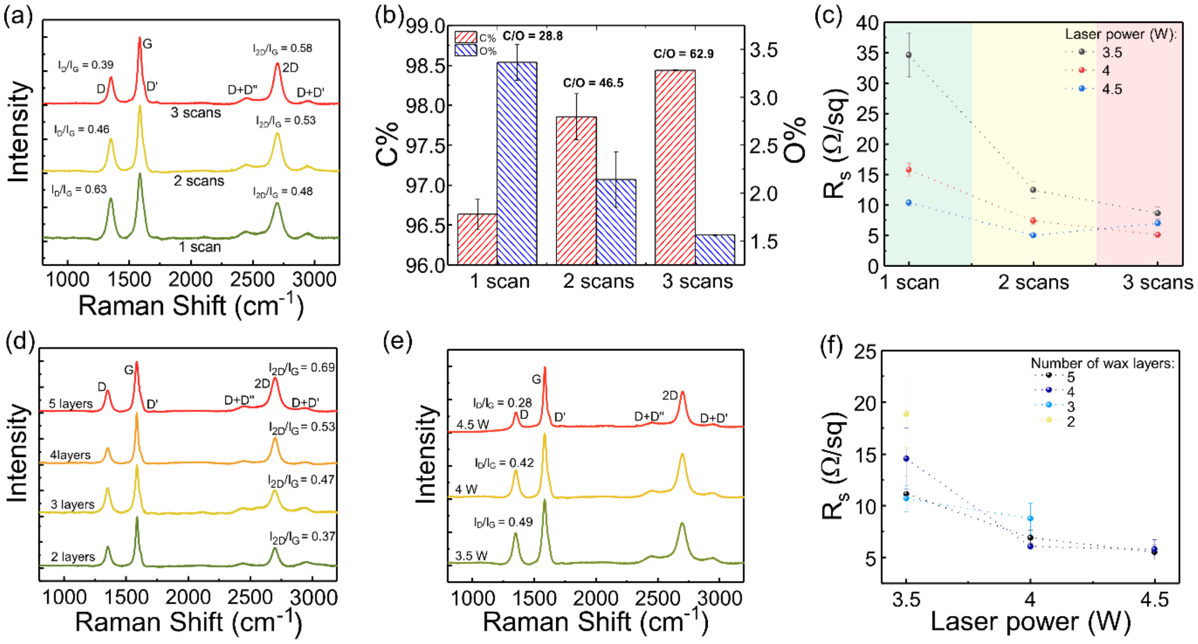

Figure 6.2 - Characterization of LIG synthesized on wax-modified paper. (a) Raman spectra on the effect of the number of lasing scans used for conversion and (b) EDS relative elemental analysis of resulting LIG, using paper modified with 4 wax layers and 4 W laser power. (c) Sheet resistivity of LIG applying one to three lasing scans and varying laser powers over paper modified with 4 wax layers. (d) Raman spectra on the effect on the amount of wax used to modify paper substrates. (e) Raman spectra on the effect of increasing laser source power on LIG chemical properties. (f) Sheet resistivity measurements on the effect of increasing laser source power for LIG synthesized using three lasing scans and paper modified with varying wax layers (2 to 5).

ratio of 62.9, showing a more efficient cleavage of undesired C-O bonds and their subsequent release as gases. To determine the effect of this improvement of chemical properties upon the conductive properties, R_{sh} determination showed that the increase in lasing scans leads to a decrease of this parameter (**Figure 6.2c**). For a single lasing scan, the conversion process of paper treated with 4 wax layers leads to R_{sh} values ranging from 34.6 $\Omega.sq^{-1}$ (10.3 % RSD, n=5) to 10.38 $\Omega.sq^{-1}$ (4.7% RSD). This shows the utility of waxed paper, that allows for the synthesis of LIG with R_{sh} values on par with polyimide. When the number of lasing scans is increased, R_{sh} decreased for all the tested laser power values. For 3.5 W, triple lasing scan leads to a R_{sh} value of 8.6 $\Omega.sq^{-1}$ (11.8 % RSD), already achieving single-digit values. However, for increasing laser powers, it is possible to reduce this resistance, with R_{sh} lowering to 5.1 $\Omega.sq^{-1}$ (7.3 % RSD) for 4 W laser power and 5.0 $\Omega.sq^{-1}$ (3.8 % RSD) for 4.5 W power, using two lasing scans. The resulting R_{sh} shows improved conductivities when compared to reports in the literature for several precursor materials, such as PI, that reached minimum values around 15 $\Omega.sq^{-1}$ [10], wood, that presented R_{sh} around 10 $\Omega.sq^{-1}$ [12] and other cellulosic substrates, that reached minimum values around 30 Ω.sq^{-1} [42]. For triple lasing scan using 4.5 W power, there is an excessive laser fluence, that causes degradation of the substrate and LIG chemical structures, leading to a slight increase in R_{sh}. Thus, lasing power was limited to 4.5 W for further investigations.

After showing how the use of wax treated paper, paired with control of laser fluence, can result in improved chemical and electrical properties of LIG films, Raman analysis was employed to determine the effect of the amount of wax towards the graphitization process. In **Figure 6.2d**, Raman spectra of LIG films synthesized on paper treated with two to five wax layers, 4 W laser power and three lasing scans is presented. The main finding when comparing the spectra is the improvement of the I_{2D}/I_G ratio, that evolves from a value of 0.37 (11,0 % RSD, n=6) for two wax layers, to 0.69 (2.4 % RSD) when five layers are employed. This shows that for the same lasing conditions, the presence of increasing amounts of wax leads to more crystalline, ordered LIG chemical structures, since there is a higher density of aromatic chemical structures that boost the graphitization potential of the substrate, by acting as nucleation centers where aromatization and buildup of graphene lattices can start and progress towards highly graphitic structures. Taking the most crystalline, ordered condition of five wax layers, the effect of applied lasing power was surveyed, showing similar effects to the increase in the number of lasing scans. For progressively higher laser power (**Figure 6.2e**), the high degree of crystallinity is paired with an improvement on defect density, showing how laser fluence influences the rearrangement of carbon bonds towards more pristine 2D lattices composing the 3D LIG films. For a lasing power of 3.5 W, an I_D/I_G ratio of 0.49 (11.9 % RSD) was reached, improving to 0.28 (22.6% RSD) for 4.5 W. The fingerprints of these chemical properties, associated with these combinations, are reflected on the resulting R_{sh} measurements for conditions employing three lasing scans, presented in **Figure 6.2f**. The tendency of the conductive properties of LIG patterns is to improve with the increase in the number of printed wax layers and lasing power employed for conversion. When fewer wax layers are applied, R_{sh} values are higher and the substrate suffers excessive degradation, not being conducive for conductivity measurements. For increasing number of wax layers, higher lasing powers can be employed for conversion, since there is more material to be converted, ultimately improving the thermal resistance of the substrate and the resulting graphitization outcomes. Using these strategies, single-digit R_{sh} values can be consistently achieved, with multiple combinations reaching values around 5 Ω.sq^{-1}. Overall, this simple wax treatment of paper substrates towards improved chemical and conductive properties reaches the best values of Raman peak ratios and R_{sh} of any report using cellulosic substrates, to the best of our knowledge, showing potential for application in the development of electrodes and components for planar microelectronics. In addition, multiple experimental conditions using wax treated paper result in very attractive chemical and conductive properties.

6.3.2 Water Peel-off Transfer of Paper-based LIG

After enhancing the capability of paper substrates to be high value LIG precursors, through the introduction of aromatic moieties, its applicability towards flexible, conformable electronic elements was studied. In **Figure 6.3a**, a schematic representation of the developed transfer methodology is presented. Starting with the irradiation and patterning of any desired LIG structure, this transfer method can be applied to a versatile range of geometries targeting different applications, from interdigitated electrodes to planar electrochemical cells and other electrode formats. After the patterning of any desired functional LIG design, the paper sheet is removed from its glass support and is subjected to a wetting step. This has the purpose of mildly separating converted LIG chemical structures from any native cellulose fibers and fibrils not affected by the irradiation. Cellulose fibers and fibrils present a much higher affinity towards water, due to the abundance of hydrogen bonds, that are important at cellulose's intermolecular, fibril and fibre levels [43]. Contrarily, the converted material and its interlayer interactions are mostly dominated by π- π stacking of converted graphene layers and weak Van der Waals forces [44], creating a defined interface between native and converted material. Upon the wetting process, water interacts with cellulose fibers at the interfacial level, creating additional hydrogen bonds, that promote their separation from LIG chemical structures. Following this step, the wetted paper substrate can be applied to any desired transfer substrate, with the requirement that it possesses adhesive properties. Thus, a simple stick and peel-off process is necessary for the complete transfer of LIG functional patterns, where water acts both to separate LIG-cellulose phases and prevent the adhesion of paper to the adhesive transfer layer, due to the abundant hydrogen bonds formed between water and cellulose, without the need for any specific pressure requirements for the release of LIG onto the transfer substrate. As a transfer substrate model, a medical grade polyurethane tape with a polyacrylate glue surface was selected (Leukoplast® Fixomull), due to its elastic properties, ideal to characterize transferred LIG structures in different scenarios. However, this transfer method can be applied to a myriad of substrates, as seen in Figure D3, contingent on the presence of an adhesive layer, that can be added to any desired transfer substrate, using repositionable spray adhesives, as was performed for transfer into PDMS.

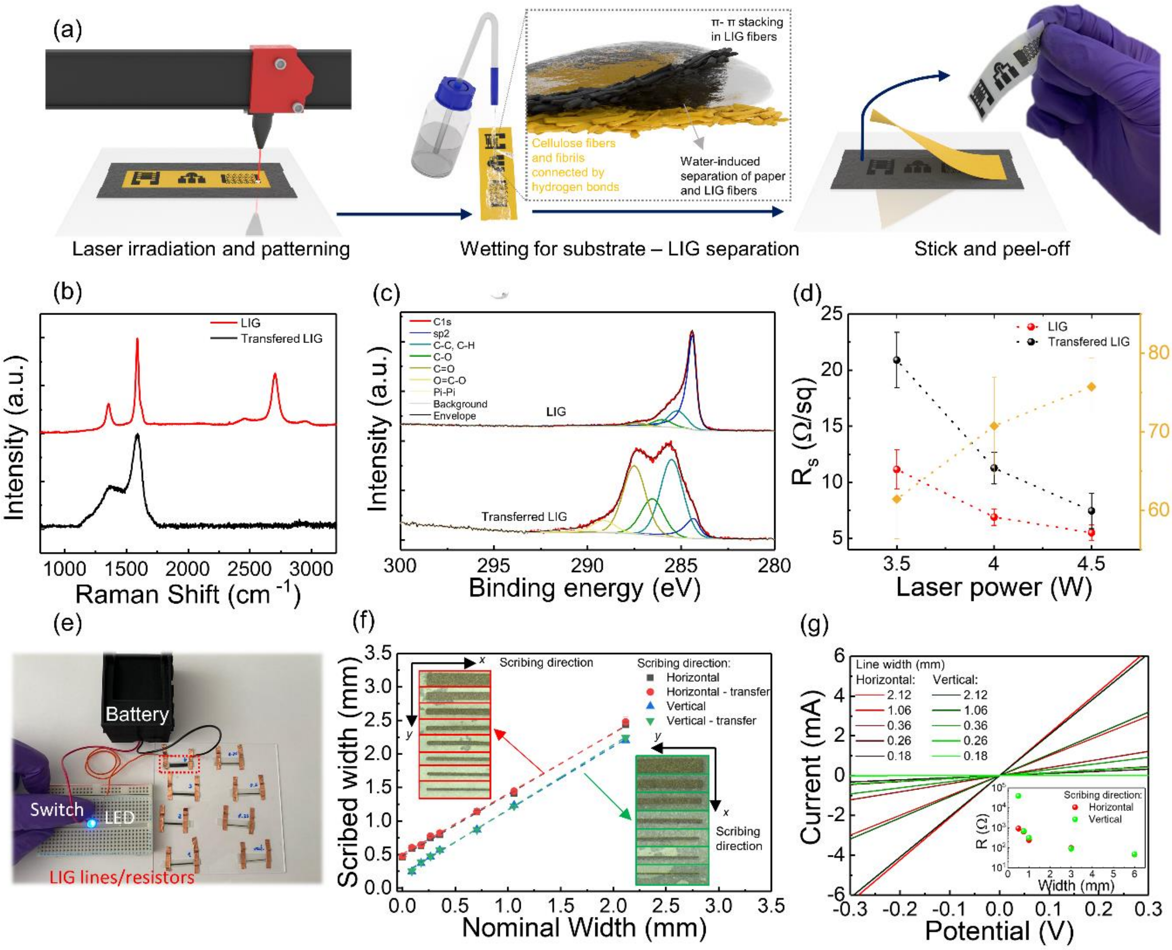

Figure 6.3 - Water induced peel-off transfer process of paper-based LIG and characterization of transferred LIG chemical structures. (a) Schematic representation of the three-step transfer process, starting with laser scribing and patterning of functional architectures, wetting of substrate and LIG patterns for mild separation and sticking and peel-off of LIG patterns onto the transfer substrate. (b) Raman and (c) XPS C1s deconvoluted spectra of pristine and transferred LIG. (d) Sheet resistivity of pristine and transferred LIG. (e) Transferred LIG electric lines and resistances at an electric circuit for connection of a battery and LED. (f) Analysis of nominal vs. scribed line widths before and after transfer, depending on scribing direction. (g) I-V curves and resistance of transferred lines, depending on scribing direction.

To characterize the chemical and conductive properties of transferred LIG, Raman spectroscopy, XPS and 4-point probe measurements were performed. In **Figure 6.3b**, a comparison is drawn between LIG synthesized using 4.5 W power and three lasing scans, over a paper substrate modified with 5 wax layers. As can be seen, the expected Raman profile of pristine LIG previously presented is achieved. However, upon the transfer of the LIG structures, the downward surface of the pattern is exposed to the excitation laser, leading to a much different Raman profile. This downward surface is mostly constituted by more amorphous carbon forms, represented by the absence of the 2D peak and the increased width of G and D peaks. This evidence was confirmed by XPS (**Figure 6.3c**), used to survey the C1s spectra of pristine and transferred LIG. For pristine LIG surface, the deconvolution of the C1s spectra shows the preponderance of the peak associated with sp^2 carbon bonds, characteristic of synthesized graphitic structures. In addition, there is a low density of different C-O bonds, characteristic of the native materials, showing a high conversion efficiency. In opposition, the surface exposed after transfer shows less density of sp^2 carbon and higher preponderance of sp^3 carbon bonds and remaining C-O, C=O and O-C=O bonds, more abundant at the native wax-printed cellulose substrate. This shows that the photothermal phenomenon governing the conversion of the substrate to LIG, upon exposure to the CO_2 laser beam, is less efficient with the increase in conversion depth, leading to less pristine graphitic structures over higher depths and more abundance of oxygen moieties. Furthermore, it can be hypothesized that considering the tubular nature of cellulose fiber architectures, fiber surfaces directly exposed to the laser beam will be more efficiently converted, while the opposing surfaces are less exposed to the high temperatures imposed over the irradiation process. This influences not only the microscopic effects over individual fibers, but also the macroscopic properties of the surface exposed after transfer. This is slightly reflected in the measured R_{sh} values for transferred and pristine LIG patterns (**Figure 6.3d**). When comparing the values after transfer, an increase in the resistive properties of patterns is observed, mainly for lower applied laser power. For 3.5 W, R_{sh} increases to 20.9 $\Omega.sq^{-1}$ (11.8 % RSD, n=5), almost doubling the resistance. For 4 W, this difference is not as significant, with R_{sh} values of 11.2 $\Omega.sq^{-1}$ (12.6 % RSD) and for 4.5 W the difference is less significant, with patterns achieving values of 7.5 $\Omega.sq^{-1}$ (11.5 % RSD), showing that the same levels of single-digit R_{sh} can still be reached for transferred LIG. However, due to the increase in amorphous carbon contents at the exposed surface after transfer, the real sheet resistance of LIG may not be reflected, because these carbon forms are the ones in contact with the measurement probes, leading to an increase in contact resistivity. This is also an important consideration for applications where the surface chemistry and conductivity of LIG are key parameters. In conjunction with sheet resistance, pattern thickness was analyzed by cross-section measures (Figure D4). For increasingly higher power regimens, pattern thickness increases, as expected by the higher temperatures that affect cellulosic structures at higher depths (**Figure 6.3d**). Taking into consideration these thickness values, estimation of conductivity shows the improved conductive properties when compared to other reports of paper-based LIG (Table D1). For LIG bound to paper and synthesized using 4.5 W, a mean conductivity of 24.3 $S.cm^{-1}$ (11.1% RSD, n=5) was reached, reaching values as high as 28.2 $S.cm^{-1}$. For transferred LIG patterns using the same condition, mean conductivity of 19.3 $S.cm^{-1}$ was reached. Comparing these metrics with other LIG forms, this paper-based LIG reaches similar conductivity levels reported for PI (25 – 34 S.cm^{-1}) [10], wood (23.3 S.cm^{-1}) [45] and other engineered lignocellulosic precursors (28 S.cm^{-1}) [46], while far exceeding previous reports for paper-based LIG, as evidenced in Figure D5. Considering the porosity of paper, effective conductivity values that consider the fibrous architectures of paper can be estimated. Using the Reynolds and Hugh rule [46,47], the effective conductivity of the carbon LIG material can be estimated by normalizing the volume fraction of carbon. Taking the porosity of Whatman grade 1 paper (48 %) [48] and not considering additional porosity caused by the irradiation process and volatile release, the effective conductivity of this carbon material can reach values as high as 67.3 S.cm^{-1}.

To study the versatility of patterning and design of LIG structures and their transfer, the resolution and resistivity of LIG lines with varying widths were surveyed, to understand the influence of the directional dependency of the raster process over the conductive properties and width after irradiation, in opposition to the nominal width set in the laser control software. As can be seen in **Figure 6.3e**, these LIG lines can act as circuit elements, where the control of geometry dictates their resistive properties, allowing the flow of current in a simple circuit capable of turning an LED on and off. Lines with varying nominal widths were constructed, to determine the resulting scribed width. Depending on raster direction, the laser spot pulse density can be subjected to variations, that influence the resolution of the scribing process of any pattern, which is important in different functional designs that contain both horizontal and vertical elements within their geometry. For horizontally scribed lines, their length was scribed from left to right, following the raster movement of the laser mirror, with their width being set by consecutive raster cycles. Contrarily, for vertically scribed lines, their length was scribed from top to bottom, with the horizontal raster movement setting the width of the line. Results are presented in **Figure 6.3f**, showing a similar behavior of the scribed width for both the horizontal and vertical irradiation, with a linear variation associated with the increase in scribed width. However, it is visible that the resolution of the scribed lines varies with the scribing orientation. Vertically scribed lines have widths closer to the nominal width, while horizontally scribed lines present higher resulting widths, evidenced by the upward shift. Furthermore, it is only possible to pattern the minimum width set in the laser control software, corresponding to a width equal to the laser spot size, using a horizontal orientation. This is a result of the variation in pulse resolution of the used laser system, where for the x direction, it is set by the points per inch (PPI) setting of the laser systems. For the same set width, the number of raster cycles in the y direction is much lower than the PPI setting, resulting in these differences. For horizontal scribing direction, the lowest achieved width was 464.4 µm, while for vertical scribing, the lowest width value was 252.1 µm, with no changes after line transfer, for both raster regimens. These results were complemented with the measurement of I-V curves for patterned lines, presented in **Figure 6.3g**. The results indicate that for higher line widths, the difference in the measured resistance for horizontal and vertical scribing is not significant, with lines of 2 mm width achieving resistance values of around 50 Ω. With the decrease in patterned width, the resistance of the lines increases, with resistance of patterns in three different orders of magnitude, from 101 Ω to 10^3 Ω. Due to the variation in pulse density upon the irradiation process, there is a threshold at which the difference in resistance between vertical and horizontal scribing increases substantially, as is the case for a nominal width of 180 µm, where for horizontal scribing, the line presents a resistance of around 1kΩ, while for vertical scribing, the resistance increases to approximately 40 kΩ. These are important considerations when miniaturizing LIG functional patterns, where a careful manipulation of operational parameters is crucial to achieve fine patterns that can approximate the maximum laser resolution, close to the laser spot size (127 µm at focal point). To test the reproducibility of the transfer process, 200 lines (20 x 2.2 mm, 5 wax layers, 3 scans and 4.5 W power) were fabricated and tested in terms of their conductive properties. For a first group of 100 lines bound to the paper substrates, a mean resistance of 53.9 Ω (9.6% RSD, n=100) was reached, translating to a conductivity of 23.0 S.cm^{-1}. For the second group, made of 100 transferred lines, a mean resistance of 62.4 Ω (12.8% RSD) was reached, translating to a conductivity of 19.9 S.cm^{-1}. Furthermore, a yield of 93% was reached for the transfer group, considering unsuccessful transfer when lines showed a resistance above 2.5 standard deviations. These conductivity results, estimated by line resistance and geometry, corroborate the conductivity assessed by sheet resistance measures, confirming the good conductivity of this paper-based LIG.

6.3.3 Demonstration of flexible, wearable electronics from transferred paper-based LIG

After demonstrating the excellent and tunable conductive properties enabled by LIG synthesis on wax-modified paper and its transferred form, the same flexible, stretchable polyurethane medical grade tape was used as a model transfer substrate. Optimized synthesis conditions of five wax layers, 4.5 W power and three lasing scans were employed to exemplary pattern, transfer and assemble different components for wearable bioelectronic applications, as depicted in **Figure 6.4a**. This exemplary patterned, skin-worn patch shows that different and complex electrode and connector geometries can be transferred. However, the use of LIG as a

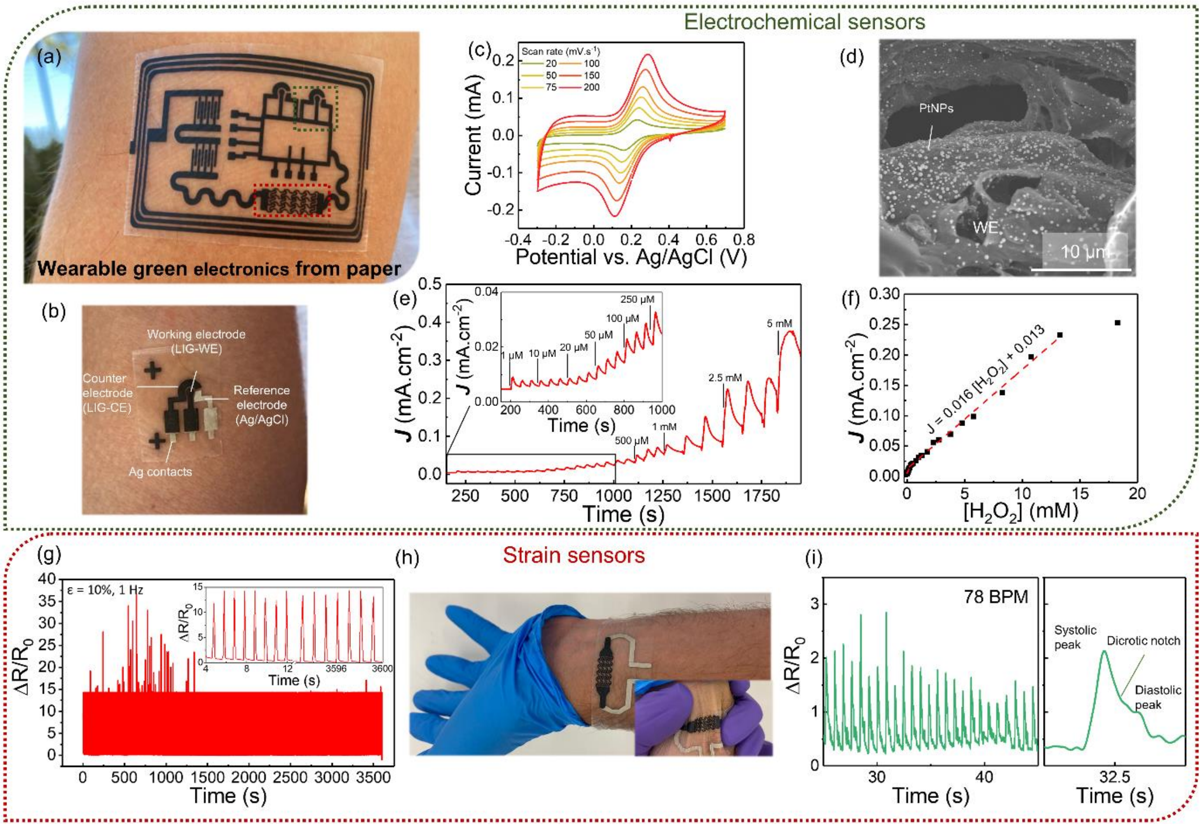

Figure 6.4 - Demonstration of flexible, wearable applications for transferred paper-based LIG. (a) Illustrative circuit with planar microelectronic elements for skin-worn functional patches. (b-f) Flexible, skin-worn electrochemical planar cell development and characterization. (b) Electrode components for the developed cells on the skin. (c) CVs for $Fe(CN)_6^{3-/4-}$ redox probes at different scan rates (20 – 200 $mV.s^{-1}$). (d) LIG-WE surface after PtNPs electrodeposition. (e) Chonoamperometry response of PtNPs modified LIG-WE towards H_2O_2 at 0.7 V applied potential. (f) Amperometric calibration of H_2O_2 sensor. (g-i) Wearable strains sensor from transferred paper-based LIG. (g) Bending strain cycling at 10% applied strain with 1 Hz frequency and 3600 cycles. (h) Strain gauge applied in the wrist, for pulse wave monitoring from the radial artery, with inset showing skin conformability of the LIG-polyurethane sensor. (i) Pulse wave signal for heart rate determination and distinction of systolic and diastolic signal phases

contact material for circuit fabrication is only exemplary, as LIG does not reach the same transport properties in terms of conductivity of contact materials such as metallic conductors.

The first targeted application is the development of flexible, three-electrode electrochemical cells for electrochemical sensing applications. In this case, LIG patterning of carbon-based working and counter electrodes (LIG-WE and LIG-CE) was performed, followed by their transfer and subsequent patterning of an Ag/AgCl reference electrode (RE) and silver contacts using laser cut masks (**Figure 6.4b**). Electrochemical properties of LIG-based WE and CE within planar cells were studied, using a standard redox probe composed of ferri/ferrocyanide ions, with cyclic voltammograms showing the characteristic anodic and cathodic peaks related to the electron transfer in this quasi-reversible process (**Figure 6.4c**). Low peak potential separations were achieved, below 200 mV for all the tested scan rates, showing the very good electron transfer capabilities of the electrode surface. Applying the Nicholson method [49,50] for the determination of the HET rate constant k_0 (Figure D6), an estimated value of 1.03×10^{-2} $cm.s^{-1}$ (23.9% RSD, n=5) was reached, which improves on previous reports from paper-based LIG electrochemical sensors [34,51] and is in the same order of magnitude for LIG synthesized on polymeric substrates [52]. Another important aspect analyzed using the Randles-Sevcik equation was the electrochemical surface area (Figure D6), that reached a value of 13.7 mm^2 (16.9% RSD), an increase compared to the 8 mm^2 geometric area of the WE. This indicates that even with the difference in surface chemistry of transferred LIG patterns previously studied, the surface morphology and chemistry allow for an efficient filling of the porous structure by aqueous electrolytes and diffusion of redox species, for effective electron transfer. To complement this characterization, EIS was used to characterize these planar, flexible cells. Nyquist and bode plots are presented (Figure D6), showing low solution resistances around 100 Ω and charge transfer resistances (RCT) of 70 Ω, also presenting low impedances, with a maximum of 1.5 kΩ for 0.1 Hz. Furthermore, the electrochemical cells were exposed to different bending regimens (Figure D7), showing that they can operate in different bending environments for application in wearable situations.

Taking advantage of the attractive properties of these cells, platinum nanoparticles (PtNPs) were electrodeposited, to serve as strong catalysts towards hydrogen peroxide (H_2O_2) decomposition, as one of the most common transduction mechanisms in various enzymatic and nonenzymatic sensing schemes used for electrochemical sensing of different metabolites in mobile, wearable sensing modalities [53]. SEM images of electrodeposited nanoparticles can be seen in **Figure 6.4d** and Figure D8, showing particles with sizes in the hundreds of nanometers, with a uniform and dense distribution over the WE surface. To note is the higher abundance of particles at more interior LIG fibers, most likely at more conductive and less amorphous LIG areas, as shown previously in the characterization of transferred LIG. Comparative CVs and EIS of electrochemical cells using the selected redox probes, before and after electrodeposition were performed (Figure D9), showing an increase in current and decrease in R_{CT}, associated with the increase in surface area given by PtNPs and their high conductivity. Proof-of-concept H_2O_2 electrochemical sensors were characterized using CV and chronoamperometry, to determine the response of PtNPs modified WE towards the decomposition of H_2O_2. In Figure D10, CVs show the appearance of both anodic and cathodic currents associated with

H_2O_2 oxidation and reduction, respectively. To calibrate this H_2O_2 sensor, anodic currents associated with oxidation of H_2O_2 at positive applied potentials were used, since these are the most commonly applied potentials when this transduction mechanism is employed for enzymatic sensing of metabolites [54]. In Figure D11, different applied potentials were used to study the progressive current increase associated with the addition of increasing concentrations of H_2O_2. A 0.7 V bias was selected and the sensor response at this applied potential is presented in **Figure 6.4e**. This sensor presents a large response range, showing the expected rise of current after the addition of H_2O_2, followed by a decrease until a steady state current level, associated with analyte consumption at electrode surface. This response was calibrated by taking the current 25 seconds after the peak associated with H_2O_2 spiking, presented in **Figure 6.4f**. The sensor presents a large linear variation range between 50 μM and 13.2 mM, with a sensitivity of 16 $\mu A.mM^{-1}.cm^{-2}$ and a LOD of 11.6 μM (3σ/S), appropriate for application in the development of more complex, enzyme-based biosensing schemes for sweat metabolite detection [54]. A comparison of several LIG-based H_2O_2 electrochemical sensors is presented in Table D2.

The second proof-of concept application for flexible, transferred LIG is its application for strain sensor fabrication towards biophysical monitoring. LIG-based strain sensors have shown to present very attractive performances in various substrates [17,55], due to the piezoresistive properties of the patterned material. Serpentine-shaped strain sensors [35] were patterned on wax-modified paper and transferred to the medical grade polyurethane tape, being submitted to bending cycles at 10% strain, for 1 hour, at 1 Hz frequency, as shown in **Figure 6.4g**. The sensor showed great stability over 3600 cycles, maintaining the same stretching and releasing signal shape, as shown by the inset. At this strain, a high gauge factor of 128.9 was achieved, potentiated both by the improved conductivity of LIG and the high flexibility of the transfer substrate, when compared to the native paper substrate. A comparison on the performance of several LIG-based strain sensors in the literature is presented in Table D3. Another interesting aspect when testing these strain gauges at higher strain regimens was the appearance of cyclic triboelectric phenomenon, arising from the polyurethane tape charging. This is visible from the spikes in $\Delta R/R_0$ in **Figure 6.4g** and in Figure D12, were strain cycling with 20% strain was performed. This is an evidence of the ability of LIG to be used as charge collecting layer in architectures for the development of triboelectric nanogenerators. [56,57] As a proof-of-concept application of a low-force sensitivity signal for non-invasive, wearable monitoring, strain gauges were applied in the radial artery, for pressure wave and heartbeat frequency monitorization, as shown in **Figure 6.4h**. A very good sensitivity and signal-to-noise ratio was achieved, allowing for a clear monitoring of the pulse waveform, as shown in **Figure 6.4i**, able to distinguish the systolic and diastolic phases of the pulse wave signal.

6.4 Conclusions

As demonstrated in this work, the full potential of paper as a LIG precursor material is still unexplored and many versatile, simple modification strategies can increase the graphitization potential of this material for laser irradiation processes towards LIG synthesis. The introduction of aromatic moieties by colored wax printing over the aliphatic-rich cellulose substrate results in a highly efficient precursor composite material, enabled by the adaptability of paper substrates towards varied modification strategies, including wax printing. This modification, paired with the meticulous control of operational laser variables, resulted in improved conductive LIG structures, with very low sheet resistances around 5 $\Omega.sq^{-1}$, translating to apparent conductivities as high as 28.2 $S.cm^{-1}$. Furthermore, very attractive crystallinity and low defect density were achieved, prospected by Raman profiles of LIG, that showed I_D/I_G ratios as low as 0.28 and I_{2D}/I_G ratios as high as 0.69. Furthermore, paper-based LIG is still unexplored in the fabrication of fully flexible, conformable components for wearable applications. As such, the developed water peel-off transfer methodology allows for paper to be used as an applicable LIG precursor in the fabrication of on-skin, conformable systems for wearable technologies. This transfer methodology achieves an efficient and complete transfer of LIG patterns, that retain their optimized, enhanced conductive and chemical properties. The multifunctionality of paper-based LIG and its transferred form was demonstrated towards the development of components for wearable systems, through the fabrication of flexible, on-skin electrochemical planar cells and strain sensors, that were tested in different scenarios. With these results, paper can be considered in the toolbox of wearable electronics materials, as a more effective LIG precursor.

References

1. Ye, R., James, D. K. & Tour, J. M. Laser-Induced Graphene. *Acc. Chem. Res.* **51**, 1609–1620 (2018).
2. Whitener, K. E. & Sheehan, P. E. Graphene synthesis. *Diam. Relat. Mater.* **46**, 25–34 (2014).
3. Krajewska, A. *et al.* Fabrication and applications of multi-layer graphene stack on transparent polymer. *Appl. Phys. Lett.* **110**, 041901 (2017).
4. Qiao, Y. *et al.* Multilayer Graphene Epidermal Electronic Skin. *ACS Nano* **12**, 8839–8846 (2018).
5. Ma, W., Zhu, J., Wang, Z., Song, W. & Cao, G. Recent advances in preparation and application of laser-induced graphene in energy storage devices. *Mater. Today Energy* **18**, 100569 (2020).
6. Renuka, H., Enaganti, P. K., Kundu, S. & Goel, S. Laser-induced graphene electrode based flexible heterojunction photovoltaic cells. *Microelectron. Eng.* **251**, 111673 (2022).
7. Sun, B. *et al.* Gas-Permeable, Multifunctional On-Skin Electronics Based on Laser-Induced Porous Graphene and Sugar-Templated Elastomer Sponges. *Adv. Mater.* **30**, 1804327 (2018).
8. Xu, Y. *et al.* Laser-induced graphene for bioelectronics and soft actuators. **14**, 3033–3050 (2021).
9. Liu, J. *et al.* Laser-induced graphene (LIG)-driven medical sensors for health monitoring and diseases diagnosis. *Microchim. Acta* **189**, 1–14 (2022).
10. Lin, J. *et al.* Laser-induced porous graphene films from commercial polymers. *Nat. Commun.* **5**, 5714 (2014).
11. Chyan, Y. *et al.* Laser-Induced Graphene by Multiple Lasing: Toward Electronics on Cloth, Paper, and Food. *ACS Nano* **12**, 2176–2183 (2018).
12. Ye, R. *et al.* Laser-Induced Graphene Formation on Wood. *Adv. Mater.* **29**, 1702211 (2017).
13. Le, T. D. *et al.* Green Flexible Graphene–Inorganic-Hybrid Micro-Supercapacitors Made of Fallen Leaves Enabled by Ultrafast Laser Pulses. *Adv. Funct. Mater.* 2107768 (2021) doi:10.1002/adfm.202107768.
14. Carvalho, A. F., Fernandes, A. J. S., Martins, R., Fortunato, E. & Costa, F. M. Laser-Induced Graphene Piezoresistive Sensors Synthesized Directly on Cork Insoles for Gait Analysis. *Adv. Mater. Technol.* **5**, 2000630 (2020).
15. Mahmood, F. *et al.* Transforming lignin into porous graphene via direct laser writing for solid-state supercapacitors. *RSC Adv.* **9**, 22713–22720 (2019).
16. de Araujo, W. R. *et al.* Single-Step Reagentless Laser Scribing Fabrication of Electrochemical Paper-Based Analytical Devices. *Angew. Chemie - Int. Ed.* **56**, 15113–15117 (2017).
17. Kulyk, B. *et al.* Laser-Induced Graphene from Paper for Mechanical Sensing. *ACS Appl. Mater. Interfaces* **13**, 10210–10221 (2021).
18. Wang, M., Yang, Y. & Gao, W. Laser-engraved graphene for flexible and wearable electronics. *Trends Chem.* **3**, 969–981 (2021).
19. Wang, L. *et al.* High modulus and high strength ultra-thin polyimide films with hot-stretch induced molecular orientation. *Mater. Chem. Phys.* **139**, 968–974 (2013).
20. Coffin, D. W. *et al.* *Mechanics of Paper Products*. *Mechanics of Paper Products* (2011). doi:10.1515/9783110254631.
21. Prabhakaran, A. & Nayak, P. Surface Engineering of Laser-Scribed Graphene Sensor Enables Non-Enzymatic Glucose Detection in Human Body Fluids. *ACS Appl. Nano Mater.* **3**, 391–398 (2020).
22. Dallinger, A., Keller, K., Fitzek, H. & Greco, F. Stretchable and Skin-Conformable Conductors Based on Polyurethane/Laser-Induced Graphene. *ACS Appl. Mater. Interfaces* **12**, 19855–19865 (2020).
23. Lamberti, A., Clerici, F., Fontana, M. & Scaltrito, L. A Highly Stretchable Supercapacitor Using Laser-Induced Graphene Electrodes onto Elastomeric Substrate. *Adv. Energy Mater.* **6**, 1600050 (2016).
24. Griesche, C., Hoecherl, K. & Baeumner, A. J. Substrate-Independent Laser-Induced Graphene Electrodes for Microfluidic Electroanalytical Systems. *ACS Appl. Nano Mater.* **4**, 3114–3121 (2021).
25. Wang, W. *et al.* Fingerprint-Inspired Strain Sensor with Balanced Sensitivity and Strain Range Using Laser-Induced Graphene. *ACS Appl. Mater. Interfaces* **14**, 1315–1325 (2022).

26. Liu, H. *et al.* Flexible and Degradable Multimodal Sensor Fabricated by Transferring Laser-Induced Porous Carbon on Starch Film. *ACS Sustain. Chem. Eng.* **8**, 527–533 (2020).
27. Luong, D. X. *et al.* Laser-Induced Graphene Composites as Multifunctional Surfaces. *ACS Nano* (2019) doi:10.1021/acsnano.8b09626.
28. Zhang, C. *et al.* Human motion-driven self-powered stretchable sensing platform based on laser-induced graphene foams. *Appl. Phys. Rev.* **9**, 011413 (2022).
29. Sinha, K., Meng, L., Xu, Q. & Wang, X. Laser induction of graphene onto lignin-upgraded flexible polymer matrix. *Mater. Lett.* **286**, 129268 (2021).
30. Nine, M. J., Tran, D. N. H., Tung, T. T., Kabiri, S. & Losic, D. Graphene-Borate as an Efficient Fire Retardant for Cellulosic Materials with Multiple and Synergetic Modes of Action. *ACS Appl. Mater. Interfaces* **9**, 10160–10168 (2017).
31. Dogan, M., Dogan, S. D., Savas, L. A., Ozcelik, G. & Tayfun, U. Flame retardant effect of boron compounds in polymeric materials. *Composites Part B: Engineering* vol. 222 109088 (2021).
32. Kaur, S., Mager, D., Korvink, J. G. & Islam, M. Unraveling the dependency on multiple passes in laser-induced graphene electrodes for supercapacitor and H2O2 sensing. *Mater. Sci. Energy Technol.* **4**, 407–412 (2021).
33. Park, H., Kim, M., Kim, B. G. & Kim, Y. H. Electronic Functionality Encoded Laser-Induced Graphene for Paper Electronics. *ACS Appl. Nano Mater.* **3**, 6899–6904 (2020).
34. Pinheiro, T. *et al.* Laser-Induced Graphene on Paper toward Efficient Fabrication of Flexible, Planar Electrodes for Electrochemical Sensing. *Adv. Mater. Interfaces* **8**, 2101502 (2021).
35. Ji, Z. & Zhang, M. Highly sensitive and stretchable piezoelectric strain sensor enabled wearable devices for real-time monitoring of respiratory and heartbeat simultaneously. *Nami Jishu yu Jingmi Gongcheng/Nanotechnology Precis. Eng.* **5**, 013002 (2022).
36. *Safety Data Sheet Solid Ink-Black, Cyan, Yellow, Magenta*. (2007).
37. Kumar, A., Dixit, U., Singh, K., Gupta, S. P. & Beg, M. S. J. Structure and Properties of Dyes and Pigments. *Dye. Pigment. - Nov. Appl. Waste Treat.* (2021) doi:10.5772/INTECHOPEN.97104.
38. Wu, D., Ni, B., Liu, Y., Chen, S. & Zhang, H. Preparation and characterization of side-chain liquid crystal polymer/paraffin composites as form-stable phase change materials. *J. Mater. Chem. A* **3**, 9645–9657 (2015).
39. Yuen, C. W. M., Ku, S. K. A., Choi, P. S. R., Kan, C. W. & Tsang, S. Y. Determining Functional Groups of Commercially Available Ink-Jet Printing Reactive Dyes Using Infrared Spectroscopy. *Res. J. Text. Appar.* **9**, 26–38 (2005).
40. Müller, S. & Müllen, K. Facile synthetic approach to novel core-extended perylene carboximide dyes. *Chem. Commun.* 4045–4046 (2005) doi:10.1039/B509220E.
41. Le, T. D., Park, S., An, J., Lee, P. S. & Kim, Y. Ultrafast Laser Pulses Enable One-Step Graphene Patterning on Woods and Leaves for Green Electronics. *Adv. Funct. Mater.* **29**, 1902771 (2019).
42. Mendes, L. F., de Siervo, A., Reis de Araujo, W. & Longo Cesar Paixão, T. R. Reagentless fabrication of a porous graphene-like electrochemical device from phenolic paper using laser-scribing. *Carbon N. Y.* **159**, 110–118 (2020).
43. Wohlert, M. *et al. Cellulose and the role of hydrogen bonds: not in charge of everything*. *Cellulose* vol. 29 1–23 (Springer Science and Business Media B.V., 2022).
44. Rozpłoch, F., Patyk, J. & Stankowski, J. Graphenes bonding forces in graphite. *Acta Phys. Pol. A* **112**, 557–562 (2007).
45. Dreimol, C. H. *et al.* Sustainable wood electronics by iron-catalyzed laser-induced graphitization for large-scale applications. *Nat. Commun. 2022 131* **13**, 1–12 (2022).
46. Edberg, J. *et al.* Laser-induced graphitization of a forest-based ink for use in flexible and printed electronics. *npj Flex. Electron.* **4**, 17 (2020).
47. Reynolds, J. A. & Hough, J. M. Formulae for Dielectric Constant of Mixtures. *Proc. Phys. Soc. Sect. B* **70**, 769 (1957).
48. Koursari, N., Arjmandi-Tash, O., Trybala, A. & Starov, V. M. Drying of Foam under Microgravity

Conditions. *Microgravity Sci. Technol.* **31**, 589–601 (2019).

49. Nicholson, R. S. Theory and Application of Cyclic Voltammetry for Measurement of Electrode Reaction Kinetics. *Anal. Chem.* **37**, 1351–1355 (1965).
50. Lavagnini, I., Antiochia, R. & Magno, F. An extended method for the practical evaluation of the standard rate constant from cyclic voltammetric data. *Electroanalysis* **16**, 505–506 (2004).
51. Kulyk, B. *et al.* Laser-induced graphene from paper for non-enzymatic uric acid electrochemical sensing in urine. *Carbon N. Y.* (2022) doi:10.1016/J.CARBON.2022.06.013.
52. Muzyka, K. & Xu, G. Laser-induced Graphene in Facts, Numbers, and Notes in View of Electroanalytical Applications: A Review. *Electroanalysis* **34**, 574–589 (2022).
53. Yu, H. *et al.* Recent Progress of the Practical Applications of the Platinum Nanoparticle-Based Electrochemistry Biosensors. *Front. Chem.* **9**, 282 (2021).
54. Cargill, A. A., Neil, K. M., Hondred, J. A., McLamore, E. S. & Claussen, J. C. Effect of platinum nanoparticle deposition parameters on hydrogen peroxide transduction for applications in wearable electrochemical glucose biosensors. in *Smart Biomedical and Physiological Sensor Technology XIII* vol. 9863 98630E (SPIE, 2016).
55. Carvalho, A. F. *et al.* Laser-Induced Graphene Strain Sensors Produced by Ultraviolet Irradiation of Polyimide. *Adv. Funct. Mater.* **28**, 1805271 (2018).
56. Zhao, P. *et al.* Replacing the metal electrodes in triboelectric nanogenerators: High-performance laser-induced graphene electrodes. *Nano Energy* **75**, 104958 (2020).
57. Kim, D. W., Lee, J. H., Kim, J. K. & Jeong, U. Material aspects of triboelectric energy generation and sensors. *NPG Asia Mater. 2020 121* **12**, 1–17 (2020).
58. Wu, H. *et al.* Materials, Devices, and Systems of On-Skin Electrodes for Electrophysiological Monitoring and Human–Machine Interfaces. *Adv. Sci.* **8**, 2001938 (2021).

7

PAPER-BASED, LASER-INDUCED GRAPHENE BIOELECTRODES FOR SKIN-INTERFACED BIOELECTRONICS APPLICATIONS

The development of mechanically compliant, functional materials toward skin-integrated electronic systems has been a rapidly evolving field, aiming at flexible and even stretchable architectures, that can be mounted into curved skin surfaces and adapt to its changing topography and biomechanics. One of the components required for functional bioelectronic systems is bioelectrodes that can robustly interact with the skin, to perform sensing or stimulation tasks. In this chapter, paper-based laser-induced graphene is studied as a compatible material for skin-integrated systems, by assessing its surface characteristics, its biocompatibility and material-skin interface properties. Scoping the distribution of LIG surface chemical properties by Raman signal mapping was performed, to understand the distribution of this conductive material and its implications when in contact with the skin. Assays with human fibroblast cell culture were performed, to demonstrate the good biocompatibility of the material when in contact with biological tissue. Electrical properties of the material when in contact with the skin were also surveyed, by impedance studies of LIG-based bioelectrodes with different areas. Based on these results, paper-based, transferred LIG/PU bioelectrode architectures were used to develop two proof-of-concept applications for skin-integrated bioelectronic sensing systems. The first application is the deployment of paper-based LIG as dry electrode for electrophysiological signal acquisition, namely electrocardiogram and electromyogram. The same bioelectrodes were also used to develop electrode arrays, in the form of a chest scale patch for the acquisition of 6 precordial lead ECG and high-density surface EMG acquisition for motion recognition. The second application for paper-based LIG bioelectrodes is an iontophoresis stimulation system, for the delivery of cholinergic agents and sweat secretion activation. The delivery of carbachol as a model cholinergic agent was studied, demonstrating the capability of stimulating up to 60 µL of sweat with a 10-minute stimulation period, over a period of 1 hour. The iontophoresis system was also integrated with a flexible LIG-based enzymatic glucose sensor, aiming at non-invasive sweat glucose quantification.

7.1 Introduction

Bioelectronics has emerged as a robust technology, anchored on ongoing research on materials that combine several key features, such as mechanical flexibility with robust compliance, stretchability, biocompatibility, adhesion to tissue surfaces and breathability [1,2]. Depending on the target biological tissue to be interfaced, careful consideration on material design is needed, to diminish the mechanical mismatch and possible inflammatory response, either for implantable systems that interact with internal organ tissues or for epidermal applications, where the device is in contact with exterior skin surface [1]. To achieve this, several material classes have been studied, to develop soft conductors that can simultaneously participate in charge conduction and robustly adhere and adapt to biological tissue surfaces [3]. These include metal conductors, in the form of thin films, fillers or liquid metals [4–6], conducting polymers [7], hydrogels [8] and carbon nanomaterials [9]. Beyond materials, considerate shapes and form-factors also aid in achieving conformability, including substrates with nature-inspired adhesive surfaces [10] or conductive serpentine or kirigami conductive material architectures [3]. Material innovations paired with their integration in functional systems have allowed bioelectronics to meet several requirements for biomedical device development, for diverse purposes including diagnostics and therapeutics, along with other uses such as human machine interfacing [11].

For diagnostics, wearable bioelectronic devices have enabled the collection of useful physiological information, that can be integrated within diagnostic criterion for several complications. An example is the collection of physical and electrophysiological signals, such as heart rate and the electrocardiogram (ECG), that can be used in the diagnosis and management of cardiovascular diseases [12]. With the deployment of soft, user-friendly devices based on advanced materials, real-time, long-term patient monitoring outside of clinical settings may be improved for chronic scenarios [13]. For biochemical-based diagnostics, the staple consumer wearable bioelectronics product has been continuous glucose monitors (CGMs), used in the management of diabetes mellitus. These are based on minimally invasive, hypodermic needle-based systems, that measure glucose levels in circulating interstitial fluid. Using electrochemical transduction, needles are modified to serve as bioelectrodes for signal generation, based on enzymatic reactions [14]. Recently, alternative devices have been researched, to decrease the invasiveness of CGMs. These include microneedle-based devices, that keep similar principles to current CGMs [15], or patch-like electronic skin (e-skin) devices, that can access sweat as a biological fluid matrix, where glucose can be sampled and measured through electrochemical transduction [16]. Most notably, enzymatic glucose sensors have demonstrated their capability for detection of glucose in different physiologically relevant orders of magnitude, from the millimolar levels characteristic of blood (2-40 mM) and interstitial fluid (2 - 22 mM) to the micromolar level characteristic of sweat (10 μM - 1.11 mM), by careful selection of biosensing schemes and highly sensitive mediators, showing an increasing acceptance for wearable biochemical sensor development [17]. Furthermore, such types of devices have been increasingly investigated for the measurement of different analytes in sweat for several diagnostic and prognostic purposes, such as for cystic fibrosis [18], kidney function [19], gout, [20] inflammation [21] or human stress response [22], strengthening the knowledge and interest in the potential uses of sweat as a valuable diagnostic source. For therapeutics, several applications can be fulfilled with soft, wearable e-skin devices and implantable bioelectronics, from stimulation and actuation to drug delivery [23]. Bioelectrodes capable of performing such tasks can be integrated with diagnostic elements within closed loop systems, that can detect abnormalities and actuate accordingly to the measured data. One example is for ECG detection of signal abnormalities related to cardiovascular disease, that can be connected to implantable heart pacing devices for electrotherapy [12,24]. For biochemical analysis, closed loop systems in diabetes mellitus have also been developed, where CGMs determine glucose levels and communicate with insulin pumps, where control algorithms determine the need for insulin administration [25]. Thus, future material and technological developments of soft, skin-interfaced bioelectronic systems may allow for alternative form factors and biodetection methodologies, to reach higher technology readiness levels and market implementation in several biomedical diagnostics and therapeutic settings.

Regarding the fabrication of skin-interfaced bioelectronics, DLW has increasingly been selected as a route to synthesize and pattern low-thickness, conductive, flexible geometries from several material precursors, aiming at different functions, from electrophysiology applications to on-skin biochemical detection [26]. Using conductive polymer hydrogels based on PEDOT:PSS as source materials for patterning, Won et al. [27] developed a method to write highly conductive bioelectrodes with excellent aqueous stability, for neural signal recording and stimulation. Another example is the patterning of molybdenum dioxide (MoO_2) from a metal salt precursor over a SEBS substrate, to developed bioelectrodes for different applications, including on-body temperature sensing, ECG signal acquisition, UV sensors and biochemical sweat sensors for glucose, uric acid and caffeine detection. For the glucose sensor a sensitivity of 15.7 $nA.\mu M^{-1}$ was achieved. Another example is the use of laser carbonization to pattern conductive carbon materials as bioelectrodes. In the work by Sharifuzzaman et al. [28], a MXene/fluoropolymer substrate was used as a precursor to write bioelectrodes for sweat glucose sensing and ECG acquisition. The enzymatic sweat sensor presented a sensitivity of 77.2

μA.mM^{-1}.cm^{-2}, a linear range between 10 μM and 2 mM and a limit of detection of 10 μM. For the ECG electrodes, a signal-to-noise ratio of 37.63 dB was achieved. Based on laser-induced graphene (LIG), several examples of highly efficient sweat glucose biosensors have been reported, based on different precursors, including PI [29–35], PES [36] and lignin [37]. Regarding the biodetection mechanisms, most sensors rely on ultrasensitive elements, that can very efficiently oxidize or reduce hydrogen peroxide (H_2O_2) and generate amperometric signals in the presence of low glucose concentrations, mostly relying on platinum nanoparticles (PtNPs) for this purpose [29,32,35]. Alternative mechanisms include highly sensitive mediators, such as Prussian Blue [37] and nonenzymatic methods, using transition metal nanostructures, such as copper or nickel [33]. Most of these reports have been employed in *in-vivo* scenarios [29–32] or tested with collected sweat samples [34,35,37], demonstrating their capability for integration in bioelectronic systems for sweat metabolite sensing. In this regard, enzymatic sensing is still preferred to nonenzymatic methods, since for the latter, efficient promotion of an alkaline environment for the sensing reaction is needed, requiring additional elements in the system that can promote an increased pH [38]. While most of these sweat glucose biosensors have been tested *in vivo* by sweat induction through physical exercise, the fabrication of LIG-based iontophoresis systems for sweat induction has been recently demonstrated. This allows for a single step fabrication of all the required bioelectrodes for sweat induction and sensing in a single PI chip substrate, for controlled sweat induction and prolonged sweat sensing towards high-frequency sampling and continuous analysis [21,39]. However, no other LIG precursors have been translated towards iontophoresis system development.

For electrophysiology applications, LIG bioelectrodes have also been shown to be alternatives to conventional metal-based electrodes. Using PI substrates, LIG bioelectrodes for ECG acquisition have been reported [40–42], serving as dry bioelectrodes where the conductive material is directly interfaced with the skin, without the need for conductive gels. For these electrodes, the area and architecture influence their performance, allowing for good signal-to-noise-ratios (SNR) of 31.07 dB, showing comparable signal acquisition capabilities when compared to commercial electrodes [42]. Besides ECG, other biosignals have been acquired with LIG electrodes, including surface electromiography (sMEG), electroencephalography (EEG) and electrocorticography (ECoG) [43–46], based on the low-impedance capabilities of LIG. However, since PI does not possess adhesive capabilities for an efficient electrode placement over the target tissue, alternative strategies have been used to develop highly flexible bioelectrode systems for electrophysiology applications. These mostly rely on transfer strategies, that separate the LIG from its PI precursor. In the work by Zhang et al. [44], PI-derived LIG in transferred into a

SEBS flexible membrane, for multi-purpose biosignal electrodes with good SNR of 35.78 dB. Dallinger et al. [47] demonstrated the transfer of PI derived LIG onto polyurethane (PU) for EMG signal acquisition, while Sun et al. [48] demonstrated LIG transfer to breathable elastomer/sugar composite substrates for ECG and sEMG recording. Based on the versatility of DLW patterning and different transfer strategies, more complex applications based on bioelectrode arrays have been developed for several electrophysiology applications. An example is the transfer of PI-derived LIG onto PDMS, to construct chest scale patches for the measurement of ECG precordial leads, demonstrated by Yang et al. [49]. Another example is the cryogenic transfer of PI-derived LIG onto highly stretchable hydrogels, demonstrated by Lu et al. [50], used to develop bioelectrode patches for implantable heart biopotential detection.

From this set of materials and device assembly strategies, DLW and LIG are becoming robust resources for the development of skin-interfaced bioelectrode assemblies for several purposes. However, in the pool of precursor materials, petroleum-based polymers, mainly PI, have been the main research focus, while naturally available, more abundant materials lack behind in technological research and development implementation stages. In this chapter, the paper-derived LIG developed and studied in previous chapters is used for the fabrication of skin-interfaced bioelectrodes, towards flexible, wearable biosensing. Based on laser processing approaches, complex bioelectrode geometries and their assembly with seamless integration strategies are demonstrated, to develop robust e-skin patches for electrophysiological signal detection and biochemical sweat analysis, towards biomedical diagnostic devices. Firstly, paper-derived and transferred LIG surface properties are characterized, along with its biocompatibility and electrical characteristics when in contact with skin tissue. After scoping these properties, LIG-based bioelectrodes for ECG and sEMG signal acquisition were developed and characterized, in terms of their ability to acquire electrical activity signals, through SNR analysis. Based on these electrodes, two different electrode array assemblies were developed. The first one was designed as a chest-scale patch, to acquire 6 chest leads and perform the 12-lead ECG protocol. The second bioelectrode array was designed as a high-density sEMG array, tested in the posterior forearm for hand motion recognition. For on-skin biochemical analysis, paper-based LIG electrodes were tested as anode and cathode within a iontophoresis system for the stimulation of sweat, using the delivery of the slowly-metabolized cholinergic agent carbachol [51]. The principles for sweat secretion stimulation using these electrodes were established, regarding the stimulation current, resulting carbachol delivery, sweat rate and secreted volume. As a proof-of-concept, sweat glucose detection was attempted, by development and integration of a high-sensitivity enzymatic glucose sensor, constructed over flexible LIG-based electrochemical cells. A first *in vivo* test of the integrated device was performed with one subject, by measuring the current response of the sensor when exposed to stimulated sweat at a fasted state and after a meal.

7.2 Experimental section

Reagents and Materials

During this work, ultrapure Milli-Q water laboratory grade (conductivity < 0.1 µS.cm^{-1}) was used to prepare all solutions. Sodium tetraborate decahydrate ($Na_2B_4O_7$ $10H_2O$), potassium chloride (KCl), chroroplatinic acid hexahydrate (H_2PtCl_6 $6H_2O$), sulfuric acid (H_2SO_4), agarose, n-(3-Dimethylaminopropyl)-N'ethylcarbodiimide hydrochloride (EDC), n-hydroxi-succinimide (NHS), glucose oxidase (GOx, 158526 units/g), phosphate buffer powder and D-glucose were purchased from Sigma. Carbamylcholine chloride (carbachol) was purchased from Thermo Fisher Scientific. Sodium chloride was purchased from ITW Reagents. All reagents were used as received, without further purification. 75 µm thickness Kapton ® film (DuPont) and Whatman chromatography paper grade 1 (Whatman International Ltd., Floram Park, NJ, USA) were used for laser irradiation and LIG formation. Leukoplast Fixomull transparent medical grade polyurethane tape was used as LIG transfer substrate. This substrate is composed of three layers, with a bottom plastic liner layer, a middle polyurethane layer with a polyacrylate glue adhesive (54 µm) and a protective glassine paper layer. 3M 468MP double-sided adhesive transfer tape was used for device assembly. This tape is composed of an acrylic adhesive (130 µm) with a glassine kraft paper protective lining. For silver track patterning and reference electrode patterning, silver conductive ink (AG-510 silver ink, surface resistivity: <0015 Ω/square/mil, Conductive Compounds, Inc., Hudson, NH) and silver/silver chloride (Ag/AgCl) ink (AGCL-675, Conductive Compounds, Inc., Hudson, NH) were used. Spectra 360 electrode gel (Parker Laboratories) was used for experiments with gelled electrodes. Ag/AgCl gelled electrode (Kendall ™, Cardinal Health) were used as comparison in impedance studies.

LIG synthesis and characterization

LIG synthesis was performed on two substrates, namely PI and paper. A CO_2 laser system (VLS 3.50, Universal Laser Systems) with a 10.6 µm wavelength, beam diameter at focus of 0.127 mm, maximum power of 50 W and maximum engraving speed of 1270 mm.s^{-1} was used. For PI, optimized LIG synthesis conditions were employed on a 75 µm film, using a laser power of 4.2 W, an engraving raster speed of 101.6 mm.s^{-1} and a negative beam defocus of 0.79 mm.

For LIG synthesis on paper, substrates were pre-treated with sodium tetraborate and 4 wax layers, as presented in **Chapter 6**. After treatment, two LIG engraving cycles were performed. The first was performed with a laser power of 6 W and an engraving speed of 152.4 mm.s^{-1}. For the second engraving cycle, the same engraving speed was used, but with a laser power of 5 W. A negative beam defocus of 0.79 mm was used in both engraving cycles. After paper-derived LIG synthesis, water-induced peel-off transfer was performed, as presented in **Chapter 6**, by interfacing the adhesive polyurethane medical grade tape with water and gently sticking the paper substrate to the humid surface. After applying slight pressure, peeling-off of the paper substrate is performed, resulting in LIG pattern transfer. Raman characterization was performed in three material study groups, namely PI-derived LIG (PI-LIG), paper-derived LIG (P-LIG) and transferred paper-derived LIG (LIG@PU), using a Renishaw inVia Reflex micro-Raman spectrometer equipped with an air-cooled CCD detector and a HeNe laser. The laser beam was focused through a 50x Olympus objective lens. Measurements were performed with a 532 nm laser, to perform Raman signal mapping over sample surfaces. Electrical characterization of samples was performed using a 4-point probe Biorad HL 5500 equipment at room temperature. SEM characterization was performed using a Hitachi Regulus SU8220 system.

LIG biocompatibility assays

Biocompatibility assays were performed for PI-LIG and transferred LIG@PU samples, with a 15 mm diameter circular shape. Human fibroblasts cells were seeded onto LIG samples placed in cell culture plate wells and an empty well, under a minimum essential medium (MEM) for 7 days. After 7 days, a Live/Dead Cell Double Staining Kit (Sigma-Aldrich) was used to assess cell viability. Staining solution was prepared by mixing 10 µL of calcein-AM solution with 5 µL propidium iodide solution, followed by the addition of 2.5 mL of PBS solution. From this mixture, 200 µL was added to each well and images were captured using a Carl Zeiss Axiovert 40 inverted microscope. Cell metabolic activity was also assessed after 7 days, through Presto Blue assay. For this, 20 µL of Presto Blue Cell Viability Reagent (Invitrogen, ThermoFischer Scientific) was added to each well, followed by fluorescence readings using a SpectraMax i3x (Molecular Devices) microplate reader, for analysis. After this, the cells were fixed with 4% paraformaldehyde for 15 min, washed 3 times with PBS and stained with DAPI and phalloidin, for fluorescence cell nucleus and actin filament visualization, using a Zeiss LSM 700 confocal microscope.

Fabrication and assembly of bioelectrodes

LIG bioelectrodes were fabricated using the same three material study groups where material characterization was performed. For PI-LIG and P-LIG bioelectrode fabrication, circular electrodes with different diameters (2, 5 and 10 mm) were engraved, followed by laser cutting a circular hole (2 mm) in the substrates for placement of snap buttons. Polyurethane (PU) medical grade substrate was laser cut with circular opening for the electrodes and rectangular opening for manual screen-printing of silver tracks. After silver track patterning and ink curing in a hot plate at 75 ºC for 15 minutes, snap buttons were inserted at their designed location and an additional PU tape layer was used for encapsulation and anchoring of snap buttons. For LIG@PU, electrodes were engraved on a paper substrate and the same hole for snap button placement was laser cut on the substrate, for alignment. The snap button entrance was then cut in the PU substrate, followed by water-induced peel-off transfer onto the substrate. After drying the transfer substrate, the protective glassine paper layer of the PU medical grade tape was laser cut (15 W, 250 mm.s^{-1}) to create a mask for manual screen-printing of silver tracks connecting the LIG electrode to the snap button. After silver track curing, PU transfer tape was laser cut with electrode openings and used to encapsulate the electrode silver tracks and anchor the snap buttons.

Bioelectrode impedance measurements

Electrode-skin impedance analysis of electrodes was performed using a PalmSens 4.0 potentiostat (PalmSens Compact Electrochemical Interfaces) able to perform potentiostatic and galvanostatic electrochemical impedance spectroscopy (EIS). For the first set of experiments, PI-LIG, P-LIG and LIG@PU electrodes were gelled with a small volume of conductive electrode gel over electrode surface. For impedance measurements, three electrodes were placed in the anterior forearm, with 4 cm distance between them, following similar electrode placement protocols [40,52]. After placement, galvanostatic impedance spectroscopy was performed, with an applied DC current bias of 0 A and an AC bias of 1 µA, frequencies between 100 kHz and 0.5 Hz and 40 sampling frequency points. For each acquisition, five consecutive measures were performed with these conditions. For PI-LIG and LIG@PU dry electrodes, the same protocol was followed, without adding conductive gel to the electrode surface.

Fabrication and assembly of electrode arrays

Chest-scale bioelectrode patches for ECG acquisition and bioelectrode arrays for high-density sEMG acquisition were fabricated using LIG@PU. For the chest-scale patch, six electrodes with 5 mm diameter were patterned on the paper substrate. PU transfer substrate was submitted to laser processing, by cutting the top protecting glassine paper layer, to open areas for electrode transfer and mark the patch contour, without affecting the underlying PU layer. To do this, a laser power of 7 W and a cutting speed of 250 mm.s^{-1} were applied, with a focused laser beam. After removing the glassine paper areas for electrode placement, transfer of each individual electrode is performed in their specific location. After transfer, a laser cut glassine paper mask with serpentine silver track outlines is attached again to the PU substrates, followed my manual screen printing of silver ink. After curing the silver serpentine tracks, a laser cut layer made from the same PU tape with electrode openings is used to encapsulate the silver tracks. For the sEMG high-density bioelectrode array, similar fabrication protocols are used, with some differences. Firstly, LIG electrode with 5 mm diameter were patterned onto the paper substrate. Secondly, the PU transfer substrate was laser cut to establish via holes for connections with underlying device layers, followed by water-induced peel-off transfer. This underlying layer was composed of the PU transfer substrate, which was submitted to laser processing to cut a mask for serpentine silver tracks in glassine paper protective lining, without damaging the underlying PU adhesive. Silver was patterned in the via holes and in serpentine tracks, followed by thermal curing. After curing, the electrode layer was attached to the serpentine silver track layer, by aligning the via holes. After this, an additional PU layer was laser cut with electrode openings and attached over the electrode layer, for device encapsulation.

Biosignal acquisition and processing

ECG and EMG signal acquisition with individual LIG bioelectrodes was performed using a BITalino (r)evolution Board Kit (PLUX Biosignals) and its embedded ECG and EMG sensors. The ECG sensor has a gain of 1019, a bandwidth between 0.5-100 Hz and a 16-bit resolution, while the EMG sensor has a gain of 1009, bandwidth between 25-480 Hz and a 10-bit resolution. For both ECG and EMG signals acquisition, 1 kHz sampling frequency was used. For each ECG acquisition, three LIG electrodes were used. The positive electrode was placed under the left clavicle, the negative electrode was placed under the right clavicle and the ground electrode was placed in the lower right abdomen region, working as the right-leg electrode. For EMG signal acquisition, three LIG electrodes were used. The positive electrode was placed on the bicep muscle, closer to the elbow, while the negative electrode was placed closer to the shoulder, with a 4 cm gap between electrodes, centered around the muscle peak. The ground electrode was placed in the elbow. For each acquisition, four bicep contractions were performed, by flexion with a 5 kg weight.

For the chest-scale patch, 12-lead ECG acquisition was performed using a ADS1298ECG-FE evaluation board, with a 500 Hz sampling frequency. For the limb leads, singular LIG@PU electrodes were used, while the chest leads were measured through the chest-scale patch. All measurements were made at rest. For the sEMG high-density electrode array, a BITalino (r)evolution Plugged Kit was used, connecting 5 EMG sensors to the board. For the first channel, a ground electrode was included, serving as reference for all the remaining channels. The bioelectrode array was tested in the proximal part of the posterior forearm, placed above the muscles that control finger extension. Signal processing was performed using Python programming language and the signal processing toolbox NeuroKit2 [53]. For ECG, the raw signal was converted to the measurement units (mV), followed by identification of signal waves. For SNR analysis, extraction of signal noise through a Weiner filter [54] was performed, followed by SNR calculation for each cardiac cycle:

$$SNR = 20log_{10}\left(\frac{V_{pp}^{signal}}{V_{pp}^{noise}}\right),\ V_{pp}\text{ - peak-to-peak amplitude} \tag{7.1}$$

For EMG processing, raw signals were also converted to the standard unit, followed by signal offset correction. From the corrected signal, rectification was performed, followed by determination of root-mean-square (RMS) EMG signal envelope. From the RMS EMG envelope, muscle contraction periods were identified, followed by SNR calculation for each contraction, using the rest state period preceding contractions as the noise segment:

$$SNR = 20log_{10}\left(\frac{RMS\ (signal)}{RMS\ (noise)}\right) \tag{7.2}$$

Fabrication, assembly and testing of iontophoresis device

Fabrication of iontophoresis stimulation modules was made using similar methods to the electrophysiological bioelectrode arrays. Two design conformations were developed, the first one to perform stimulated sweat secretion rate and volume analysis and the second one for integration with electrochemical sensing modules. Two electrodes with 0.6 cm^2 area were patterned in a paper substrate, to serve as anode and cathode. Subsequently, the electrodes were transferred to the PU substrate, followed by patterning of silver serpentine tracks, using glassine paper masks processed by laser cutting. For the first device configuration, the transfer substrate was also laser cut with an opening, to access and collect iontophoresis-stimulated sweat for analysis. After transfer, the silver tracks were encapsulated with another layer of PU adhesive tape with electrode openings. For the second device configuration, three additional layers were attached above the electrode layer. The first encapsulation layer was a PET substrate, with laser cut electrode openings. This layer was additionally treated with UV ozone lamp for 1 hour, to improve its hydrophilicity. The second layer was made from a double-sided flexible adhesive, laser cut with electrode openings and a microfluidic network. The final layer was made from the same PET substrate and double-sided adhesive, laser cut with electrode openings and a sweat accumulation layer, serving to encapsulate the microfluidic layer and attach the device to the skin surface.

After device assembly, agarose hydrogels containing the cholinergic agent were produced. Agarose was dispersed in deionized water to make 3 % w/v concentration, followed by heating the mixture in a microwave for 1 minute, until agarose is dissolved. The mixture was placed on a hotplate, to keep the solution heated. For the anode hydrogel, carbachol was added to a concentration of 0.5 % (w/v). For the cathode hydrogel, NaCl was added to the same concentration. Finally, the mixture was cast onto a glass mold (8x8 cm) and left for gelation at 4 °C. Hydrogel pads were then laser cut to the shape of the electrodes and placed in the device. Prior to device mounting on the skin, ethanol was used to clean the skin surface of any contaminants. To perform iontophoresis carbachol delivery, varying currents (100 - 450 μA) were applied between the anode and cathode, using a PalmSens4 potentiostat, using chronopotentiometry, for a period of 10 minutes. For sweat rate and volume estimation, a gravimetric method was employed [51], in which an absorbing chromatography paper pad was used to collect the stimulated sweat, and weighted to determine sweat rate, using the following equation:

$$Rate\ (\mu L.min^{-1}) = \frac{\Delta w\ (g) * 10^3\ \mu L.g^{-1}}{t(min)}\ ,\ \Delta w\text{ - weight difference of sweat collection pad} \quad (7.3)$$

Fabrication of sweat glucose sensor and device integration

For the fabrication of wearable sweat glucose biosensors, the same approach presented in **Chapter 6** for flexible electrochemical sensor fabrication was performed. Using LIG electrochemical cells on PU substrate, the working electrode was modified to reach high sensitivity to glucose. Firstly, PtNPs were electrodeposited, through cyclic voltammetry techniques, by scanning a potential window between -0.2 and 0.7 V at 50 mV.s^{-1} for 15 cycles, using a 2.5 mM platinum salt solution in 60 mM H_2SO_4. After electrodeposition, electrode surface was activated with the EDC/NHS method, for covalent attachment of enzymes. 20 μL of 10 mM EDC and 20 mM NHS mixture was drop-casted onto the electrode surface and incubated at room temperature for 4 hours. After this, the electrode was dried and 10 μL of a 10 mg.mL^{-1} GOx solution in PBS was drop-casted onto the electrode, followed by drying at 4 °C overnight. Finally, 0.5 % (w/v) agarose hydrogel was prepared as previously presented, and 10 μL was drop-casted over the electrode surface, followed by drying at 4 °C overnight. Testing of this enzymatic sensor was performed using the same protocol presented in **Chapter 5**. The sensor was placed in a beaker with 100 mL electrolyte solution (deionized water, KCL, PBS buffer and artificial sweat), with a magnetic stirrer at 150 rpm. Chronoamperometry was performed for continuous current analysis, using a 0.5 V applied potential, to track current changes by pipetting specific volumes of a stock glucose solution (100 mM) dissolved in the same electrolyte.

Glucose sensor integration with the iontophoresis module was made by placing and aligning a functionalized sensor between the iontophoresis electrode layer and the PET encapsulation layer, when assembling the iontophoresis module. Using this modular approach, different sensors targeting glucose or other analytes can be individually processed and easily integrated in the device. For this case, the PET layer contains a laser cut opening so that flowing sweat can interact with the electrochemical sensor. For device testing, a stimulation cycle was performed, followed by a chronoamperometry measure (0.5 V) of sensor current, to take the signal associated with the fasted state. After a high-calory meal, the same stimulation protocol was performed, to retrieve fresh sweat, followed by chronoamperometry current measurement.

7.3 Results and Discussion

7.3.1 Surface characterization of LIG and biocompatibility assessment

The first stage when surveying the capabilities of paper-based LIG (P-LIG) and its transferred form (LIG@PU) for flexible, conformable bioelectrode development was to study different key properties, needed for efficient implementation within skin-interfaced devices. Firstly, the distribution of the material over a laser processed surface was studied, through Raman spectroscopy mapping. This has the purpose of understanding the distribution of chemical properties over material surface, to scope LIG phases getting in contact with the skin. Along with this characterization, the contact angle of each material was also assessed, to determine aqueous contact properties. Results are presented in **Figure 7.1a-c**, for each study group, along with two representative Raman spectra for each group. As seen for PI-LIG (**Figure 7.1a**), used as a control material, Raman spectroscopy mapping of I_D/I_G and I_{2D}/I_G peak ratios shows a variation of chemical structures. In red, most of the analyzed surface shows a predominance of lower I_D/I_G values, as low as 0.135. However, some areas show a significant increase in the I_D/I_G ratio, with values up to 0.688. These variations are usually associated with surface topography of this porous material, where lower ratios are characteristic of more elevated zones, while

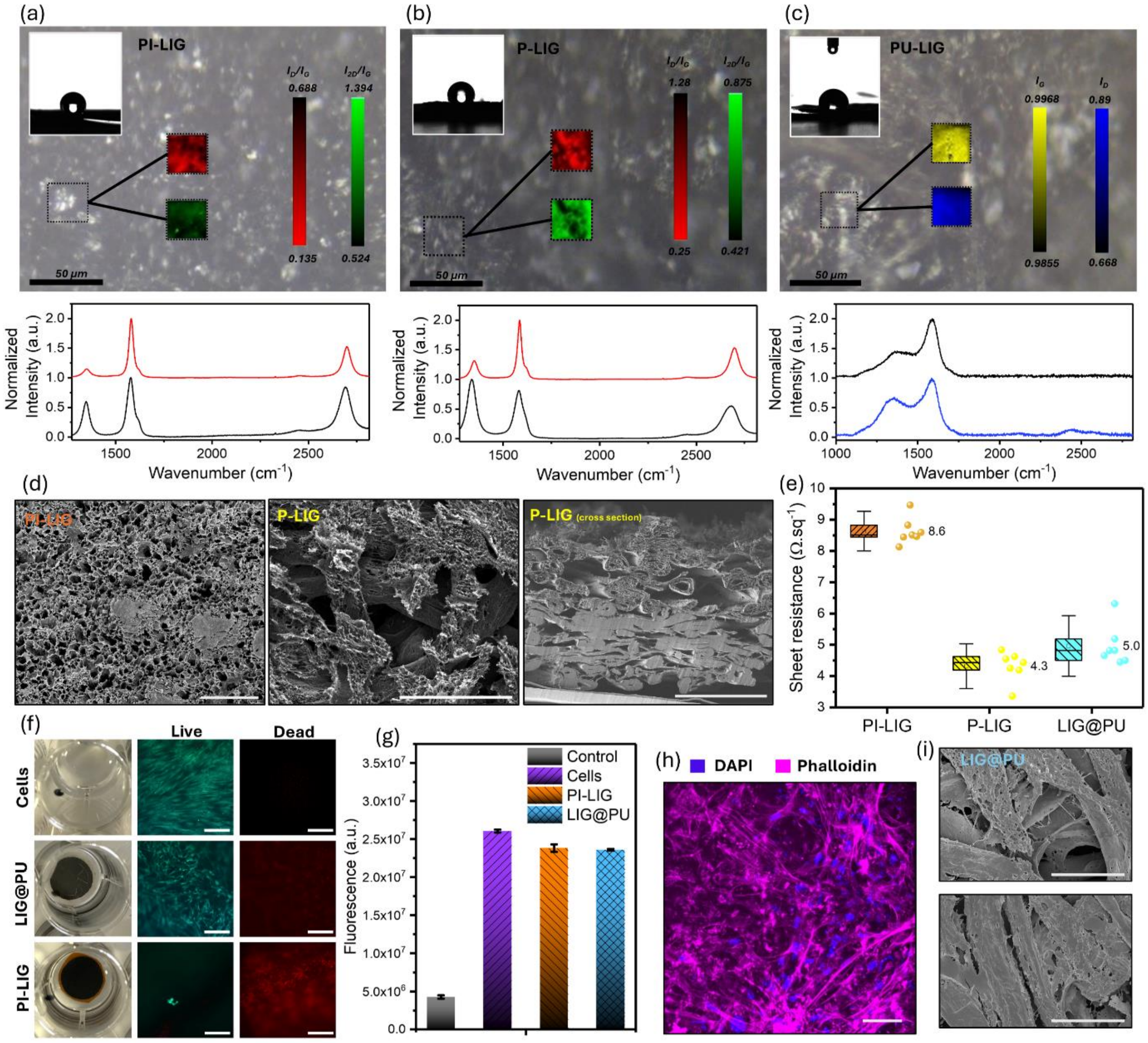

Figure 7.1 - PI-LIG, P-LIG and LIG@PU surface, electrical characterization and biocompatibility assessment. Surface Raman mapping and contact angle analysis of (a) PI-LIG, (b) P-LIG and (c) LIG@PU. (d) SEM imaging of PI-LIG and P-LIG. Scale bar 100 µm. (e) Sheet resistance analysis of LIG materials. (f) Live/dead assays of human fibroblasts cultured over PI-LIG and LIG@PU. Scale bar 100 µm. (g) Presto Blue assays for cell viability testing. (h) Fluorescence imaging of marked cell nuclei and actin structures. Scale bar 50 µm. (i) SEM imaging of LIG@PU before (top) and after (bottom) cell culture. Scale bar 50 µm.

deeper regions tend to present higher defect density. In green, the I_{2D}/I_G ratio shows similar heterogeneity, reaching values as high as 1.394. Interestingly, the areas where higher I_{2D}/I_G ratio values are present do not match with lower I_D/I_G ratio values, further indicating the heterogeneity in the chemical structure and turbostratic and layered nature of graphene lattices. This can be further seen in the two representative Raman spectra taken from a higher (black) and lower (red) defect density area, showing differences in peak intensity, width and position. For

P-LIG (**Figure 7.1b**), similar trends are observed for both peak ratios, with slight variations. Firstly, the degree of variation for the I_D/I_G ratio is accentuated, most likely related to the native porous and fibrous structure of the precursor paper substrate, in comparison with the homogenous surface of PI. Thus, higher elevation and depth differences lead to a more marked difference of graphitized zones. While low ratio values being more common in the sampled surface area, the presence of more defective zones when compared to PI is visible, with ratio values as high as 1.28. This can be seen by the Raman spectra representative of this higher defective area, where more intense D peaks compared to G peak are common. For the I_{2D}/I_G ratio, less variation is visible, with values reaching as high as 0.875. Still, when comparing the representative Raman spectra, a broadening and position shift of the 2D peak is clearly visible, indicating different degrees of graphitization efficiency within the same sample. Taking the lowest I_D/I_G, crystallite size in the *a* axis (*La*) was computed for PI-LIG and P-LIG, showing very appealing values of 142.4 and 76.9 nm, which are outstanding when compared to the literature [55]. For transferred LIG@PU, the inversion of the material portrayed in P-LIG occurs, exposing a more amorphous carbonized material where G and D peak show a broader width and the 2D peak is absent. Thus, mapping of I_D and I_G was performed, to study the homogeneity of chemical structures (**Figure 7.1c**). When comparing both peak intensities, it is visible that for almost the entirety of the sampled area, the I_G is almost unchanged, while I_D show considerable variation, portrayed in the representative Raman spectra, indicating varying degrees of sp^2 carbon hybridization clustering [56]. Comparing all three groups, it is visible that LIG@PU appears as more homogeneous regarding its chemical structures, which may benefit the interfacing with the skin. However, the reduced graphitic nature of the material could decrease its capability of conducting electrical stimuli from and to the skin. Furthermore, it presents a more hydrophilic nature (89.6 º), when compared to the hydrophobic nature of PI-LIG (131.9 º) and P-LIG (123.9 º), as shown in inset images for the contact angle analysis, which may also influence its skin interfacing dynamics [57].

To accompany surface Raman mapping, SEM analysis of LIG surfaces was performed, to compare their morphology (**Figure 7.1d**). For PI-LIG, a very porous structure with uniformly distributed pores is visible, while for P-LIG, laser-induced porosity is mostly visible over more elevated cellulose fibers. This increased porosity promoted by the laser irradiation process also leads to an increased surface area for the material, which can promote a higher contact area when interfaced with the skin, leading to more efficient electrical stimuli transmission [58]. Additional cross-section analysis of P-LIG was performed, to determine the thickness of graphitized portion and subsequent LIG@PU layer after transfer. As can be seen, the top portion of the paper substrate is graphitized, showing an increase in fiber porosity within the laser graphitized depth, without damaging the fibrous cellulose structures. Furthermore, incorporated wax is decomposed after the irradiation, since inter-fiber spaces are emptied. Varying thicknesses of P-LIG are obtained, depending on cellulose fiber organization, around ~ 80 µm. For LIG@PU (**Figure 7.1i, top**), SEM imaging shows less porous fiber structures, arising from the inversion of material surface after transfer. Regarding the electrical conductivity of LIG materials, sheet resistance (R_{sh}) measurements show single-digit values for all the study groups. PI-LIG presented a median value of 8.6 $\Omega.sq^{-1}$, while P-LIG showed a lower resistivity, at 4.3 $\Omega.sq^{-1}$. After transfer, LIG@PU shows a median sheet resistance of 5.0 Ω.sq-1, showing that there is a negligible effect of the inversion of exposed materials surface towards the overall surface resistivity.

Biocompatibility assays of PI-LIG and LIG@PU were performed, to assess the biocompatibility of the materials when in contact with live human tissue. P-LIG was not tested for biocompatibility, since the material detaches from the paper substrate when in contact with water, not allowing for cell seeding. Human fibroblasts were seeded onto the tested substrates and allowed to proliferate for 7 days. After this period, a live/dead assay was performed (**Figure 7.1f**), to determine the viability of cells. As can be seen, a control of cells seeded in an empty culture plate well show a uniform and ordered distribution of living fibroblasts for the calcein fluorescence image, along with small fluorescence intensity in the propidium iodide channel, related to dead cells. For LIG@PU, high density of cells is also visible over the material surface, indicating a good cell viability and interaction of cells with this carbon material, with dead cells presenting a much smaller fluorescence. In terms of fibroblast organization, a more irregular distribution is visible, attributed to the irregular topography of the LIG surface, without detriment to cell proliferation. When compared to PI-LIG, it is visible that a very small portion of cells adhered to the material surface and proliferated, with the live channel showing only a small cluster of living cells. For the dead channel, much higher fluorescence is visible, confirming a decreased cell viability. To confirm these results, Presto Blue assay was also performed after 7 days, to determine cell viability and activity (**Figure 7.1g**). As a general control, the fluorescence was taken from a well without cells, to determine the reduction of resazurin to resorufin arising from the culture medium. For the cell control, a significant increase in the fluorescence was observed, as expected from the live/dead assay. Interestingly, a similar 6-fold increase in fluorescence is observed both for PI-LIG and LIG@PU, indicating that cells culture in these two substrates present good viability and metabolic function. While for LIG@PU, these results are in accordance with live/dead assays, the contrary is observed for PI-LIG. This can be hypothetically explained by the greater hydrophobicity of PI-LIG, shown in **Figure 7.1a**, that hinders the capability of cells to efficiently adhere to the substrate and proliferate over its surface. However, seeded cells may migrate to other areas, such as the surrounding PI substrate or the unoccupied well area, adhering and proliferating in these zones. Such cells remain viable and metabolically active, giving rise to the fluorescence signal observed from the Presto Blue assay. While this indicates that pristine PI-LIG is not a good substrate for cell culture, this shows that it does not release relevant toxic graphene nanostructures to the culture medium, that could lead to low cell viability. In contrast, LIG@PU shows good fibroblast cell proliferation potential, indicating its good biocompatibility. To further study the behavior of fibroblast interacting with LIG@PU surface, fluorescence imaging was taken of fixed cells marked with DAPI and phalloidin (**Figure 7.1h**) along with SEM images (**Figure 7.1i**). For fluorescence images, cell nuclei are clearly distinguished, while actin filaments indicate a good interaction of cells with the substrate and between them. For SEM images of the substrate before and after cell culture, visible cell-induced structures are present over cellulose fiber structures, complementing confocal microscope images.

Material surface characterization and biocompatibility assays show that transferred LIG@PU possesses promising characteristics for skin interfacing, when compared to its PI-LIG and P-LIG counterparts. Its good chemical surface homogeneity, comparable electrical conductivity and good biocompatibility shows its potential for long-term contact with skin tissue. Thus, further study of this material within bioelectrode architectures was explored, namely its skin contact impedance, along with PI-LIG serving a control material.

7.3.2 LIG bioelectrode-skin impedance analysis

Electrical interface properties of LIG materials with the skin were studied for two different electrode configurations. The first was by gelling LIG bioelectrodes, for comparison with commercial wet Ag/AgCl electrodes. The second consisted of directly interfacing LIG surfaces with the skin, to study the materials as dry bioelectrodes. In **Figure 7.2a**, a schematic representation of LIG@PU bioelectrodes is presented, along with the skin placement protocol for EIS measurements, conformability after skin placement and the equivalent skin-electrode circuit considered in the experiments. Bioelectrodes were constructed with circular geometry, with diameters of 2, 5 and 10 mm. For robust connection with measurement equipment, LIG was connected through silver ink tracks to snap buttons, retrieved from used commercial Ag/AgCl electrodes. Regarding the electrode placement and impedance measurement protocol, different methods have been used in the literature, including four, three and two electrodes placed in the skin [59]. For these experiments, three electrodes were employed in the anterior forearm,

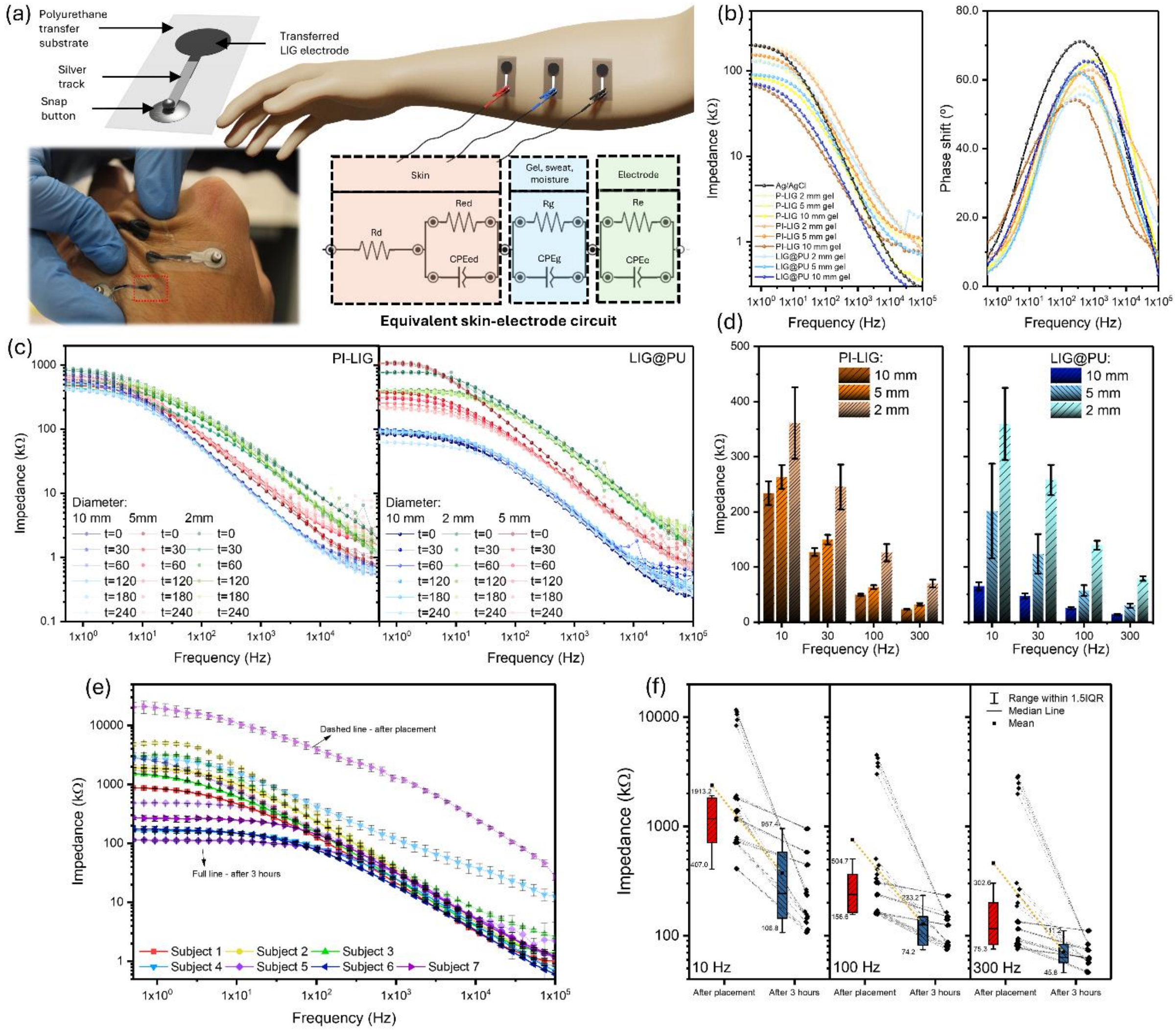

Figure 7.2 - LIG bioelectrode-skin impedance characterization. (a) Schematic representation of electrode construction, placement in the skin and equivalent circuit model. (b) Bode plot of absolute impedance and phase shift of gelled LIG and commercial Ag/AgCl electrodes. (c) Impedance bode plot of PI-LIG and LIG@PU electrode over a 4 hour period and electrode diameter of 2, 5 and 10 mm. (d) Bar plot comparison of absolute impedance for 10, 30, 100 and 300 Hz AC signal frequencies. (e) Impedance analysis of LIG@PU electrodes with 5 mm diameter for different subjects (n=7), after electrode placement and after 3 hours. (f) Impedance analysis of electrode response at different frequencies.

where a reference electrode was placed between the positive and negative electrodes, as performed previously in the literature for skin impedance EIS protocols [52,60]. When employing an AC stimulus through the skin with varying frequencies, the electrode material, electrode-skin interface and skin layers will respond differently to its propagation, depending on their intrinsic properties. For the electrode, usually an equivalent circuit model consisting of a parallel RC circuit is used, where R_e represents the charge transfer resistance between the electrode and electrolyte layer (e.g. gel, moisture) and the capacitive element (CPE_e) represents the double layer formed upon charge transfer between the interface, which is frequency dependent. Depending on the use of a wet or dry configuration, a second RC layer represents a similar interface, between the electrolyte and the first skin layer (R_g and CPE_g). Because of the dielectric properties of the stratum corneum, a following RC layer can be used to model the behavior of the epidermis (R_{ed} and CPE_{ed}), followed by a resistive element (R_d) representing the underlying, more conductive tissues that propagate the electrical stimuli [61]. Because of the heterogeneous characteristics of the LIG electrode surfaces and of the skin, composed of varying cell organizations and other components, the capacitive interface properties are not modeled as ideal capacitors, usually replaced by pseudocapacitive elements, such as the constant phase element (CPE) [59,61], as portrayed in the equivalent circuit in **Figure 7.2a**. Although several more complex circuit models that describe the hierarchical electrical skin properties have been presented [62], a simpler circuit model was used to interpret the acquired impedance spectra of LIG bioelectrodes.

The first experiment was performed on the three study groups (PI-LIG, P-LIG and LIG@PU) with a gelled configuration, by retrieving the impedance and phase shift Bode plots for each group and electrode diameter, along with Ag/AgCl electrodes (1 healthy subject, male, 30 years old) (**Figure 7.2b**). Results show that LIG gelled electrodes show a very similar behavior to commercial electrodes, presenting the expected increase in impedance for lower frequencies, related to the capacitive properties of the electrode-skin interfaces. Regarding the electrode area, a trend of decreasing impedance for higher electrode areas is visible, which is expected, since a higher electrode-skin contact area is established, with impedance being inversely related to electrode surface area. Overall, gelled LIG electrodes present low impedance values, especially at lower frequencies, characteristic of electrophysiological signal features (ECG - 0.5 to 150 Hz or muscle fiber activity - 0 to 500 Hz). Furthermore, impedance curve slopes and phase shift profiles show slight variations, that indicate varying cut-off frequencies of the electrodes, around ~10 Hz. Since skin impedance is highly influenced by several factors, including skin hydration, abrasion, electrode location, contact pressure and gel contact area, such variations are expected.

Studies of dry electrode configuration were performed, using PI-LIG and LIG@PU electrodes. No further studies were conducted with P-LIG electrodes, since the material easily broke and detached from the paper substrate during measurements, making the electrodes unreliable for long-term, direct skin interfacing. Bode plots and comparative impedance bar plots for PI-LIG and LIG@PU electrode sets are presented in **Figure 7.2c-d**, for long-term analysis of electrodes mounted to the skin over a 4-hour period. For dry PI-LIG bioelectrodes, it is visible that increasing electrode area leads to a decrease of absolute impedance values for higher frequencies. Regarding electrode stability, impedance variation over time is relatively stable. For LIG@PU, greater variation is verified, regarding both electrode size and stability over time. As expected, electrodes with 2 mm diameter show the largest absolute impedance, especially for higher frequencies. For a 10 mm diameter electrode, significantly lower impedances are reached, when compared to PI-LIG. For 10 Hz frequency, PI-LIG shows an impedance of 234.1 ± 21.4 kΩ, when compared to an impedance of 64.9 ± 7.5 kΩ for LIG@PU. For higher frequencies, this difference is less significant. In the case of 100 Hz, PI-LIG shows an impedance of 49.5 ± 1.8 kΩ, while LIG@PU shows an impedance of 25.1 ± 2.3 kΩ. This may be related to the much higher conformability of the PU substrate, when compared with PI, that improves the contact area and pressure of the conductive material with the skin, increasing the electrode-skin contact points. In terms of the stability over time, LIG@PU electrode show a trend of progressive decrease of impedance. This may be associated with its more hydrophilic properties, permitting moisture and sweat to interact with the electrode, working as electrolyte within the porous interface. Finally, analysis of area-normalized impedance shows that even though larger electrodes present more attractive absolute impedance regimens, smaller electrodes show lower area-normalized impedance. For LIG@PU, 10 mm diameter electrodes show an area-normalized impedance of 51.9 kΩ.cm^2, 5 mm diameter electrodes an impedance of 39.6 kΩ.cm^2 and 2 mm diameter electrode a value of 11.3 kΩ.cm^2, for a 10 Hz frequency. This may indicate an improved conformability and more robust skin-electrode contact, also showing good prospects for electrode miniaturization. From the collected impedance profiles, fitting tests were performed, using the fitting tool from the PSTrace potentiostat control software (Figure E1). Although the circuit presented in **Figure 7.2a** showing a good fitting with the collected curves, a great variability in the values for the resistive elements does not provide quantitative information for comparison between commercial Ag/AgCl electrodes, gelled and dry LIG electrodes.

Finally, a study of LIG@PU dry bioelectrode skin impedance with larger subject sample size was performed (**Figure 7.2e-f**). Seven healthy subjects (4 female and 3 male) were submitted to the same electrode placement and impedance measurement protocol, using 5 mm diameter electrodes and with impedance being measured after electrode placement and after 3 hours. Bode plots show a significant variability of impedance responses between the subjects, which is more common for dry electrode assays. Since no skin preparation protocol was implemented for the subjects prior to electrode placement, different skin conditions for each subject were expected. After placement, median impedance values of 1174.8 kΩ, 238.4 kΩ and 155.3 kΩ for 10 Hz, 100 Hz and 300 Hz were observed, respectively. From all the subjects, only one statistical outlier was identified. After 3 hours, in which subjects resumed their normal daily tasks, a consistent trend of electrode-skin impedance decrease is confirmed. Decrease to 243.7 kΩ, 125.0 kΩ and 63.2 kΩ were observed for the same frequencies. Interestingly, the outlier (subject 7) identified after electrode placement is not an outlier after 3 hours, indicating that a problem with the electrode placement may be the reason for the elevated impedance values.

According to these results, LIG-based bioelectrodes show themselves as potential candidates for skin interfacing, both for acquisition of electrophysiological signals as well as for electrical stimulation. The impedance regimens of gelled electrodes are comparable to commercial Ag/AgCl electrodes, while dry electrodes present more elevated impedances, mostly within the kΩ range in the relevant frequency domain of ECG and EMG signals, showing good prospects for electrophysiological signal acquisition. For lower frequencies, the higher variability may hinder the efficient acquisition of biosignals characterized by lower frequency domain, such as the EEG. Thus, further studies of dry LIG bioelectrodes for ECG and EMG acquisition were performed.

7.3.3 ECG and EMG acquisition using dry LIG bioelectrodes

Using dry configuration, LIG-based bioelectrodes were benchmarked in terms of their capability to acquire the ECG and EMG biosignals (**Figure 7.3**). For ECG, three standard bipolar leads are usually measured, following the Einthoven triangle, where the heart generated potential is measured though the difference between a positive and negative electrode. Lead I detects the heart potential difference between the left (positive) and right (negative) arm, lead II the difference between the left leg (positive) and right arm (negative) and lead III changes the negative electrode of lead II to the left arm. Using this method, different directional heart potential propagation and signal profiles can be scoped, to retrieve physiological information of heart function.

A first lead I ECG acquisition assay was performed, to compare commercial Ag/AgCl gelled electrodes with PI-LIG and LIG@PU dry bioelectrodes with 10 mm diameter (1 healthy subject, male, 30 years old) (**Figure 7.3a**). Eight second filtered signal segments and extracted noise are presented for the three electrode types. As can be seen, clear distinction of ECG peaks is achieved, with low noise contribution and similar signal amplitudes for all the electrodes. For Ag/AgCl electrodes, a mean V_{pp} of 1.78 ± 0.24 mV was registered, while for LIG bioelectrodes, a mean V_{pp} of 1.38 ± 0.23 mV and 1.30 ± 0.18 mV were registered for LIG-PI and LIG@PU. A slight decrease is observed for dry bioelectrodes, which was expected, due to the absence of gel and smaller electrode area (1.77 cm^2 for Ag/AgCl electrodes and 0.79 cm^2 for dry LIG bioelectrodes). Thus, dry bioelectrodes present a good capability for ECG acquisition, comparable to commercial alternatives.

The second ECG acquisition assay was performed with PI-LIG and LIG@PU dry bioelectrodes with a 10 mm diameter, to determine long term acquisition capability (**Figure 7.3b**).

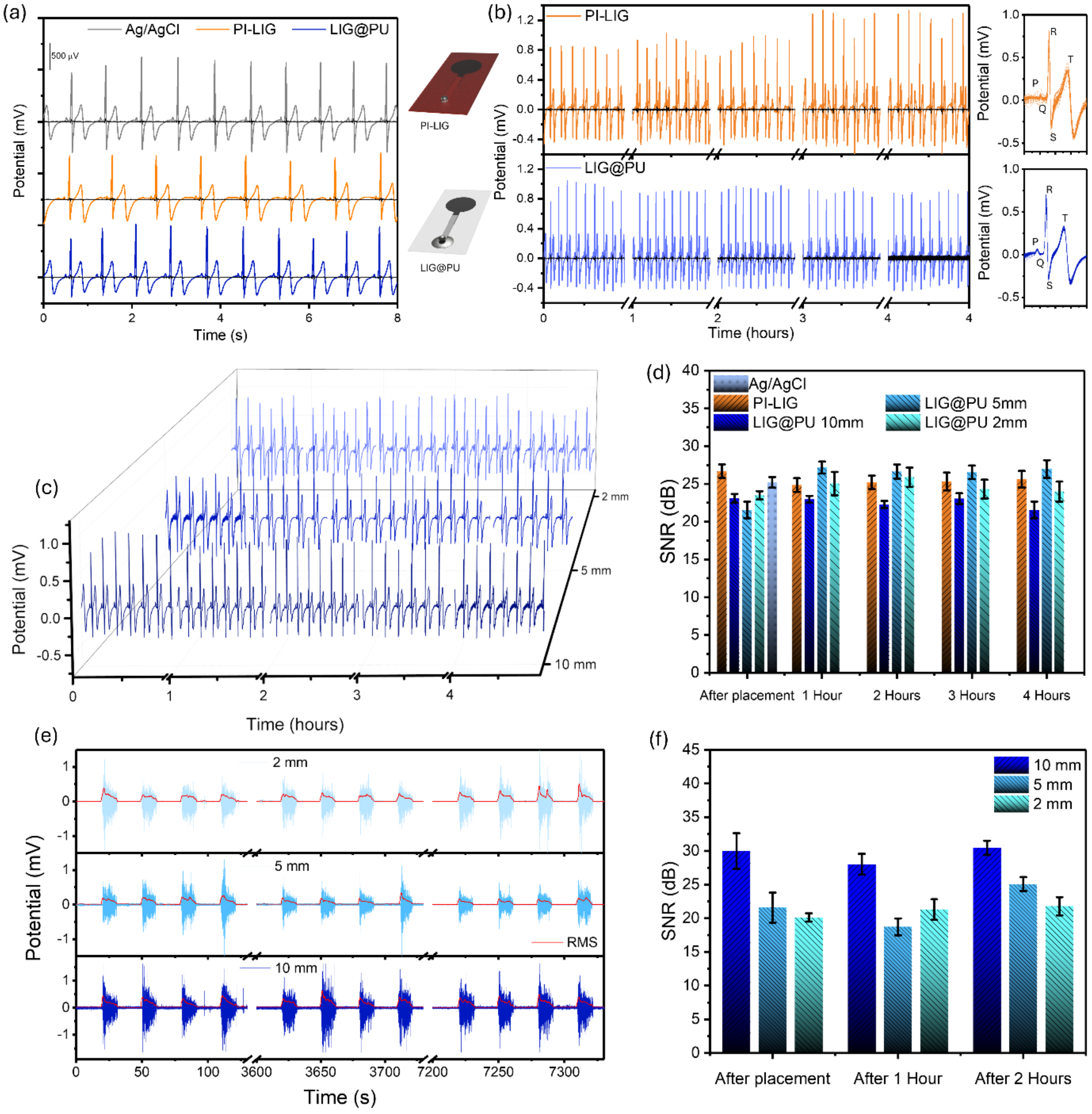

Figure 7.3 - ECG and EMG signal acquisition with LIG bioelectrodes. (a) Signal comparison between Ag/AgCl electrode and LIG bioelectrodes. (b) Long-term ECG acquisition comparison between PI-LIG and LIG@PU bioelectrodes with 10 mm diameter and extracted signal segments. (c) Long-term ECG acquisition comparison of LIG@PU bioelectrode with different diameters (2, 5 and 10 mm). (d) SNR analysis of ECG signals. (e) EMG signal comparison of long-term acquisition of bicep muscle contraction using LIG@PU electrode with different diameters. (f) SNR analysis of EMG signals.

Filtered signal segments are presented for acquisitions every hour, over a 4-hour period, along with extracted noise (60 second acquisitions were performed, but 7 second segments are presented in the graph). Although extracted noise signal showing some variation over the acquisition period, its intensity is not sufficient to mask any signal features. For LIG@PU, very stable signals were acquired, with only the acquisition performed after 4 hours showing a higher contribution of noise. ECG signal segments were extracted and overlayed, for the first acquisition period (t=0). For PI-LIG, a heart rate of 54 BPM was measured, since 54 signal segments were extracted, showing the presence of more signal artifacts. For LIG@PU, 74 BPM was registered, with segments showing a more stable signal with less artifacts. Overall, the absence of an adhesive layer for the PI substrate decreases the conformability of the electrode, leading to a less efficient electrode interfacing with the skin and more motion induced artifacts. For the PU substrate, the surrounding adhesive properties allow for highly conformable adherence to the skin, decreasing the occurrence of electrode sliding over the skin, induced by normal body motions. Following this analysis, long-term ECG acquisition was performed for LIG@PU bioelectrodes with different diameters (**Figure 7.3c**). For all electrode sizes, efficient signal acquisition is achieved, demonstrating the ability of the electrodes for long-term ECG monitoring. For 5 mm diameter electrodes, ECG acquisition was also performed 1 day after electrode placement, retaining its operation without signal degradation (Figure E2). To compare all the tested electrode conditions, SNR analysis was performed (**Figure 7.3d**). To do this, SNR was computed for each ECG signal cycle. It can be observed that all dry LIG bioelectrode acquisitions present an SNR with the same magnitude as the one for gelled Ag/AgCl electrodes (25.2 ± 0.7 dB). For PI-LIG, stable SNR overtime is observed, varying from 26.7 ± 0.9 dB after placement to 25.6 ± 1.1 dB after 4 hours. For LIG@PI, 10 mm diameter electrodes presented the lowest SNR, varying from 23.1 ± 0.6 dB to 21.6 ± 1.1 dB. While these electrodes show the largest surface area, leading to greater signal intensity detection, they can also be more susceptible to surrounding electrostatic noise. For 5 mm and 2 mm electrodes, slightly higher SNR are observed, although for some conditions, greater noise contribution to the signal is observed. For 5 mm electrodes, the signal after placement shows a lower SNR, which stabilizes for the following acquisitions, while 2 mm electrodes also show some SNR variability over time. For the 5 mm electrodes after 24 hours placement, an SNR of 25.1 ± 0.8 dB was computed (Figure E2). Since no electrode shielding protocol was implemented, varying noise contributions were observed. However, this did not hinder efficient ECG acquisition, validating LIG bioelectrodes for dry electrode configurations.

EMG signal acquisition was also performed using LIG@PU bioelectrodes with different diameters (**Figure 7.3e**). Electrical signal of bicep muscle was acquired for four contractions and resting periods, every hour for a period of 2 hours. For all the electrodes, a clear distinction between the muscle activation periods during contraction is visible, with steady electrical activity during contraction and low signal intensity during relaxation periods, associated with the underlying muscle tone and surrounding electromagnetic noise. Overlaying the EMG signals, the computed RMS signal envelope is also presented, showing the amplitude waveform of the signal. For all the electrode diameters, very similar contraction profiles were observed. To further characterize the electrodes, SNR analysis was performed (**Figure 7.3f**). SNR was computed for each individual contraction and the mean SNR value was determined for all acquisition periods. As observed, the 10 mm electrodes present the highest SNR, both due to capture of higher signal amplitudes and lowered noise contribution. In the case of EMG, higher electrode area is more impactful on the capability of acquiring more signal, since a greater number of underlying muscle fibers are being scoped by the surface electrodes, while more muscle electrical activity can be generated if higher loads are applied to the muscle. For ECG, heart muscle fiber contraction is physiologically controlled by the organism and the signal travels through more tissue, leading to a less significance of the electrode size towards signal amplitude. For these electrodes, an SNR of 30.0 ± 2.7 dB was calculated after electrode placement, maintaining a value of 30.4 ± 1.1 dB after two hours. For smaller electrodes, progressively lower SNR is obtained for each acquisition period, being the only exception the 5 mm electrodes, one hour after placement, presenting a lower SNR when compared to the 2 mm electrodes. Besides this condition, the 2 mm electrodes present the lowest SNR, changing from 20.1 ± 0.6 dB to 21.8 ± 1.4 dB after the two-hour testing period. For the 5 mm electrode, greater variability is observed, with SNR values of 21.6 ± 2.2 dB, 18.7 ± 1.3 dB, and 25.1 ± 1.0 dB for each acquisition. Since no standardized control of muscle load was used, differences in muscle contraction associated with muscle condition and fatigue can occur, also associated with a poorer electrode placement and contact with the skin, leading to these differences. Overall, paper-based, transferred LIG electrodes present good electrophysiological signal acquisition capabilities within a dry electrode configuration, showing themselves as more accessible, future alternatives for deployment towards diagnostic and prognostic criteria where electrophysiological signals are of use.

7.3.4 LIG bioelectrode arrays

Based on LIG@PU bioelectrodes, more complex e-skin patches can be developed, to demonstrate the versatile capabilities of laser processing for seamless device fabrication and processing, to access more user-friendly e-skin patches with considerate form factors. Using the same laser tool for not only synthesizing LIG electrodes with different geometries, but also for attentive electrode organization, placement and processing of flexible substrates is demonstrated, for the development of ECG and sEMG electrode patches. The first proof-of-concept electrode array was developed for 6 precordial ECG lead recording (**Figure 7.4a**). A schematic representation of this e-skin electrode patch is demonstrated, consisting of 4 main elements. A PU substrate is laser cut and used as template to establish patch shape and the electrode layer. After electrode transfer, laser cut glassine paper masks are used for silver ink printing for conductive serpentine tracks, used to connect the device with an appropriate connector for interfacing with the signal acquisition instrumentation. The final element is an encapsulating PU adhesive layer, that acts both as an electrical insulator for decreased parasitic capacitance signals acquired over the patch and as the adhesive surface for device attachment to the skin. A representation of device fabrication steps is presented in Figure E3. Such a device is placed in the chest, to measure the chest leads (V1 to V6) in reference to the center of the Einthoven triangle. V1 and V2 electrodes are placed in the fourth intercostal space, to the right and left of the sternum. V3 is placed diagonally to V1 and V2 electrodes. V4, V5 and V6 electrodes are placed on the same level, between the fifth and sixth rib, in the midclavicular, anterior axillary and midaxillary lines, respectively. With this placement, V1-V2 leads are considered the septal leads, retrieving information on the ventricular septum, while V4-V5 leads record the anterior wall and V5-V6 leads observe the lateral wall of the left ventricle. This is usually the ECG protocol performed in a clinical setting, when heart function is under analysis. For the sEMG high density electrode array, similar electrode components are used in the assembly of this e-skin device, with one extra element (**Figure 7.4b**). In this case, the PU transfer layer was laser cut with via holes, serving both to encapsulate the underlying silver serpentine track layer and access it through via holes, for contact with the LIG electrodes and signal propagation towards the acquisition equipment. Since a higher density of electrodes is included in this device (16 electrode with 5 mm diameter), overlay of silver serpentine tracks with LIG electrode could occur during the fabrication process, if they were placed in the same device layer. Thus, efficient vertical device connections and assembly are also demonstrated, using the laser processed materials and substrates used here. A representation of device fabrication steps is presented

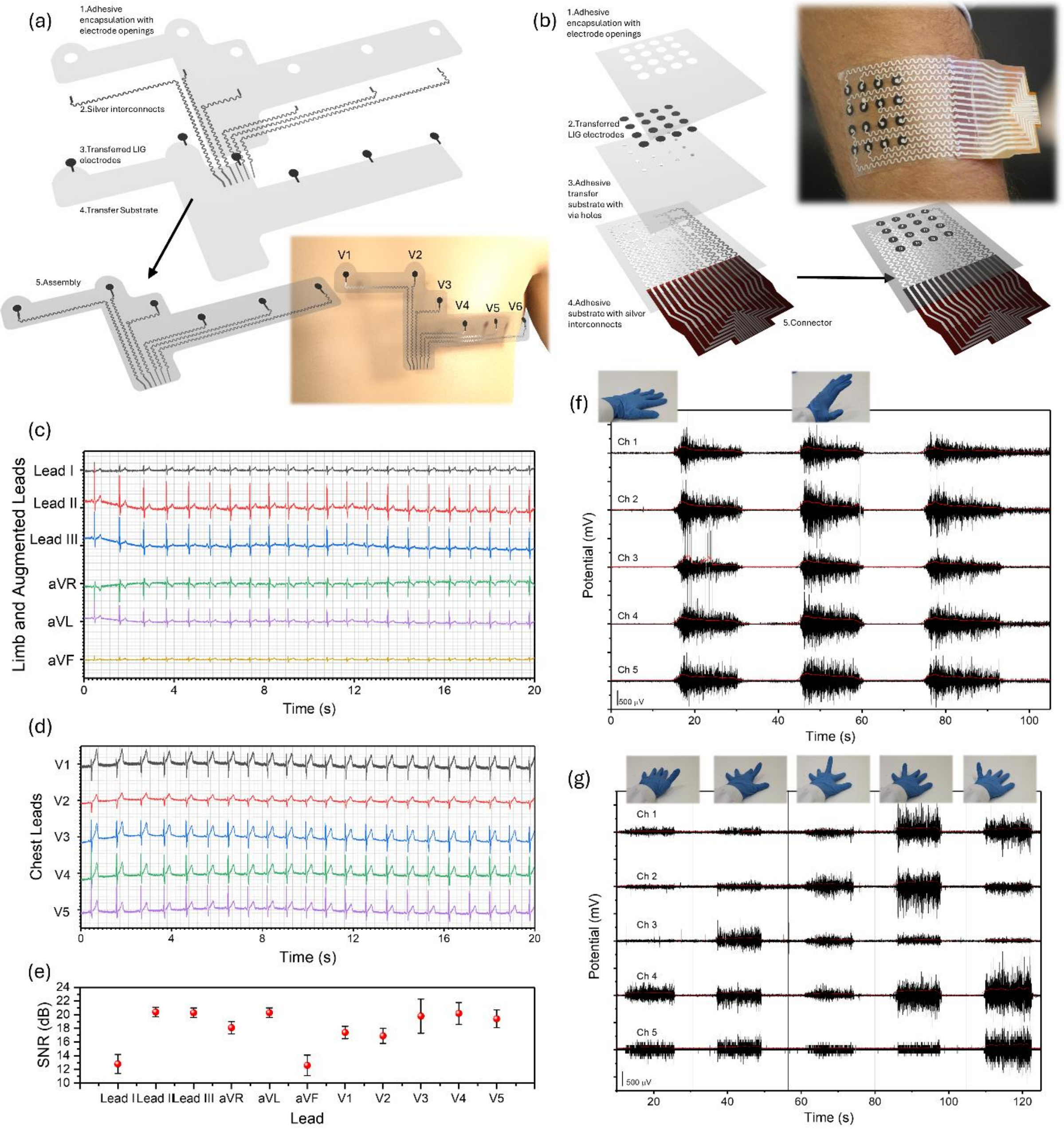

Figure 7.4 - Paper-based laser-induced graphene bioelectrode arrays. Schematic representation of components and placement of (a) chest-scale patch for 6 chest lead acquisition and (b) sEMG electrode array for motion recognition. Signals for (c) limb and augmented limb leads and (d) chest leads of 12 lead ECG protocol performed with LIG electrode and array patch. (e) SNR analysis of ECG leads. sEMG signals of five channels during (f) wrist extension and (g) individual finger extension.

in Figure E4. This electrode patch can be placed in several muscles, to detect muscle contraction in different locations simultaneously.

12-lead ECG acquisition protocol was performed using the developed ECG chest-scale patch. For this protocol, limb leads I, III, III and augmented limb leads aVL, aVR and aVF were detected using individual LIG@PU electrodes (**Figure 7.4d**), while the chest leads (V1-V6) were acquired with the chest patch (**Figure 7.4e**). Variations in heart potential signal components can be clearly distinguished, as expected, since different leads scope the propagation of heart potentials in different vectors in the frontal and horizontal plane of the body. Some features, such as the inversion of the waves for the aVR lead and changes in intensity for the R and S waves for the V1-V5 leads are clearly visible, in accordance with previous reports [49]. From the acquisition, only the V6 lead did not record any signal, for several patches tested during the fabrication optimization period, probably due to a fault in connection to the acquisition device. SNR analysis was performed for each lead signal (**Figure 7.4e**), showing values comparable to previous analysis, only decreasing for lower intensity signal leads, namely lead I and aVF.

Testing of the sEMG electrode array was performed in two phases, the first by acquiring signals related to muscle activation during wrist extension at 90º relative to the forearm (**Figure 7.4f**), followed by signals related to extension of individual fingers (**Figure 7.4g**). To measure these signals, 5 channels were used, each one comprising two electrodes in a bipolar configuration. Channel 1 was recorded between electrodes 1-2, channel 2 was recorded between electrode 5-6, channel 3 between electrode 9-10, channel 4 between electrodes 3-12 and channel 5 between electrodes 4-11. Six electrodes were left unused but could be plugged using other acquisition instrumentation that could support additional channels. For wrist extension, all five channels present consistent activation periods, related to three extension cycles, with consistent amplitudes and synchronized relaxation and contractions periods (**Figure 7.4f**). Although the electrodes in each channel are mounted over different forearm muscles, they are all activated upon the extension, leading to consistent signals in all channels. For each channel, an SNR of 17.7 ± 3.0 dB, 24.0 ± 1.1 dB, 26.1 ± 3.3 dB, 24.3 ± 0.2 dB and 16.4 ± 4.2 dB were computed. Further testing of the electrode arrays was performed to detect signals associated with finger extension movements, aiming at motion recognition and human machine interfacing applications. With the same channel configurations and electrode patch placement in the forearm, positional location of the electrode was tested to acquire signals from several muscles that control finger extension. As can be seen in the sEMG signals acquired for all channels, different signal profiles are visible, in terms of muscle activation and signal intensity, depending on the movement (**Figure 7.4g**). For thumb extension, channels 4 and 5 present a significant increase in electrical activity, while channels 1 to 3 show small to negligible signal amplitude. For the index finger, channel 3 presents a significant amplitude increase, since its placement is contiguous with the *extensor digitorum muscle*, that does not participate in thumb extension. This channel shows activity for the remaining finger extension movements. For the middle finger, channel 2 shows the higher intensity of all the channels, while for the ring finger, channels

1 and 2 present a high activation intensity, decreasing for channel 3. Finally, for little finger extension, significant activation in channel 1 is obtained, while channels 4 and 5 increase their activity significantly, associated with the activation of the *extensor digiti minimi*, that specifically contracts for little finger extension. Overall, clear identification of individual finger motions is possible, demonstrating the possibility of integrating these bioelectrode arrays with classification algorithms for motion identification. With considerate electrode organization and placement, applications such as human machine interfacing or functional prosthetics can be envisioned.

7.3.5 LIG-based iontophoresis device for sweat stimulation and sensing

An important function that bioelectrode can perform is electrical stimulation of biological tissues, which can have important biomedical applications, including the movement of charged and neutral molecules trough tissue barriers, by the action of electrical fields, for drug delivery applications. Transferred, paper-based LIG electrode were tested for this final purpose, serving as iontophoresis electrodes for the delivery of the cholinergic agonist agent carbachol, targeting drug induced sweat secretion for metabolite biosensing purposes. A schematic representation of the LIG-based iontophoresis electrodes, integrated with an epifluidic module for sweat transportation and sweat electrochemical sensor for glucose quantification is portrayed in **Figure 7.5a**. Two rectangular shaped electrodes with curved edges and an area of 0.6 cm^2 were patterned and transferred onto the PU substrates, followed by modular assembly of epifluidic and sensing components, depending on the experiments performed with the device. Overall, device components additionally comprise the three electrode electrochemical sensing module, with modified WE for glucose sensing, an encapsulating layer with hydrophilic properties and opening for iontophoresis and electrochemical sensing electrodes, a microfluidic channel layer and a final encapsulation layer that seals the microfluidic channel and allows for adherence of the device to the skin, as shown in the picture (device without the electrochemical sensing module, for visualization of the microfluidic channel). For connection with the current source providing the electrical stimulus for iontophoresis, a silver track connector fabricated on PI was also integrated with the device, for connection with a flexible flat cable connector. This system was tested in two stages, the first one involving the individual testing of the iontophoresis module, and the second by developing and characterizing an ultrasensitive sweat glucose sensor for integration and proof-of-concept sweat metabolite sensing.

7.3.5.1 Testing of LIG-based iontophoresis module for sweat stimulation

In a first testing stage, the LIG-based iontophoresis module was individually tested, without electrochemical sensor integration, to evaluate its operation mode, carbachol delivery capabilities, sweat secretion outcomes and establish a stimulation protocol to be employed for *in-vivo* experiments. In this regard, several parameters are of importance, regarding the current profile used for stimulation, the charge delivered to the skin, the drug delivery dose, effects on the skin, as well as outcomes related to resulting sweat secretion rates over time and overall sweat secretion volumes, conducive for efficient sweat sampling and measurement. A schematic representation of iontophoresis process (**Figure 7.5b**) depicts the steps involved in the sweat secretion stimulation, starting with the flow of current from the anode through the hydrogel and the skin, towards the cathode. The anode hydrogel contains a 0.5 % (w/v) concentration of carbachol, which due to its positive charge, moves along the current path and onto the skin, until reaching eccrine sweat glands. At this stage, the binding of carbachol with acetylcholine receptors promotes the secretion of sweat to the skin surface, where it can be collected. A sweat collection protocol for sweat rate and secreted volume analysis was performed with a device comprising only the iontophoresis electrodes and an opening for sweat collection was used (**Figure 7.5c**). With this opening, iontophoresis stimulation could be performed, followed by placement of an absorbent paper pad in-between the electrode, that absorbs and collects secreted sweat. Before establishing this device design and implementation for analysis of the iontophoresis protocol, other designs and strategies were attempted, including microfluidic analysis, that found to be less efficient when compared to the gravimetric method, since they required more complex image analysis (Figure E5).

For the stimulation protocol, constant current profiles were employed, to assess the influence on generated sweat. **Figure 7.4d** shows the potential profile associated with the application of 100 µA current for 5 minutes, along with the charge delivered during this iontophoresis period. While the applied current is constant, the potential changes and stabilizes over time, associated with the resistive load of different layers and their interface, either from the hydrogel or the skin tissue layers. Furthermore, sudden peaks are visible, associated with motion artifacts caused by friction between the hydrogel and the skin. This implies that for a consistent current application over the stimulated skin area, tight adherence is required, so that charge does not flow through reduced areas, increasing current density and possible skin discomfort and lesion. As for the charge, the constant applied current implies a linear increase in delivered charge, accumulating for the stimulation period. **Figure 7.4e** shows the effects of iontophoretic stimulation on skin-electrode impedance, demonstrating a significant decrease

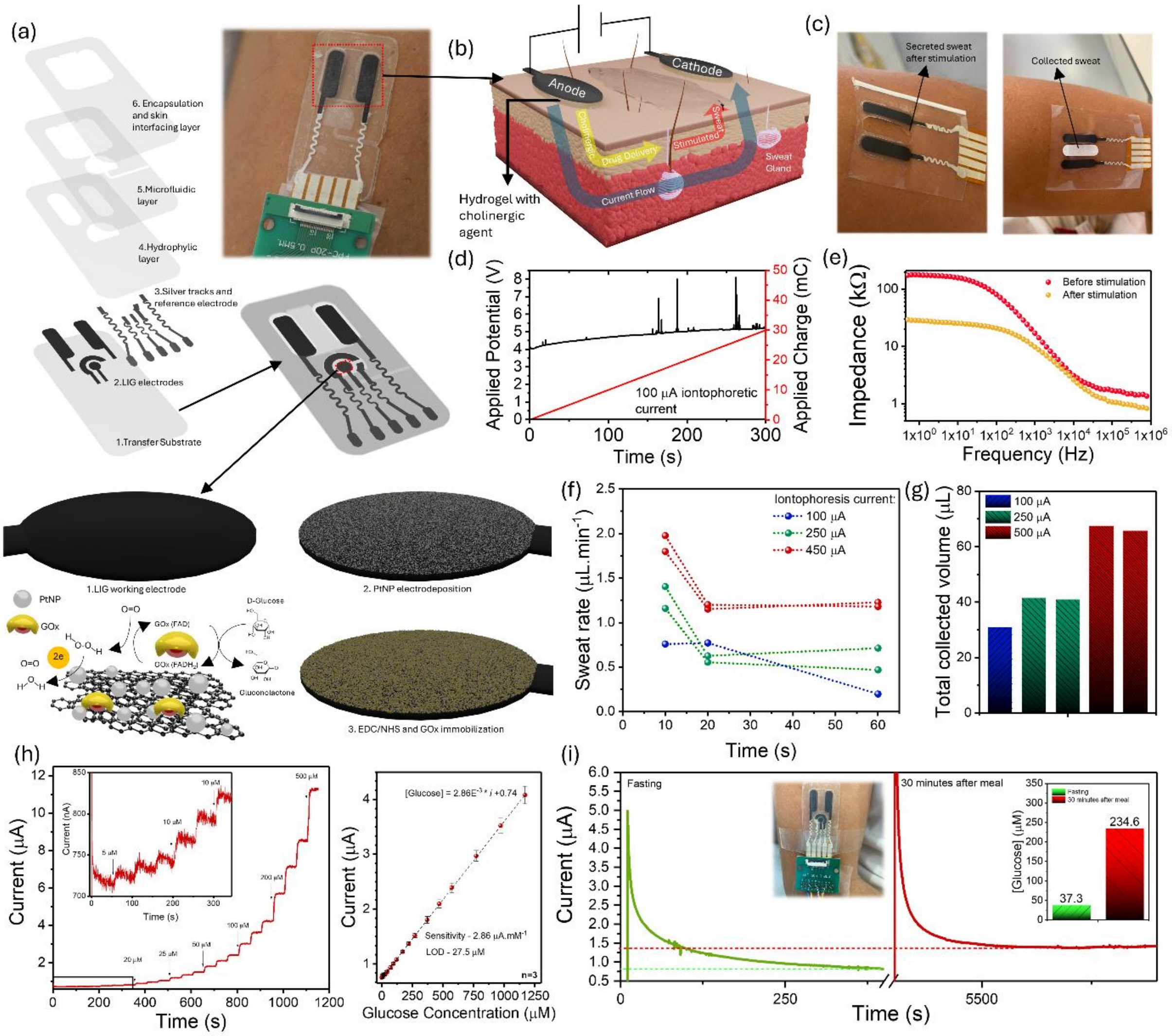

Figure 7.5 - LIG-based iontophoresis patch for sweat glucose detection. (a) Scheme of device components and assembly, placement in the skin, electrochemical biosensor modification strategy and biosensing scheme for sweat glucose detection. (b) Working principle of iontophorestic cholinergic agonist delivery for sweat stimulation. (c) Iontophoresis module for sweat rate and volume estimation. (d) Representative iontophoresis protocol, by application of 100 µA and resulting potential and charge profile. (e) Electrode-skin impedance before and after iontophoresis protocol. (f) Sweat rate for iontophoresis protocol with different stimulation currents and (g) total collected sweat volume. (h) Electrochemical sweat glucose sensor response curve and calibration curve. (i) Testing of integrated iontophoresis device and resulting sensor response curve at a fasting state and after a meal.

in impedance, associated with the secretion of sweat and higher hydration of skin tissues under the anode, along with accumulation of charged molecules over the stimulated area.

To determine the effect of iontophoretic current, different currents were employed for a 10-minute stimulation period, using five devices, and secreted sweat volume was analyzed, to determine the sweat rate one hour after stimulation. The experimental iontophoretic currents, resulting charge and estimated carbachol dose are presented in **Table 7.1**. Depending on the applied current, different current and charge densities are delivered to the area underneath the electrode. Regarding current density, this is an important consideration regarding possible adverse effects to the skin, such as irritation and burns. Regarding the charge, it is directly related to the delivery and movement of charged molecules and can be used to estimate the amount of drug being delivered to the skin. Using the Faraday constant (F = 96485 C.mol^{-1}), that represents the amount of electricity carried by one mole of electrons, and considering the monovalent nature of carbachol, the theoretical carbachol weight being transported to the skin can be computed. According to previous reports of iontophoretic delivery, the presence of competing, small ionic species and other factors reduces the efficiency of delivery to around 30 % of this theoretical value [51], while other factors, such as cholinergic hydrogel concentration also influences the delivery and sweat gland stimulation [18]. According to these considerations, estimated carbachol delivery of 34, 85 and 150 µg shows similar values to previous studies employing this cholinergic agent [39,51].

Table 7.1 - Iontophoretic current application protocols for sweat rate estimation.

Current (mA)	Current density (mA.cm^{-2})	Charge density (mC/cm^{-2})	Estimated carbachol delivery (µg)
0.1	0.17	100	~35
0.25	0.42	250	~85
0.45	0.75	450	~150

Sweat rate profile for the tested iontophoretic current doses are presented in **Figure 7.5f**, showing the calculated sweat rate after the 10-minute stimulation period, 20 minutes and 1 hour after stimulation. As expected, the increase in current and associated higher carbachol delivery leads to an increase in sweat rate, consistent over time. For 100 µA current, tested in one device, a sweat rate of 0.8 µL.min^{-1} was registered after stimulation, dropping to 0.2 µL.min^{-1} after 1 hour. For 250 µA current, tested in two devices, sweat rates above 1 µL.min^{-1} are observed after stimulation, also maintaining higher rates after 1 hour, at 0.5 and 0.7 µL.min^{-1}. For the highest applied current of 450 µA, sweat rates approximating 2 µL.min^{-1} are achieved, maintaining levels above 1 µL.min^{-1} for the entire testing period. In terms of the total extracted sweat volume (**Figure 7.5g**), a value of 31 µL was stimulated with a current of 100 µA, increasing to values around 40 and 65 µL for 250 and 450 µA. Although the sweat rates achieved with this paper-based LIG iontophoresis device being below other reports for carbachol delivery, that have reached values above 3 µL.min^{-1} [39], the resulting sweat volumes are sufficient for efficient sweat sampling, using the microfluidic design presented in **Figure 7.4a**, which has a volume capacity of 15 µL. Thus, these results show an efficient sweat secretion stimulation for all the current values, with the capacity for manipulating the resulting sweat rates and volumes generated by the device. From these three conditions, a current of 250 µA was selected for proof-of-concept integration with epifluidics and glucose electrochemical sensing module.

7.3.5.2 Electrochemical sweat sensor characterization and integration for on-skin glucose monitoring

For the construction of the electrochemical glucose biosensor, different alternatives were considered, based on the LIG-based glucose biosensors developed in **Chapter 3** and **Chapter 5**. While mediated and unmediated glucose test strips presented in **Chapter 3** are based on enzymatic methods, showing great specificity and capability for glucose quantification in complex sample matrices, the biosensing schemes were designed to reach glucose quantification in higher concentration ranges for blood glucose levels, not being suitable for the low concentrations found in sweat. Furthermore, no enzyme and mediator immobilization strategy beyond the deposition was implemented, which is needed for longer term, stable sensor operation.

For the nonenzymatic glucose sensor presented in **Chapter 5**, the sensitivity and linear ranges reached with the glucose oxidation promoted by CuNPs allows for an efficient quantification. Thus, an attempt was made to use these LIG/CuNPs sensors. To do this, sensors were produced following the same methods and transferred onto PU substrate. These nonenzymatic glucose sensors based on transition metal nanostructures suffer from a key disadvantage when compared to enzymatic sensors, related to the need for an alkaline medium that promotes the recognition reaction. While performing the measurements in alkaline medium is straightforward when testing individual sensors, this raises an issue when integrating them with the iontophoresis device, since sweat shows a more neutral to slightly acidic pH. Thus, means of promoting a localized alkaline environment are needed, so that glucose molecules in sweat can participate in the reaction with copper nanostructures. To do this, an agarose layer (0.5 % w/v) with 0.1 M NaOH concentration was drop-cast over the electrodes for this purpose. These modified electrodes were tested in deionized water and showed amperometric response associated with the increase in glucose in the testing matrix (Figure E6). However, the analytical characteristics of the sensor fell short of the requirements needed for efficient glucose detection in the range found in sweat, which is further explained in the Annex E.

Thus, a different approach was taken, to develop a highly sensitive electrochemical biosensor using enzymatic detection mechanisms. To do this, the LIG-based H_2O_2 electrochemical sensors presented in **Chapter 6** were further developed to serve as the basis for electrochemical sweat glucose sensing. A schematic representation of the construction of these sensors is presented in **Figure 7.5a**, where the WE was functionalized using the same PtNP electrodeposition protocol, to introduce this catalytic material that promotes H_2O_2 oxidation and an associated amperometric signal. After electrodeposition, GOx was covalently bound to the carbon electrode surface through EDC/NHS coupling, serving as the biological recognition element for glucose detection. With this sensor functionalization protocol, a biodetection scheme based on glucose oxidation by GOx and its flavin adenine dinucleotide (FAD) structure initiates the reaction, leading to the consumption of O_2 to produce H_2O_2. H_2O_2 can then be oxidized by the surface bound PtNPs under a constant potential bias, being transformed back into O_2 and H_2O and releasing two electrons, that generate the amperometric signal related to glucose levels in circulation over the WE surface. Before integration with the iontophoresis device, the sensor was tested, to determine suitable operation potentials (Figure E7), with a potential of 0.5 V being selected for the chronoamperometry experiments. Sensor calibration was performed, using this potential and a PBS testing solution. Besides PBS, other electrolytes (deionized water, KCl and artificial sweat) were tested, to determine if the sensors maintained stable operation, which was verified, only with some changes in sensor response times, associated with differences in ionic content and resulting solution resistance (Figure E7). As can be seen from the sensor response curve in PBS (**Figure 7.5h**), current steps associated with low glucose concentrations down to 5 µM are distinguishable from the background current, portraying its good sensitivity. Furthermore, consistent current increase is achieved for each glucose concentration being added to the sensor, showing its great stability over continuous operation. To calibrate the sensor, current values taken after stabilization for each glucose addition step were taken and plotted vs. the corresponding glucose concentration (n=3). A resulting linear range between 5 µM and 1.17 mM was reached, with a sensitivity of 2.86 $\mu A.mM^{-1}$ ($29.73\ \mu A.mM^{-1}.cm^{-2}$) and a LOD of 27.5 µM.

With these analytical parameters, the sensors show a compatible performance to detect and quantify physiological levels of glucose in sweat. Thus, sensor integration was performed, by assembling a sensor with the iontophoresis device and the epifluidic module, for delivery of stimulated sweat onto the surface of the sensing electrodes. One proof-of-concept *in-vivo* measure was performed, with the integrated epidermic device mounted laterally in the upper arm (**Figure 7.5i**). A first iontophoresis sweat stimulation step (250 µA, 10 minutes) was performed, and an amperometric measure of sensor response was taken 5 minutes after the end of the stimulation period, to ensure filling of the microfluidic network. The resulting amperometric signal corresponds to a fasted state. Current values in the lower portion of the detection range were measured, at 830 nA, with a corresponding concentration of 37 μM, according to sensor calibration. After a high calory meal, a second sweat stimulation was performed, 1 hour after the meal, and after a total period of 1 hour and 10 minutes, a second amperometric measurement was taken. The reason for this timing is related with glucose metabolism and the time needed for glucose to reach the blood stream, as well as the lag time between the transference of glucose between blood and other circulating fluid, which in the case of sweat, has been estimated to be 10-20 minutes [63,64]. The resulting current show a marked increase, to levels around 1.4 μA, corresponding to a glucose level of 234 μM. A second device was assembled with a sensor taken from a new fabrication batch, showing similar results (Figure E8), although the baseline current taken at a fasted state situating below the levels established in the calibration curve. However, once again, increased current after a meal was registered, showing that the sensor still points to the trend of increasing glucose levels.

7.4 Conclusions

Paper-based LIG was successfully implemented in different scenarios for epidermal bioelectronic applications, showing its compatibility for the construction of functional bioelectrodes, that can participate in several sensing and stimulation tasks. As shown through characterization experiments, graphitized materials synthesized by DLW of different polymers, more specifically PI and waxed paper, show heterogeneous chemical composition throughout its surface, scoped by Raman mapping of the characteristic graphene peaks' intensities, associated with their porous nature. While for PI-LIG and P-LIG, very low defect density and efficient graphitization characterizes the material surface, transferred LIG@PU shows an amorphous carbon structure, which could influence the electrical interfacing of electrodes with the skin. Furthermore, the change in hydrophobicity of LIG@PU is also relevant in this scenario. While all the LIG materials tested in this chapter present outstanding conductivity, represented by single-digit sheet resistance regimen, LIG@PU presented better biocompatibility and flexibility for interfacing with biological tissue. P-LIG was not suitable for this purpose, since its mechanical characteristics and poorer binding to the paper substrate leads to breakage and detachment, which led to it not being tested for biocompatibility and signal acquisition experiments. For PI-LIG, its hydrophobicity did not allow to retrieve robust information about its biocompatibility, since cells did not adhere to its surface. Contrarily, LIG@PU shows good biocompatibility, confirmed by the adherence and proliferation of human fibroblast in its surface. In terms of its interfacing with the skin, LIG@PU showed similar electrode-skin impedances when compared to PI-LIG, either when gelled or as dry electrode, demonstrating that its more amorphous carbonized surface does not diminish the capability of electrical signals to be carried from and onto the skin. Strengthened by this evidence, ECG signal acquisition with LIG@PU dry bioelectrode demonstrated similar results when compared with commercial Ag/AgCl and PI-LIG electrodes, while benefiting from increased conformability, allowing for comfortable long-term ECG monitoring, tested up to 24 hours, with electrode retaining good SNR values and clear signal component determination. Similarly, sEMG monitoring also showed efficient signal acquisition using LIG@PU electrodes, demonstrating the capability for electrode miniaturization without significant loss of performance, with electrodes as small as 2 mm in diameter. Taking advantage of the seamless device fabrication and integration promoted by DLW, more complex electrode arrangements and device architectures were implemented within bioelectrode arrays, with the chest-scale ECG patch showing the preservation of similar SNR and ECG feature visualization, allowing for a more user-friendly 12-lead ECG protocol performance, with less material and electrode waste. For the sEMG electrode array, efficient electrical muscle activity can be acquired by multiple channels simultaneously, in this case capable of distinguishing finger motion. However, the ease of changing electrode organization and placement within similar patches can easily allow for other applications to be envisioned, where multichannel EMG signal acquisition may be required. Furthermore, adapting electrode organization and patch sizes to different users, either for the ECG or EMG devices, can also be easily performed though DLW. For stimulation, LIG@PU bioelectrode performed adequately as anode and cathode for current delivery to the skin, for iontophoretic agonist delivery and sweat stimulation through iontophoresis, as well as for the construction of flexible, high-sensitivity electrochemical glucose biosensors. Efficient carbachol delivery allowed for the generation of sufficient sweat volumes for sampling and sensing of sweat, within an integrated iontophoresis-biosensor epidermal device. Although the results indicate the satisfactory operation of the device for sweat glucose detection, further testing of the device is needed to confirm these results. This would require testing with more subjects and be benchmarked against other glucose detection technologies, by using BGMs or CGMs, and measuring glucose levels simultaneously to the iontophoresis-based device. Furthermore, only single measures were performed before and after meal administration. For higher sampling rates approximating CGMs (glucose levels sampled every 1 to 10 minutes) [65], which are the gold standard for continuous glucose analysis, further development of the iontophoresis and epifluidic modules would be required, to allow for more frequent sweat stimulation, efficient sampling and retrieving of sweat glucose levels.

Overall, the suitability of paper as a precursor material for the fabrication of LIG-based wearable bioelectrodes using the developed fabrication methods holds promise for more sustainable and accessible diagnostic tools, for several biomedical application scenarios.

References

1. Lee, S. *et al.* Permeable Bioelectronics toward Biointegrated Systems. *Chem. Rev.* **124**, 6543–6591 (2024).
2. Cheng, L., Li, J., Guo, A. & Zhang, J. Recent advances in flexible noninvasive electrodes for surface electromyography acquisition. *npj Flex. Electron.* **7**, 39 (2023).
3. Wang, C., Wang, C., Huang, Z. & Xu, S. Materials and Structures toward Soft Electronics. *Adv. Mater.* **30**, 1801368 (2018).
4. Gablech, I. & Głowacki, E. D. State-of-the-Art Electronic Materials for Thin Films in Bioelectronics. *Adv. Electron. Mater.* **9**, 2300258 (2023).
5. Cole, T., Khoshmanesh, K. & Tang, S.-Y. Liquid Metal Enabled Biodevices. *Adv. Intell. Syst.* **3**, 2000275 (2021).
6. Zhang, Y. *et al.* Tailor-Made Gold Nanomaterials for Applications in Soft Bioelectronics and Optoelectronics. *Adv. Mater.* **36**, 2405046 (2024).
7. Gao, X. *et al.* Bioelectronic Applications of Intrinsically Conductive Polymers. *Adv. Electron. Mater.* **9**, 2300082 (2023).
8. Yuk, H., Lu, B. & Zhao, X. Hydrogel bioelectronics. *Chem. Soc. Rev.* **48**, 1642–1667 (2019).
9. Rastogi, S. K., Kalmykov, A., Johnson, N. & Cohen-Karni, T. Bioelectronics with nanocarbons. *J. Mater. Chem. B* **6**, 7159–7178 (2018).
10. Baik, S. *et al.* Bioinspired Adhesive Architectures: From Skin Patch to Integrated Bioelectronics. *Adv. Mater.* **31**, 1803309 (2019).
11. Dong, W. *et al.* Soft human–machine interfaces: design, sensing and stimulation. *Int. J. Intell. Robot. Appl.* **2**, 313–338 (2018).
12. Sunwoo, S.-H. *et al.* Soft bioelectronics for the management of cardiovascular diseases. *Nat. Rev. Bioeng.* **2**, 8–24 (2023).
13. Clausen, D. *et al.* Chronic Biosymbiotic Electrophysiology. *Adv. Funct. Mater.* 2407086 (2024) doi:10.1002/adfm.202407086.
14. Kumar Das, S., Nayak, K. K., Krishnaswamy, P. R., Kumar, V. & Bhat, N. Review—Electrochemistry and Other Emerging Technologies for Continuous Glucose Monitoring Devices. *ECS Sensors Plus* **1**, 031601 (2022).
15. Kim, G., Ahn, H., Chaj Ulloa, J. & Gao, W. Microneedle sensors for dermal interstitial fluid analysis. *Med-X* **2**, 15 (2024).
16. Khor, S. M., Choi, J., Won, P. & Ko, S. H. Challenges and Strategies in Developing an Enzymatic Wearable Sweat Glucose Biosensor as a Practical Point-Of-Care Monitoring Tool for Type II Diabetes. *Nanomaterials* **12**, 221 (2022).
17. Lee, H., Hong, Y. J., Baik, S., Hyeon, T. & Kim, D. Enzyme-Based Glucose Sensor: From Invasive to Wearable Device. *Adv. Healthc. Mater.* **7**, 1701150 (2018).
18. Emaminejad, S. *et al.* Autonomous sweat extraction and analysis applied to cystic fibrosis and glucose monitoring using a fully integrated wearable platform. *Proc. Natl. Acad. Sci. U. S. A.* **114**, 4625–4630 (2017).
19. Nyein, H. Y. Y. *et al.* A Wearable Electrochemical Platform for Noninvasive Simultaneous Monitoring of Ca 2+ and pH. *ACS Nano* **10**, 7216–7224 (2016).
20. Yang, Y. *et al.* A laser-engraved wearable sensor for sensitive detection of uric acid and tyrosine in sweat. *Nat. Biotechnol.* **38**, 217–224 (2020).
21. Tu, J. *et al.* A wireless patch for the monitoring of C-reactive protein in sweat. *Nat. Biomed. Eng.* **7**, 1293–1306 (2023).
22. Torrente-Rodríguez, R. M. *et al.* Investigation of Cortisol Dynamics in Human Sweat Using a Graphene-Based Wireless mHealth System. *Matter* **2**, 1–17 (2020).
23. Zhang, Z. *et al.* Soft Bioelectronics for Therapeutics. *ACS Nano* **17**, 17634–17667 (2023).
24. Zhang, Q. *et al.* Multi-functional adhesive hydrogel as bio-interface for wireless transient

pacemaker. *Biosens. Bioelectron.* **263**, 116597 (2024).

25. Hartnell, S., Fuchs, J., Boughton, C. K. & Hovorka, R. Closed-loop technology: a practical guide. *Pract. Diabetes* **38**, 33–39 (2021).
26. Xu, K. *et al.* Toward Integrated Multifunctional Laser-Induced Graphene-Based Skin-Like Flexible Sensor Systems. *ACS Nano* (2024) doi:10.1021/acsnano.4c09062.
27. Won, D. *et al.* Digital selective transformation and patterning of highly conductive hydrogel bioelectronics by laser-induced phase separation. *Sci. Adv.* **8**, 3209 (2022).
28. Sharifuzzaman, M. *et al.* MXene/Fluoropolymer-Derived Laser-Carbonaceous All-Fibrous Nanohybrid Patch for Soft Wearable Bioelectronics. *Adv. Funct. Mater.* **33**, 2208894 (2023).
29. Garland, N. T. *et al.* Wearable Flexible Perspiration Biosensors Using Laser-Induced Graphene and Polymeric Tape Microfluidics. *ACS Appl. Mater. Interfaces* **15**, 38201–38213 (2023).
30. Lorestani, F. *et al.* A Highly Sensitive and Long-Term Stable Wearable Patch for Continuous Analysis of Biomarkers in Sweat. *Adv. Funct. Mater.* **33**, 2306117 (2023).
31. Sun, H., Song, S., Zhao, G., Wang, X. & Liu, G. A Flexible and Wearable Chemiresistive Biosensor Fabricated by Laser Inducing for Real-Time Glucose Analysis of Sweat. *Adv. Mater. Interfaces* **10**, 2300281 (2023).
32. Wang, Y. *et al.* One-step laser synthesis platinum nanostructured 3D porous graphene: A flexible dual-functional electrochemical biosensor for glucose and pH detection in human perspiration. *Talanta* **257**, 124362 (2023).
33. Zhu, J. *et al.* Laser-induced graphene non-enzymatic glucose sensors for on-body measurements. *Biosens. Bioelectron.* **193**, 113606 (2021).
34. Zhang, Z. *et al.* Portable glucose sensing analysis based on laser-induced graphene composite electrode. *RSC Adv.* **14**, 1034–1050 (2024).
35. Yoon, H. *et al.* A chemically modified laser-induced porous graphene based flexible and ultrasensitive electrochemical biosensor for sweat glucose detection. *Sensors Actuators, B Chem.* **311**, 127866 (2020).
36. Luo, Y. *et al.* Stretchable and Flexible Non-Enzymatic Glucose Sensor Based on Poly(ether sulfone)-Derived Laser-Induced Graphene for Wearable Skin Diagnostics. *Adv. Mater. Technol.* **7**, 2101571 (2022).
37. Lei, Y., Alshareef, A. H., Zhao, W. & Inal, S. Laser-Scribed Graphene Electrodes Derived from Lignin for Biochemical Sensing. *ACS Appl. Nano Mater.* **3**, 1166–1174 (2020).
38. Strakosas, X. *et al.* A non-enzymatic glucose sensor enabled by bioelectronic pH control. *Sci. Rep.* **9**, 10844 (2019).
39. Wang, M. *et al.* A wearable electrochemical biosensor for the monitoring of metabolites and nutrients. *Nat. Biomed. Eng.* **6**, 1225–1235 (2022).
40. Gerardo, D. *et al.* Optimization of dry laser-induced graphene (LIG) electrodes for electrocardiography (ECG) signals monitoring. *Appl. Phys. A* **130**, 197 (2024).
41. Romero, F. J. *et al.* Inexpensive and flexible nanographene-based electrodes for ubiquitous electrocardiogram monitoring. *npj Flex. Electron.* **3**, 12 (2019).
42. Houeix, Y. *et al.* Dry Laser-Induced Graphene Fractal-like ECG Electrodes. *Adv. Electron. Mater.* **10**, 2300767 (2024).
43. Zhang, Q. *et al.* Three-in-One Portable Electronic Sensory System Based on Low-Impedance Laser-Induced Graphene On-Skin Electrode Sensors for Electrophysiological Signal Monitoring. *Adv. Mater. Interfaces* **10**, 2201735 (2023).
44. Zhang, S. *et al.* Highly conductive, stretchable, durable, skin-conformal dry electrodes based on thermoplastic elastomer-embedded 3D porous graphene for multifunctional wearable bioelectronics. *Nano Res.* **16**, 7627–7637 (2023).
45. Lu, Y., Lyu, H., Richardson, A. G., Lucas, T. H. & Kuzum, D. Flexible Neural Electrode Array Based-on Porous Graphene for Cortical Microstimulation and Sensing. *Sci. Rep.* **6**, 33526 (2016).
46. Park, R. *et al.* Laser-Assisted Structuring of Graphene Films with Biocompatible Liquid Crystal

Polymer for Skin/Brain-Interfaced Electrodes. *Adv. Healthc. Mater.* 2301753 (2023) doi:10.1002/adhm.202301753.

47. Dallinger, A., Keller, K., Fitzek, H. & Greco, F. Stretchable and Skin-Conformable Conductors Based on Polyurethane/Laser-Induced Graphene. *ACS Appl. Mater. Interfaces* **12**, 19855–19865 (2020).
48. Sun, B. *et al.* Gas-Permeable, Multifunctional On-Skin Electronics Based on Laser-Induced Porous Graphene and Sugar-Templated Elastomer Sponges. *Adv. Mater.* **30**, 1804327 (2018).
49. Yang, J. *et al.* Facile Fabrication of Robust and Reusable PDMS Supported Graphene Dry Electrodes for Wearable Electrocardiogram Monitoring. *Adv. Mater. Technol.* **6**, 2100262 (2021).
50. Lu, Y. *et al.* Stretchable graphene–hydrogel interfaces for wearable and implantable bioelectronics. *Nat. Electron.* **7**, 51–65 (2023).
51. Simmers, P., Li, S. K., Kasting, G. & Heikenfeld, J. Prolonged and localized sweat stimulation by iontophoretic delivery of the slowly-metabolized cholinergic agent carbachol. *J. Dermatol. Sci.* **89**, 40–51 (2018).
52. Lee, M. S., Paul, A., Xu, Y., Hairston, W. D. & Cauwenberghs, G. Characterization of Ag/AgCl Dry Electrodes for Wearable Electrophysiological Sensing. *Front. Electron.* **2**, 700363 (2022).
53. Makowski, D. *et al.* NeuroKit2: A Python toolbox for neurophysiological signal processing. *Behav. Res. Methods* **53**, 1689–1696 (2021).
54. B.R., M. & M.R., S. ECG Denoising Using Wiener Filter and Kalman Filter. *Procedia Comput. Sci.* **171**, 273–281 (2020).
55. Cheng, L. *et al.* Flash healing of laser-induced graphene. *Nat. Commun.* **15**, 2925 (2024).
56. Ferrari, A. C. & Robertson, J. Interpretation of Raman spectra of disordered and amorphous carbon. *Phys. Rev. B* **61**, 14095–14107 (2000).
57. Wang, X., Liu, Y., Cheng, H. & Ouyang, X. Surface Wettability for Skin-Interfaced Sensors and Devices. *Adv. Funct. Mater.* **32**, 2200260 (2022).
58. Romero, F. J. *et al.* Inexpensive and flexible nanographene-based electrodes for ubiquitous electrocardiogram monitoring. *npj Flex. Electron.* **3**, 12 (2019).
59. Lu, F. *et al.* Review of Stratum Corneum Impedance Measurement in Non-Invasive Penetration Application. *Biosensors* **8**, 31 (2018).
60. Yang, L. *et al.* Insight into the Contact Impedance between the Electrode and the Skin Surface for Electrophysical Recordings. *ACS Omega* **7**, 13906–13912 (2022).
61. Li, G., Wang, S. & Duan, Y. Y. Towards conductive-gel-free electrodes: Understanding the wet electrode, semi-dry electrode and dry electrode-skin interface impedance using electrochemical impedance spectroscopy fitting. *Sensors Actuators B Chem.* **277**, 250–260 (2018).
62. Bora, D. J. & Dasgupta, R. Estimation of skin impedance models with experimental data and a proposed model for human skin impedance. *IET Syst. Biol.* **14**, 230–240 (2020).
63. La Count, T. D., Jajack, A., Heikenfeld, J. & Kasting, G. B. Modeling Glucose Transport From Systemic Circulation to Sweat. *J. Pharm. Sci.* **108**, 364–371 (2019).
64. Saha, T. *et al.* A Passive Perspiration Inspired Wearable Platform for Continuous Glucose Monitoring. *Adv. Sci.* 2405518 (2024) doi:10.1002/advs.202405518.
65. Breton, M. D., Shields, D. P. & Kovatchev, B. P. Optimum Subcutaneous Glucose Sampling and Fourier Analysis of Continuous Glucose Monitors. *J. Diabetes Sci. Technol.* **2**, 495–500 (2008).

8
CONCLUSIONS AND OUTLOOK

8.1 Summary and conclusions

Laser-induced graphene has rapidly become a very popular material in the scientific literature, when versatile, efficient patterning of conductive graphene-based geometries is targeted as the approach for device microfabrication. In contrast with other widespread technologies, such as additive manufacturing and printed electronics, the simple, one-step synthesis and simultaneous patterning, without intricate pre-processing requirements, has made it a resourceful approach for planar geometry definition in several materials. With this thesis, the capabilities of DLW for LIG synthesis is further expanded for alternative substrates and novel fields of applications.

Through the comprehensive study presented in this work, laser processing frameworks needed for efficient graphitization of paper substrates, both in terms of the resulting LIG material properties and its shaping, are delineated. As shown, considerate laser irradiation protocols, where different operational parameters are studied, show the capability for high-efficient graphitization, reaching paper-derived, graphitized patterns with conductive properties comparable to the state-of-the-art for aromatic polymer precursors. Along with this, the tailoring of paper substrate modifications, with fire-retardant and wax, boosts this graphitization potential, where paper's cellulose aliphatic structures serve as the template for graphene lattice build-up. With the generated knowledge on these DLW synthesis and patterning processes, prototyping of different applications has been demonstrated, further showing the introduction of DLW as a tool for the development of paper electronics in several areas. For this work in specific, paper-derived LIG was implemented in different bioelectronics applications, showing its compatibility for the fabrication of electrochemical and wearable biosensing applications. To reach these results, each chapter was devoted to advancing the knowledge on DLW and device fabrications using paper.

In **Chapter 3**, an initial scoping of the graphitization potential of two paper substrates was compared, namely chromatography paper and office paper, along with their potential to construct paper-based electrochemical sensors. Both paper substrates were successfully implemented for this purpose, with wax playing a key role in the impermeabilization of the substrates for interfacing with liquid electrolytes. From the two paper substrates, chromatography paper showed the best graphitization potential and resulting electrochemical properties when used in the patterning of LIG electrodes, related with its exclusive cellulose content. For commercial office paper, the presence of additives diminished the capability of the thermochemical laser stimulus in substrate graphitization, resulting in higher resistivity. However, further study of commercially available, ubiquitous paper sources, including office paper, would allow for improvements and more use cases for these substrates. Using chromatography paper, efficient prototyping of paper-based LIG glucose electrochemical biosensors was demonstrated, using two distinct biosensing schemes. For the mediated glucose bionsensor, a preclinical validation trial demonstrated a good TRL, with the sensors operating under a simulated real environment with real samples. While paper graphitization potential was demonstrated, further improvement could be made in this regard, by studying and modeling the laser irradiation protocols leading to graphitization.

In **Chapter 4**, a detailed study of laser irradiation parameters and their influence on graphitization outcomes and electrochemical properties was performed. The basis of this study was to further deepen the results from Chapter 3 and identify underlying irradiation parameters key in the efficient graphitization of the substrate. By considering alternative irradiation parameter (PW and PRF instead of power and speed), it was demonstrated that PW is the main driver in initiating substrate graphitization, since it is directly related with heat accumulation and the thermal tolerance of the material. For a narrow interval of PW values, the tolerance of the material for carbonization and graphitization is reached, and if surpassed, excessive damage of the substrate occurs. Within this interval, control of material properties is set by parameters associated with energy density, namely PRF, laser beam defocus and number of laser patterning cycles. For electrochemical properties, the charge transfer capabilities of electrochemical cells are also susceptive of tuning, depending on the same laser processing parameters, reaching very appealing operation for redox-based electrochemical sensing.

In **Chapter 5**, the capabilities of DLW for the one-step synthesis of composite materials were implemented. To demonstrate the compatibility of chromatography paper substrates to hold metal salt precursors through its capillarity properties, a copper sulfate precursor was absorbed into paper and submitted to laser irradiation, resulting in a LIG/CuNPs hybrid material synthesized in a one-step approach. This approach presents some advantages, including reduced fabrication steps and could be replicated for other metal salt precursors, being a disadvantage the reduced control of NP size and distribution. Translating the synthesis approach for the fabrication of a modified WE, highly sensitive nonenzymatic glucose sensors were constructed, showing analytical capabilities for the quantification of glucose in sweat. Although this good analytical performance and ability to quantify glucose in artificial sweat samples, a key disadvantage of such sensors still needs to be addressed, related with their inability to detect glucose in neutral medium. The need for alkaline electrolytes diminishes the integration potential of these transition metal-based nonenzymatic sensors within more complex devices for *in-vivo* sensing.

In **Chapter 6**, the principles for the translation of paper-derived LIG for wearable biosensing device fabrication were established, based on material transfer strategies. Firstly, the enhancement of electrical properties for the paper-derived LIG were demonstrated, by controlling the precursor substrate composition, in terms of its wax composition. This is a crucial step, to allow for LIG layers with sufficient thickness to be efficiently transferred onto other substrates. Furthermore, this also allows for the transferred patterns to maintain similar conductivity before and after transfer. Through the developed water-induced peel-off strategy, LIG patterns can be transferred in their entirety, due to the action of water in separating the precursor substrate from the laser synthesized patterns. Because of the porous structure of the paper substrate, other LIG transfer strategies are not compatible with paper, such as casting of elastomeric polymers, because cellulose fibers become interlaced with transfer materials. With the action of water, interfacing paper with adhesive substrates and subsequent separation for peel-off transfer becomes possible. Thus, intricate LIG patterns can be transferred, with the method being tested by the construction of different sensing devices for wearable sensing purposes.

In **Chapter 7**, the full implementation of paper-based LIG for the construction of functional devices for wearable sensing is tackled, where transferred LIG geometries serve as bioelectrodes for the acquisition and delivery of electrical stimulus in skin-interfaced devices. Initial characterization demonstrated the good biocompatibility of the material when in contact with live tissue, scoped by cell culture of human fibroblasts, with skin-electrode electrical interface properties and charge carrying capabilities of the electrodes conducive for electrophysiological signal acquisition. This was mostly implemented with LIG dry electrode configurations, where the direct interfacing of the LIG bioelectrodes with the skin showed efficient ECG and EMG signal acquisition capabilities, categorized by the high SNR values obtained for different electrode sizes. For stimulation, LIG bioelectrode demonstrated their ability for charge carrying towards the skin, for iontophoretic drug delivery of cholinergic agonists, targeting sweat secretion stimulation. Using carbachol delivery, sufficient sweat volumes can be generated for sweat sensing applications, where a proof-of-concept glucose sweat sensing systems was developed and tested. Although the LIG-based iontophoresis and integrated LIG-based electrochemical sweat glucose sensor demonstrating the capability to discern different sweat glucose levels, further technological development of the system is needed, aiming at long-term sweat glucose analysis, approximating the operation of state-of-the-art CGMs and their IF glucose level quantification.

Overall, the principles for laser processing of paper substrates for LIG synthesis and their translation for different bioelectronics applications are demonstrated in this work, applicable for future implementation in different applications beyond sensing, such as energy harvesting and storage or physical sensors, and using other polysaccharide-based polymers, that present similar chemical structures to cellulose. Thus, future work is envisioned to improve the development and readiness level of the methods and technologies developed in this thesis.

8.2 Outlook and future directions

DLW is rapidly developing into a robust technology, that may find future implantation in industrial microfabrication of electronics and bioelectronics. The laser technology market is an evolving one, where applications ranging from optical communications, spectroscopy to laser surgery stand out. From these, laser material processing is already present in several industrial fabrication frameworks, for laser cutting, engraving, marking or welding. In this regard, as showed in this work and in the evolving body of literature related to DLW, functional material patterning is rising in prevalence. Specifically related to this thesis, several aspects may be addressed in the future, to further potentiate this shift from research to large-scale development.

This thesis focused on two implementation levels, firstly related to laser material synthesis and secondly related to laser processing for bioelectronics device fabrication. Thus, specific improvements and future work addressing both these stages are of relevance.

Regarding LIG synthesis methods developed in this thesis, a comprehensive study of process-property optimization of CO_2 laser parameters and precursor material composition have been performed, focusing mostly on three specific outcomes, namely chemical properties, electric conductivity and electrochemical charge transfer capabilities when used as electrodes within electrochemical cells. However, systematization of other LIG properties, including material morphology, hydrophobicity, porosity, thermal conductivity and patterning resolution may be important in future studies, when targeting other possible material applications. This may be performed using the methods developed here for CO_2 lasers, but also using alternative laser sources and laser beam guiding systems, such as UV lasers and galvanometer-based deflection systems. Using such tools, novel laser processing frameworks based on the ones presented in this work may arise, focusing on outcomes such as high-resolution patterning, that may potentiate device miniaturization. Another important aspect is related to material property variability. Although the results presented in this work show low variations in the properties of paper-derived LIG, mostly in terms of its conductivity, larger-scale studies scoping this aspect would be relevant. A final aspect related with large-area and high-throughput material processing would be the compatibilization of laser-induced synthesis with R2R or S2S processing. Although out of the scope of this work, the development of large-scale technologies for paper processing and other precursor material and integration with laser sources, for material functionalization, would strengthen the interest of industrial partners in these technologies.

In the interface between laser material and device processing, the developed water induced peel transfer method was shown to be an attractive technique for moving paper-based LIG patterns into different support substrates. In the current developmental stage, all its use in this work was performed manually, both in terms of attaching the paper substrates to the transfer materials and in the peel-off stage. Although good material transfer yields being reached, with negligible loss of material functionality after transfer, some incidence of slight material breaking was observed. To further refine this method, attempts for automatization of material attachment and peel-off steps would be beneficial to further mature this technology. In addition, this method was also shown to be able to produce stand-alone LIG films, by detachment of the LIG patterns by only immersing the paper substrate in water, which could be an interesting approach to follow when attempting to layer LIG with underlying functional materials, which is a limitation of the DLW technology.

Finally, some improvements and future work can be envisioned at the level of the devices developed in this work. Starting with the different electrochemical biosensors demonstrated here, each instance would benefit from larger-scale pilot studies, with enough samples for statistical analysis of device analytical performance and user feedback. In this regard, the developed paper-based glucose test strips already have a sufficient TRL for such studies, since they have already been tested in a simulated real environment. Similarly, the wearable LIG bioelectrodes for ECG and EMG monitoring could also be considered for similar analysis, since testing *in vivo* was already performed in this work. Benchmarking the iontophoresis sweat stimulation device against commercial apparatus would be favorable for other applications, such as using the device for sweat collection within cystic fibrosis diagnosis. For the skin-interfaced iontophoresis-based sweat sensing system, further development is needed to reach pilot testing stage, both in device construction and operation. Since sweat is a complex fluid that changes its properties, depending on the sweat secretion conditions and for different individuals, additional device elements may be needed for efficient detection of metabolites. These include additional sensors, such as for temperature or sweat rate, that can participate in *in-situ* sensor calibration. *In-situ* calibrations have been reported in the literature as being important to compensate for different conditions, such as temperature, sweat pH or electrolyte levels, that may affect electrochemical signals. Additionally, further research on iontophoretic stimulation protocols is needed, to time sweat stimulation, transportation, sampling and sensing for long-term metabolite detection. While the iontophoresis stimulation protocols presented in this work showing an efficient sweat volume generation, it would be beneficial to achieve more frequent stimulation cycles, that generate lower volumes of sweat, so that higher sweat sensing frequency could be employed and an operation approximating continuous monitoring could be idealized. Finally, each device was tested with laboratory analysis equipment, mostly using portable potentiostats. To fully translate these LIG-based sensing devices, either in the paper substrates or wearables, into fully functioning systems, custom made instrumentation is needed, including all the necessary ICs for signal acquisition, conditioning and transmission.

Overall, the development of the technologies presented in this work showcases the rising interest of the scientific community with DLW and LIG, which is expanding its use cases in several fields. While the proofs of concept presented in this work focusing primarily on biomedical applications for diagnosis and prognosis, specifically with applicability for chronic complications such as diabetes mellitus, future emerging technologies may benefit from the fabrication frameworks put forward by multifunctional laser material processing. Future agricultural and environmental sensing strategies, to novel materials within the space technology field, are recent examples where interest in laser material processing is rising, to take advantage of multifunctionality, technological accessibility and degrees of freedom for novel device development, which hopefully are strengthened by the work presented in this thesis.

A

Appendix for Chapter 3

Paper substrate was submitted to irradiation without any fire-retardant treatment, to assess the effect laser had over paper fibers. As seen in Figure A1a, without any sodium borate treatment, there is complete ablation of superficial fibers, with no conversion of cellulose into any visually identifiable graphitic material. In opposition, in Figure A1b, there is an identifiable conversion of the paper fibers into graphitic material, identified by the dark color resulting from laser irradiation (laser operation coordinates P10S10 applied in both cases).

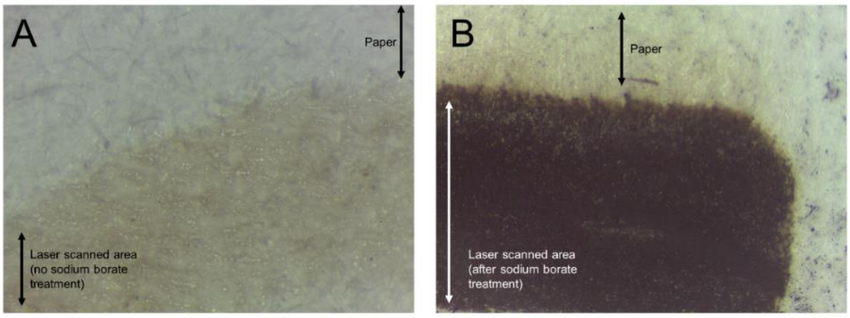

Figure A1. Effect of laser irradiation before and after sodium borate treatment.

Contact angle analysis of two LIG surfaces obtained with laser operational parameters P10S10 for chromatography paper (a) and office paper (b). For chromatography paper, the measured contact angle for chromatography paper was 108.1° and for office paper, it was 106.6°, showing the hydrophobic characteristics of the LIG's surface.

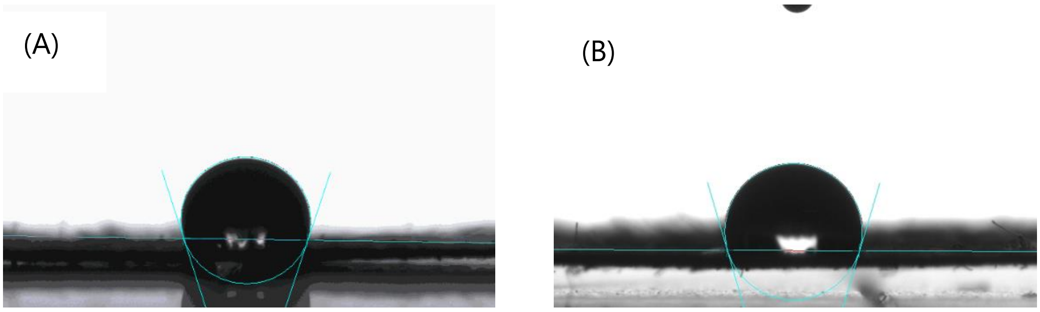

Figure A2. Contact angle analysis of LIG surface produced using laser operation parameters

C 1s spectrum of paper with diffused wax, prior to laser irradiation, is presented in Figure A3a, showing the presence of four different forms of carbon bonds, C-C/C-H, C-O, C=O and O=C-O, at 284.2, 285.9, 287.4 and 288.4 eV respectively. Upon laser irradiation, changes related to photothermal conversion of carbon bonds are present for both paper-types used for LIG synthesis, in Figures S2B and C. In these spectra, there is the appearance of sp2 carbon bonds characteristic of graphene structures, located at 283.8 eV. However, there are some differences between the C 1s spectra, namely the intensity of sp2 domain varied for chromatography paper, with more preponderant C-C domain, while for office paper, the sp2 domain is preponderant. These results confirm the production of graphene, however since there is inter-sample variability regarding the location of the measurements, this may have affected XPS measurements, translating in a reduced preponderance of the sp2 domain in the measurement performed for chromatography paper, that is not representative of the chemical nature of the synthesized LIG network as a bulk.

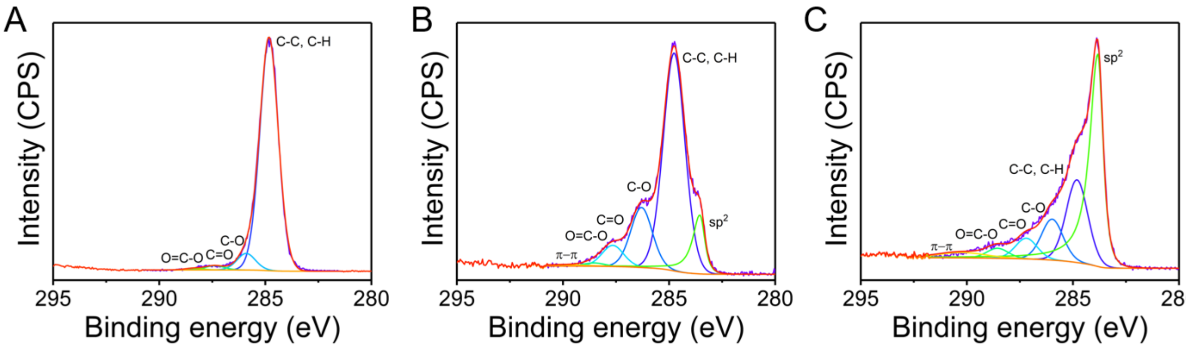

Figure A3. Paper-based LIG XPS characterization. (A) C 1s spectra of waxed paper prior to laser irradiation. (b) C 1s spectra of paper-based LIG produced from chromatography paper. (c) C 1s spectra of paper-based LIG produced from office paper.

Table A1. LIG chemical and electrical characteristics

Power/Speed Coordinates	Whatman paper					Office paper				
	I_{2D}/I_G	I_D/I_G	R_{sh}	C (%)	O (%)	I_{2D}/I_G	I_D/I_G	R_{sh}	C (%)	O (%)
P6S6	0.132 ±0.085	1.580 ±0.142	329 ±60.0	72.8 ±5.4	24.7 ±4.9	0.073 ±0.037	1.321 ±0.256	-------- --------	58.9 ±3.1	37.3 ±3.9
P8S8	0.397 ±0.084	1.398 ±0.214	75.5 ± 3.68	79.3 ±4.6	18.5 ±4.7	0.228 ±0.106	1.495 ±0.129	387.7 ±135.6	61.6 ±3.8	35.9 ±4.0
P10S10	0.616 ±0.095	1.281 ±0.173	56.0 ± 12.3	85.3 ±2.7	12.4 ±2.3	0.269 ±0.113	1.331 ±0.135	217.7 ± 21.8	65.5 ±2.1	32.9 ±2.0

Electrochemical pre-treatment using the supporting electrolyte (0.1 mM KCl) in a potential window between -2 and 2 V was used to improve the activity of the electrodes and achieve reproducible measures for characterization, as is usually performed. 1 In Figure A4, CVs for the first and tenth potential scanning are presented, top inset showing an increase in current of approximately 100 µA after pre-treatment end. CVs are also shown for the redox probe behavior before and after pre-treatment (using two different electrochemical systems) in bottom inset. Prior to electrochemical pre-treatment, it is visible that lower anodic and cathodic peak currents are achieved, with high peak separation. After pre-treatment, more defined redox peaks are shown, with improved electron transfer kinetics portrayed by the decrease in peak potential separation. This electrochemical pre-treatment was imposed on all electrodes prior to characterization with Fe(CN)63-/ Fe(CN)64- electrochemical couple.

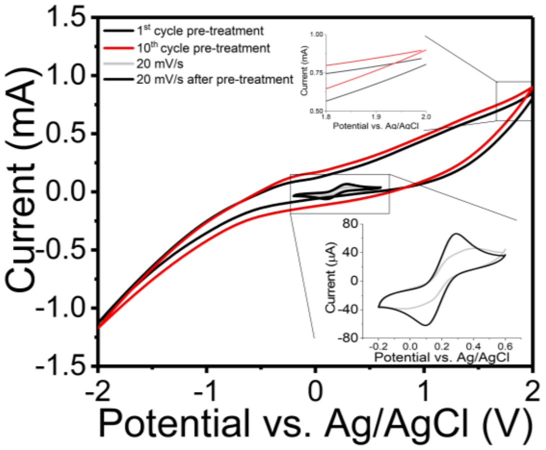

Figure A4. Electrochemical pre-treatment imposed on electrochemical systems prior to characteri-

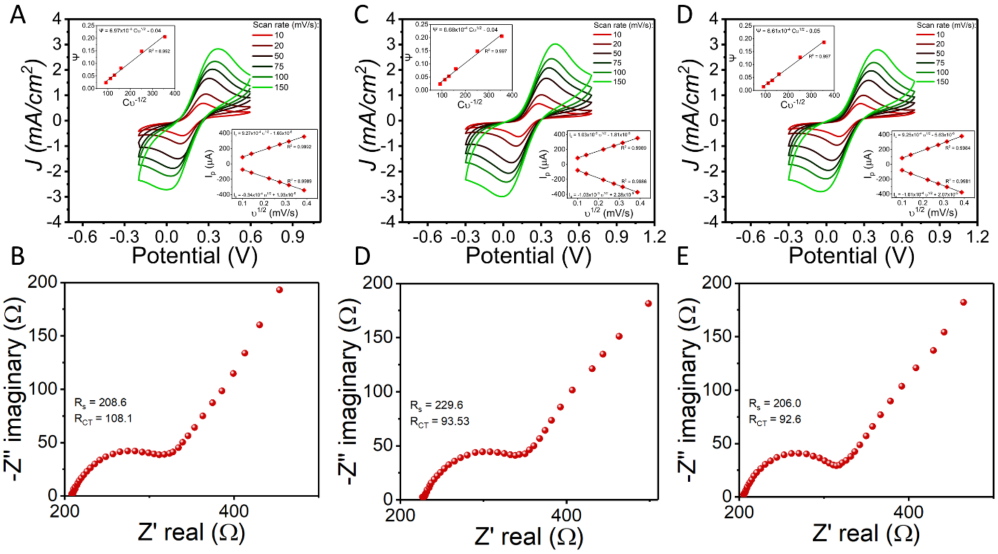

Figure A5. Cyclic voltammograms and EIS characterization for chromatography paper electrochem-

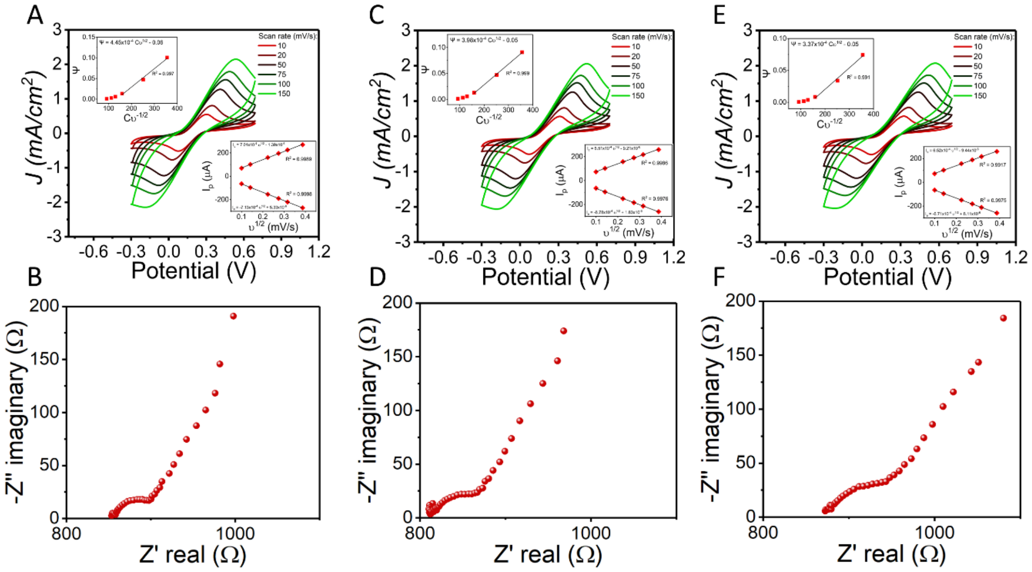

Figure A6. Cyclic voltammograms and EIS characterization for office paper electrochemical systems.

B

APPENDIX FOR CHAPTER 4

Spot radius calculations based on gaussian beam distribution:

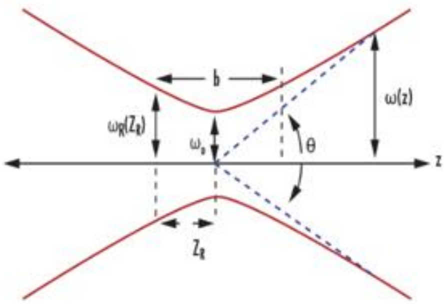

$$z_R = \frac{\pi \omega_0^2}{\lambda}$$

$$\omega(z) = \omega_0 \sqrt{1 + \left(\frac{z}{z_R}\right)^2}$$

$$Z_R = \frac{b}{2}$$

$$\omega_R = \omega(Z_R) = \sqrt{2} \cdot \omega_0$$

$$R(z) = z\left[1 + \left(\frac{z_R}{z}\right)^2\right]$$

$$\theta = \frac{\lambda}{\pi\, \omega_0}$$

Table B1. Spot size radius and area calculation.

z (mm)	ω(z) (μm)	Spot area (mm^2)
- 0.79	76.0	0.018
0	63.5	0.013
0.48	68.4	0.015
1.75	112.7	0.040
3.02	172.7	0.094

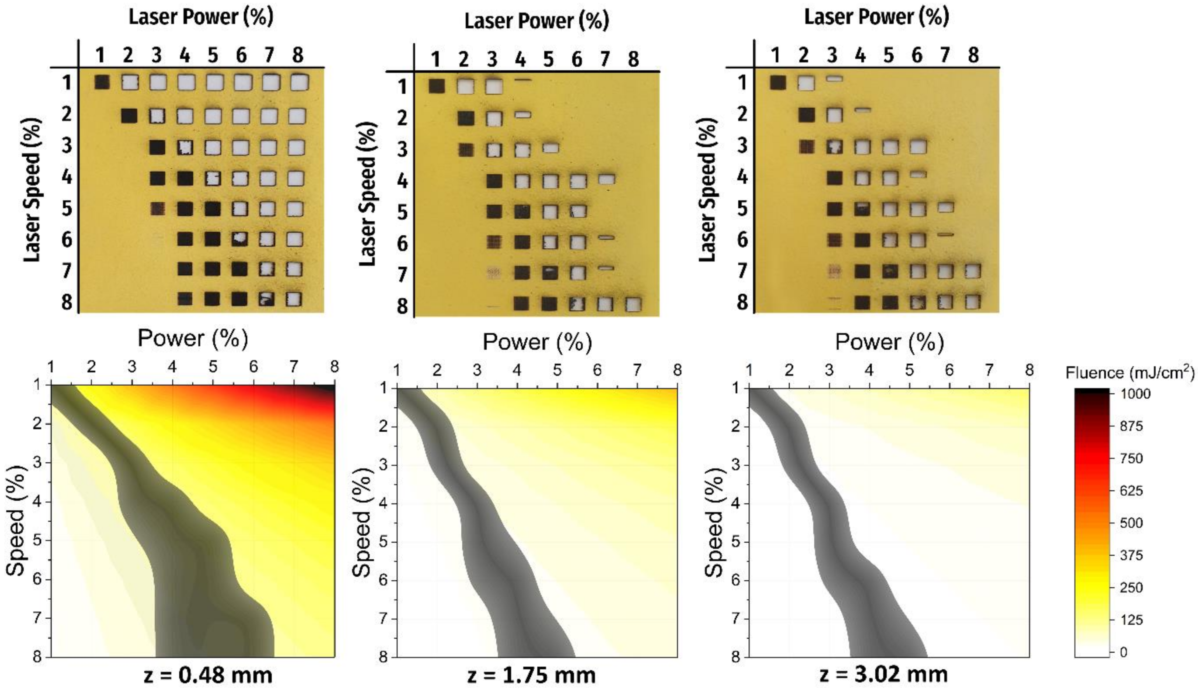

Figure B1 – Optimization matrices and distribution of graphitization regions for distinct defocus values.

Table B2 – Average sheet resistance values and respective relative standard deviations for all tested laser parameters at different defocus levels.

			-0.79 mm		0.48 mm		1.75 mm		3.02 mm	
Parameters	**PRF (Hz)**	**PW (µs)**	**$\overline{R_s}$(Ω sq^{-1})**	**RSD (N=4)**	**$\overline{R_s}$(Ω sq^{-1})**	**RSD (N=4)**	**$\overline{R_s}$(Ω sq^{-1})**	**RSD (N=4)**	**$\overline{R_s}$(Ω sq^{-1})**	**RSD (N=4)**
P1S1	250	40	-	-	-	-	53075	66 %	2514.7	31 %
P2S2	500	40	-	-	477	20 %	-	-	-	-
P3S3	750	40	121.63	31 %	425	15 %	-	-	-	-
P3S4	1000	30	-	-	489.75	22 %	-	-	2043.7	13 %
P3S5	1250	24	-	-	-	-	-	-	18168	116 %
P4S3	750	53	23.38	7 %	-	-	-	-	-	-
P4S4	1000	40	57.95	12 %	248	13 %	-	-	-	-
P4S5	1250	32	159.25	20 %	419.5	4 %	-	-	-	-
P4S6	1500	26.7	-	-	488	52 %	-	-	4742	35 %
P4S7	1750	22.9	-	-	411	10 %	-	-	2760.7	34 %
P4S8	2000	20	-	-	-	-	-	-	1485.7	17 %
P5S4	1000	50	23.03	3 %	-	-	-	-	-	-
P5S5	1250	40	33.78	5 %	-	-	-	-	-	-
P5S6	1500	33.3	51.95	8 %	611.25	50 %	-	-	-	-
P5S7	1750	28.6	58.63	4 %	918	9 %	-	-	-	-
P5S8	2000	25	92	5 %	535.5	22 %	-	-	-	-
P6S6	1500	40	21.85	10 %	-	-	-	-	-	-
P6S7	1750	34.3	27.55	3 %	-	-	-	-	-	-

P6S8	2000	30	31.83	5 %	806.75	41 %	-	-	-	-
P7S8	2000	35	21.93	11 %	-	-	-	-	-	-

Table B3. Average sheet resistance results and respective relative standard deviations for single, double and triple lasing scanning LIG samples.

	Single Scan		Double Scan		Triple Scan	
Parameters	$\overline{R_s}$(Ω sq^{-1})	**RSD (N=4)**	$\overline{R_s}$(Ω sq^{-1})	**RSD (N=4)**	$\overline{R_s}$(Ω sq^{-1})	**RSD (N=4)**
P3S3	121.63	31 %	-	-	-	-
P4S3	23.38	7 %	24.33	13 %	-	-
P4S4	57.95	12 %	-	-	-	-
P4S5	159.25	20 %	-	-	-	-
P5S4	23.03	3 %	25.7	3 %	-	-
P5S5	33.78	5 %	21.3	2 %	20.48	14 %
P5S6	51.95	8 %	-	-	-	-
P5S7	58.63	4 %	-	-	-	-
P5S8	92	5 %	-	-	-	-
P6S6	21.85	10 %	16.15	2 %	41.68	69 %
P6S7	27.55	3 %	25.98	27 %	15.25	8 %
P6S8	31.83	5 %	28.15	13 %	19.38	3 %
P7S8	21.93	11 %	14.78	2 %	14	14 %

Table B4. Average ID/IG and I2D/IG ratio values and respective standard deviation percentages for all tested laser operation power, speed, defocus levels, and scan number parameters.

	I_D/I_G		I_{2D}/I_G	
Parameters	**Average**	**RSD (N=5)**	**Average**	**RSD (N=5)**
P4S6 (3.02 mm)	1.12	15 %	0.40	15 %
P4S6 (1.75 mm)	1.01	11 %	0.34	4%
P4S6 (0.48 mm)	0.82	18 %	0.49	8%
P4S6 (-0.79 mm)	0.99	11 %	0.28	10 %
P5S6	0.58	6%	0.44	9 %
P6S6	0.63	9 %	0.41	6 %
P7S6	0.71	12 %	0.39	7 %

Table B5. Tested riboflavin modified pH sensors sensitivity summary with respective y-intercept and R2 values.

Sensors	**Sensitivity mV pH^{-1}**	**y-intercept (mV)**	**R^2**
1	-81.2	-120.5	0.9824
2	-74.9	-176.3	0.9582
3	-74.4	-116.9	0.9803
4	-82.5	-148.1	0.975
5	-74.3	-143.7	0.9936
6	-77.8	-197.2	0.9821
7	-79.3	-184.6	0.9747
8	-80.6	-99.4	0.9805
Average	-78.2 ± 3.37	-148.3 ± 35.19	0.9784 ± 0.01000

C

APPENDIX FOR CHAPTER 5

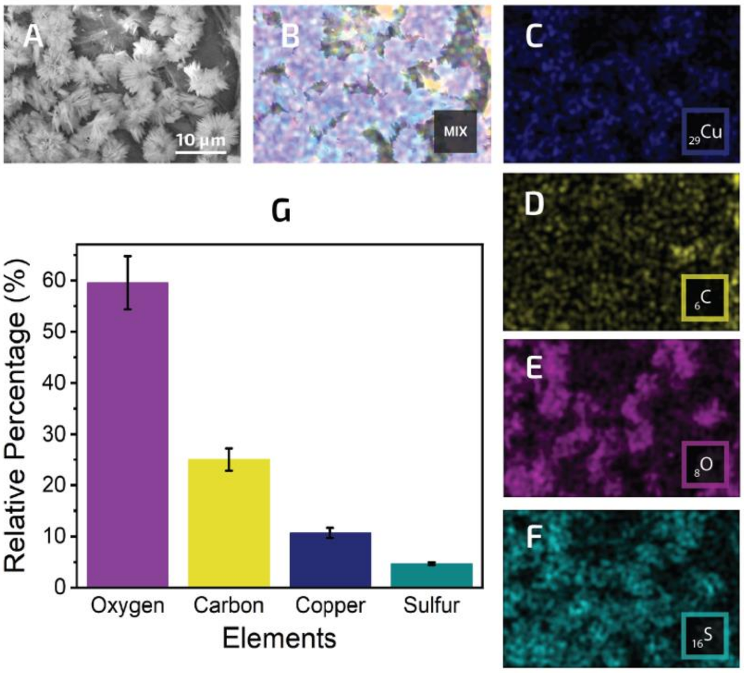

Figure C1 – SEM/EDS analysis of paper surface with deposited CuSO4.

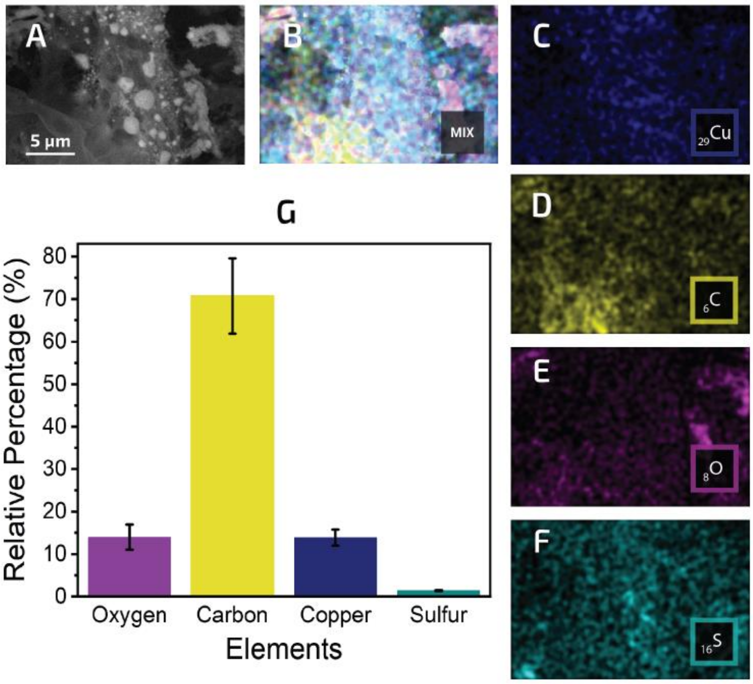

Figure C2 – SEM/EDS analysis of LIG/CuNPs composites by one-step laser synthesis.

Table C1. Electrochemical parameters of CuNPs/LIG based sensors.

Electrodes	ECSA (mm2)	ECSA/Ag	k0 (10-3 cm/s)
#1	14.72	3.00	8.04
#2	13.18	2.68	9.09
#3	12.07	2.46	8.39
#4	14.81	3.02	8.76
Average	13.70	2.79	8.57
RSD (%)	9.61		5.30

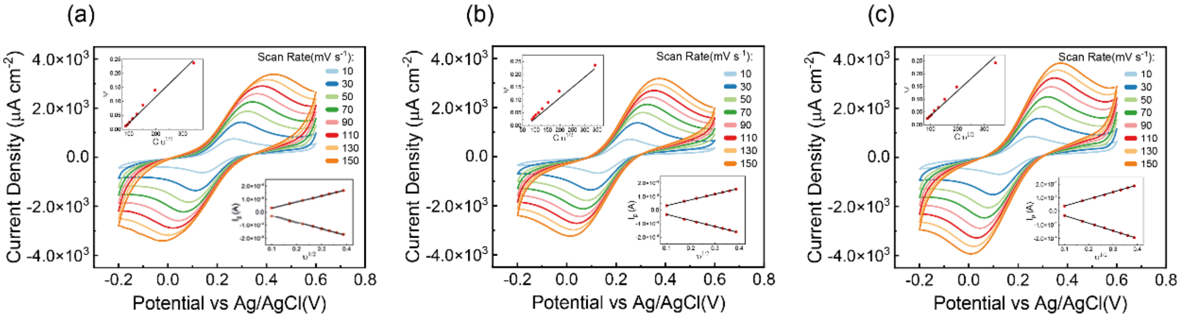

Figure C3 – Electrochemical characterization of CuNPs/LIG electrodes. (a-c) Cyclic voltammograms of three different CuNPs/LIG sensors obtained for a scan rate range of 10 to 150 mV.s^{-1}, using 5 mM $[Fe(CN)_6]^{3-/4-}$ as redox probe. Both insets represent auxiliary plots for the determination of the kinetic parameters: the right graph is a plot of peak currents vs square root of corresponding scan rate and the left one is a plot of kinetic parameter Ψ vs C.v$^{-1/2}$.

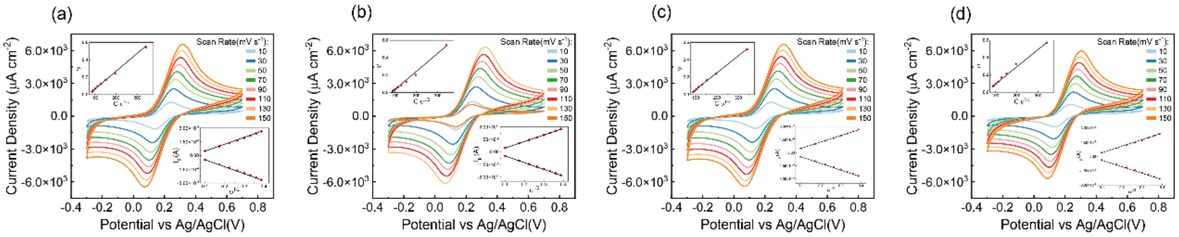

Figure C4 - Electrochemical characterization of LIG electrodes. (a-c) Cyclic voltammograms of four different LIG sensors obtained for a scan rate range of 10 to 150 mV.s^{-1}, using 5 mM $[Fe(CN)_6]^{3-/4-}$ as redox probe. Both insets represent auxiliary plots for the determination of the kinetic parameters: the right graph is a plot of peak currents vs square root of corresponding scan rate and the left one is a plot of kinetic parameter Ψ vs C.v$^{-1/2}$.

Current calculation process for calibration, where the data extracted from the chronoamperograms was treated as follows:

1. The current values were extracted in the instant before each glucose addition and 20 seconds after that, which was the time interval for the current stabilization.

2. Next, the in−1 value was subtracted from the in to determine the current variation (Δin) corresponding to each glucose addition.

3. Finally, the Δin value was added to the cumulative current responses previously registered, so that each current response is dependent on the total glucose concentration inside the beaker.

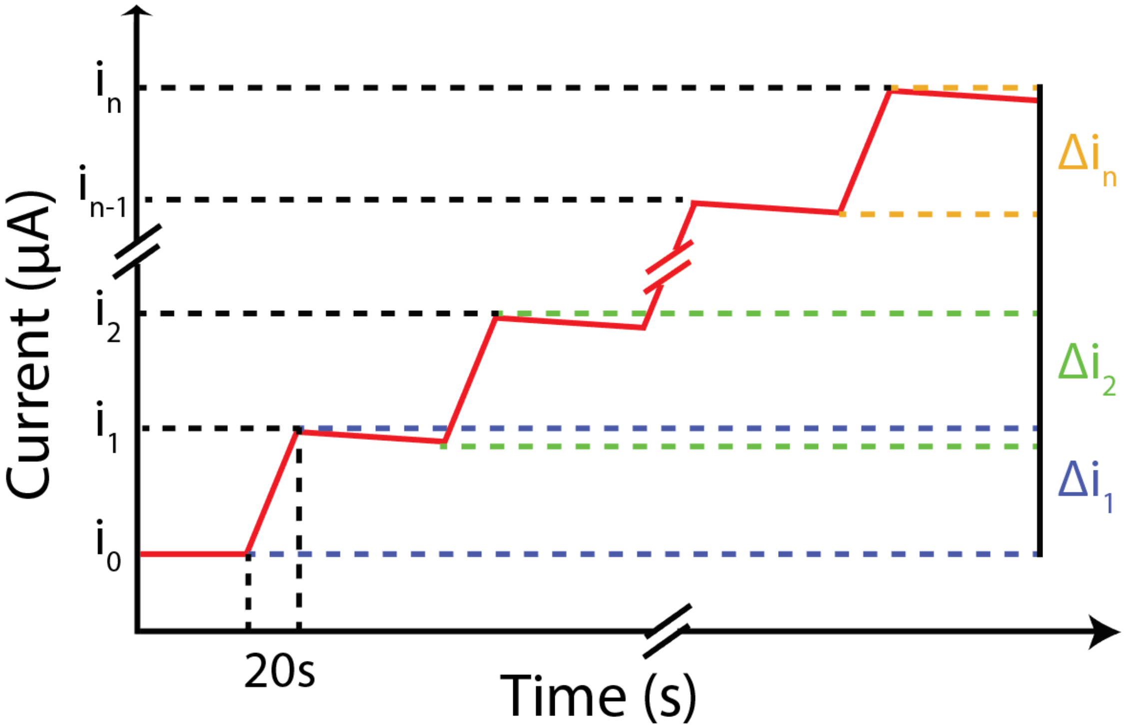

Figure C5 – Representative chronoamperogram and current steps showing the process for sensor current calibrations.

D

Appendix for Chapter 6

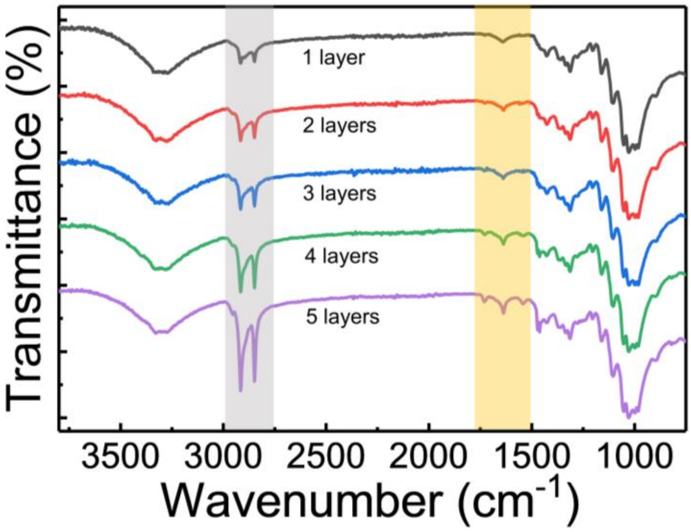

Figure D1 – FTIR spectra of chromatography paper substrates modified with increasing number of wax layers, showing the increase in intensity of peaks associated with both paraffin wax and yellow dye giving color to the printing wax

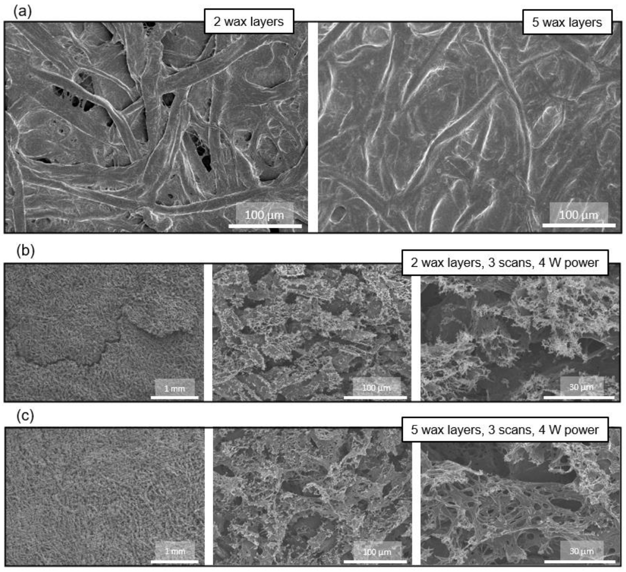

Figure D2 – SEM analysis of waxed paper and resulting LIG. (a) Paper-wax composite produced using 2 and 5 printing cycles. (b, c) LIG synthesized on wax-paper composite made with (b) 2 wax layers and (c) 5 wax layers.

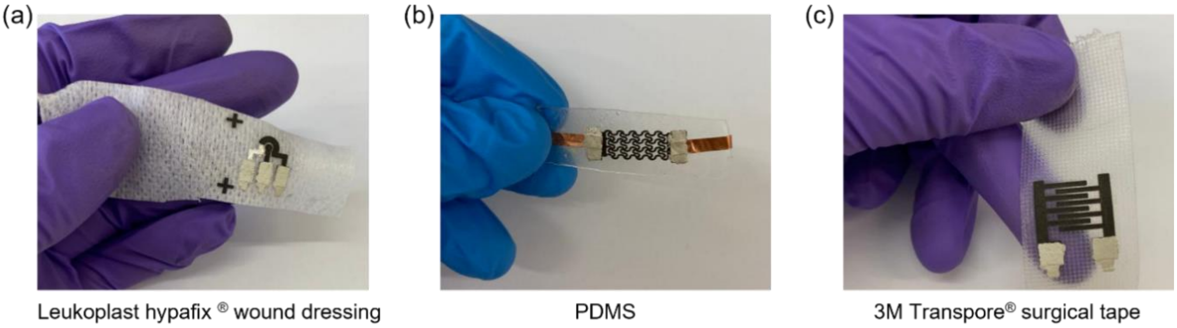

Figure D3 – Transferred LIG patterns over various substrates. (a) Transfer of electrodes for the fabrication of planar electrochemical cells on Leukoplast hypafix ® wound dressing. (B) Strain gauge transferred over PDMS, after spraying of a layer of repositionable adhesive for anchoring of LIG structures. (c) Transfer of interdigitated electrodes over 3M Transpore ® surgical tape containing a mild adhesive layer.

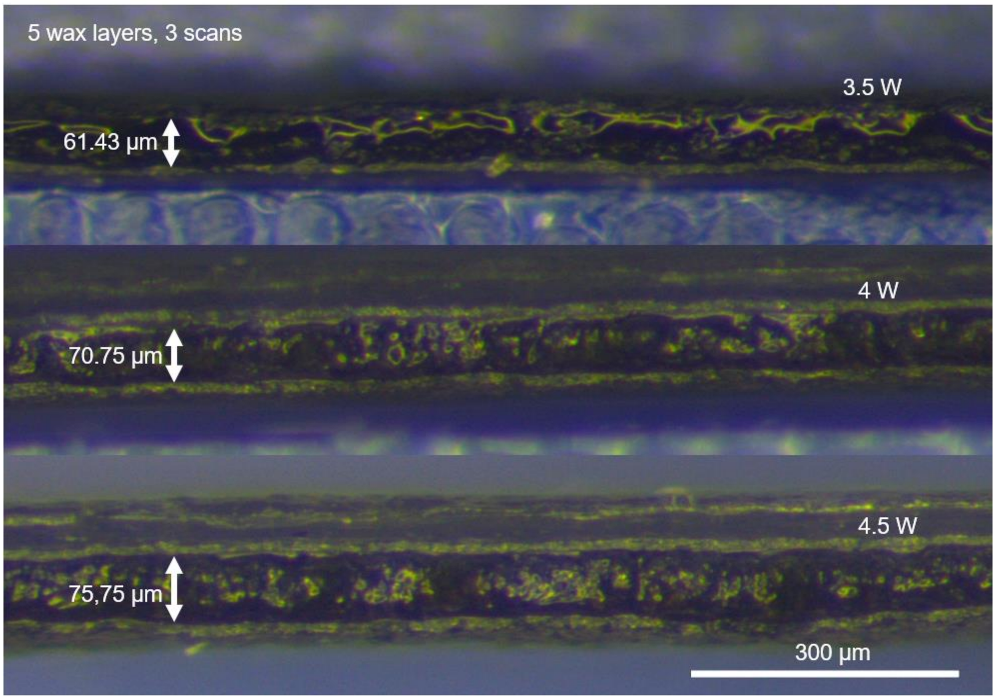

Figure D4 – Cross-section analysis of LIG squares used for conductivity assessment.

Table D1 – Comparison of Raman chemical features and conductivity of LIG from different precursors.

Precursor	Laser Source	I_D/I_G	I_{2D}/I_G	Sheet resistance ($\Omega.sq^{-1}$)	Conductivity (S.cm-1)	Ref
PI	IR, CO_2	0.5	----	15	25	1
PI	IR, CO_2	1	1	36.9	34.4	2
PEI	IR, CO_2	0.2	0.65	15	6.7	3
Phenolic resin	IR, CO_2	----	----	40	4	4
Nomex paper	IR, CO_2	----	0.95	15	8.9	5
Wood	IR, CO_2	0.8	0.6	10	1.25	6
Wood	UV femtosecond laser (343 nm)	0.63	----	10	2.75	7
Wood with catalyst	IR, CO_2	0.25	0.75	20	25	8
Leaves	Yb-doped femtosecond fiber laser	----	----	23.3	4.8	9
Forest-based ink	IR, CO_2	----	----	3.8	28	10
Paper	IR, CO_2	0.88	0.84	61.5	0.95	11
Paper	IR, CO_2	0.5	----	32	2.94	12
Paper	IR, CO_2	0.6	1.3	56	5.95	13
Paper	IR, CO_2	----	----	100	1.17	14
Paper	$Nd:YVO_4$ UV (355 nm)	----	----	132	2.0	15
Xylan	IR, CO_2	----	----	186	0.67	14
Wax-treated paper	IR, CO_2	0.28	0.69	5	28.2	This work

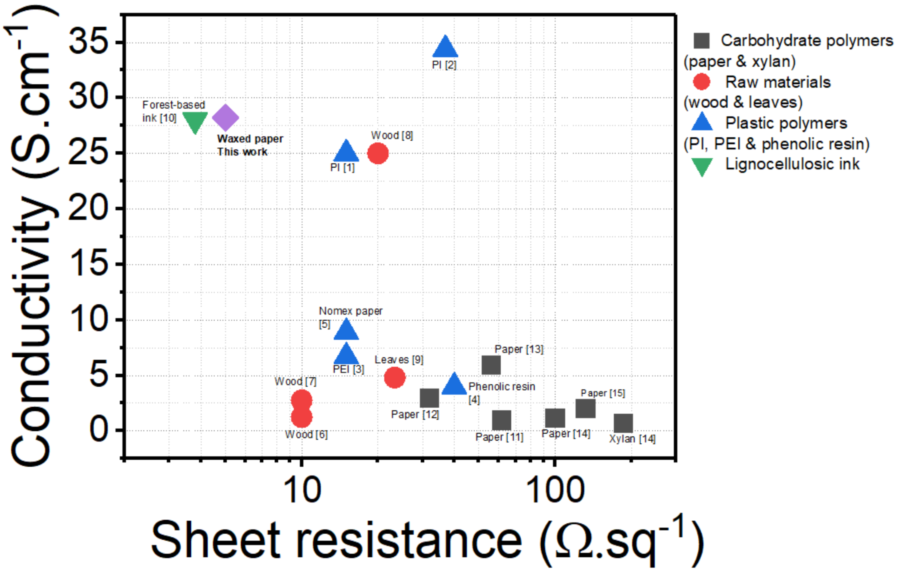

Figure D5 – Plot of sheet resistance vs. apparent conductivity of several LIG films produced from different precursor groups, including carbohydrate polymers, raw materials, plastic polymers and formulated inks.

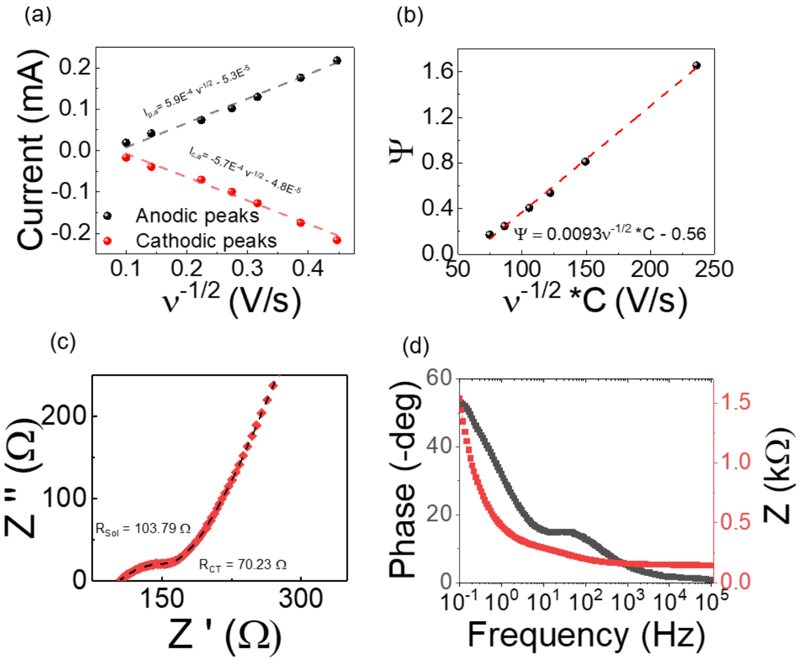

Figure D6 – Characterization of electrochemical planar cells. (a) Plot of anodic and cathodic peak currents vs. square root of scan rate, for calculation of electrochemically active area through the Randles Sevcik equation. (b) Plot of dimensionless kinetic parameter Ψ vs. square root of scan rate for the calculation of rate constant k0. (C) Nyquist plot of an electrochemical cell for solution and charge transfer resistance determination. (D) Corresponding Bode plot.

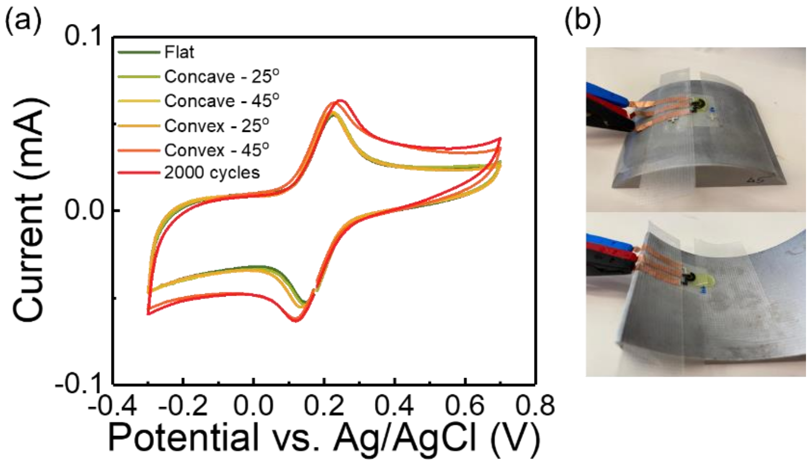

Figure D7– Characterization of electrochemical cells at different bending angles using CV at 50 mV.s^{-1}. (a) CVs showing small variation in peak position and current for concave (25 and 45o) and low convex (25o) angles and small increase in current and peak separation for high convex angle (45o) and after 2000 bending cycles with 5% strain, caused by a mild separation of LIG fibers and increase in the surface area of the LIG electrodes. (b) Image of electrochemical cells at concave and convex testing angles.

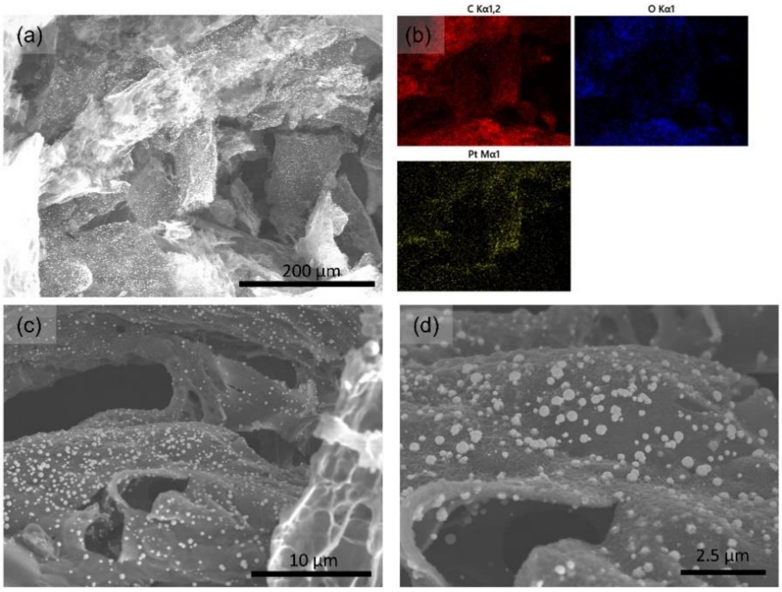

Figure D8 – SEM micrographs of electrodeposited PtNPs. (a) Far-off view of electrode surface, with a uniform distribution of particles at electrode surface. (b) EDS mapping of elemental distribution for C, O and Pt. (c and d) Magnified view of PtNPs distribution, showing a spherical geometry and sizes around 100 to 500 nm.

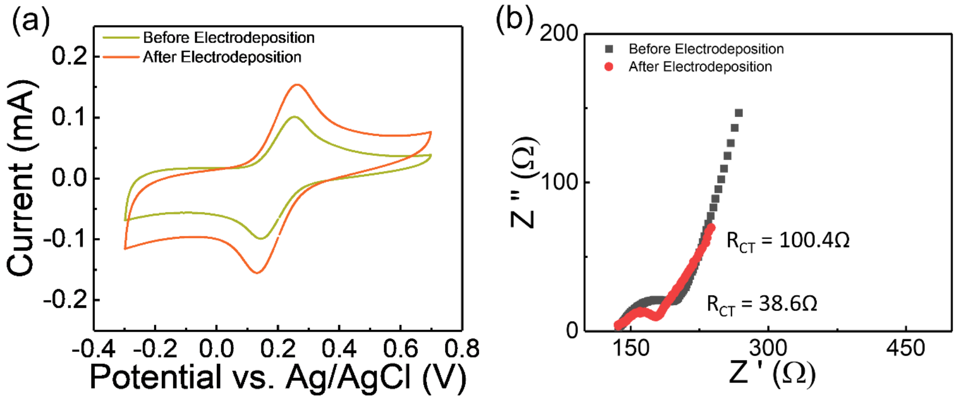

Figure D9 – Characterization of planar cells before and after PtNPs electrodeposition. (a) CVs at 50 mV.s^{-1}, showing an increase in peak currents for electrodeposition at the WE. (b) Nyquist plots showing decreased charge transfer resistances.

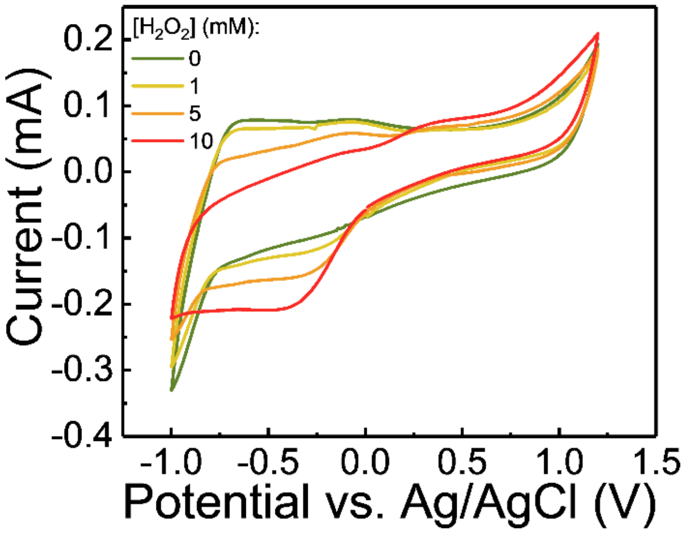

Figure D10 – CVs of the response of PtNPs modified WE in the presence of different concentrations of H_2O_2 in PBS buffer at 50 mV.s^{-1}. Both anodic currents at positive potential biases and cathodic current at more negative potential biases are visible, due to both oxidation and reduction of H2O2 at platinum modified electrode surface. Positive applied potentials were selected for analysis of sensor performance.

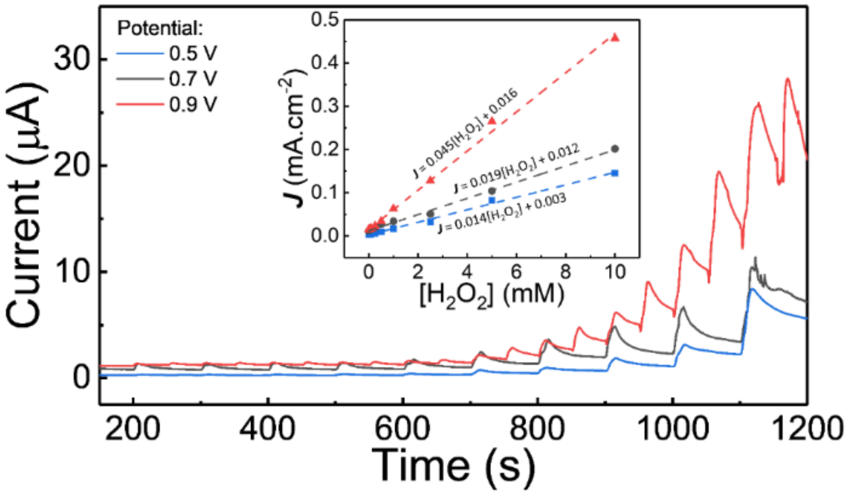

Figure D11 – Chronoamperometry study of sensor response to increasing concentration of H2O2 at different applied potentials (0.5 to 0.9 V), showing variation in sensitivity.

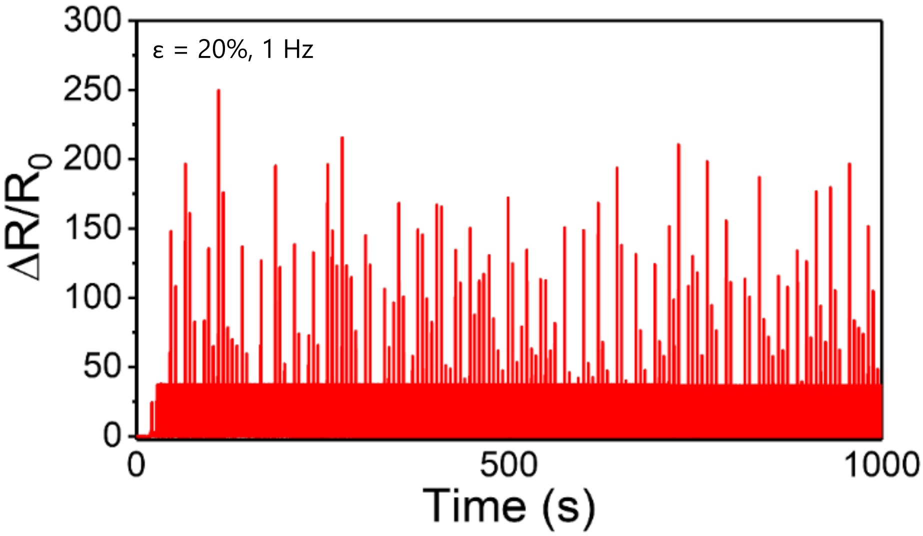

Figure D12 – Response of flexible strain gauges to bending strain cycling at 20% strain and 1 Hz frequency, showing the presence of triboelectric effects attributed to the polyurethane transfer substrate, as seen by the spikes in $\Delta R/R_0$.

Table D2 – Comparison of LIG-based electrochemical hydrogen peroxide sensors.

Material	Linear range (μM)	Sensitivity ($\mu A.mM^{-1}.cm^{-2}$)	LOD (μM)	Ref
PI-LIG/Au/PtNPs	10-3760	69.33	2.2	16
PI-LIG/sputtered PtNPs	0.5-5000	248.4	0.1	17
PI-LIG/Cu-Ru NPs	10-4320	136.7	1.8	18
PI-LIG/PB in electropolymerized PEDOT	10-1760	24.33	2.5	19
PI-LIG/ZnO	0.8-14600	276.8	190	20
PI-LIG/MWCNT	2000-12000	6.25	----	21
PI-LIG/PB	1-200	0.1	0.26	22
PI-LIF/AgNPs	10-550	28.6	2.8	23
Wax modified Paper-LIG/PtNPs	50-13200	16	11	This work

PtNPs – platinum nanoparticles; MWCNT – multiwalled carbon nanotube; PB – prussian Blue; PEDOT - Poly(3,4-ethylenedioxythiophene); ZnO – zinc oxide; AgNPs – silver nanoparticles

Table D3 – Comparison of LIG-based strain sensor performance.

Material	Laser Source	Strain/Dynamic range	GF	Ref
PI-LIG	IR, CO2	1.4 %	11.2	24
PI-LIG	UV, Nd:YVO4	1%	26	25
PI-LIG transferred to PDMS	IR, CO2	Up to 100%	20000	26
PI-LIG transferred to PU	IR, CO2	Up to 100%	70	27
PI-LIG transferred to silicone rubber	IR, CO2	31.8 %	37.8	28
Lignin embedded PDMS-LIG	UV, 355 nm	70 %	20	29
Lignin-LIG transferred to elastomeric DragonskinTM	IR, CO2	14 %	960	30
Kevlar textile-LIG	Femtosecond YB fiber laser, 1030 nm	7 %	185.2	31
Paper-LIG	IR, CO2	1.67 %	41.9	12
Paper-LIG transferred to PU	IR, CO2	20 %	128.9	This work

References

1. Lin, J. *et al.* Laser-induced porous graphene films from commercial polymers. *Nat. Commun.* **5**, 5714 (2014).
2. Meng, L., Turner, A. P. F. & Mak, W. C. Conducting polymer-reinforced laser-irradiated graphene as a heterostructured 3D transducer for flexible skin patch biosensors. *ACS Appl. Mater. Interfaces* **13**, 54456–54465 (2021).
3. Chyan, Y. *et al.* Laser-Induced Graphene by Multiple Lasing: Toward Electronics on Cloth, Paper, and Food. *ACS Nano* **12**, 2176–2183 (2018).
4. Zhang, Z. *et al.* Visible light laser-induced graphene from phenolic resin: A new approach for directly writing graphene-based electrochemical devices on various substrates. *Carbon N. Y.* **127**, 287–296 (2018).
5. Wang, G. *et al.* Nomex paper-based double-sided laser-induced graphene for multifunctional human-machine interfaces. *Carbon N. Y.* **193**, 68–76 (2022).
6. Ye, R. *et al.* Laser-Induced Graphene Formation on Wood. *Adv. Mater.* **29**, 1702211 (2017).
7. Le, T. D., Park, S., An, J., Lee, P. S. & Kim, Y. Ultrafast Laser Pulses Enable One-Step Graphene Patterning on Woods and Leaves for Green Electronics. *Adv. Funct. Mater.* **29**, 1902771 (2019).
8. Dreimol, C. H. *et al.* Sustainable wood electronics by iron-catalyzed laser-induced graphitization for large-scale applications. *Nat. Commun. 2022 131* **13**, 1–12 (2022).
9. Le, T. D. *et al.* Green Flexible Graphene–Inorganic-Hybrid Micro-Supercapacitors Made of Fallen Leaves Enabled by Ultrafast Laser Pulses. *Adv. Funct. Mater.* 2107768 (2021) doi:10.1002/adfm.202107768.
10. Edberg, J. *et al.* Laser-induced graphitization of a forest-based ink for use in flexible and printed electronics. *npj Flex. Electron.* **4**, 17 (2020).
11. Park, H., Kim, M., Kim, B. G. & Kim, Y. H. Electronic Functionality Encoded Laser-Induced Graphene for Paper Electronics. *ACS Appl. Nano Mater.* **3**, 6899–6904 (2020).
12. Kulyk, B. *et al.* Laser-Induced Graphene from Paper for Mechanical Sensing. *ACS Appl. Mater. Interfaces* **13**, 10210–10221 (2021).
13. Pinheiro, T. *et al.* Laser-Induced Graphene on Paper toward Efficient Fabrication of Flexible, Planar Electrodes for Electrochemical Sensing. *Adv. Mater. Interfaces* **8**, 2101502 (2021).
14. Kulyk, B. *et al.* Conversion of paper and xylan into laser-induced graphene for environmentally friendly sensors. *Diam. Relat. Mater.* **123**, 108855 (2022).
15. Kulyk, B. *et al.* Laser-Induced Graphene from Paper by Ultraviolet Irradiation: Humidity and Temperature Sensors. *Adv. Mater. Technol.* **7**, 2101311 (2022).
16. Yoon, H., Nah, J., Kim, J., Xuan, X. & Park, J. Laser-Induced Graphene Stamp for High Performacne Elecrochemical Sensing Applications. *Proc. IEEE Int. Conf. Micro Electro Mech. Syst.* **2019-January**, 537–540 (2019).
17. Zhang, Y. *et al.* Laser-induced Graphene-based Non-enzymatic Sensor for Detection of Hydrogen Peroxide. *Electroanalysis* **31**, 1334–1341 (2019).
18. Thirumalai, D. *et al.* In situ synthesis of copper-ruthenium bimetallic nanoparticles on laser-induced graphene as a peroxidase mimic †. doi:10.1039/d0cc07518c.
19. Meng, L., Turner, A. P. F. & Mak, W. C. Conducting Polymer-Reinforced Laser-Irradiated Graphene as a Heterostructured 3D Transducer for Flexible Skin Patch Biosensors. *Cite This ACS Appl. Mater. Interfaces* **13**, 54465 (2021).
20. Zanoni, J. *et al.* Dual transduction of h2o2 detection using zno/laser-induced graphene composites. *Chemosensors* **9**, 102 (2021).
21. Settu, K., Lai, Y. C. & Liao, C. T. Carbon nanotube modified laser-induced graphene electrode for hydrogen peroxide sensing. *Mater. Lett.* **300**, 130106 (2021).
22. Matias, T. A. *et al.* Prussian blue-modified laser-induced graphene platforms for detection of hydrogen peroxide. *Microchim. Acta* **189**, 1–9 (2022).
23. Zhao, G. *et al.* High-performance hydrogen peroxide micro-sensors based on laser-induced fabrication of graphene@Ag electrodes. *Appl. Surf. Sci.* **565**, 150565 (2021).
24. Kaidarova, A. *et al.* Wearable multifunctional printed graphene sensors. *npj Flex. Electron. 2019 31* **3**, 1–10 (2019).
25. Carvalho, A. F. *et al.* Laser-Induced Graphene Strain Sensors Produced by Ultraviolet Irradiation of Polyimide. *Adv. Funct. Mater.* **28**, 1805271 (2018).
26. Rahimi, R., Ochoa, M., Yu, W. & Ziaie, B. Highly Stretchable and Sensitive Unidirectional Strain Sensor via Laser Carbonization. *ACS Appl. Mater. Interfaces* **7**, 4463–4470 (2015).
27. Dallinger, A., Keller, K., Fitzek, H. & Greco, F. Stretchable and Skin-Conformable Conductors Based on

Polyurethane/Laser-Induced Graphene. *ACS Appl. Mater. Interfaces* **12**, 19855–19865 (2020).

28. Huang, L. *et al.* Wearable Flexible Strain Sensor Based on Three-Dimensional Wavy Laser-Induced Graphene and Silicone Rubber. *Sensors* **20**, 4266 (2020).
29. Lee, C. W. *et al.* Fabrication of laser-induced graphene-based multifunctional sensing platform for sweat ion and human motion monitoring. *Sensors Actuators A Phys.* **334**, 113320 (2022).
30. Yang, S. *et al.* Lignin-derived porous graphene for wearable and ultrasensitive strain sensors. *J. Mater. Chem. C* **10**, 11730–11738 (2022).
31. Kim, Y. J. *et al.* Direct-laser-conversion of Kevlar textile to laser-induced-graphene for realizing fast and flexible fabric strain sensors. *CIRP Ann.* **71**, 473–476 (2022).

E

APPENDIX FOR CHAPTER 7

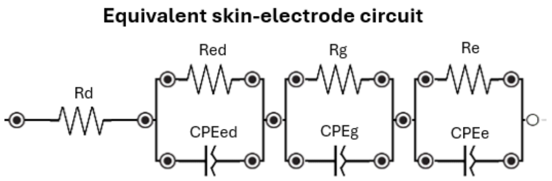

Element	Re	Rg	Red	Rd
Ag/AgCl	9.20E4	2.70E4	2.37E4	377.9
PI-LIG gel	5.21E4	1.00E12	4672	506.6
PI-LIG dry	6.38E4	2.94E4	3480	218.5
LIG@PU gel	3.66E4	8172	2.53E4	247.7
LIG@PU dry	8681	3.864	1.75E4	243.9

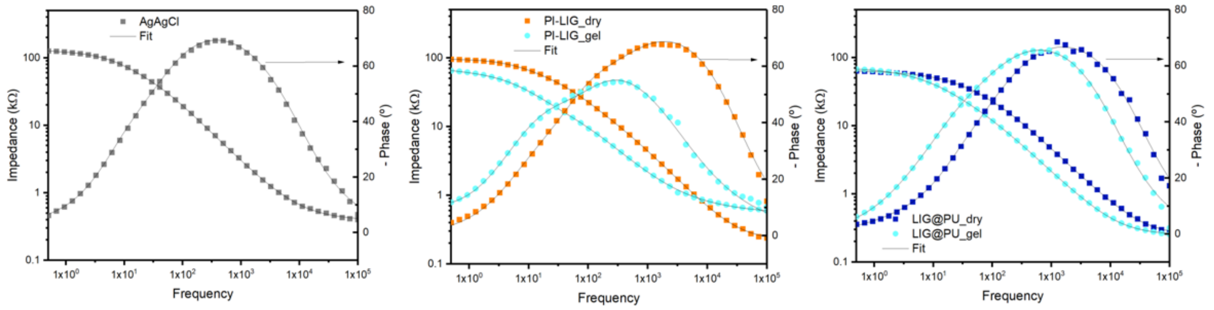

Figure E1 - Bode plot fitting according to the presented equivalent skin-electrode circuit for Ag/AgCl electrodes, gelled and dry LIG electrodes and resulting values for the resistive elements of the circuit.

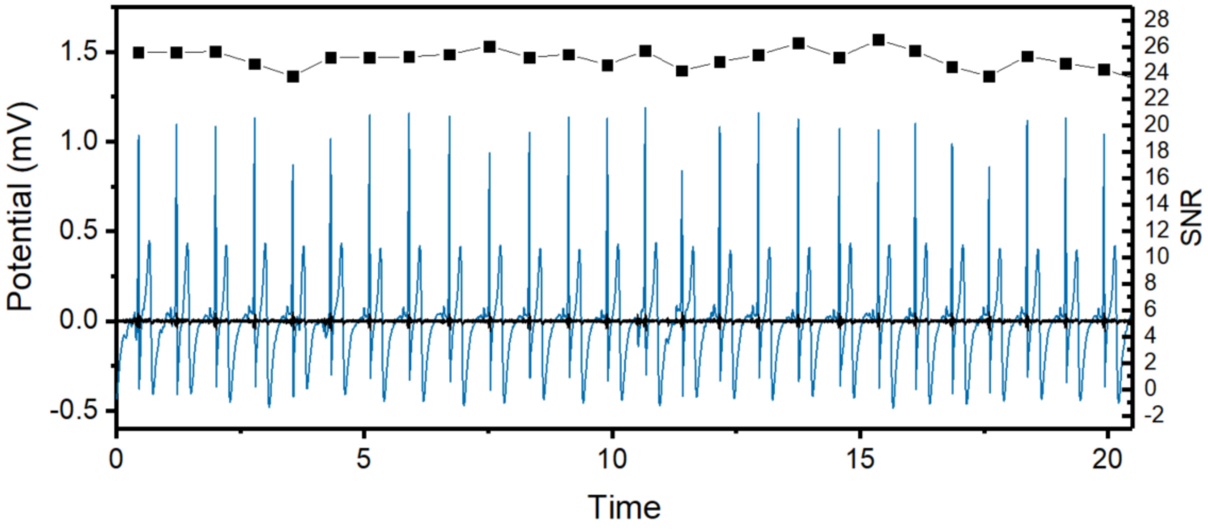

Figure E2 - ECG signal acquisition using LIG@PU dry electrodes with 5mm diameter, 24 hours after placement, with corresponding SNR values for each signal segment (period between consecutive P waves)

1. Laser processing of transfer substrate

2. Paper-based LIG bioelectrode transfer

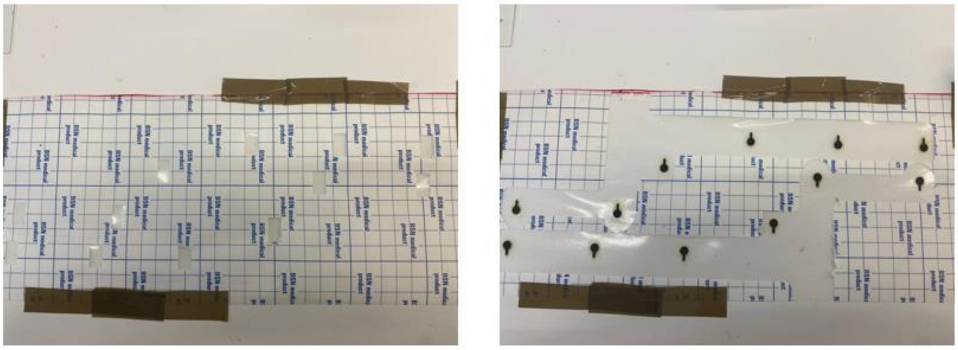

3. Silver serpentine track patterning

4. Connector placement and device encapsulation

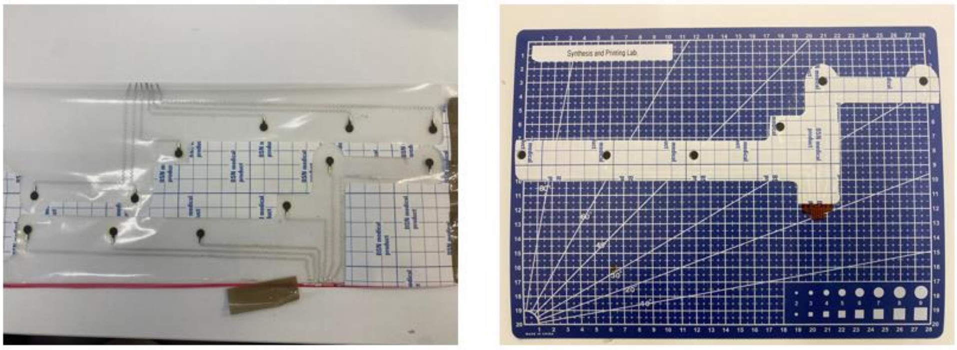

Figure E3 - Laser processing and assembly step for the chest-scale ECG patch.

A. Electrode layer

A1. Electrode trasfer onto PU substrate (w/ via holes)

A2. Electrode layer encapsulation

A3. Inversion and via hole filling with silver ink

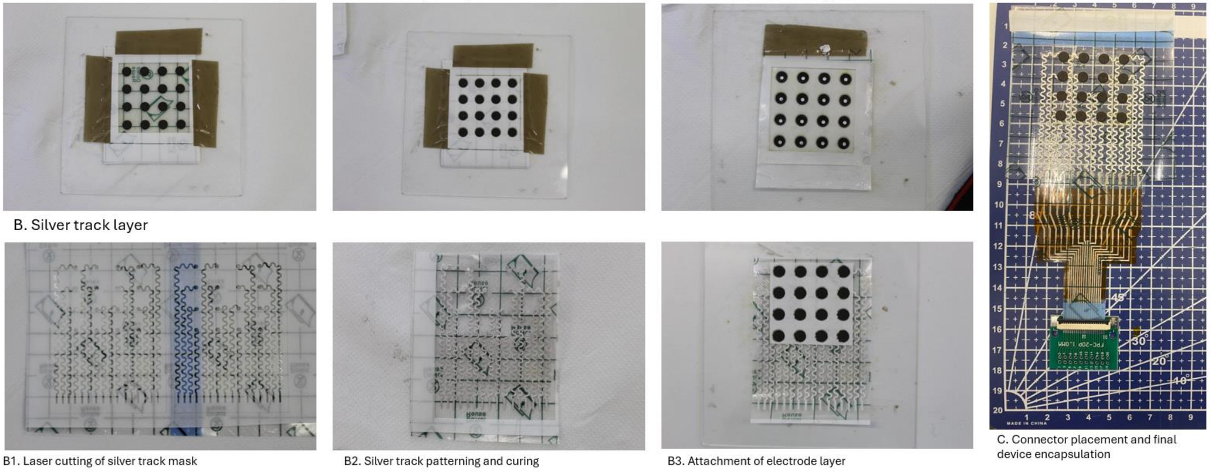

B. Silver track layer

B1. Laser cutting of silver track mask

B2. Silver track patterning and curing

B3. Attachment of electrode layer

C. Connector placement and final device encapsulation

Figure E4 - Laser processing and assembly steps for the sEMG electrode array patch.

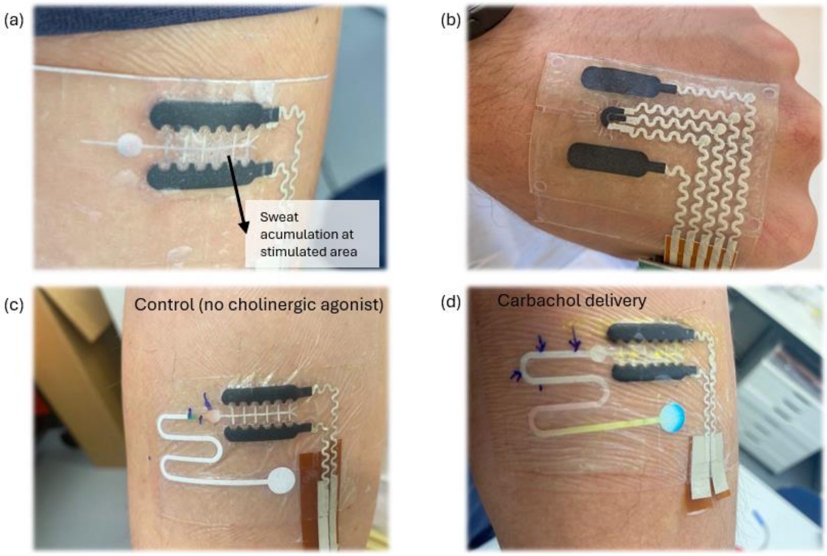

Figure E5 - Different LIG bioelectrode designs and assembly for sweat volume estimation. (a) Indented electrode with paper microfluidic network for sweat accumulation. The microfluidic network did not have the necessary length for efficient sweat accumulations. (b) Rectangular electrodes with epifluidic network for sweat accumulation and transportation. This device presented too many layers (accumulation, inlet, microfluidic and encapsulation layers), when constructing the epifluidic module, leading to inefficient capture of sweat. (c) Control testing of indented iontophoresis electrode integrated with a long paper microfluidic element, where no carbachol is delivered (hydrogels containing NaCl). Sweat accumulation due to baseline perspiration is visible, using a colored dye immobilized in microfluidic network. (d) Testing of carbachol delivery using the paper microfluidic network, showing a complete filling of the paper microfluidic network (~30 µL). For higher volumes, larger microfluidic component was needed, requiring a larger area, while image processing was required for analysis of collected sweat volume.

Transferred LIG/CuNPs were constructed by the same methods presented in Chapter 5, where copper sulfate precursor was dop-casted in a specified area of the paper substrate, followed by laser synthesis and patterning of the working and counter electrodes. After this, electrodes were transferred onto the PU substrates, followed by Ag/AgCl reference electrode and silver track patterning. Before measurement, the sensor was submitted to a copper oxidation step, as described in Chapter 5, to further oxidize copper and have more density of Cu(II). After this, an agarose layer (0.5 % w/v) with 0.1 M dissolved NaOH was drop-casted onto the working electrode and left to dry in 4ºC. The sensors were able to detect current increases associated with glucose addition, but only for higher concentrations (>100 µM). Furthermore, there is shift in the linearity for the sensor response over time, probably associated with the loss of hydroxide ions over time (not permanently immobilized within the agarose polysaccharide), diminishing its suitability for long term glucose detection when integrated with the iontophoresis module. Thus, an enzymatic sensing approach was taken, although further investigation regarding the modification with porous, alkaline membranes may be a possible solution for this issue.

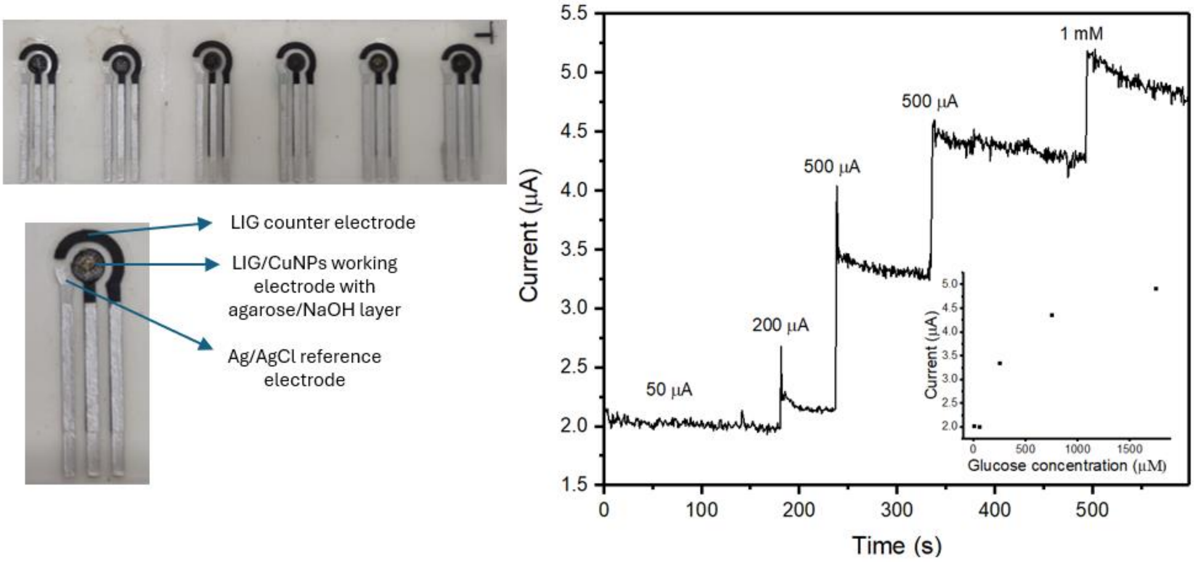

Figure E6 - Transferred LIG/CuNPs sensors for sweat glucose sensor and a representative device response curve.

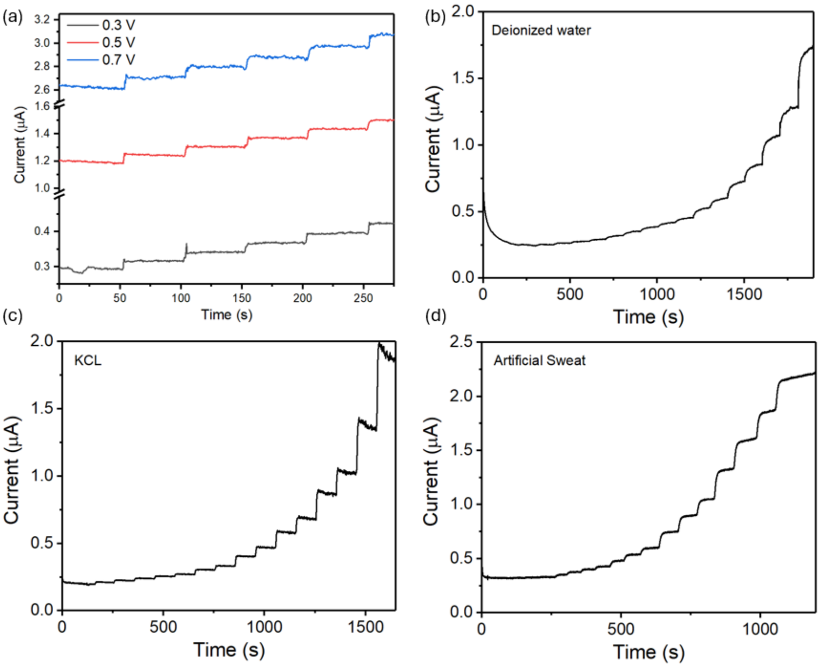

Figure E7 -Enzymatic glucose sweat biosensor testing. (a) Testing of device response for different potential biases, by consecutive addition of 100 μM glucose. Sensor response curves using (b) deionized water, (c) KCl and (d) artificial sweat electrolytes.

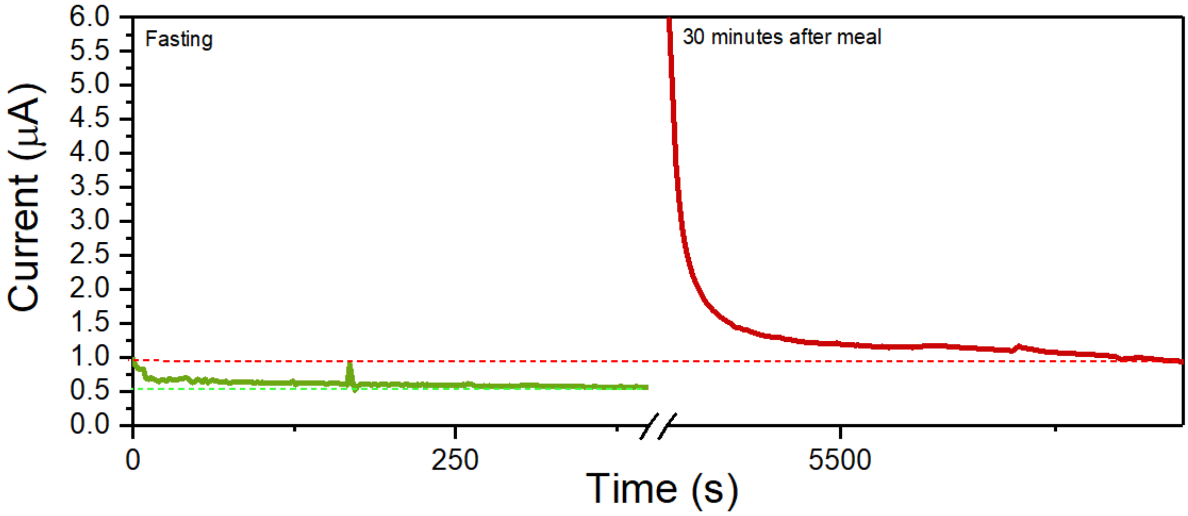

Figure E8 -Sweat glucose detection protocol for a second iontophoresis/sweat glucose sensor integrated device. Although an increase in sensor current is detected after a meal, the current level at a fasted state falls below the minimum values achieved for the calibration curve. This sensor was taken from a different fabrication batch, indicating that more investigation on sensor response and calibration are needed. In-device integration strategies that monitor pH, temperature, electrolyte levels or other factors may be needed in future investigations for more robust sweat glucose detection levels.

Skin-Interfaced, Graphene-based Bioelectronics
for Biomedical Applications

Tomás Pinto e Cruz de Oliveira Pinheiro

2024